

Ion production and optical set-up for single Ytterbium ion trap experiment

by

Lakhi Sharma
10PP16A32021

A thesis submitted to the
Academy of Scientific & Innovative Research
for the award of the degree of
DOCTOR OF PHILOSOPHY
in
SCIENCE

Under the supervision of

Dr. Subhasis Panja
&
Dr. Subhadeep De



CSIR - National Physical Laboratory
New Delhi, India



Academy of Scientific and Innovative Research
AcSIR Headquarters, CSIR-HRDC campus
Sector 19, Kamla Nehru Nagar,
Ghaziabad, U.P. – 201 002, India

August 2021

Certificate

This is to certify that the work incorporated in this Ph.D. thesis entitled, “*Ion production and optical set-up for single Ytterbium ion trap experiment*”, submitted by **Lakhi Sharma** to the Academy of Scientific and Innovative Research (AcSIR) in fulfillment of the requirements for the award of the Degree of *Doctor of Philosophy in Sciences*, embodies original research work carried-out by the student. We, further certify that this work has not been submitted to any other University or Institution in part or full for the award of any degree or diploma. Research material(s) obtained from other source(s) and used in this research work has/have been duly acknowledged in the thesis. Image(s), illustration(s), figure(s), table(s) etc., used in the thesis from other source(s), have also been duly cited and acknowledged.

(Signature of Student)

Lakhi Sharma

(Signature of Co-Supervisor)

Dr. Subhadeep De

(Signature of Supervisor)

Dr. Subhasis Panja

STATEMENTS OF ACADEMIC INTEGRITY

I **Lakhi Sharma**, a Ph.D. student of the Academy of Scientific and Innovative Research (AcSIR) with Registration No. **10PP16A32021** hereby undertake that, the thesis entitled “***Ion production and optical set-up for single Ytterbium ion trap experiment***” has been prepared by me and that the document reports original work carried out by me and is free of any plagiarism in compliance with the UGC Regulations on “*Promotion of Academic Integrity and Prevention of Plagiarism in Higher Educational Institutions (2018)*” and the CSIR Guidelines for “*Ethics in Research and in Governance (2020)*”.

Signature of the Student

Date:

Place:

It is hereby certified that the work done by the student, under my/our supervision, is plagiarism-free in accordance with the UGC Regulations on “*Promotion of Academic Integrity and Prevention of Plagiarism in Higher Educational Institutions (2018)*” and the CSIR Guidelines for “*Ethics in Research and in Governance (2020)*”.

Signature of the Co-supervisor (if any)

Name: Dr. Subhadeep De

Date:

Place:

Signature of the Supervisor

Name: Dr. Subhasis Panja

Date:

Place:

Acknowledgement

My interest in scientific research got piqued in the course of studying the fluorescence spectrum of the Indian firefly as a part of my Dissertation Thesis while pursuing a Master's Degree in Physics. This instance enhanced my curiosity and interest in the field of research which finally led me to embracing the path of Ph.D. thus landing me to the "Single trapped ion optical frequency standard (STIOS)" laboratory of CSIR - National Physical Laboratory (CSIR - NPL). The journey of a research life is never easy, it brings both ups and downs but apart from being difficult, it is interesting too. The motto during the exhausting times is not to be daunted by it, instead to collect the experiences and keep advancing. Despite all the hindrances and setbacks at certain moments, my Ph.D. journey has been a successful and a memorable one due to the efforts of many people around me. I would like to thank these people and give them due acknowledgement for their contributions and support throughout the journey of my PhD work.

In the first place, I extend a deep sense of gratitude towards my parents who have been constant pillars of support for me. Their tremendous moral support and unswerving belief in me and my potential encouraged me to overcome various arduous situations in my life. I also thank them and my elder brothers for always being supportive of my higher education; and my sisters-in-law and younger sister for always standing by my side in times of emotional affliction. My genuine and heartfelt acknowledgement goes to my Ph.D. supervisors Dr. Subhasis Panja and Dr. Subhadeep De for their proficient guidance and fruitful discussions over regular meetings which played a vital role in accomplishing my Ph.D. thesis work. It is because of their informations and instructions that I could avail additional academic opportunities like attending various schools, conferences and workshops, which in many ways have supplemented my knowledge, research aptitude and a better understanding of works going on in my research area. I always got influenced by their massive dedication towards research and scientific temperament. I would also like to thank them for their propositions at times when I am stuck in the mid of an experiment, for their timely examination of my scientific drafts inspite of their busy schedules and also for bearing my flaws with great patience. I also received both constructive and harsh criticism during my journey but this has indeed led to my growth as a researcher.

I am highly grateful to my Thesis Doctoral Advisory Committee (DAC) members Dr. Jiji Pulikkotil, Dr. Parveen Saini and Dr. Mukesh Jewariya and current H.O.D. of our division, Dr. Anurag Gupta as their scientific opinions and dialogues while assessing presentations of my Doctoral work have refined my knowledge as well as content of my thesis. Uplifting words of appreciation and encouragement from Sub-divisional head Dr. Ashish Agarwal and

former H.O.D. of our division, Dr. V. N. Ojha have always been impelling to keep doing better. My sincere vote of thanks also goes to Dr. Mahesh Kumar, Dr. Preetam Singh, Dr. Rajeev Rakshit and Dr. Manju Singh of CSIR-NPL for allowing access to their laboratory and research facilities. I owe a debt of gratitude to my Physics tutor, the late Amarendra Dey who encouraged me to pursue this degree.

One's Ph.D. life may be stressful and exasperating at certain times owing to failures at workplace or other administrative/bureaucratic issues. A positive work environment is therefore an essential element for staying sane during this journey and I have been lucky enough to have got labmates who have always been reassuring. To be far away from home for the first time was down-heartening for me but the amicable, lively, cheerful and considerate nature of my senior labmates Neha Batra, Atish Roy and Sankar Majhi gave me a congenial atmosphere. I shall really cherish conversations during break times, those sudden Momo plans and all the good times spent with my junior labmates Harish Rathore and Shubham Utreja. My other labmates Neelam and Richa are also a delight to work with. I extend my deep sense of acknowledgement to my labmate, my friend, my all-time mentor and my beloved husband Atish Roy for always being helpful and untiringly supportive in all aspects, both personal and professional matters. I thank him for investing his time for all of our thought-provoking scientific discussions, doubt clearance and for persistently being alongside me and teaching me the right scientific approach and for augmenting my confidence and enlivening me on awful days.

A special word of gratitude goes to the entire family of Time and Frequency Metrology Subdivision; and its technical staff including: Ved Prakash Ji, Sajjan Ji, Devender Ji, Prem Ji and Kaushik Ji, who have always been there for guidance and help in various administrative processes. A special mention of thanks to the HRD members of our institute Soma Ma'am, Manju Ma'am, Joshi Sir and Reena Ma'am for their co-operation and fast processing of paper works related to my PhD or for attending conferences as well as to the members of Workshop of CSIR-NPL for timely and desired accomplishment of tasks rendered to them. I would like to thank Director, CSIR-NPL and Academy of Scientific and Innovative Research (AcSIR) for allowing me to carry out my research work in this esteemed laboratory and Department of Science and Technology (DST) for INSPIRE fellowship. Last but not the least, I am thankful to my dear friends Nikita, Sandhya, Shital, Sadiya, Sadaf, Damini, Pooja and Jyoti Saroha for their love, encouragement, help and counselling to overcome occasional pessimism. It is actually impossible to bring up each and every person's name who had an impact on my work but I am immeasurably grateful to each one of them as with such amazing people, my Ph.D. journey has been a wonderful one despite of various obstacles.

Above all, a doctoral degree is not a cake walk, it's a roller coaster ride, there are highs and lows in this journey but there are moments of WOW too. It teaches time management, independent creative thought, self motivation, *etc.*; and the quest for learning should be kept on to keep striding further. At last, I would like to thank the Almighty for rendering me the

knowledge, ability and patience to embark on this research study and to persist and accomplish it satisfactorily.

Table of Contents

1. <i>Introduction</i>	3
1.1 Optical frequency standards	4
1.1.1 Types of optical clocks	6
1.2 Principle of ion confinement within an ion trap	8
1.2.1 Yb ion optical clock	10
1.2.2 Experimental protocol	11
1.3 Objective of the thesis	15
2. <i>Estimation of electrical loads and BBR shift associated to Ion-trap and resonator assembly</i>	19
2.1 Introduction	19
2.2 Methodology	21
2.2.1 Analytical methods	22
2.2.2 Numerical method	26
2.2.3 Experiment	29
2.3 Results and Discussions	30
2.4 Conclusion	36
3. <i>A low-divergent atomic oven and its atomic flux distribution</i>	39
3.1 Introduction	39
3.2 Oven design and its atomic flux distribution	41
3.2.1 Initial designs	42
3.2.2 Working design	43
3.2.3 Modified atomic flux distribution	45
3.3 Results and discussions	48
3.3.1 Theoretical simulations	48
3.3.2 Experimental results	53
3.4 Conclusion	55

4. <i>An imaging system with sub-micron resolution for detecting fluorescence from a single trapped ion</i>	57
4.1 Introduction	57
4.2 Design of the lens system	59
4.2.1 Aberration theory	59
4.2.2 Methodology	62
4.2.3 Design	63
4.3 Results and Discussions	63
4.3.1 Choosing the desirable lens system	64
4.3.2 Optical performance of L _o -O1-M1 system	65
4.3.3 Fabrication tolerance	68
4.3.4 Mounting	69
4.3.5 Method for performance analysis	70
4.4 Advantages of L _o -O1-M1 system	71
4.5 Applications of an imaging system	74
4.5.1 Spatial thermometry of ions	74
4.6 Conclusion	75
5. <i>Frequency stabilization of a diode laser to a hyperfine transition of molecular iodine for trapped Yb ion</i>	77
5.1 Introduction	77
5.2 Theory	79
5.3 Experimental setup	81
5.3.1 Setting up the Iodine cell	81
5.3.2 Optics and electronics setup	82
5.4 Results and Discussions	85
5.4.1 SAS signal	85
5.4.2 Lock signal	88
5.4.3 Noise density profile	89
5.5 Conclusion	90
6. <i>Absolute frequency measurement for $^1S_0 \rightarrow ^1P_1$ transition of Yb atoms and its isotope-selective photoionization</i>	93
6.1 Introduction	93
6.2 Schemes for photoionization loading of Yb ions	95
6.3 Experimental set-up	96
6.4 Results and Discussions	98
6.5 Conclusion	102

7. Conclusion 103

References 107

List of Figures

1.1	Schematic representation of an atomic frequency standard showing the three key ingredients: Natural oscillator, Local oscillator and a Frequency counter. The local oscillator’s frequency is pre-stabilized to a ULE cavity to probe the desired atomic transition. Signal from the probed transition is sent to a servo loop which generates and sends an error signal to the clock laser to tune its frequency to the atomic resonant frequency. The light is finally sent to the frequency counter to measure the clock cycle. BS: Beam Splitter, AOM: Acousto-optic modulator, $\lambda/4$: Quarter waveplate, $\lambda/2$: half waveplate.	5
1.2	Evolution of atomic clocks based on the improvement of fractional uncertainties in frequency.	6
1.3	(a) Energy level diagrams for $^{171}\text{Yb}^+$ showing the relevant transitions useful for building an optical ion clock and (b) Schematic showing the experimental protocol and various lasers required for different purpose in the experiment. . .	12
1.4	An outlook of the “Single trapped ion optical frequency standard” experiment in developing stage at CSIR - NPL.	14
2.1	Ion-trap system of our experiment where the resonator (R) and ion-trap (T) are connected via a connector (C). The inserts show schematics of each part R , C and T where sources of the loads are indicated.	22
2.2	Electrical circuitry of (a) resonator (R), (b) connector (C), (c) ion trap (T) and (d) equivalent (E) of all three components. C_i , R_i and L_i as shown in the circuits denote capacitance, resistance and inductance, respectively, where the subscript i refers to R , C and T , respectively.	25
2.3	Meshed structures of (a) ion trap and (b) resonator obtained during COMSOL simulation	27
2.4	Snapshot of COMSOL window as seen when one starts using the software. It provides a user friendly platform for physics modelling, simulations with all necessary tools including a quick access toolbar, settings window, plot windows, information window, <i>etc.</i>	28

2.5	Snapshots showing steps to creating a model for studying related physics using COMSOL by choosing (a) plane, (b) study type and (c) physics and (d) defining the orderly sequence of operations in model tree of model wizard which includes the geometry, material, mesh size, boundary conditions, <i>etc.</i> (e) shows the mesh created for model of outer trap electrodes.	29
2.6	Experimental set-up for measurement of operating parameters of resonator at loaded and unloaded conditions.	30
2.7	Variation of the (a) resonant frequency and (b) quality factor with capacitance for the resonator itself (green) and for the resonator + connector without the ion-trap connected to it (red). The experimental data (black) and theoretically fitted lines to it are shown, where the width of the lines depict fitting inaccuracy. The measured capacitance (blue) of connector and the combination of connector and trap are indicated on the fitted curves and also shown in the inserts.	33
2.8	(a) Excess capacitance, C_{ex} and phase difference, ϕ and (b) the BBR shift, at RF amplitudes 250 V (cyan), 500 V (blue), 750 V (green) and 1000 V (red) at the trap electrodes; resulting from the machining inaccuracy are shown.	35
3.1	(a) and (c) shows the initial designs for oven with (b) and (d) the corresponding atomic deposition.	42
3.2	(a) Drawing of the dark wall oven and its holders for UHV mounting. (b) Schematic of the capillary consisting of three regions: reservoir, collimator and dark wall. (c) Details of components of the developed oven.	44
3.3	Picture showing the oven (a) inside the testing chamber and (b) assembled into the final UHV chamber.	45
3.4	Angular profile of atoms for different ovens such as, reservoir (blue), reservoir attached to a collimator (red) and dark wall oven (green). Inset shows critical and truncated angle (red) and half-width angle (blue) for different lengths of the capillary. Here, we consider $T = 249^\circ\text{C}$, $L = 65$ mm, $L_H = 35$ mm, $L_C = 30$ mm and $a = 0.45$ mm.	47
3.5	Snapshot of the COMSOL window showing simulation for temperature distribution in the oven at current 2.7 A. The model tree in model wizard shows the orderly sequence of operations including geometry, material, physics, mesh, study, plot groups, <i>etc.</i>	49
3.6	Numerically simulated variation of temperature (in $^\circ\text{C}$) along the length of the capillary for: (a) ovens with collimator and (c) in the presence of cold absorber. (b,d) show variation of the collimator's length L_H with current and corresponding reservoir temperature for a fixed operating voltage = 1.7 V.	50

3.7	(a) Variation of Yb vapor pressure (orange) and its mean free path (green) with temperature. (b) Output Yb flux with increasing temperature for bright oven with collimator (cyan) and dark wall oven (black) are shown. The discrete points in cyan and black are the corresponding numerical values, its inset emphasizes the critical temperature. Flux of atoms at different (c) cut off angles and (d) oven temperatures for fixed trap electrode voltage of 250 V (magenta), 350 V (black), 450 V (blue) and 550 V (red) that are available to be captured in our ion trap.	51
3.8	Images of the Yb atoms, deposited on a glass sample, taken from Digital Microscope at (a) 4 A, (b) 3.2 A and (c) 2.3 A, respectively.	53
3.9	Measured spatial profiles of Yb spot for: (a) end-to-end heating of the capillary at 2.3 A, (b) dark wall oven operated at 2.3 A (magenta), 3.2 A (cyan) and 4 A (green). (c) Relative angular profiles along with the fitted curves. (d) Variation of experimentally obtained truncated angle values for varying cold end length along with the fitted model.	54
3.10	Temperature dependence of the atomic flux coming out of the dark wall oven, as estimated numerically using COMSOL (blue) and using the measured $f(\theta)$ distribution function (red).	55
4.1	A wave from a point at a distance h from the origin in the object plane is incident on the entrance pupil from which it then propagates through an optical system towards the exit pupil. The entrance pupil, exit pupil and the image point are referred to by (y_e, z_e) , (y, z) and (Y, Z) , respectively.	60
4.2	Schematic of the imaging system considering a variety of objectives O1 - O4 and magnifiers M1 - M5. Lenses and wavefront corrector plates (WCP) are indicated as L_i and P_i , respectively, where i is their numbers. The collection lens L_o , and optics in objective, magnifier are of standard 25 mm and 50 mm diameter, respectively. For the L_o -O1-M1 combination, indicated length scales are $X_o = 31.6$ mm, $X_1 = 60.4$ mm, $X_2 = 58.2$ mm, $X_3 = 34$ mm and $X_4 = 4154$ mm.	64
4.3	(a) Strehl ratio (SR) and (b) spherical aberration (SA) for all possible combinations of objectives (O1 - O4) and magnifiers (M1 - M5) those we have studied.	65
4.4	(a) Point spread functions (PSF) simulated by OSLO (blue), and calculated from analytical relation (filled with cyan) at the final image of the L_o -O1-M1 combination. The PSF at the intermediate image plane (red) is shown for comparison. (b) Variations of SR (blue) and SA (purple) due to deviation of magnifier M1 from its ideal position <i>i.e.</i> $X_3 = f_{L3}$ is shown, which tunes the magnification. Images are shown in the insets for at a glance quality comparison.	68

4.5	Images of trapped ions on (a) xy (c) yz planes. Corresponding variation of SR and SA as the ion's position deviates from best focus. Depth of field (DOF) and Field of View (FOV) are indicated.	69
4.6	A 3D drawing showing the planned scheme for mounting the lens assembly with appropriate optics tube and accessories for easy position adjustment to avoid misalignment.	70
4.7	SolidWorks drawing of the (a) front and (b) rear view of the PMT mount. The 2 inch circular grooving at front side is to hold a SM2 lens tube. The holes at the front and bottom planes are to secure the PMT and the optics post. . . .	71
4.8	(a) OSLO drawing of lens system used for testing using USAF target (b) Surface Data sheet of the OSLO simulation showing the input parameters for the displayed lens combination system and (c) the Paraxial setup editor giving the resultant parameters as numerical aperture and magnification.(d) A USAF 1951 resolution test target consisting of groups 2 to 7 of elements of different resolutions. (e) Images obtained from the detector for elements of Group 6 and Group 7 of a USAF-1951 resolution target. The inset shows the resolved first element of Group 7.	72
4.9	(a) Change in SR (green empty circle) and SA (blue empty circle) values of the images due to inaccurate positioning of the collection lens L_o with respect to its focus f_{L_o} . Corresponding SR (green full circle) and SA (blue full circle) after incorporating corrections by tuning the magnifier's position are also shown. (b) SR and SA at different wavelengths (corresponding to different species), <i>e.g.</i> , 369.5 nm (Yb^+), 382 nm (Ra^+), 397 nm (Ca^+), 422 nm (Sr^+), 461 nm (Sr), 493.5 nm (Ba^+), 646 nm (Lu^+) and 852 nm (Cs).	73
4.10	Broadening of point spread function as modelled for different spatial extents resulting from ion's thermal motion.	74
5.1	Absorption Spectra of hyperfine transitions of molecular iodine from 739.03 nm to 739.06 nm at 450 °C. Difference in frequencies between the desired setpoint and available hyperfine transition is shown.	80
5.2	Arrangement for heating the Iodine cell: (a) Iodine cell with the cold finger. A heating tape is wrapped round the cell for its uniform heating. (b) Layers of aluminium foil and fibre glass wool wound around the vapor cell for insulation so that surrounding optics remain unaffected.	82
5.3	(a) Schematic and (b) Experimental set-up for carrying out SAS of iodine. Here, M: mirror, L: convex lens, L' : concave lens, f: focal length of lens, PBS: polarizing beam splitter, $\lambda/2$: half waveplate, $\lambda/4$: quarter waveplate, EOM: electro optic modulator and AOM: acousto optic modulator.	83

5.4	(a) Doppler broadened absorption spectrum (red) and Doppler free spectrum (magenta) of molecular iodine obtained experimentally, (b) positions of hyperfine transitions obtained from IodineSpec5 (blue) and from SAS experiment (magenta) and their corresponding error signals (green) for a wavelength scan from 739.0332 nm to 739.0349 nm with vapor cell heated to 450 °C. A total of six Doppler free peaks are observed which are labelled as 1-6; almost all of them are resolved.	86
5.5	Variation of peak amplitude of Doppler free feature labelled 4 with increasing (a) cell temperature and (b) pump beam power, along with the fits.	87
5.6	Error signal (red) for peak (magenta) and their corresponding lock signals (green and blue, respectively) when laser is stabilized to top of the peaks for (a) experimentally obtained saturation absorption peak of a ₁₀ component and (b) SHG cavity peak of the laser system.	88
5.7	(a) Frequency drift of the fundamental frequency of the cooling laser when locked to SAS peak no. 4 over 50 hours and (b) the corresponding histogram with the Gaussian fit for linewidth determination.	89
5.8	Voltage spectral density of noise floor of the spectrum analyser (green), error signal when locked to the top of SAS signal (blue) and SHG cavity peak (red).	90
6.1	Energy level diagram for Yb relevant to its photoionization. (a) Scheme 1: a 2-photon ionization process (b) Scheme 2: a 3-photon ionization process.	95
6.2	Schematic of the optical set-up for carrying out isotope selective fluorescence spectroscopy followed by ionization. Here, M: mirror, L: convex lens, L': concave lens, S: beam sampler, $\lambda/2$: half waveplate, BB: beam blocker and PBS: polarizing beam splitter.	97
6.3	(a) A 3D illustration of Yb atomic beam interacting orthogonally with coupled 399 nm and 369 nm laser beams, Snapshot of oven operating inside the test chamber when the laser frequency is scanned: (b) At non-resonant condition (c) At resonant condition.	98
6.4	Fluorescence excitation spectra of Yb isotopes. Different isotopes are labelled and their excitation frequencies are plotted relative to that of ¹⁷⁴ Yb.	99
6.5	(a) Frequency drift of the 399 nm when locked using WS7 wavelength meter over 14 hours and (b) the corresponding histogram with the Gaussian fit for linewidth determination.	100
6.6	Signal trace for two-photon ionization of ¹⁷¹ Yb at oven current of 2.3 A.	101

List of Tables

2.1	Estimated values of the loads resulting from different parts of the ion-trap system. AC resistances are indicated by superscript ‘ac’.	32
2.2	Values of the loads obtained through different methods	34
4.1	Estimated values of parameters for different lens combinations that we studied, where the magnifiers in conjunction with O1 are shown here. Abbreviations are Asp: asphere, WCP: Wavefront corrector plate, Ach: achromat, and PC: plano convex lens.	66
4.2	Specifications of the L _o -O1-M1 lens system	67
4.3	Estimated values of various optical excellence parameters obtained using OSLO for wavelengths corresponding to different atom/ion species.	73
5.1	Details of the hyperfine transitions observed in R(78) (1-11) line of molecular iodine.	87
6.1	Absolute frequency measurement of the $^1S_0 \rightarrow ^1P_1$ transition for the naturally occurring isotopes of Yb	100

Chapter 1

Introduction

Experimenting on atomic ions and studying various dynamic processes within it can unravel many new phenomena or uncover established theories. An ion is interwoven with many processes in nature and so to have a higher precision in any related study or measurement, it is to be treated individually so that it has no interaction with its immediate environment causing perturbations. This alienation from the environment can be achieved by its confinement at isolated condition. Confinement of ions was made possible by Wolfgang Paul and Hans George Dehmelt in the late 1950s and early 1960s by their inventions of Paul trap and Penning trap, respectively [1–9].

Since the invention of ion traps, trapped ions have opened up many enthralling research areas in Physics. It has a versatile range of applications in mass spectrometry, laser cooling, studying non-neutral plasma and ion Coulomb crystals, studying various quantum effects, antimatter experiments, spectroscopy experiments, and many more [10–15]. Many other experiments based on basic physics also use trapped ions, such as, measuring hyperfine splitting of atomic energy levels, high precision measurements of fundamental quantities in atomic physics, measuring atomic parity non-conservation (APNC) due to exchange of a boson between electrons and nucleons, measuring electric dipole moment with atomic and molecular ions, measuring electron-proton mass ratio with molecular ions, *etc.* The most significant contribution and widely researched application of trapped ions can be seen in the arena of quantum information processing and frequency standards [16, 17].

A frequency standard or an atomic clock based on a trapped ion, besides measuring 1 second precisely and accurately, has immense applications in different fields. A few major applications are: relativistic geodesy [18, 19] enhancing navigation and timekeeping capabilities, radar, radio astronomy [20–22]; testing fundamental physics such as Einstein’s theory of relativity, detection

of gravitational wave, and aid in navigation with better precision and geoid monitoring *etc.* [23, 24]. CSIR-National Physical Laboratory (CSIR-NPL) is the National Measurement institute (NMI) of India and is therefore entrusted with the responsibility of realization, maintenance and dissemination of the local Universal Coordinated Time (UTC-NPLI) and Indian Standard Time (IST). Here, we are working towards trapping a single Ytterbium-171 ion ($^{171}\text{Yb}^+$) for developing an optical frequency standard. The primary objective in this experiment is trapping and laser cooling a single ion. The following sections expound optical clocks, their types, ion trapping principle, and experimental protocol of the ongoing frequency standard experiment at CSIR - NPL.

1.1. Optical frequency standards

A frequency standard or an atomic clock is basically an oscillator whose frequency is driven by and stabilized with respect to an atomic transition having ultra-narrow linewidth (Hz to sub mHz level). The time elapsed corresponding to the cycles of radiation produced by the said transition defines one second and constitutes a clock. Such atomic standards are far more stable compared to their mechanical counterparts as atomic transitions are ideally not prone to perturbations created by external environmental changes; they are therefore known to be the most stable as well as accurate timekeeping devices. The working principle of an atomic clock is presented schematically in Fig. 1.1. As can be seen, key components of an atomic clock are a reference oscillator (*i.e.*, a precise atomic transition) which is isolated from the environment; another frequency source or oscillator (laser), the output signal of which is locked to that precise atomic transition and eventually used to realize the unit of time or frequency. A feedback electronics keeps on correcting the local oscillator's *i.e.*, laser's output frequency by comparing it to that of the reference oscillator.

The performance of any frequency standard is defined by two important parameters: instability and inaccuracy. Instability refers to the fluctuations of a measured output about its average value; it is a type of statistical uncertainty. Most widely used protocol for measuring fluctuations in clock frequency over a time period is Allan deviation or Allan variance [25, 26]. Inaccuracy, elseways, refers to the shift in the average value of a measured parameter which cannot be measured but based on the probable sources of error, it can be estimated [16, 25]. The clock instability, σ_y for an averaging period τ is given by,

$$\sigma_y = \frac{\Delta f}{f_o \sqrt{N}} \sqrt{\frac{T_c}{\tau}}, \quad (1.1)$$

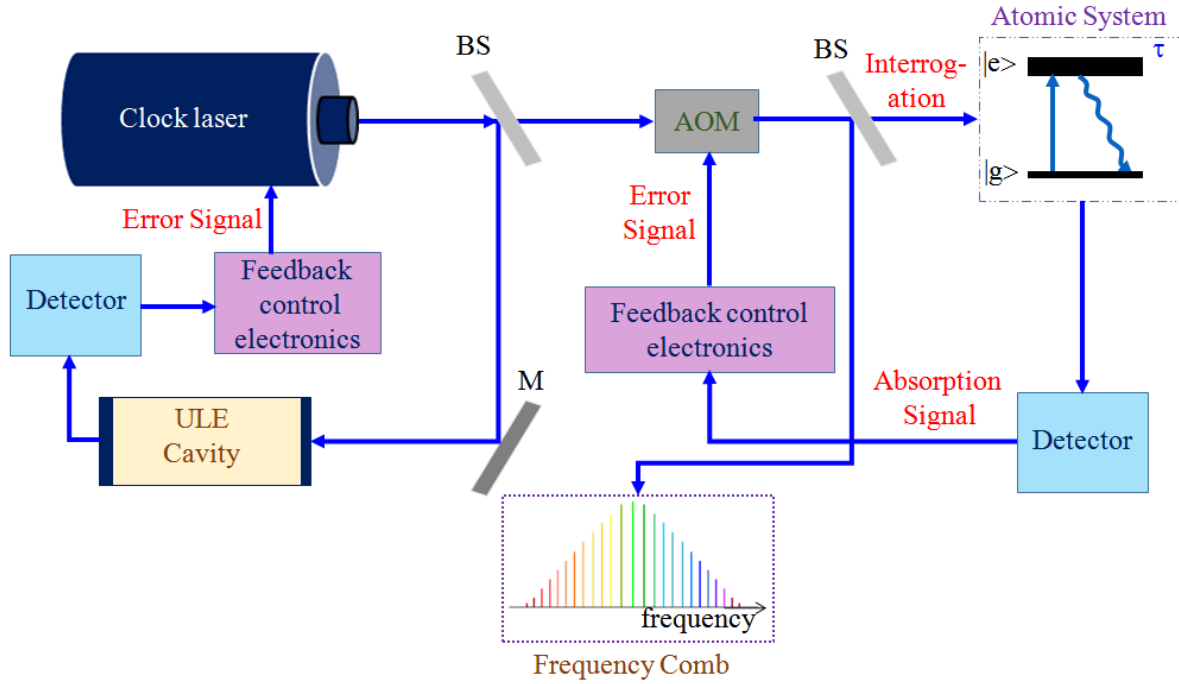


Fig. 1.1: Schematic representation of an atomic frequency standard showing the three key ingredients: Natural oscillator, Local oscillator and a Frequency counter. The local oscillator's frequency is pre-stabilized to a ULE cavity to probe the desired atomic transition. Signal from the probed transition is sent to a servo loop which generates and sends an error signal to the clock laser to tune its frequency to the atomic resonant frequency. The light is finally sent to the frequency counter to measure the clock cycle. BS: Beam Splitter, AOM: Acousto-optic modulator, $\lambda/4$: Quarter waveplate, $\lambda/2$: half waveplate.

where Δf is the transition linewidth, f_o is the reference oscillation frequency, N is the number of probed species and T_c is time for single measurement [27,28]. Here, $f_o/\Delta f$ gives the quality (Q)-factor and $\sqrt{T_c/N\tau}$ gives signal-to-noise ratio. It is clear from Eqn. 1.1 that narrow linewidth, higher clock frequency, large number of species and longer averaging periods are preferable for the better performances of a clock.

In 1955, Louis Essen and J. V. L. Parry realized first such atomic standard of frequency and time interval, which was based on the interrogation of ground state hyperfine transition of $^{133}\text{Cesium}$ (^{133}Cs) atoms in the microwave region [29]. In 1967, the Comité International des Poids et Mesures (CIPM) adopted the Cs standard as the SI definition of time and frequency. Technological development over more than five decades, in particular, development of laser cooling techniques [30], have helped to reduce the measurement uncertainty to which the centre frequency of the hyperfine transition of ground state ^{133}Cs atom can be measured to $\sim 10^{-16}$ [20,31–33]. However, clocks with even better accuracy and stability remain as essential requirement for many of the applied research as well as to address many advanced physics

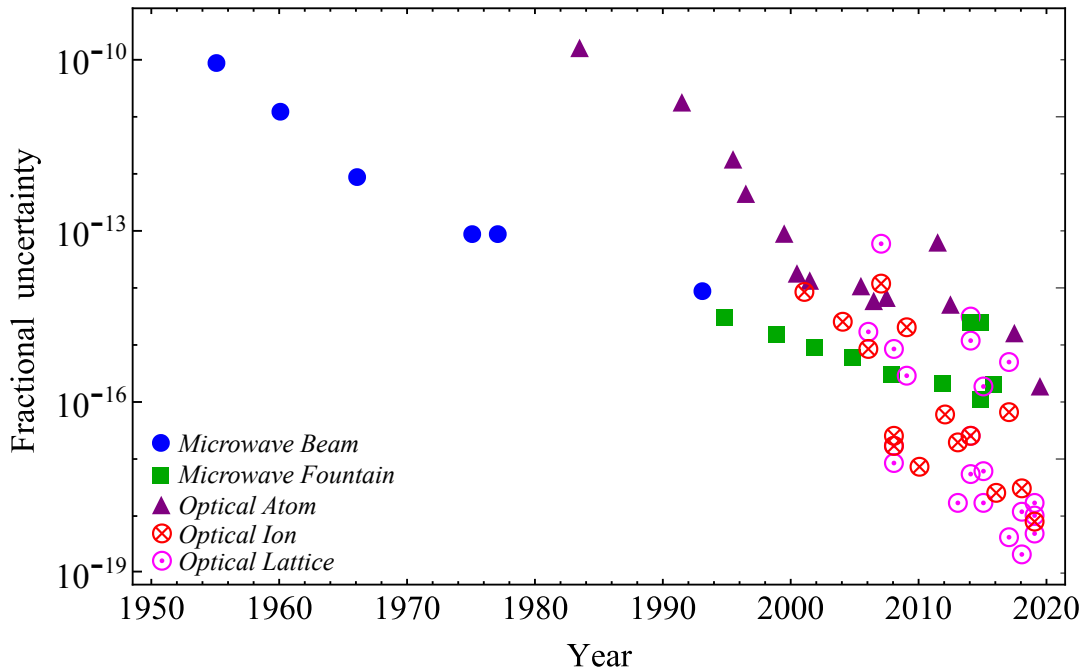


Fig. 1.2: Evolution of atomic clocks based on the improvement of fractional uncertainties in frequency.

problems related to communications, surveillances, testing temporal constancy of fine structure constant or testing electron proton mass ratio [24]. Precision experiments like detecting gravitational waves or testing general relativity require a clock with accuracy $\sim 10^{-18}$ or better [34, 35]. It is evident from Eqn. 1.1 that accuracy as well as stability of a clock increases with the increase of operational frequency of the clock, so an optical clock with operational frequency of several hundreds of THz is capable of providing orders of magnitude higher accuracy than the microwave Cs atomic clocks. With the advent and maturity of certain technologies, specifically speaking, the optical frequency comb, realization of optical standards became possible [17]. The evolution of performances of atomic clocks from microwave domain to optical regime has been shown in Fig. 1.2 and at present, the optical frequency standards are superior to the microwave ones in terms of both stability and accuracy.

1.1.1 Types of optical clocks

Activities on time & frequency metrology in optical domain have been carried out either by trapping neutral atoms or ions [17, 36, 37]. The neutral atoms are confined within optical lattices tuned to so called “magic wavelength” by inducing a dipole moment in the atom and exerting a force on this dipole through a laser field gradient [38, 39]. On the other hand, ions are confined within radio frequency (RF) ion trap and in order to avoid any perturbation of the

ionic clock transition due to Columbic interaction among the charged particles, only a single ion is preferred to be interrogated in the field free region of the trap centre [37, 40].

- **Atom-based Optical clock:** Alkaline earth (-like) atoms such as, calcium (Ca), mercury (Hg), magnesium (Mg), strontium (Sr), ytterbium (Yb), *etc.* those have narrow intercombination transition are some of the choices for developing atom-based optical clocks [41]. Neutral atom-based optical clocks are of two types: (a) atoms interrogated in free space, *i.e.*, free space standards (b) atoms interrogated by confining within optical lattice, *i.e.*, Optical lattice clocks. As evident in Eqn. 1.1, large number of interrogating species *i.e.* atoms implies a better signal to noise ratio and higher stability for a clock but at the same time, it is prone to many systemic shifts, dominated by collisional shifts [42]. Free space frequency standards have therefor been explored by several groups [43–46] but it was very difficult to achieve improvement in the fractional frequency uncertainty better than 10^{-15} and so researchers turned towards the optical lattice based clocks.

Optical lattice clocks are the new class of atomic clocks based on trapping of thousands to millions of cold atoms in potential energy wells [47, 48]. These energy wells or lattice sites are formed by focusing light to a waist-size of 50-100 μm in one direction and back-reflecting the same light onto itself to create a standing-wave pattern. The lattice laser wavelength is tuned to a so-called magic value, where both the states involved in clock transition are equally shifted, thus giving a zero differential shift. In optical lattices, several thousands of atoms are interrogated at a time, hence they are capable of providing better signal strength compared to single trapped ion clocks [49, 50]. NIST, USA developed and demonstrated an Yb lattice clock with stability of 1.4×10^{-18} [48] and have achieved the record frequency precision of 2.5×10^{-19} for ^{87}Sr [51], which is the best known optical clock till date.

- **Ion-based Optical clock:** Atomic ions with alkali-like or quasi-alkali-like atomic structure such as $^{199}\text{Hg}^+$, $^{88}\text{Sr}^+$, $^{40}\text{Ca}^+$, $^{171}\text{Yb}^+$ or, atomic ions with atomic structure similar to alkaline earth elements as aluminium ($^{27}\text{Al}^+$) and indium ($^{115}\text{In}^+$) are used in building single ion optical clocks. Invention of RF ion trap, commonly known as Paul trap paved the way to providing an unperturbed environment for confining an ionic species to perform various experiments on it [3, 45, 52]. The single trapped ion within an RF trap in an optical clock is cooled to milliKelvin temperature by laser cooling [53] and can be interrogated over longer period of time since the ion is free from inter atomic and Columbic interaction and in that way can have a very long coherence time [54]. Another key advantage of single trapped ion based optical clocks is that some of the optical transitions of these ions are extremely insensitive to the external perturbations like magnetic field or electromagnetic radiation of the ambient temperature field [55, 56]. The trap electrode

material is to be chosen keeping in mind the probable dominant systematic shifts that may perturb the clock frequency. Ion based clocks provide Doppler free environment but due to a single ion, it has to compromise with lower signal-to-noise ratio. Hence, it requires a very high resolution and diffraction limited imaging system for single ion detection [57] whereas clock transition is detected by employing electron shelving technique [58]. Thermal motion associated with time-averaged confining potential called as secular motion and driven oscillatory motion at applied RF frequency known as micro-motion are associated with trapped ions [59]. The NIST; SYRTE, NICT; NPL UK, NRC; MPIQ, NICT; PTB, NPL UK; NIST UK groups have worked on trapped $^{27}\text{Al}^+$, $^{40}\text{Ca}^+$, $^{88}\text{Sr}^+$, $^{115}\text{In}^+$, $^{171}\text{Yb}^+$, $^{199}\text{Hg}^+$, respectively and most of them have achieved appreciable fractional frequency uncertainty of the order of 10^{-17} .

1.2. Principle of ion confinement within an ion trap

For three dimensional confinement of ions, a binding force F pulling the ions radially inwards towards a central point is required with F having a linear dependence on position *i.e.*,

$$F \sim -r, \quad (1.2)$$

where r is position vector of the ion. Equation 1.2 denotes that potential energy E takes the form

$$E \sim ax^2 + by^2 + cz^2, \quad (1.3)$$

where a , b and c are coefficients determining curvature of potential ϕ . Assuming to create a trapping potential using electrostatic field to trap an ion of charge Q , ϕ can be written as,

$$\phi = \frac{\phi_o}{2r_o^2}(ax^2 + by^2 + cz^2), \quad (1.4)$$

where r_o is a trap size related parameter and ϕ_o is externally applied potential. To satisfy Laplace condition, $\Delta\phi = 0$ or $\nabla^2\phi = 0$; this gives $a + b + c = 0$ opening up two scenarios:

1. $a = -b = 1$ and $c = 0$, giving rise to a two dimensional quadrupole potential,

$$\phi = \frac{\phi_o}{2r_o^2}(x^2 - y^2), \quad (1.5)$$

which has a shallow axial confinement potential suitable for trapping chain of ions.

2. $a = b = 1$ and $c = -2$, giving rise to a three dimensional quadrupole potential,

$$\phi = \frac{\phi_o}{2r_o^2}(x^2 + y^2 - 2z^2), \quad (1.6)$$

resulting a cylindrically symmetric trap preferable for trapping single ion.

As can be seen here, the radial and axial co-ordinates have opposite sign, implying formation of a saddle-shaped potential, hence an unstable trap. This points towards the Earnshaw's theorem which states that charged particles cannot be trapped using electrostatic field alone [60,61]. The solution is combination of the static field with (i) a magnetic field establishing an electromagnetic trap called Penning trap or (ii) an oscillating electric field forming a radio-frequency trap called Paul trap.

In metrology experiments, a Paul trap is preferable over Penning trap in order to avoid imprecise measurements in presence of magnetic field. For a Paul trap, applied potential ϕ_o is,

$$\phi_o = U + V \cos \omega_{rf}t, \quad (1.7)$$

where U is a static electric field and $V \cos \omega_{rf}t$ is an oscillating electric field with V and ω_{rf} being its amplitude and driving frequency, respectively. The equations of motion of the trapped ion of mass M are equivalent to Mathieu's differential equations [62] as,

$$\frac{d^2u_i}{dt^2} + (a_i - 2q_i \cos 2\tau)u_i = 0, \quad i = 1, 2, 3, \quad (1.8)$$

where

$$u_1 = x, \quad u_2 = y \quad \text{and} \quad u_3 = z, \quad (1.9)$$

$$a_x = a_y = -\frac{4QU}{Mr_o^2\omega_{rf}^2}, \quad \text{and} \quad a_z = \frac{8QU}{Mr_o^2\omega_{rf}^2}, \quad (1.10)$$

$$q_x = q_y = \frac{2QV}{Mr_o^2\omega_{rf}^2}, \quad \text{and} \quad q_z = -\frac{4QV}{Mr_o^2\omega_{rf}^2}, \quad (1.11)$$

$$\tau = \frac{1}{2}\omega_{rf}t. \quad (1.12)$$

The solution to Eqn. 1.8 follows from Floquet theorem [63,64] and it describes the trapped ion's motion. The stability of the solution depends on the dimensionless parameters, a_j and q_j also known as Mathieu's parameters which are a function of Q/M , r_o , ω_{rf} , U and V . The parameters $q_{x,y}$, $a_{x,y}$ and q_z , a_z govern the ion's motion in x , y and z direction, respectively. A stability diagram ($a_j - q_j$ diagram) called Mathieu stability curve for the solution of Eqn. [62] is obtained where $a - q$ overlapping region is the stability region. A particle remains trapped

if the solutions lie in the stability region, otherwise it gets ejected. For a three-dimensional confinement, acceptable values of a_j and q_j are those for which the obtained solution is stable in both radial and axial directions simultaneously [3, 65]. The final motion of the trapped particle is a harmonic oscillation whose amplitude is modulated by trap's driving frequency ω_{rf} resulting in a driven motion called “micromotion” along with a slower secular motion called “macromotion” at frequency $\omega_{u_i} = \beta_{u_i} \omega_{rf}$ with $\beta_{u_i} = \sqrt{a_{u_i} + q_{u_i}^2/2}$.

1.2.1 Yb ion optical clock

The choice of experimental species for an atomic clock depends on parameters such as the chosen atoms or ions should have a forbidden/narrow line-width transition to be used as the clock transition and a strong allowed transition so that they can be efficiently prepared by laser cooling. Also, the transitions involved in the experiment for building the clock should be in the near ultra-violet to near infrared domain so that the required lasers are easy to build and easy to handle too. We chose to trap $^{171}\text{Yb}^+$ to build the atomic clock in optical domain. The chosen $^{171}\text{Yb}^+$ is one of the eight candidates recommended by CIPM for secondary representations of the second (SRS) *i.e.* it can be used for redefinition of the SI unit of time and frequency [66,67]. It possesses three transitions suitable for clocks namely: $|^2S_{1/2}, F = 0\rangle \rightarrow |^2F_{7/2}, F = 3\rangle$ at 467 nm, $|^2S_{1/2}, F = 0\rangle \rightarrow |^2D_{3/2}, F = 2\rangle$ at 436 nm and $|^2S_{1/2}, F = 0\rangle \rightarrow |^2D_{5/2}, F = 2\rangle$ at 411 nm with natural linewidths of 1 nHz, 3 Hz and 22 Hz, respectively. We chose the ultra-narrow octupole transition at 467 nm as the reference oscillator in our experiment as this E3 transition is advantageous for various reasons, the most important one being its $m_F = 0$ clock transition states which nullifies first order Zeeman shift. It contains a strong transition $|^2S_{1/2}\rangle \rightarrow |^2P_{1/2}\rangle$ which can be availed for laser cooling and ion detection purpose. Also, in the ultra high vacuum (UHV) of the order of 10^{-11} torr required for single ion trapping, hydrogen atoms present inside the chamber may form hydride with the trapped ion, thus disturbing its trapping lifetime. However, trapped Yb^+ provides longer storage times as its cooling laser provides the photo-dissociation resonance for YbH^+ [68]. So, formed YbH easily dissociates to Yb^+ and gets re-trapped, thus discarding the requirement to re-load the ions. The required lasers are easily commercially available. Additionally, this rare earth element is a fascinating candidate for probing certain basic physics problems *e.g.* parity violation [69], measurement of temporal variation of fine structure constant [70], search of ultralight scalar dark matter [71] *etc.* Many other groups have also worked on $^{171}\text{Yb}^+$ worldwide and have attained appreciable results [72–74].

1.2.2 Experimental protocol

The energy level diagram of $^{171}\text{Yb}^+$ for the experiment with all relevant transitions and the schematic illustrating the planned experiment for a single ion optical clock is depicted in Fig. 1.3(a,b), respectively. Developing a state-of-the-art atomic clock in the optical domain necessitates the successful establishment and assemble of numerous components. To start with, an ion-trap housed within a UHV chamber is required for preventing collisions with residual gases in order to achieve maximum trapping life of the ion. For trapping the ion, we are using an end-cap type Paul trap as it provides maximum optical access for focusing multiple laser beams at the centre of the trap [75,76]. It has a pair of inner and outer electrodes made of Tantalum to which oscillating and static electric fields are applied, respectively. Molybdenum is used to create the structure holding the trap and screws whereas macor is chosen for insulation. The inner and outer diameters of the outer electrode and diameter of inner electrode are 1.4 mm, 2 mm and 1 mm, respectively. Values of trap operation parameters for our trap geometry are $a_z = -2a_x = -2a_y = 0$ and $q_z = -2q_x = -2q_y = 0.28$ are $\omega_{rf} = 15$ MHz [77]. A vacuum of the order of 10^{-11} mbar is desirable to minimize trapped particle's collision with the background gases. The ultra-high vacuum chamber used in the experiment is fabricated of non-magnetic stainless steel, SS316LN and consists of a pair of size CF-75 port, two pairs of size CF-35 ports and three pairs of mutually orthogonal size CF-16 ports. These ports facilitate mounting the ion trap and other components of the experiment as well as provides unhindered optical access to the trap. Materials used for constructing the trap and chamber are chosen taking into consideration their vacuum compatibility, thermal, electrical, mechanical, chemical properties *etc.* The detailed design and geometry of the end-cap type Paul trap and UHV chamber used in our experiment can be found in Ref. [77–80].

A step-up resonant transformer is required for delivering narrow bandwidth, high voltage RF which is a critical requirement for trapping potential. Use of such transformer evades undesirable power reflection due to impedance mismatching. For loading ions in the trap, a collimated flux of Yb atoms has to be produced and subsequently photoionized using 399 nm and 369.5 nm lasers. Depending on the trap depth, certain number of ions get trapped. Thermal motion associated with time-averaged confining potential called as secular motion and driven oscillatory motion at applied RF frequency known as micromotion are associated with trapped ions [59]. To stabilize ions' motion by reducing their internal energy, they are laser cooled by driving the strong electric dipole transition $|^2S_{1/2}, F = 1\rangle \rightarrow |^2P_{1/2}, F = 0\rangle$ transition using 369.5 nm laser. For detection of ion/ions trapped in the potential, fluorescence induced at 369.5 nm is collected and directed to a Photo-multiplier tube (PMT). Step-by-step decrease in trapping potential by gradual decrease in applied RF voltage until PMT shows minimum

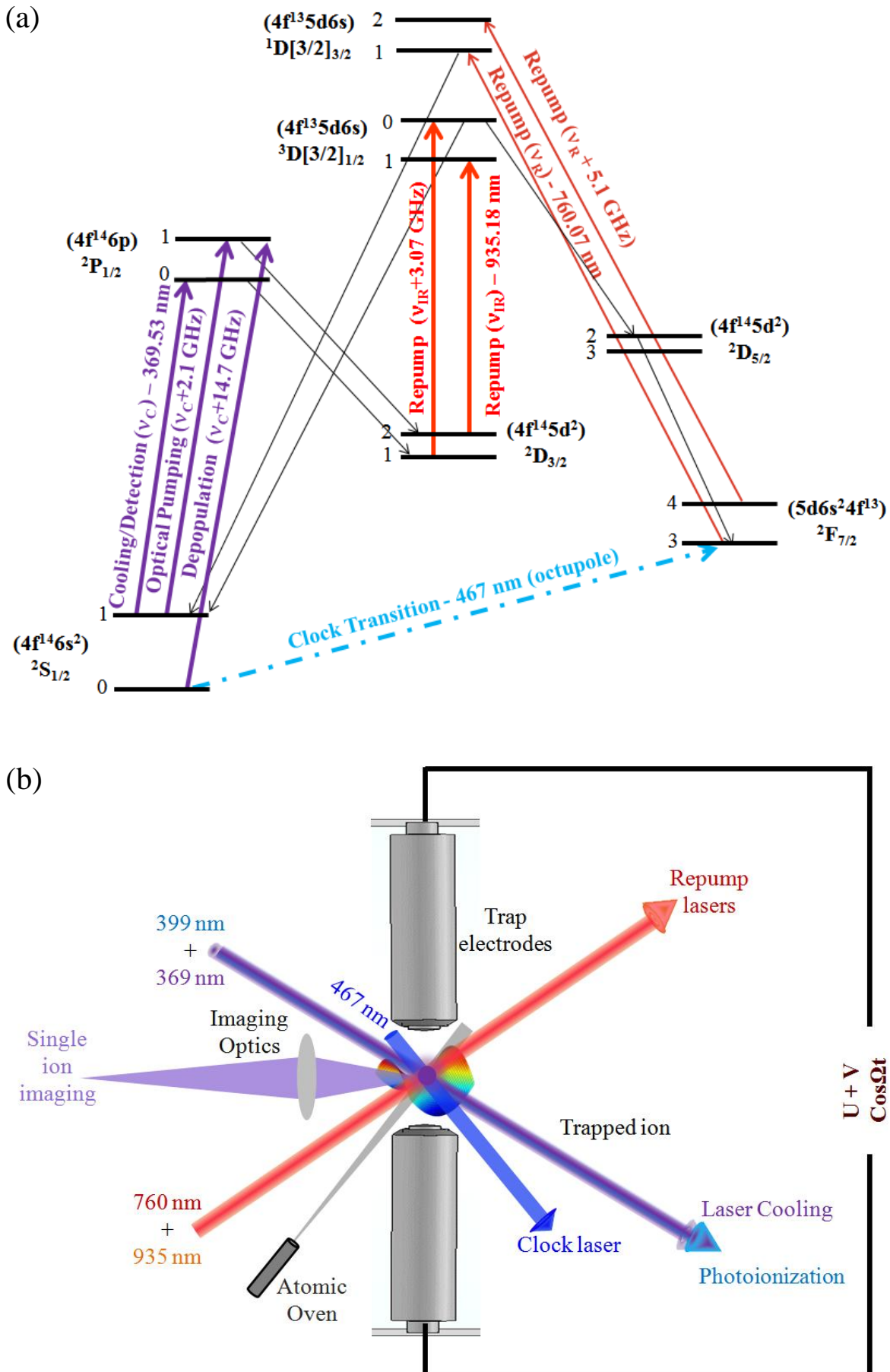


Fig. 1.3: (a) Energy level diagrams for $^{171}\text{Yb}^+$ showing the relevant transitions useful for building an optical ion clock and (b) Schematic showing the experimental protocol and various lasers required for different purpose in the experiment.

signal for collected photons ensures presence of a single ion. This is further confirmed by a high resolution imaging system which forms image of the trapped species on an Electron Multiplying Charge-Coupled Device (EMCCD). As can be seen in Fig. 1.3, there is a finite probability of the ion decaying to the metastable $|^2D_{3/2}, F = 1, 2\rangle$ states or the low-lying $|^2F_{7/2}, F = 3, 4\rangle$ states having longer lifetimes of 52.7 ms and 5.4 years, respectively. Thus, the ion needs to be pumped back to the cooling cycle for which repump lasers at 935 nm and 760 nm are used. Another probable scenario is the ion jumping to a hyperfine ground state $|^2S_{1/2}, F = 0\rangle$; so, 369.5 nm modulated by 14.7 GHz is used to uninterrupted the cooling cycle. For similar reasons, modulated frequencies of the repump lasers are also used (See Fig. 1.1). Once the ion's motion is anchored, it is prepared for clock transition probing for which cooling laser shifted by 2.1 GHz is applied which excites the ion to $|^2P_{1/2}, F = 1\rangle$ from where it spontaneously settles at $|^2S_{1/2}, F = 0\rangle$. Having prepared the state, the octupole clock transition is finally probed at 467 nm. Once the clock transition of narrow linewidth is probed, the experimental clock setup proves useful only if the oscillation cycles of the probing laser can be counted to institute it as a timescale. An optical frequency counter solves this challenge [81, 82] and so the invention of optical frequency comb by T. W. Hänsch and J. L. Hall is a boon for precise frequency standards experiments as it bridges the gap between optical and microwave frequencies [83–86].

In practice, any physical quantity can never be measured with absolute certainty. Various uncontrollable effects introduce uncertainties and also limit the accuracy by which we can measure the resonant frequency of the natural oscillator. In order to overcome or minimize them; causes of existence of such systematic error and magnitude assessment are to be known prior hand so that their contributions to the clock uncertainty budget could be evaluated and the unperturbed frequency can be rebuilt. Several such most common systematic shifts limiting performance of optical clocks are Doppler shift, Electric & Electromagnetic field based shifts, Magnetic field based shift, Gravitational shift, Collisional shift, *etc.* To eliminate first order Doppler shift, the interrogating ions are cooled to sub milliKelvin region by laser cooling. Presence of $\Delta m_F = 0$ levels in the clock transition nullifies first order Zeeman shift. Helmholtz coils are used to minimize Earth's magnetic field effects on the measurement. Excess or non-uniform electric field shifts ion's position from trap centre resulting to increased micromotion. To compensate for this, additional voltage is applied to two pairs of electrode fitted into the UHV chamber in the radial plane. Automation of such precision frequency metrology experiment is also a necessary task for running it reliably and continuously over several hours or days, minimizing manual errors [87]. Various computer controlled electronic devices such as DC power supply to supply voltages to the ion trap and compensation electrodes [88, 89], constant current source for heating atomic oven and driving Helmholtz coils, shutter drivers for controlling exposure time of lasers, frequency drivers for acousto optic modulator (AOM) and electro optic modulator (EOM) used for shifting laser frequencies, *etc.* are used. Figure

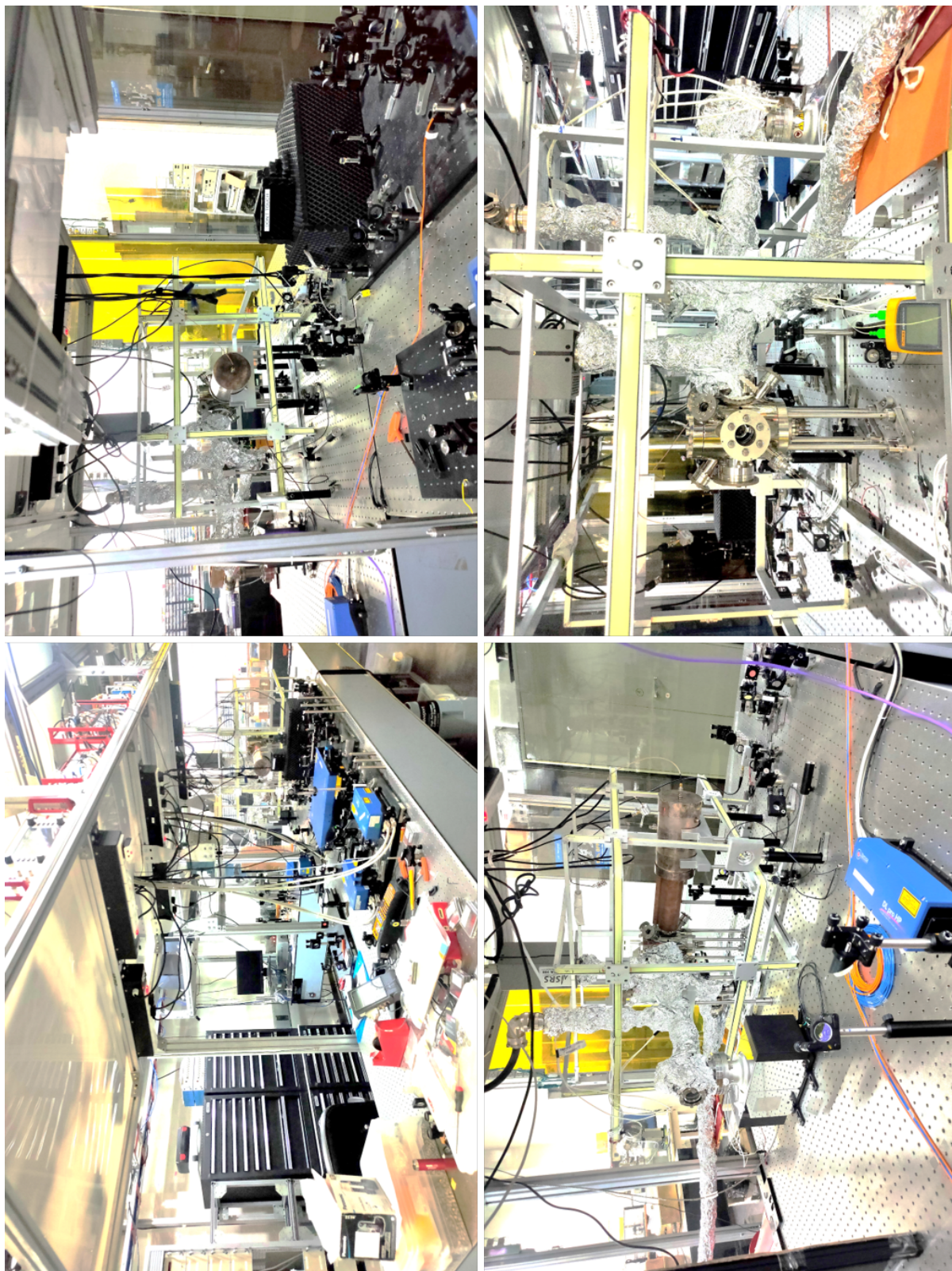


Fig. 1.4: An outlook of the “Single trapped ion optical frequency standard” experiment in developing stage at CSIR - NPL.

1.3(a,b) shows the use of five lasers along with their modulated frequencies in the precision experiment. Long term frequency stabilization of each of these lasers is an important requisite to ensure higher probability of the transition involved. This brief description of the plan of the experiment gives an overview of the simultaneous requirement of optics, electronics, atomic physics, vacuum technology and automation to build an optical frequency standard or optical clock for most precise and accurate realization of SI second. It shows the necessity of a plethora of tasks, small and big for its accomplishment. Figure 1.4 depicts photographs of experimental setups of the laboratory where the Yb ion trap experiment is going on.

1.3. Objective of the thesis

The following problems relevant to trapping and cooling of $^{171}\text{Yb}_+$ within an RF trap for building an optical frequency standard have been chosen to be addressed in the present thesis work:

1. An ion trap is a vital part of the said experiment, to which high voltage radio frequency (RF) is delivered via an inductively coupled helical resonator for creation of the trapping potential. Accurate estimation of capacitive, inductive and resistive loads related to the ion trap-resonator assembly is important for constructing the helical resonator with desired resonant frequency for supplying high voltage RF to the ion trap.
2. Different systematic shifts exist in such experiments, which gives an error in the absolute frequency realisation. Their pre-evaluation is therefore necessary for error budget estimation.
3. Deposition of atomic vapor emitted from the oven on the trap electrodes may lead to additional undesired electric field, known as patch potential, leading to unwanted systematic shift *i.e.*, Stark shift. An atomic delivering narrow-divergent beam is hence a pre-requisite in such experiments so that patch potential is avoided.
4. Single-ion based clock has to compromise with lower signal-to-noise ratio, hence, it requires a very high resolution and diffraction limited imaging system for detection of laser-induced fluorescence and for characterization of the trapped species.
5. Laser frequency stabilization is also an important aspect in such experiments to ensure high probability of desired atomic transitions throughout the experiment.
6. Additionally, the neutral Yb atoms released from the oven are to be ionized for subsequent trapping for which lasers at 399 nm and 369 nm are used. The $^1\text{S}_0 \rightarrow ^1\text{P}_1$ transition in

neutral Yb is the first isotopic-selective stage in 2-photon ionization of Yb for which the absolute frequency of this transition corresponding to Yb-171 isotope is to be measured.

This thesis, therefore focusses on developing the requisite components or building blocks for the main experiment in addition to systematic shift calculations.

Chapter wise outline of the thesis is as follows:

Chapter 1 features the introduction to ion trap experiments and their applications in different areas of Physics, in particular to time and frequency metrology. It reviews and discusses in details about optical clocks, its working mechanism, and its varied potential in other precision experiments for studying various advanced physics problems. The chapter also highlights specifically on Ytterbium ion based optical clock, its experimental requisites and the focus of this thesis work.

Chapter 2 focusses on the ion trap-helical resonator connections for generating the harmonic potential to trap ion. Importance of having a theoretical and numerical study of various parameters (capacitive, resistive and inductive loads) related to its construction prior hand are discussed and related theoretical, numerical and experimental analysis have been detailed. The chapter briefly discusses systematic shifts that can affect frequency measurement in ion-trap experiments extending it to estimation of BBR shift resulting from any excess capacitive load.

Chapter 3 highlights the design details of a narrow-divergent dark wall atomic oven, its necessity in the experiment and discusses the related theory and experimental results. Designs of different tried ovens and related failures are also briefed.

Chapter 4 describes the design of high-resolution imaging system for fluorescence detection of a trapped ion/ions. It discusses on image formation for a point source along with related aberrations and image quality analysis parameters and working of the design in terms of these optical excellence deciding parameters alongside its comparison to other reported designs.

Chapter 5 highlights the importance of laser frequency stabilization in precision spectroscopy experiments and various available techniques for the same. It discusses the experimental setup and results obtained for Saturated Absorption Spectroscopy (SAS) of Iodine performed for stabilizing the cooling laser (369.5 nm). Various optical set-ups tried for SAS and probable reasons of their failure are also discussed.

Chapter 6 describes optical setup for recording photo-excitation spectroscopy of neutral Yb

is described in this chapter. It reports the obtained fluorescence spectrum and the measured transition frequency for various isotopes of Yb along with sources of uncertainty in these values. This measurement is the first step towards carrying the 2 photon ionization of Yb-171.

Finally, Chapter 7 concludes the output of the thesis in a nutshell, importance of the work done and their significance in the overall experiment. It also discusses the possible applications and future scope of the research work carried out.

Chapter 2

Estimation of electrical loads and BBR shift associated to Ion-trap and resonator assembly

Publication: Lakhi Sharma, A. Roy, S. Panja, and S. De, Estimation of the ion-trap assisted electrical loads and resulting BBR shift, *Scientific Reports* **8**, 16884 (2018).

2.1. Introduction

Confinement of an ion in an ultra high vacuum (UHV) domain is a prelude to its seclusion from its immediate environment, thus facilitating its manipulation and interrogation. Ion traps are the essential precision tools used in a wide range of areas of physics [90], either for guiding [91,92] or for trapping [1, 2] ions to study them in a well-controlled environment. These traps confine motion of ions using electric and magnetic fields. For time and frequency metrology purpose, Paul traps employing a combination of electrostatic and radio-frequency field to generate ion trapping potential is used, to avoid systematic shifts resulting from magnetic field. The three dimensional potential well resulting in Paul trap is of the form,

$$\phi(x, y, z, t) = (U_{DC} + V_{AC} \cos \Omega t) \frac{x^2 + y^2 - 2z^2}{2r_o^2}, \quad (2.1)$$

where U_{DC} , V_{AC} and Ω are the static voltage, amplitude and frequency of alternating voltage applied to trap electrodes, respectively. Furthermore, $r = \sqrt{x^2 + y^2}$ and z are the trap's axes and $r_o^2 = 2z_o^2$, with $2z_o$ being separation between trap electrodes. To create a trapping potential giving longer sustaining trapped ions, Paul traps require a narrow band radio frequency (RF) with high amplitude at the desired parameters. The ion trap is equivalent to an LCR-circuit having impedance different than the 50Ω output impedance of an RF source. Direct connection of an RF source via an amplifier to an ion trap will therefore lead to the RF being partially

reflected towards the source thus causing damages. Also, amplifier's noise will inject itself into the trap causing its heating [93]. Using a directional device following the RF source and amplifier is a standard technique to avoid unwanted power reflection due to impedance mismatching. So, the RF is generally delivered via an intermediate resonator whose resonant condition is tuned to obtain the desired RF parameters [94, 95]. The resonator filters out the amplifier noise but for maximum filtering, it should have a high quality factor (Q-factor). Resistive output impedance of the amplifier decreases the Q-factor of the resonator; hence it is decoupled by connecting the resonator via capacitive or inductive coupling. Over the last few decades, increasing application of the ion-traps for mass spectrometry, precision measurements, generating ion-qubit for quantum computation, development of optical clocks, *etc.* [90] has been demanding high quality RF oscillator and resonator together with improvement in all the associated technologies to achieve an overall high performance.

Let us have a brief review of the relevant work on the RF resonator and oscillator. Jones *et al.* reported novel design of an RF generator that allows for tuning of the resonant frequency which varies with the external capacitive loads [96,97]. Recently, Reza *et al.* reported a tunable Colpitts oscillator that also tunes the RF at a desired frequency [98]. In many cases, the resonant frequency of an RF generator is adjusted by adding extra capacitor in parallel to the ion-trap's intrinsic capacitance but that degrades the quality factor (Q-factor) and efficiency of the power transferred to the trap electrodes. As reported in Ref. [99], the operating frequency of their indigenously developed RF amplifier got shifted by about 13.6 % than it was designed for, which is due to the lack of prior knowledge on the load of their ion-trap. Helical resonators are commonly used for this purpose and it consists of two helical coils as primary and secondary antenna for RF signal coupling and a cylindrical copper shield to avoid transmission loss [95, 106]. The design for the same was first presented by Macalpine and Schildknecht [100]. In all these above-mentioned cases, prior analysis and accurate estimation of the electrical loads will help in proper designing of the RF oscillator since its associated loads decide its resonant frequency. In some applications, feedback controlled RF oscillators are used to enhance the stability [101]. There, a Phase-Lock-Loop locks the resonant frequency, which depends on the extra phase added to the RF due to the propagation delay [102]. Estimation of the loads that are attached to the RF generator and their electrical equivalent circuitry analysis helps in proper designing of the feedback system. For ion ejections, fast discharge of the RF after switching it off is required, otherwise the ions are deflected due to residual oscillations [103]. As the characteristic discharge time of a RF source depends on the effective inductive and capacitive loads [104], estimation of these is required prior to designing of the RF supply.

So far, efforts have been made for novel designing of the RF generator and resonator for developing high performance ion-traps. In this chapter, we show a pathway for accurate es-

timation of the capacitive, inductive and resistive loads resulting from an ion-trap and its associated system. We have discussed on estimation and experimental verification of electrical equivalent loads resulting from different sources of our precision ion trap and resonator assembly that will be used for building an Yb-ion optical clock [78, 79]. This helps us to build a helical resonator [105, 106] of desired resonant frequency. In clock experiments, many systematic shifts result from various sources and their estimation is vital to evaluate the total systematic uncertainty budget of a frequency standard. Black Body Radiation (BBR) shift is one such dominant type which may result from resistive heating of the ion-trap. A detailed calculation of the ion trap system loads also helps in determining the associated BBR shift.

2.2. Methodology

Our ion-trap system, which is attached to an amplified RF source, consists of three parts : a helical resonator **R**, a connector **C** and the end cap type Paul trap **T**. Their arrangements are shown in Fig. 2.1. The equivalent inductances, L_i ; capacitances, C_i and resistances, R_i resulting from various components, as indicated by the subscript (i), of an ion-trap appear as loads. Here, we have identified as well as estimated possible sources of loads that contribute to L_L , C_L and R_L which are then validated through experiment. The resonant frequency, f_0 and Q -factor, Q_0 of a helical resonator itself can be estimated as,

$$f_0 = \frac{1}{2\pi} \sqrt{\frac{1}{L_R C_R}}, \quad (2.2)$$

$$Q_0 = \frac{1}{R_R} \sqrt{\frac{L_R}{C_R}}, \quad (2.3)$$

where L_R , C_R and R_R are the inductance, capacitance and resistance of the resonator, respectively [95]. In a loaded condition, *i.e.*, when the ion-trap is attached to the resonator via a connector, the f_0 and Q_0 changes as,

$$f' = \frac{1}{2\pi} \sqrt{\frac{1}{(L_R + L_L)(C_R + C_L)}}, \quad (2.4)$$

$$Q' = \frac{1}{R_R + R_L} \sqrt{\frac{L_R + L_L}{C_R + C_L}}, \quad (2.5)$$

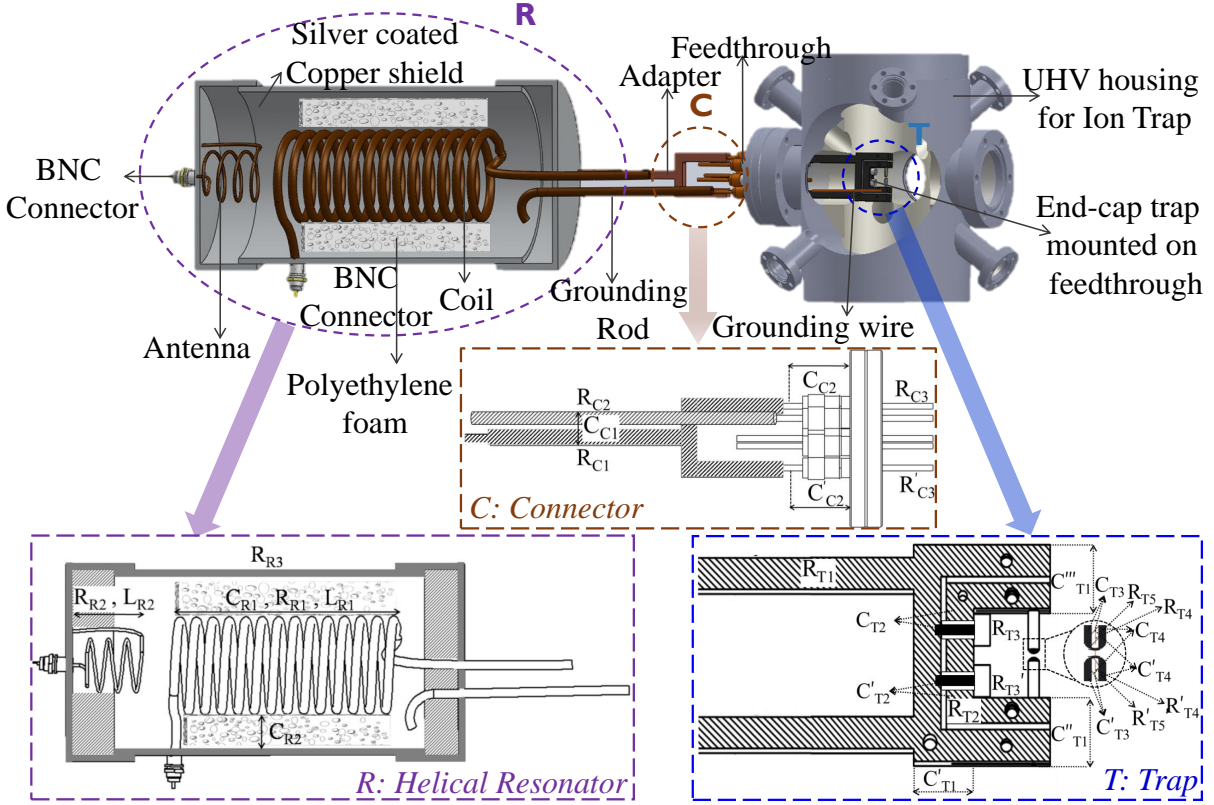


Fig. 2.1: Ion-trap system of our experiment where the resonator (**R**) and ion-trap (**T**) are connected via a connector (**C**). The inserts show schematics of each part **R**, **C** and **T** where sources of the loads are indicated.

where L_L , C_L and R_L are the inductive, capacitive and resistive loads, respectively. The ratio of the effective RF voltage, V' at the trap electrode relative to the input voltage, V is given as,

$$k_{RF} = \frac{V'}{V} = \sqrt{\frac{R_R C_R}{(R_R + R_L)(C_R + C_L)}}. \quad (2.6)$$

2.2.1 Analytical methods

For analytical estimation of loads, already established formulae are used, which rely on certain assumptions and are described in this subsection. As for example, C_i values are estimated assuming parallel plate capacitors. Thus, we do not expect them to be as accurate as for the numerical techniques but this shows inaccuracy of the estimation in case it is done only analytically.

Helical Resonator (R): The helical resonator consists of a helical coil, an antenna coil and a shield. The primary antenna coil is made of a hollow copper wire of outer diameter 2 mm, it has 3 turns each of diameter 35 mm. A copper tube of diameter 6 mm is wound around a cylindrical object of diameter 56 mm to make up the secondary helical coil of diameter 62 mm; it consists of 14 turns. The resonator shield is a hollow, copper cylinder of outer diameter 120 mm and height 210 mm [105,106]. The antenna and the secondary coil have self inductances, L_{R1} and L_{R2} ; resistances, R_{R1} and R_{R2} and a parasitic capacitance, C_{R1} . Capacitance C_{R2} results from the shield-air-coil combination. In the present design, the copper enclosure is silver coated to reduce oxidation of the copper shield and eventually the electromagnetic radiation loss, which introduces a resistance R_{R3} . Electrical circuitry comprising of these loads are shown in Fig. 2.2(a). For calculation of the self capacitance of a helical coil of height h_c and outer diameter d_c , the modified Medhurst equation [107] as given by D. W. Knight [108] is,

$$C_{coil} = \frac{4\epsilon_0\epsilon_x}{\pi} \left[1 + \frac{k_c}{2} \left(1 + \frac{\epsilon_i}{\epsilon_x}\right)\right] \frac{h_c}{\cos^2 \Psi}, \quad (2.7)$$

where ϵ_0 , ϵ_i and ϵ_x are permittivities of free space, inside and outside mediums of the coil, respectively and Ψ is the pitch angle. The coefficient k_c is expressed as,

$$k_c = 0.717439 \frac{d_c}{h_c} + 0.933048 \left(\frac{d_c}{h_c}\right)^{\frac{3}{2}} + 0.106 \left(\frac{d_c}{h_c}\right)^2, \quad (2.8)$$

where the numerical pre-factors are the empirical coefficients [108]. Assuming the shield and the coil as coaxial cylinders, the shield-to-coil (s-c) capacitance is calculated using the relation,

$$C_{s-c} = 2\pi\epsilon_o\epsilon_r h_c \left(\ln \frac{d_s}{d_c}\right)^{-1}, \quad (2.9)$$

where d_s is the inner diameter of the shield and ϵ_r is the relative permittivity of any dielectric material in between. For proper positioning of the coil, the space between the shield and coil is partially filled with polyethylene foam of permittivity 2.22. Hence, following the Eqns. (2.7-2.9), the capacitances of the coil and shield-to-coil are,

$$C'_{coil} = m C_{coil}|_{\epsilon_i, \epsilon_x=1} + n C_{coil}|_{\epsilon_i=1, \epsilon_x=2.22}, \quad (2.10)$$

$$C'_{s-c} = m C_{s-c}|_{\epsilon_r=1} + n C_{s-c}|_{\epsilon_r=2.22}, \quad (2.11)$$

here $m=0.46$ and $n=0.54$ are the filling factors for air and foam, respectively. Inductance of the coil is estimated as,

$$L_{coil} = 39.37 \frac{\mu_0}{16\pi} \frac{h_c d_c^2}{\tau^2} \left[1 - \left(\frac{d_c}{d_s}\right)^2\right], \quad (2.12)$$

where τ is the winding pitch of the coil and the numerical term arises from unit conversion

of the formula, as given in Ref. [109] to the SI. The DC resistance of a part of length l and cross-sectional area A is given by,

$$R_{dc} = \frac{\rho l}{A}, \quad (2.13)$$

where ρ is the resistivity of the material. AC resistances for the RF carrying parts are different and those are important to be calculated. For a cylindrical rod of diameter D , the AC resistance [110] is ,

$$R_{ac}^c = \frac{R_{dc}}{\pi} \frac{A}{D\delta}, \quad (2.14)$$

where the skin depth of the material is $\delta = 503 \sqrt{\rho/\omega_{RF} \mu}$ with ω_{RF} and μ being the applied frequency and the relative permeability of the material, respectively. R_{R1} and R_{R2} are calculated using Eqns. (2.13) and (2.14).

Connector (C): A connector is used to interface the helical resonator with the ion-trap, which is assembly of a Y-shaped copper adapter, a grounding rod and an electrical feedthrough (Fig. 2.1). The Y-shaped adapter is used for symmetric distribution of the RF to the ion-trap electrode pair. The trap is screwed to two radially symmetric electrical pins of the feedthrough for firm and stable mounting. The capacitance, C_{C1} arises between the adapter and the grounding rod along with the feedthrough pins whereas C_{C2} and C'_{C2} results from the feedthrough pins and its flange. The adapter, grounding rod, feedthrough pins also carry resistances R_{C1} , R_{C2} and R_{C3} , respectively. The rectangular parts of the connector of width w and thickness t carrying RF has an AC resistance [111] which is given as,

$$R_{ac}^r = R_{dc} \frac{K_c}{1 - e^{-x}}, \quad (2.15)$$

where $x = 2(1+t/w)\delta/t$, current crowding factor $K_c = 1 + (1 - e^{-0.048p}) [0.06 + 0.22 \ln(w/t) + 0.28(t^2/w^2)]$ and $p = \sqrt{A}/1.26\delta$. Equivalent electrical circuitry of all the loads described in this section are shown in Fig. 2.2(b).

Trap (T): The ion-trap electrodes are made of Tantalum, whereas its holding structure is made of Molybdenum and Macor [79]. The holder mounts the ion-trap inside an Ultra High Vacuum (UHV) chamber via an electrical feedthrough. Capacitances in the trap arise out of the inner electrode holder to outer electrode holder with dielectric macor in between. This capacitance, C_{T1} is estimated part-by-part as C'_{T1} , C''_{T1} and C'''_{T1} as shown in Fig. 2.1. The capacitances resulting from the mounting bolts and the electrode holders are C_{T2} and C'_{T2} , respectively and from the inner-to-outer electrodes are C_{T3} , C'_{T3} , C_{T4} and C'_{T4} . Resistances

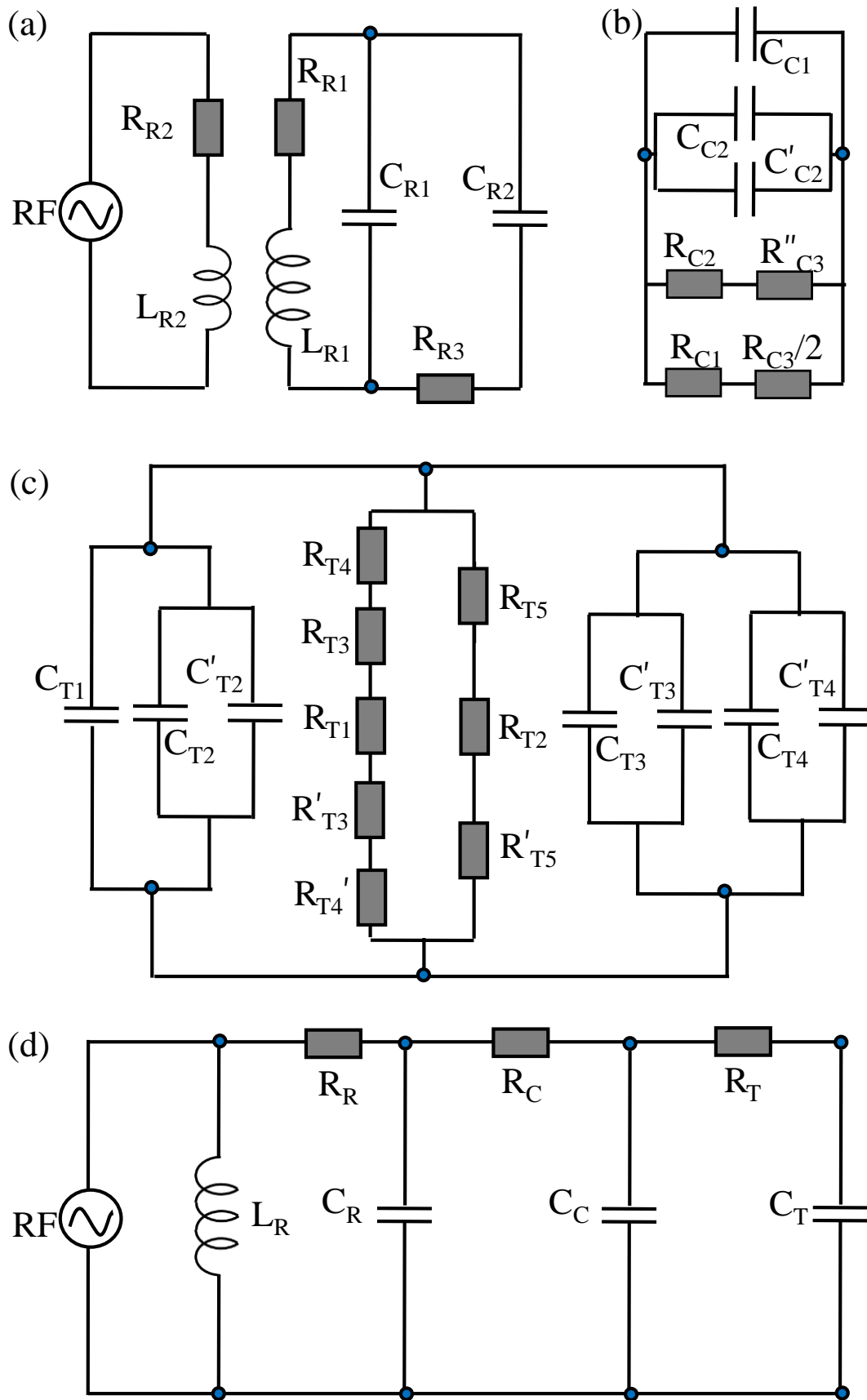


Fig. 2.2: Electrical circuitry of (a) resonator (**R**), (b) connector (**C**), (c) ion trap (**T**) and (d) equivalent (**E**) of all three components. C_i , R_i and L_i as shown in the circuits denote capacitance, resistance and inductance, respectively, where the subscript i refers to **R**, **C** and **T**, respectively.

result from the inner electrode holder, R_{T1} ; outer electrode holder, R_{T2} ; bolts, R_{T3} ; inner and outer electrode, R_{T4} , R_{T5} and R'_{T4} and R'_{T5} , respectively. Trap's inner and outer electrode holders can be considered as parallel plates spaced apart by macor of thickness d . In that case, the capacitances are calculated as,

$$C = \epsilon_0 \epsilon_r \frac{A}{d}. \quad (2.16)$$

Since, the trap electrodes are cylindrical in shape, their in-between capacitance is calculated from Eqn. (2.9) by replacing h_c , d_c and d_s with the length, inner and outer diameters of the outer and inner electrodes, respectively. Equation (2.15) gives R_{T1} whereas Eqn. (2.14) is utilized for calculating R_{T3} and R_{T4} . The electrical equivalent circuitry of the loads associated to the ion-trap is shown in Fig. 2.2(c).

2.2.2 Numerical method

We performed finite element analysis (FEA) via a commercial software, COMSOL Multiphysics (COMSOL) for numerical estimation of various L_i , C_i and R_i values. The geometric designs of the parts are fed into the COMSOL and subdivided into finite size elements as per the user's choice. The software analyzes them and generates a final solution using variational method. The computational time increases dramatically with finer mesh size, however, after a certain mesh size, the incremental change of the computed value is well within the limit of our desired accuracy. We use the AC/DC electromagnetics module of COMSOL as the subnodes: electrostatics interface, electric current and magnetostatics allow direct computation of capacitances, resistances and inductances, respectively. Figure 2.3 shows the segmentation of the ion trap and the resonator into fine meshes as a part of FEA for numerical estimation of desired loads. Step by step guide to using COMSOL for load calculation with modelling for capacitance is as follows:

- Figure 2.4 shows the opening window of COMSOL which consists of Model builder and Graphics window. The complete details of the model to be studied such as its geometry, materials, physics interface to solve the problem, boundary conditions, *etc.* are fed in the model builder. Post processing, its model tree reflects the analysis of results, reports generated and other visualizations. The Graphics window presents interactive graphics for the geometry, mesh, and operations such as rotating, panning, zooming, *etc.*
- Under model wizard of Model builder, 3D space dimension is selected, AC/DC → Electric Fields and Currents → Electrostatics is added and under study type General Studies →

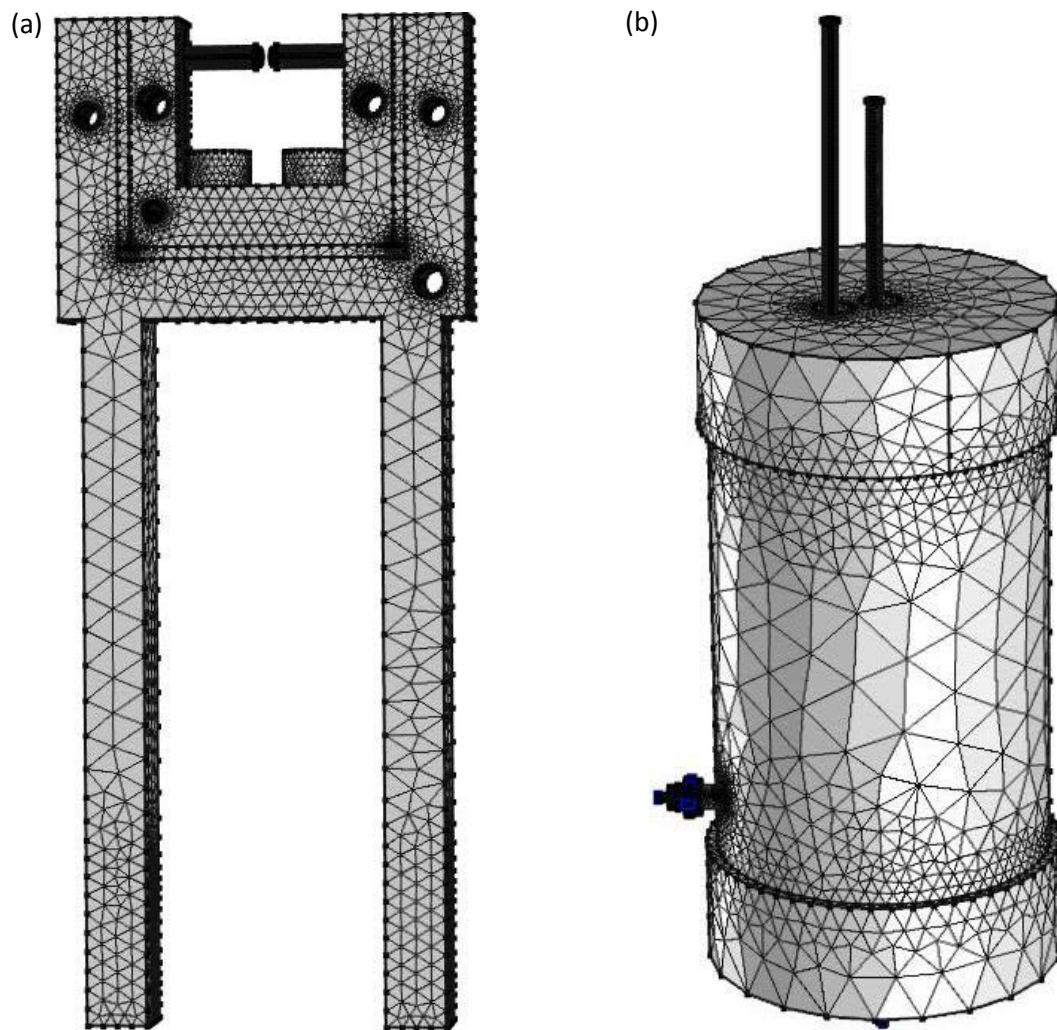


Fig. 2.3: Meshed structures of (a) ion trap and (b) resonator obtained during COMSOL simulation

Stationary is chosen, as shown in Figure 2.5(a,b,c), respectively.

- Next comes geometry of the model which can be either constructed using the features Geometry toolbar in or a CAD file can be directly imported from SolidWorks.
- A set of selections are to be made for setting up the physics such as metal and insulator parts; and ground and terminal boundaries of the model using the Definitions and Physics toolbar. Material of various parts of the model and voltage on the boundaries are also assigned.
- Under Mesh settings, size of mesh element which discretizes the model is set. Mesh size affects computation time and accuracy of the results, for all analysis, we chose “fine” element size.

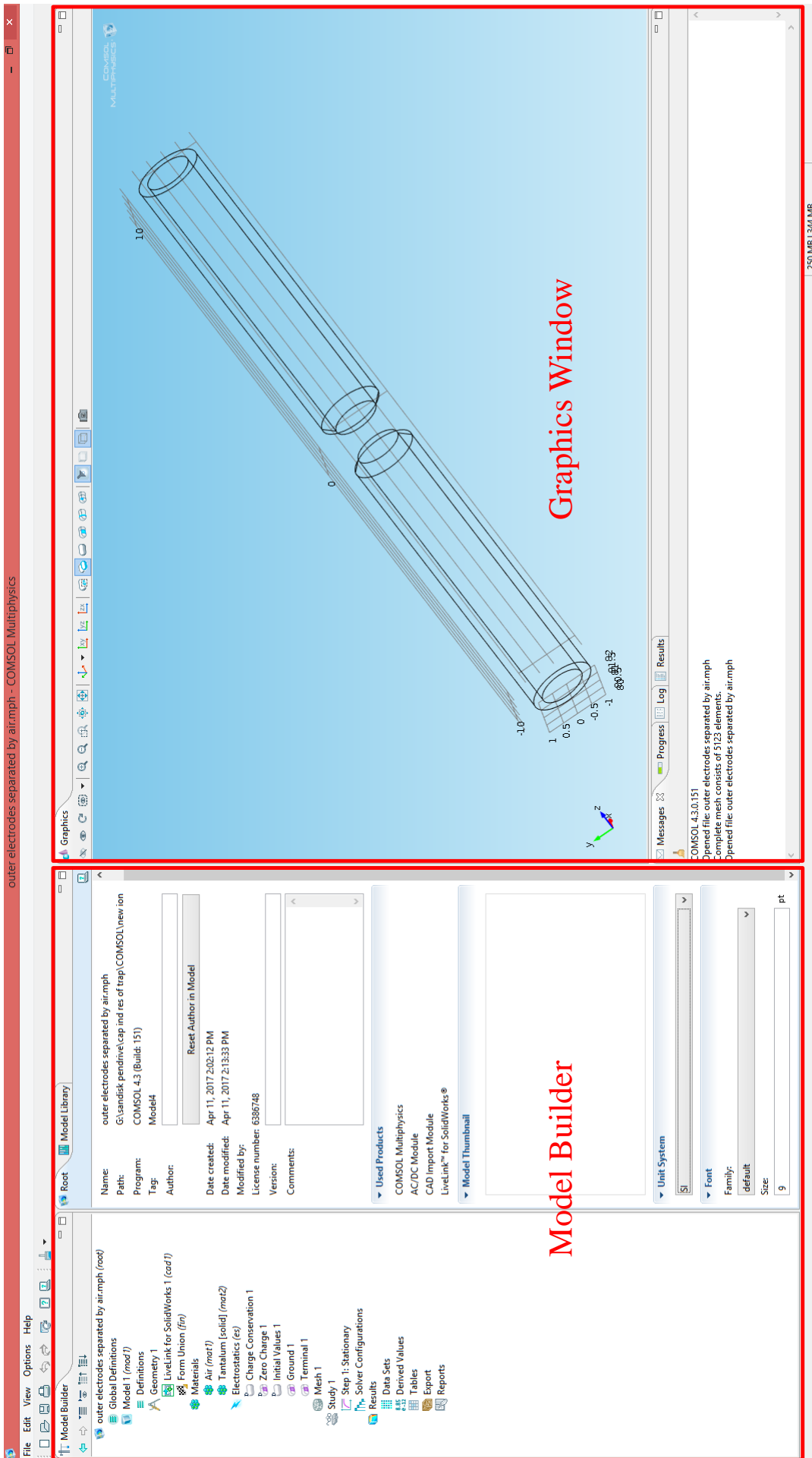


Fig. 2.4: Snapshot of COMSOL window as seen when one starts using the software. It provides a user friendly platform for physics modelling, simulations with all necessary tools including a quick access toolbar, settings window, plot windows, information window, *etc.*

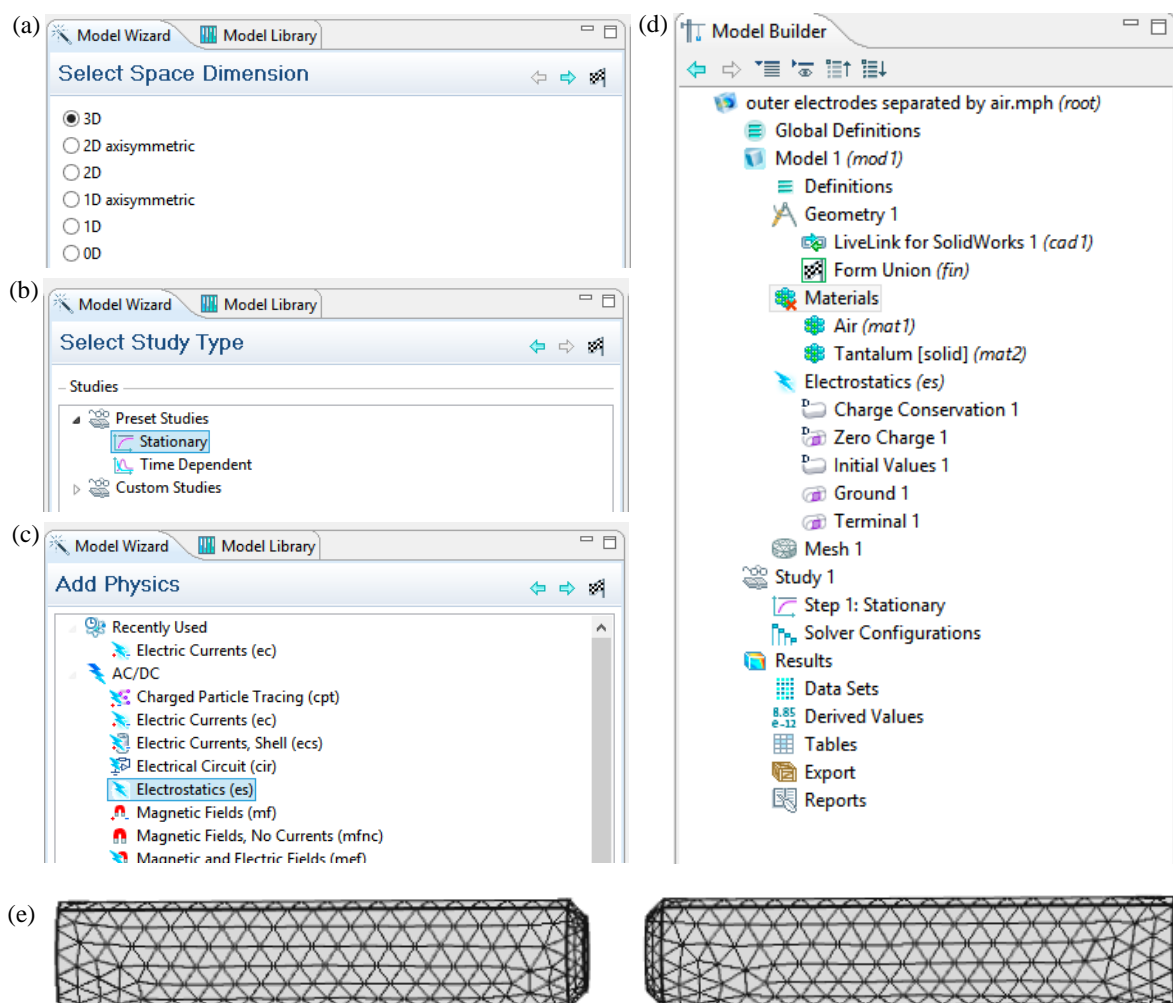


Fig. 2.5: Snapshots showing steps to creating a model for studying related physics using COMSOL by choosing (a) plane, (b) study type and (c) physics and (d) defining the orderly sequence of operations in model tree of model wizard which includes the geometry, material, mesh size, boundary conditions, *etc.* (e) shows the mesh created for model of outer trap electrodes.

- Finally, under Study toolbar, Compute is selected after which results/plots are shown in the Message/Graphics display. These toolbars are shown in Fig. 2.5(d) and final mesh created for the model is depicted in Figure 2.5(e).

2.2.3 Experiment

Experimental verification of the estimated values are obtained through an indirect measurement as well as via a direct measurement of the loads using an LCR meter (Wayne Kerr 6500P). For indirect measurement, the resonant condition is obtained by scanning the RF frequency

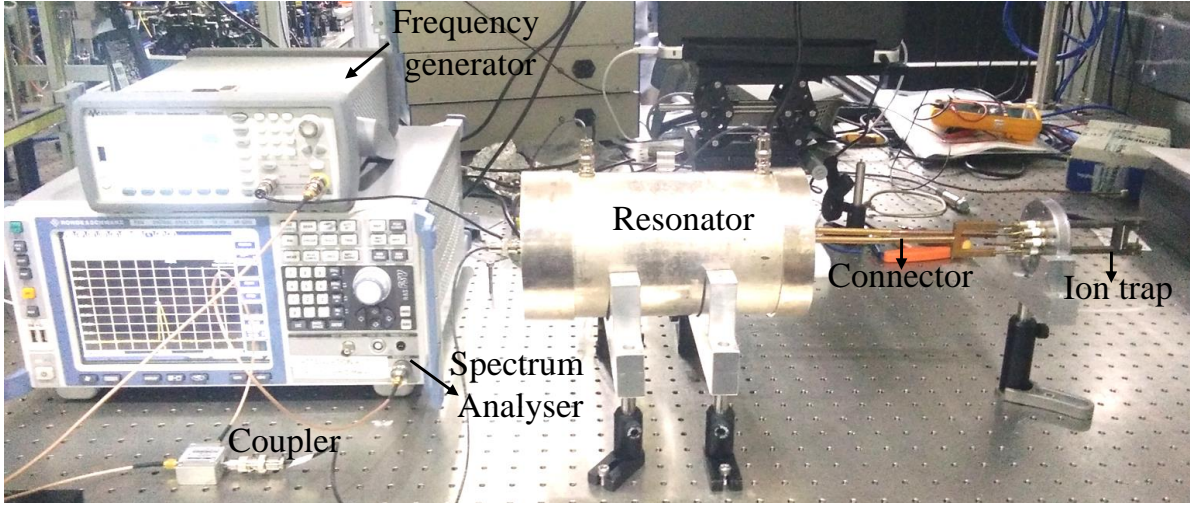


Fig. 2.6: Experimental set-up for measurement of operating parameters of resonator at loaded and unloaded conditions.

across f_0 and f' as given in Eqns. (2.2, 2.4). A small fraction of the RF ($\leq 3\%$) gets reflected from the resonator. Using a directional coupler (ZFDC-20-3-S+, MiniCircuits), this reflected signal is outcoupled to a spectrum analyzer (FSV 40, Rohde & Schwarz) for further analysis; the experimental set-up is shown in Fig. 2.6. The resonance condition is ensured by minimum reflection of the RF while tuning its frequency. The outcoupled RF is measured in a spectrum analyzer at different values of fixed capacitive loads and also in the unloaded condition of the resonator.

2.3. Results and Discussions

Simple circuitry analysis using Kirchoff's current law leads to estimation of the effective loads as following,

for the Resonator \mathbf{R} :

$$\begin{aligned}
 C_R &= C_{R1} + C_{R2}, \\
 R_R &= R_{R1} + R_{R2} + R_{R3}, \\
 L_R &= \frac{L_{R1}L_{R2}}{L_{R1} + L_{R2}},
 \end{aligned} \tag{2.17}$$

for the Connector **C**:

$$\begin{aligned} C_C &= C_{C1} + C_{C2}, \\ R_C &= \frac{(2R_{C1} + R_{C3})(R_{C2} + R_{C3})}{2(R_{C1} + R_{C2}) + 3R_{C3}}, \end{aligned} \quad (2.18)$$

for the Trap **T**:

$$\begin{aligned} C_T &= C_{T1} + 2(C_{T2} + C_{T3} + C_{T4}), \\ R_T &= \frac{A B}{A + B}, \end{aligned} \quad (2.19)$$

where, $C_{T1}=(C'_{T1}+C''_{T1}+C'''_{T1})$ as indicated in Fig. 2.1, $A=(R_{T2}+2R_{T5})$ and $B=(R_{T1}+2R_{T3}+2R_{T4})$,

for total effective loads **E**:

$$\begin{aligned} C_E &= C_R + C_T + C_C, \\ R_E &= R_R + R_T + R_C, \\ L_E &= L_R. \end{aligned} \quad (2.20)$$

The wire that is used for grounding of the trap inside of the UHV chamber results in a resistive load. The extra compensation electrodes, that are generally used for precise positioning of the ion at the trap centre, also results to finite capacitance. These values have been estimated to be orders of magnitude lower than the rest, which are therefore neglected.

The values of the loads as given in Eqns. (2.17-2.19), estimated via analytical and numerical techniques are given in Tab. 2.1. Source of errors in the numerically calculated values are two fold: accuracy a that is obtained from COMSOL for a certain mesh size and their inaccuracy b for $\pm 10\mu\text{m}$ machining tolerance. Hence, the total error is estimated to be $\pm \sqrt{a^2 + b^2}$, which is dominated by b .

In the experiment, we measure resonant frequencies and Q -factors when: (i) the resonator is attached to capacitors and (ii) the resonator is attached to the connector and capacitors. For this purpose, we use capacitors with different values that are calibrated at 0.3 % uncertainty. As shown in Fig. 2.7, the characteristic change of the resonant frequency and Q -factor due to additional capacitive load are fitted to $f(C_L) = f_0 \sqrt{C_R/(C_L + C_R)}$ and $Q(C_L) = Q_0 \sqrt{C_R/(C_L + C_R)}$, respectively, where f_0 , Q_0 and C_R are used as the fit parameters. Capacitive load resulting from a component attached to the resonator is obtained by measuring shift of the resonant frequency or Q -factor from the unloaded f_0 , Q_0 values and obtaining change of capacitance corresponding to that shift from their respective characteristic

Tab. 2.1: Estimated values of the loads resulting from different parts of the ion-trap system. AC resistances are indicated by superscript ‘ac’.

Parts	Analytical	Numerical
Resonator (R)		
C_{R1}	3.7 pF	2.067(5) pF
C_{R2}	5.7 pF	10.72(1) pF
R_{R1}	7 m Ω	8(1) m Ω
	351 m Ω^{ac}	450(5) m Ω^{ac}
R_{R2}	18 m Ω	10(4)m Ω
	820 m Ω^{ac}	610(9)m Ω^{ac}
R_{R3}	5.2 $\mu\Omega$	5.83(3) $\mu\Omega$
L_{R1}	3.1 μH	3.71(6) μH
L_{R2}	0.3 μH	0.242(5) μH
Connector (C)		
C_{C1}	8.2 pF	9.8(2) pF
C_{C2}	0.04 pF	0.038(7) pF
R_{C1}	0.22 m Ω	0.222(1) m Ω
	6 m Ω^{ac}	7(1) m Ω^{ac}
R_{C2}	454.55 $\mu\Omega$	455.8(4) $\mu\Omega$
R_{C3}, R'_{C3}	347.6 $\mu\Omega$	348.35(3) $\mu\Omega$
	10 m Ω^{ac}	9(2) m Ω^{ac}
Trap (T)		
C_{T1}	22.5 pF	22.1(3) pF
C_{T2}, C'_{T2}	0.8 pF	0.71(2) pF
C_{T3}, C'_{T3}	1.6 pF	1.5(1) pF
C_{T4}, C'_{T4}	0 pF	0.042(4) pF
R_{T1}	0.073 m Ω	0.078(1) m Ω
	70 m Ω^{ac}	85(3) m Ω^{ac}
R_{T2}	80.1 $\mu\Omega$	81.1(3) $\mu\Omega$
R_{T3}, R'_{T3}	189.44 $\mu\Omega$	197.8(3) $\mu\Omega$
	3.2 m Ω^{ac}	3.4(2) m Ω^{ac}
R_{T4}, R'_{T4}	2.816 m Ω	2.790(2) m Ω
	15 m Ω^{ac}	14(1) m Ω^{ac}
R_{T5}, R'_{T5}	780.3 $\mu\Omega$	788.6(1) $\mu\Omega$

curves, as given in Fig. 2.7. With the known values of f_0 and f' for any attached capacitance C_i , its unknown value of L_i can be estimated by using Eqns. (2.2) and (2.4). Further, as the Q_0 and Q' values are also known from experiments, using the estimated L_i values, the unknown R_i values can be obtained using the Eqns. (2.3) and (2.5). The experimental values are obtained by taking mean of the values taken from different techniques and their variance is quoted as the uncertainty. We measure $f_0 = 27.04(7)$ MHz and $Q_0 = 600(8)$, estimate them as 25.85(5) MHz and 508(1) using the numerically estimated loads in Eqns. (2.2-2.3) and also extract them as 27.5(1.0) MHz and 590(7) from the fits. Mutual agreement of these values also

validates our calculation in an independent way. The analytical, numerical and experimental values of different loads are compared in Tab. 2.2. Using the numerical and experimental

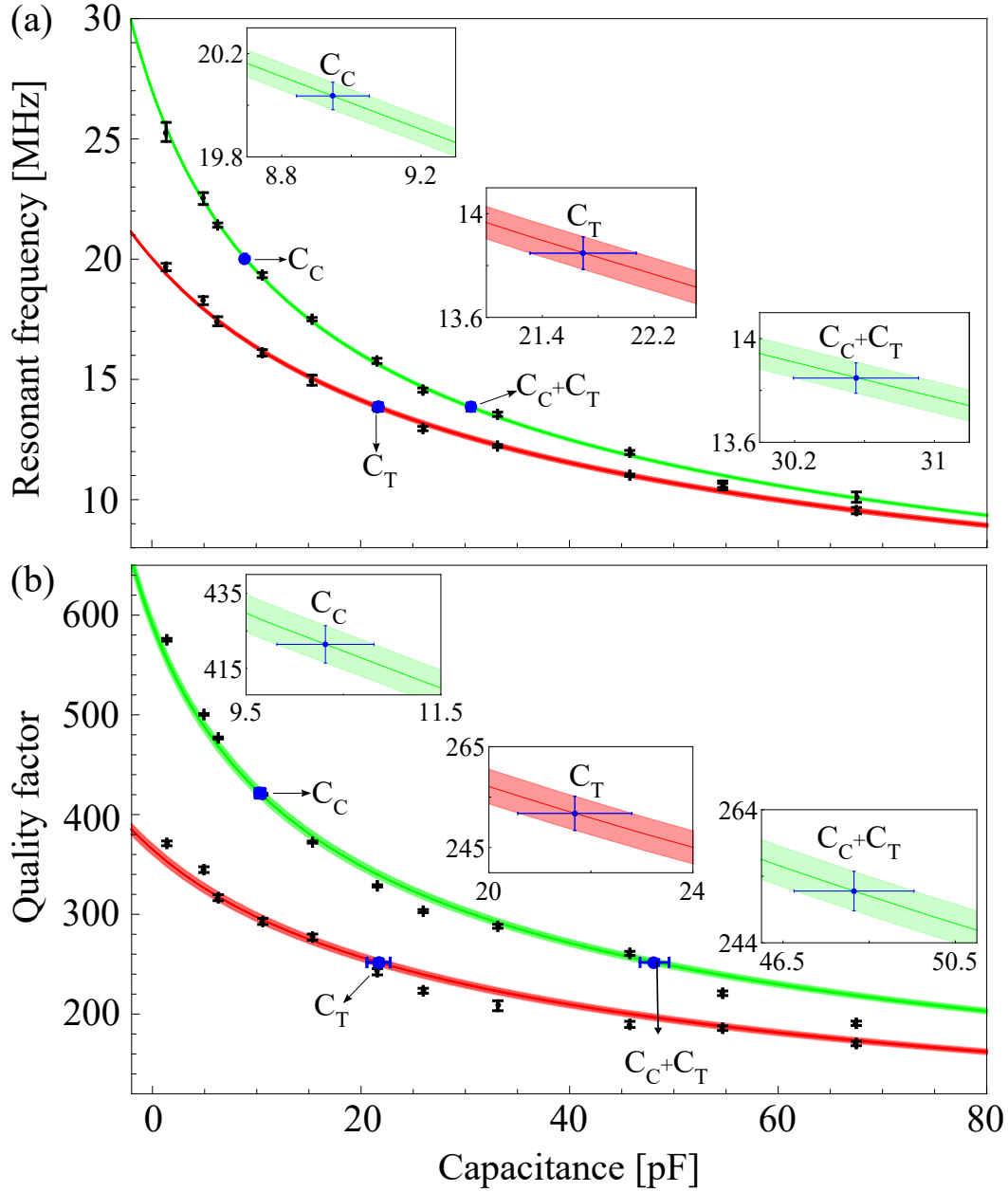


Fig. 2.7: Variation of the (a) resonant frequency and (b) quality factor with capacitance for the resonator itself (green) and for the resonator + connector without the ion-trap connected to it (red). The experimental data (black) and theoretically fitted lines to it are shown, where the width of the lines depict fitting inaccuracy. The measured capacitance (blue) of connector and the combination of connector and trap are indicated on the fitted curves and also shown in the inserts.

Tab. 2.2: Values of the loads obtained through different methods

Parts	Analytical	Numerical	Experimental
C_R	9.4 pF	12.78(2) pF	10.6(1) pF
C_C	8.24 pF	9.9(2) pF	8.6(4) pF
C_T	27.3 pF	26.7(5) pF	21.5(9) pF
R_R	1241 $m\Omega$	1062(1) $m\Omega$	981(5) $m\Omega$
R_C	28 $m\Omega$	29(9) $m\Omega$	44(2) $m\Omega$
R_T	174 $m\Omega$	182(3) $m\Omega$	162 (2) $m\Omega$
L_R	3.1 μH	3.71(1) μH	3.68(6) μH
C_E	50.4 pF	51.4(7) pF	40.7(2) pF
R_E	1373 $m\Omega$	1273(3) $m\Omega$	1183(9) $m\Omega$
L_E	3.1 μH	3.71(1) μH	3.68(6) μH

values of the loads in Eqn. (2.6), we estimate the RF voltage transfer factor, $k_{RF} \simeq 0.45$ and 0.46, respectively. Therefore, voltage at the trap is about half of that is at the output of RF resonator.

The described electrical load analysis also leads to estimation of the excess BBR shift that results from heating of the ion-trap. The resistive heating of the ion-trap electrodes due to absorption of the RF power propagating through it has already been reported elsewhere [112–114]. Here, we are estimating the BBR shift associated to heating of the trap due to current flowing through it, which originates due to finite capacitance introduced by inaccurate machining of the trap parts. The RF appears at a different phase with a relative phase difference ϕ on the trap electrodes, that are aligned axially facing each other, due to a path difference x resulting from non-negligible machining tolerances. Due to this, at any instant of time, the RF, $V_o \sin \omega_{RF} t$, appears at different voltage level, which can be modelled as a parallel plate capacitor with an unwanted excess capacitance C_{ex} kept at a potential $V_o \phi$ [59]. The phase difference, resulting from the inaccurate machining, is

$$\phi = 2\pi \left(\frac{x}{\lambda_{RF}} - p \right), \quad (2.21)$$

where p is the integer number of RF wavelength λ_{RF} that gets accommodated within x . Figure 2.8(a) shows numerically estimated values of C_{ex} for our ion-trap and calculated ϕ following the Eqn. (2.21) as a function of the machining inaccuracy. Even though there is no direct relation, the capacity factor in our ion-trap geometry is $\alpha_c = C_{ex}/\phi = 1.9$, where C_{ex} and ϕ are in fF and milli-degree, respectively. Although, in an ideal condition ($\phi = 0$), the RF electrodes stay in an open circuit condition, a finite current $I_{ex} = V_o \phi / R_{RF}$ flows through in a real trap that has certain capacity factor. A simple minded physical picture to understand this is by considering a voltage source of $V_o \phi$ V that is present in between the electrodes. In

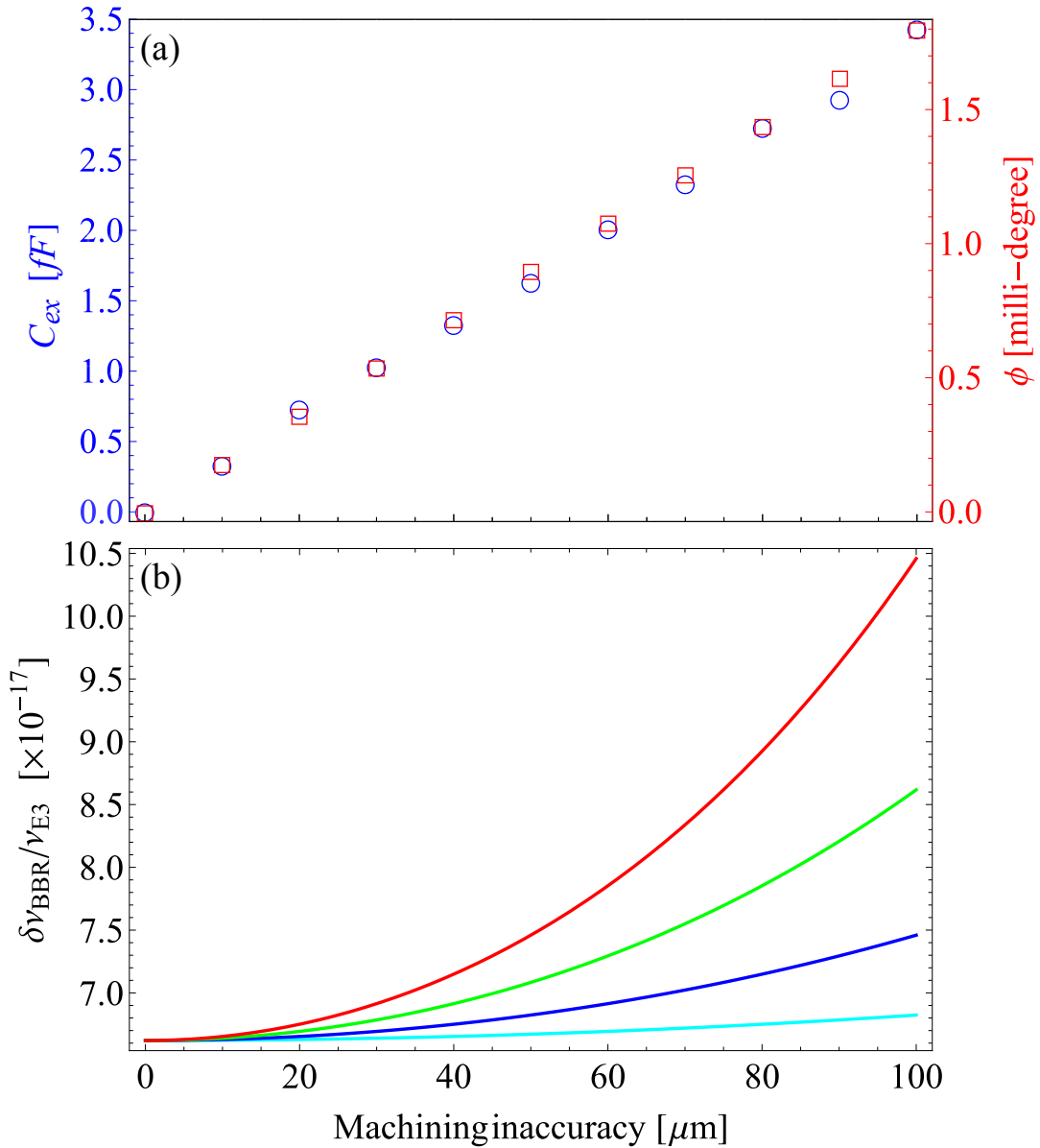


Fig. 2.8: (a) Excess capacitance, C_{ex} and phase difference, ϕ and (b) the BBR shift, at RF amplitudes 250 V (cyan), 500 V (blue), 750 V (green) and 1000 V (red) at the trap electrodes; resulting from the machining inaccuracy are shown.

that case, the resulting I_{ex} flows through the resistance R_{RF} that is present in the RF path of the ion-trap system. In a thermal equilibrium, the resistive heating due to I_{ex} will elevate temperature of the trap, which is non-negligible in many precision experiments particularly in case of an optical clock as that significantly contributes to the BBR shift [115]. The amount of temperature rise during the time of current flow (*i.e.* cycle time of the experiment and we have considered that to be 1 s just for simplicity) can be estimated following the conservation of energy as

$$\begin{aligned}\Delta T &= \frac{V_o^2 \phi^2}{R_{RF} \sum_j m_j s_j} \\ &= \frac{C_{ex}^2 V_o^2}{\alpha_c^2 R_{RF} \sum_j m_j s_j},\end{aligned}\tag{2.22}$$

where m_j and s_j are masses and specific heats of the elements j , respectively. Corresponding BBR shift due to the electromagnetic radiation at an elevated temperature T [116] can be estimated as,

$$\Delta\nu^{BBR} = -\frac{(831.945)^2}{2h} \delta\alpha_o \left(\frac{T}{300}\right)^4 [1 + \eta(T)],\tag{2.23}$$

where h is the Planck's constant, $\delta\alpha_o$ is differential scalar polarizability of the transition and $\eta(T)$ is the dynamic correction since atomic transitions other than the E1-transitions are neglected in $\delta\alpha_o$. Here, we have neglected this factor since $\eta < 0.01$ at room temperature. As an example, here we estimate $\Delta\nu^{BBR}$ at $T=(296+\Delta T)$ that is from the machining inaccuracy for the Ytterbium-ion ($^{171}\text{Yb}^+$) octupole (E3) clock transition at frequency $\nu_{E3} = 642\,121\,496\,772\,645.150$ Hz [74] and having $\delta\alpha_o = 0.859 \times 10^{-40} \text{ J m}^2 \text{ V}^{-2}$ [117]. We use our estimated values of resistances, as given in Tab. 1, to get $R_{RF} = (R_{T1} + R_{T3} + R'_{T3} + R_{T4} + R'_{T4} + R_{C1} + R_{C3} + R'_{C3})$. Figure 2.8(b) shows expected fractional BBR-shift $\Delta\nu^{BBR}/\nu_{E3}$ resulting from the machining inaccuracy of the electrodes at different amplitudes of RF of $\omega_{RF} = 2\pi \times 15$ MHz. Accurate estimation of this systematic shift carries merit for developing optical clocks with increasing accuracies as it is about two orders of magnitude higher than the present best trapped ion optical frequency standard [74].

2.4. Conclusion

We made detailed analysis of the resistive, inductive and capacitive loads that results from each part of the ion-trap system. We also performed an experiment to measure the effective loads to validate our theoretical estimations. Considering the estimated load values, the design parameters of the resonator can be chosen such that it operates as desired. This analysis shows a pathway for predicting output values, *e.g.*, resonant frequency, Q -factor of an RF resonator both in loaded and unloaded conditions prior to its construction. The RF phase difference at the tip of the electrodes resulting from the unignorable machining inaccuracy, has been estimated accurately. Its relation with one of the dominant systematic shifts in the atomic clock experiments: BBR shift is obtained, which is important to be considered in the overall systematic budget. As for example, at an RF amplitude of 1 kV at $2\pi \times 15$ MHz and with

$\pm 10 \mu\text{m}$ machining inaccuracy will result to $\pm 0.42 \text{ K}$ heating of the trap. This results to $\mp 43 \text{ mHz}$ shift for the Yb ion E3-clock transition that corresponds to fractional frequency uncertainty 6.6×10^{-17} due to the BBR effect. This exercise for precise estimation of the machining inaccuracy assisted BBR shift helps in building highly accurate optical frequency standards that are approaching to 10^{-19} level even without any cryogenic environment.

Chapter 3

A low-divergent atomic oven and its atomic flux distribution

Publication: Lakhi Sharma, A. Roy, S. Panja, and S. De, Atomic flux distribution from a low-divergent dark wall oven, *Review of Scientific Instruments* **8**, 16884 (2018).

3.1. Introduction

A collimated atomic beam source is one of the indispensable integrants of a frequency standard experiment. It provides neutral atomic flux towards the trapping potential so that the atoms can be further ionized for loading ions within the Paul trap. Such collimated atomic beam is infact a necessary requisite in many other atomic and molecular beam experiments too such as laser cooling, beam collisions, fluorescence spectroscopy, atom interferometry, *etc.* Properties of the atomic oven such as its output atomic flux, brightness, divergence, lifetime, design simplicity *etc.* depends on the applications and requirements of the experiment. The basic structure of any atomic oven consists of a reservoir where the atomic species is heated to achieve the desired vapor pressure. Depending on the atomic species, oven temperature varies, hence different heating methods such as, resistive [118], electron bombardment [119, 120] and inductive [121, 122] are being used. Resistive heating is widely used for temperatures upto 1200 °C [131–136] as controlling temperature becomes easy by regulating the current flow [135, 137–140]. Along with that, different oven geometries are used to produce intense [123–126] and collimated [127–130] source. Electron bombardment and inductive heating methods are widely used for heating upto 1800 °C [144] and above 2000 °C [?, 145], respectively. Laser ablation of solids is also a widely used technique to deliver ions to an RF trap by vaporization and ionization of material from the metal surface [146, 147].

An oven with only a reservoir with an exit hole gives larger axial beam widths. For collimation, long tube is used which is further modified with multichannel [141,142] and microcapillary array [126,143] to increase the atomic flux. The ovens can therefore have complex designs depending on specific requisites or choice of samples. Spatial distribution of atoms depend on the oven geometry whereas their velocity distribution depends on the temperature. In case it is required, velocity distribution of the atoms are modified by laser cooling technique, as an example, whereas controlling of its spatial distribution can be achieved by proper choice of the oven geometry. Also, studying atoms' distribution pattern is always a subject of interest [142,151–157]. Clausen modelled the angular distribution of molecules emerging from cylindrical tubes and analyzed its dimensional dependency [151], which was later experimentally verified by Dayton [152]. Giordmaine *et al.* studied peak beam intensities and beam widths from array of long tubes stacked in different shapes [153]. The predicted theory justifies only the centreline intensity since it assumed zero number density at the nozzle end of the tube. Olander *et al.* modified that with finite number density at the nozzle end [142]. Further, they experimentally verified their model for multichannel source [154] and demonstrated its dependency on the source size [155]. Beijerinck *et al.* measured the velocity and angular distribution of atomic beam produced from multichannel arrays in both transparent and opaque mode [141]. Krasuski studied the shapes of angular distribution at different exit zones of a tube which leads to better understanding of the atomic flux pattern [158].

Various systematic effects like unwanted electric and magnetic fields, collision effects, black body radiation, *etc.* can perturb the frequency of the clock transition. One such critical source of perturbation is patch potential arising due to differential work function between trap electrodes and atoms from oven sticking to them [130,149,150]. Ion traps are subject to anomalous heating due to such effect. Lesser systematic shift values is desirable for a good frequency standard. A collimated atomic source is the solution to minimizing the systematic shifts arise due to formation of patch potential. The on-axis beam flux from the oven is not an issue as it primarily takes off in a straight trajectory whereas it is the off-axis flux which leads to divergence and hence larger beam widths. Therefore, a narrow divergent atomic oven can be realized by controlling off-axis beam. In order to restrict deposition of the unused atoms at the experimental region of interest, many efforts are made to produce nearly collimated atomic beam [125,126,129]. Based on shadowing of the off-axis flux, three classes of ovens exist: bright wall, dark wall, and recirculating oven. Off-axis atoms striking the oven wall gets re-emitted with a $\cos\theta$ distribution in bright wall oven, absorbed in dark wall oven and re-sent to the source in recirculating oven by capillary action for re-use [148].

The requirement of an atomic oven in our experiment is to suffice the adequate amount of neutral Ytterbium (Yb) flux to be trapped, ionized and cooled at the Paul-type ion-trap

centre. The design of our indigenously developed UHV chamber within which the ion-trap is mounted at 10^{-11} mbar is such that the available distance between the trap centre and the viewport of the chamber is 117 mm [79]. The oven should be at an optimum distance from the trap centre so that the temperature of the trap is not affected by heat radiated from the oven. Also, the tip-to-tip distance between the inner electrodes of the Paul trap is 0.7 mm [78, 207] which necessitates a low-divergence atomic beam with low flux to avoid patch potential effects. In this chapter, we present the design of a dark wall oven giving narrow divergent beam. We also studied modified spatial distribution of outgoing atomic flux: theoretically modelled the distribution function, experimentally verified it and compared that with bright collimating ovens. The design results from non-homogeneous thermal distribution due to partial heating of a single capillary. This delivers a low-divergent atomic flux that has been tested to produce Ytterbium (Yb) atomic beam. Due to the dark wall at the exit end, spatial distribution is truncated above an angle. Finite Element Method (FEM) by using COMSOL Multiphysics[®] software is performed for studying the thermal distribution throughout the capillary. This facilitates to choose the suitable oven design parameters. Section 3.2 of this chapter describes details of the oven design and theoretical model of outgoing atoms' angular distribution pattern. Experimental results and associated discussions are presented in Sec. 3.3.

3.2. Oven design and its atomic flux distribution

The knowledge of flow regimes is vital while designing a molecular beam apparatus. Depending on the pressure and geometry of the vacuum equipment through which the gas is flowing, or in other words, depending on the Mean Free Path (MFP) of particles inside the apparatus, three flow regimes exist, namely, molecular flow, transition flow and continuum flow [159]. MFP given by $\lambda = kT/\sqrt{2}\pi d^2 P_{vap}$ is the average distance traversed by a particle before colliding with another particle. Here, d is atom's diameter and the vapor pressure P_{vap} at temperature T is,

$$\log P_{vap} = A + BT^{-1} + C \log T + DT^{-3}, \quad (3.1)$$

with A , B , C and D being coefficients for a particular species.

If pressure is low, MFP of the gas molecule is greater than the diameter $2a$ of the vacuum equipment characterized by the Knudsen number $K_n = \lambda/2a > 1$; this is the molecular flow regime. Under such conditions, most of the particles go out along straight trajectory as no atom-atom collisions occur inside the tube owing to its larger λ , only atom-wall collisions

eventuate. When the pressure is sufficiently high, $\lambda < 2a$ or $K_n < 0.01$, under which particles frequently collide with each other as a result of which they behave as a continuum. Transition flow results when the pressure is neither too high nor too low *i.e.* when neither molecular flow nor continuum flow subsists. In transition flow regime, $1 > K_n > 0.01$. The molecular flow regime is of our interest for designing the oven as here, majority of the particles emerge out in an undeviating path [159].

3.2.1 Initial designs

The basic parts of an atomic oven are a reservoir to store the atomic species, a collimator to pave way for the outgoing atomic flux and a heating element for metal evaporation. In the initial designs, we used a macor cavity as reservoir to store Yb pellet, with one end fitted with a normal syringe needle as collimator and the other end blocked with a push fitted metallic

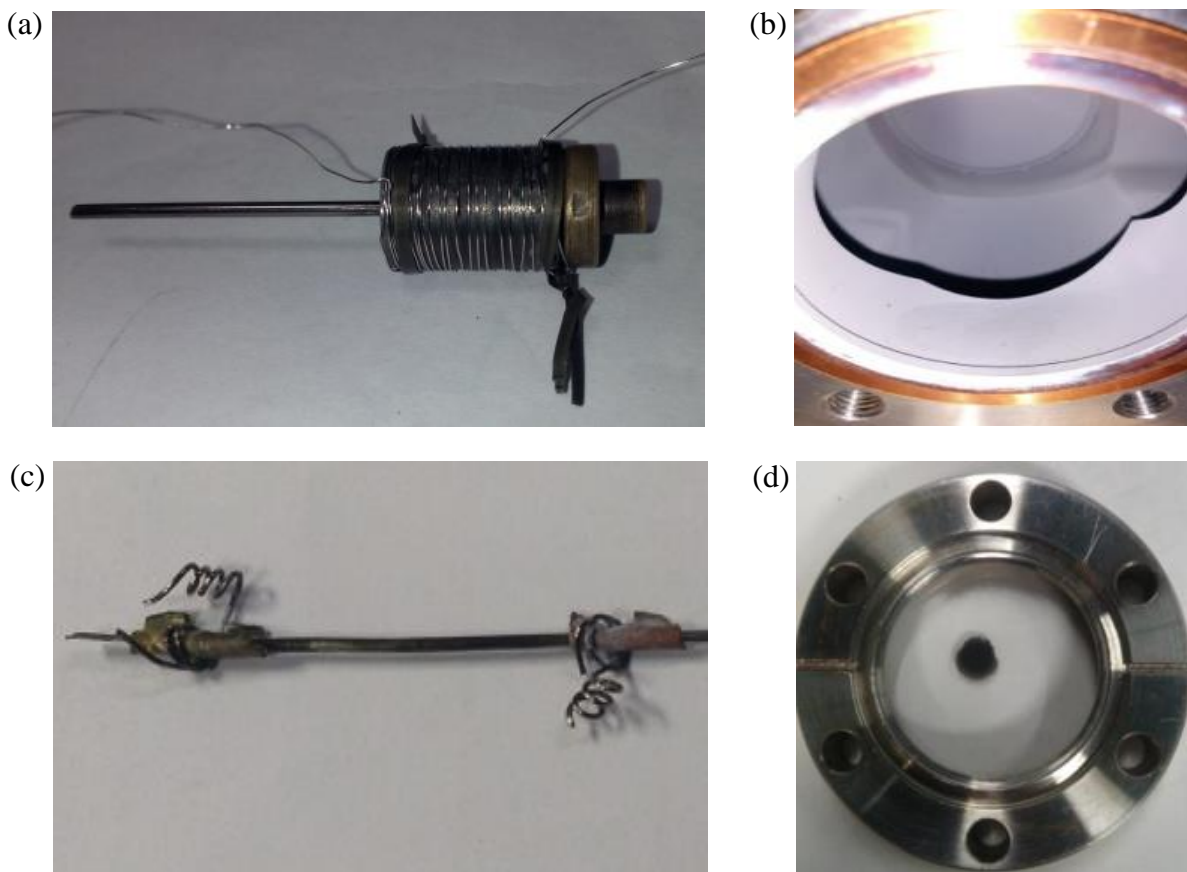


Fig. 3.1: (a) and (c) shows the initial designs for oven with (b) and (d) the corresponding atomic deposition.

cap as shown in Fig. 3.1(a). Nichrome wire due to its high melting point of 1400°C is chosen for resistive heating of macor and is wound over it. The entire set-up is installed inside a vacuum chamber backed by a turbomolecular pump creating pressure 10^{-8} mbar. After longer operating time, this design proved to be a failure as there was Yb deposition all over inside the chamber as shown in Fig. 3.1(b). This leakage resulted due to loosened ceramic-metal contact over time; due to thermal expansion of the metal cap, cracks resulted in the macor cavity. Another disadvantage of using ceramic is difficulty in its machining. In the next attempted design (Fig. 3.1(c)), we decided on to use a single capillary as both reservoir and collimator purpose to avoid any sort of leakage. We chose a seamless stainless steel capillary for the purpose with one of its ends pinched to form a closed end and serve as the crucible for Yb atoms. Tungsten wire is wound over both the open and closed end of the capillary for end-to-end heating. This solved the problem to a great extent except for a large beam width (Fig. 3.1(d)) which is unacceptable for the clock experiment as explained earlier.

3.2.2 Working design

Further modification of the oven's design has been done in order to achieve efficient and leak proof collimated atomic beam. The final working model, as shown in Fig. 3.2(a), consists of a reservoir, a collimating tube and a cold part at the exit. Aspect ratio of the collimating tube $2a/L$ defines the atomic beam flux as well as its angular divergence. Atoms are stored at the starting end of the capillary which acts as a reservoir where atomic vapor is produced and that propagates through the collimating tube. At the end of the collimating tube, the capillary is partially used as a dark wall *i.e.* a cold absorber to truncate the off-axial atoms above a certain angle. In the previously reported dark wall ovens, the reservoir, collimator and absorber are separate units and assembled together [134, 135, 160]. In our simple design, these are made out of a single 316L stainless steel (SS) capillary of inner diameter 0.9 mm and the regions are distinguishable by temperature. Thus, it is easy to mount the oven inside of a vacuum chamber. The reservoir end of the capillary is spot welded to a heating wire and closed to stop atoms from exiting. The other electrical contact is separated by a length L_E ($L_E < L$) so that current flows partially through the capillary and end part of it stays at lower temperature since thermal loss is dominating there [Fig. 3.2(b)]. By controlling the current's path, the capillary is inhomogeneously heated to create three regions widely separated in temperature. Tungsten wire of AWG 27 is used for electrical contacting of the capillary to the feedthrough pins owing to its high tensile strength of 100,000 - 500,000 psi at room temperature, good thermal conductivity of 173 W/m K and a high melting point of 3422°C . Two Macor blocks of size 12 mm \times 8 mm \times 10 mm are used for holding the capillary along their midway and

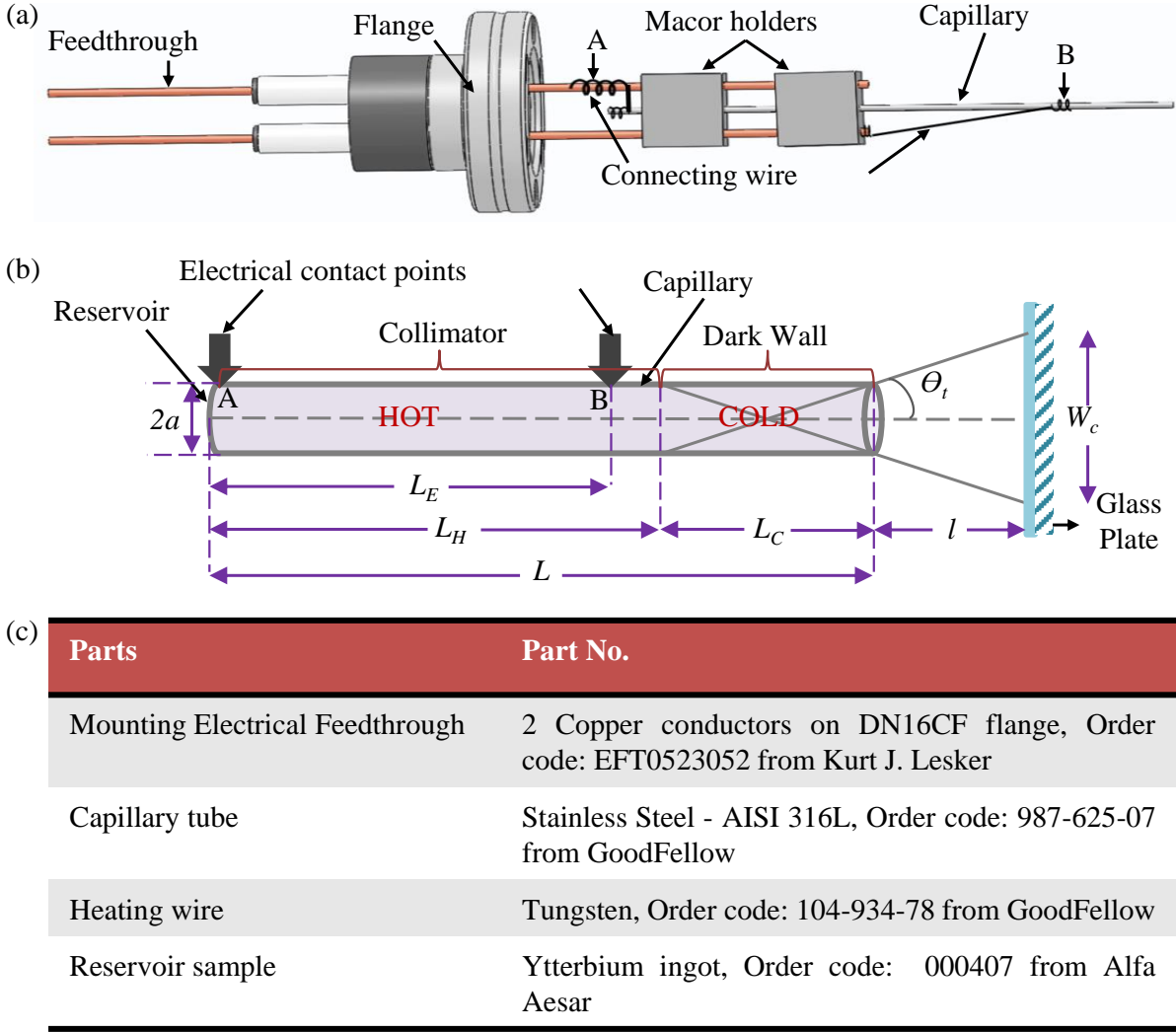


Fig. 3.2: (a) Drawing of the dark wall oven and its holders for UHV mounting. (b) Schematic of the capillary consisting of three regions: reservoir, collimator and dark wall. (c) Details of components of the developed oven.

also for firm mounting of it to the conducting pins of a standard CF16 electrical feedthrough. The cold end truncates the angular distribution at $\theta_t = \tan^{-1}(2a/L_C)$ since atoms travelling beyond that stick to the dark wall at a rate $2\pi a L_C n_o \bar{v}/4$, where $\bar{v} = \sqrt{8kT/\pi m}$ is average thermal velocity. Thus, the expected atomic beam width on a plane, *e.g.* glass plate placed at a distance l from the exit end of the capillary is,

$$W_c = 2a\left(1 + \frac{2l}{L_C}\right). \quad (3.2)$$

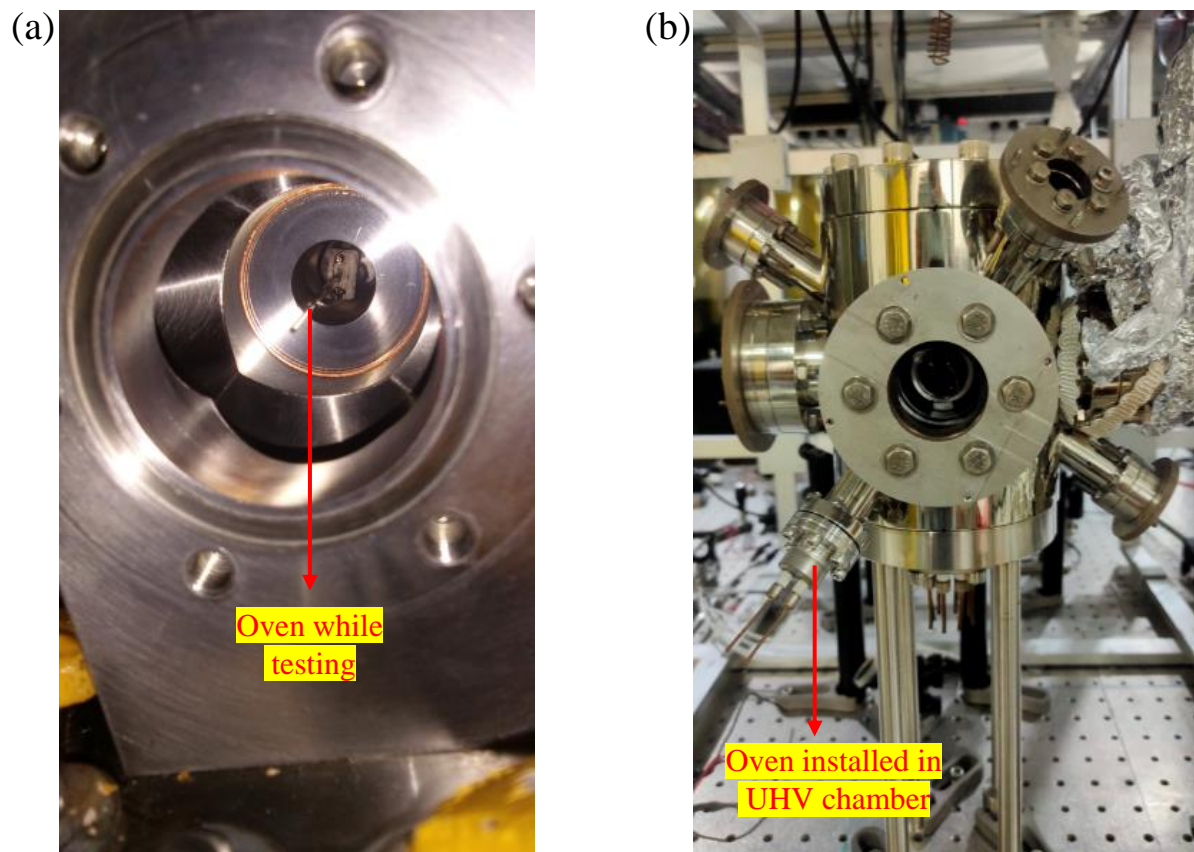


Fig. 3.3: Picture showing the oven (a) inside the testing chamber and (b) assembled into the final UHV chamber.

This assumes that atoms without colliding the wall are only coming out, which is correct for the atoms having negligible effusion coefficient at the cold end's temperature. Details of components used in developing the atomic oven along with the seller information is given in Fig. 3.2(c). Figure 3.3(a,b) shows the designed oven inside the test chamber and installed in the final UHV chamber, respectively.

3.2.3 Modified atomic flux distribution

The vaporized atoms with density n_o within the reservoir are equally probable to move along any direction with a flow rate

$$d^3\dot{N} = I(\theta)P(v)d^2\Omega dv, \quad (3.3)$$

within a solid angle $d\Omega$. Here, $I(\theta)$ and

$$P(v) = 32v^3 \frac{\exp\left(-\frac{4v^2}{\pi\bar{v}^2}\right)}{\pi^2\bar{v}^4}, \quad (3.4)$$

are the angular intensity and the normalized velocity distributions, respectively, for the atoms moving at a speed v along θ relative to the tube's axis. The angular distribution follows

$$\dot{N} = \int_{-\pi}^{\pi} I(\theta) d^2\Omega = \frac{2\pi n_o \bar{v} a^3}{3L}, \quad (3.5)$$

where \dot{N} is flow rate of atoms through a transparent tube [141]. Angular distribution of atoms exiting a wall strip of width dz situated at a distance z from the reservoir end, is given as [153],

$$dI(\theta) = \frac{n_o z \bar{v}}{4\pi L_H} 2a \sin \theta \left[1 - \left(\frac{z \tan \theta}{2a} \right)^2 \right]^{\frac{1}{2}} dz, \quad (3.6)$$

where $n(z)$ is atom's density. The centreline atomic intensity is $I(0) = n_o \bar{v} a^2 / 4$. The critical angle $\theta_C = \tan^{-1}(2a/L_H)$ is obtained from the geometry [Fig. 3.2(b)], upto which atoms exit from the collimation tube without colliding with its wall. At half angle $\theta_{\frac{1}{2}} = 1.68a/L_H$, the atomic intensity becomes $I(\theta_{\frac{1}{2}}) = I(0)/2$. The angular distribution has two components: (i) atoms that are flowing with and without hitting the wall $I_u(\theta)$, which dominates upto θ_C and (ii) atoms effusing out after hitting the wall $I_w(\theta)$, that dominates at $\theta > \theta_C$. The distribution functions as given in Ref. [153] are,

$$\begin{aligned} I_u(\theta) &= \frac{n_o \bar{v}}{4\pi} 2a^2 \cos \theta [\cos^{-1}(p) - p\sqrt{1-p^2}] + \int_0^{L_H} \frac{n(z) \bar{v}}{4\pi} 2a \sin \theta \left[1 - \left(\frac{z \tan \theta}{2a} \right)^2 \right]^{\frac{1}{2}} dz \\ &= \frac{a^2 n_o \bar{v}}{2\pi} [R(\theta) + \frac{2}{3}P(\theta)] \cos \theta, 0 < \theta \leq \theta_C, \\ I_w(\theta) &= \int_0^{2a/\tan \theta} \frac{n(z) \bar{v}}{4\pi} 2a \sin \theta \left[1 - \left(\frac{z \tan \theta}{2a} \right)^2 \right]^{\frac{1}{2}} dz \\ &= \frac{2a^3 \bar{v} n_o \cos^2 \theta}{3\pi L_H \sin \theta}, \theta_C < \theta < \pi/2, \end{aligned} \quad (3.7)$$

where

$$\begin{aligned} R(\theta) &= \cos^{-1}(p) - p\sqrt{1-p^2}, \\ P(\theta) &= \frac{1 - (1-p^2)^{\frac{3}{2}}}{p}, \end{aligned} \quad (3.8)$$

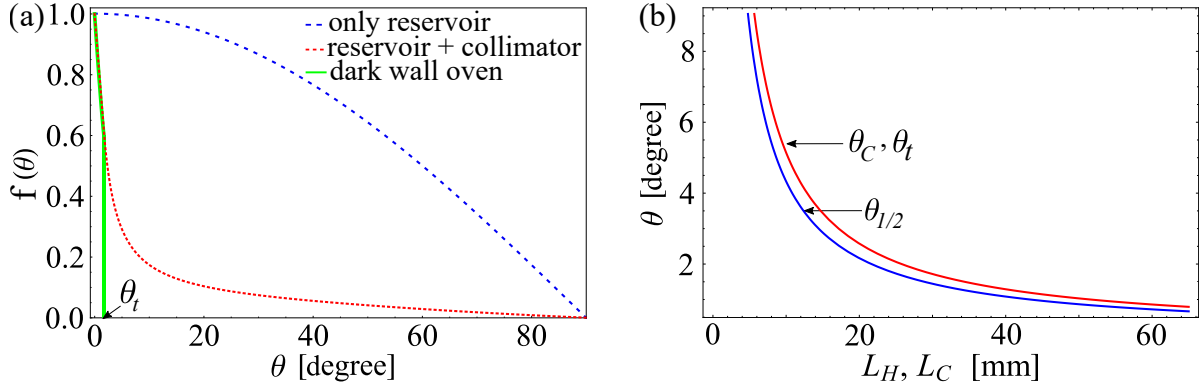


Fig. 3.4: Angular profile of atoms for different ovens such as, reservoir (blue), reservoir attached to a collimator (red) and dark wall oven (green). Inset shows critical and truncated angle (red) and half-width angle (blue) for different lengths of the capillary. Here, we consider $T = 249^\circ\text{C}$, $L = 65$ mm, $L_H = 35$ mm, $L_C = 30$ mm and $a = 0.45$ mm.

and

$$p = L_H \frac{\tan \theta}{2a}. \quad (3.9)$$

Thus, the relative angular profiles, *i.e.* $f(\theta) = I(\theta)/I(0)$ are

$$\begin{aligned} f_u(\theta) &= \frac{2}{\pi} \left[R(\theta) + \frac{2}{3}P(\theta) \right] \cos \theta, 0 \leq \theta \leq \theta_c, \\ f_w(\theta) &= \frac{8a}{3\pi L_H} \frac{\cos^2 \theta}{\sin \theta}, \theta_c \leq \theta \leq \pi/2, \end{aligned} \quad (3.10)$$

which are obtained following Giordmaine and Wang's approach [141, 153, 161]. The modified Eqn. 3.11 following Olander and Kruger model [142] considering non-zero number densities at the source and exit ends of the tube are,

$$\begin{aligned} f'_u(\theta) &= \zeta_0 \cos \theta + \frac{2}{\pi} \cos \theta \left[\zeta_1 R(\theta) + \frac{2}{3}(\zeta_1 - \zeta_0)P(\theta) \right], \\ &0 < \theta \leq \theta_C, \\ f'_w(\theta) &= \zeta_0 \cos \theta + \frac{8a}{3\pi L_H} (\zeta_1 - \zeta_0) \frac{\cos^2 \theta}{\sin \theta}, \\ &\theta_c \leq \theta \leq \pi/2. \end{aligned} \quad (3.11)$$

Here, dimensionless parameters $\zeta_0 = 4a/3L$ and $\zeta_1 = (1 - \zeta_0)$ are related to the wall collision rates at the entrance and exit of the capillary, respectively. Figure 3.4 compares angular profiles of outgoing atoms from effusive ovens with and without collimation, following $L \gg 2a$ and $L < 2a$, respectively. For comparison, truncated distribution from a dark wall oven is also shown there. The angles, θ_C , θ_t and $\theta_{\frac{1}{2}}$ for different aspect ratios of the collimator and the

dark wall tubes are shown in the inset, which suggests stronger collimation can be obtained at longer collimator lengths but at a cost of lower throughput. It is to be noted that the truncated angular distribution expected from a collimator followed by a dark wall has similar nature like θ_C but they operate at different length scales defined by values of L_H and L_C . Atoms at the tail of the distribution are mostly not useful since they are beyond capturing capability of a trapped atom experiment, hence truncation is not inefficient for the atom loading.

The rate of flow of atoms upto a velocity v and angle θ can be obtained as,

$$\begin{aligned} F_v^\theta\left(\frac{a}{L}, \frac{a}{L_H}, T\right) &= \dot{N} \int_0^\theta F(\theta) 2\pi \sin \theta d\theta \int_0^v P(v) dv \\ &= \frac{\dot{N}}{2\pi} \left[\pi \sin^2 \theta + (\zeta_1 - \zeta_0)(\sin 2\theta - 2\theta_C - 2\theta) \right] \\ &\quad \left[1 - \exp\left(-\frac{4v^2}{\pi \bar{v}^2}\right) \left(1 + \frac{4v^2}{\pi \bar{v}^2}\right) \right]. \end{aligned} \quad (3.12)$$

Here, $F(\theta) = \kappa f'(\theta)/\pi$ is the normalized angular distribution function where $\kappa = \pi I(0)/\dot{N} = 3L/8a$ [141] is the 'peaking factor' that characterizes the degree of collimation. In the spirit of our trapped Ytterbium-ion (Yb^+) optical clock experiment [80, 106, 162–165, 207], as an example, the maximum velocity v_{cap} that can be captured in the ion trap is defined by its depth given by,

$$D_{trap} = \frac{a^2 Q r^2 V^2}{4m R^4 \Omega^2}, \quad (3.13)$$

which depends on the trapping voltage, V . Here, a, z are trap geometry specific parameters, V is applied voltage at radio-frequency Ω , Q is charge and R is radius of the trapping volume. The maximum θ can either be θ_t or maximum capturing angle by the trap depending on whichever is smaller.

3.3. Results and discussions

3.3.1 Theoretical simulations

We used ‘‘Electric Currents’’ and ‘‘Fluid Flow’’ submodules of COMSOL to study steady state temperature variation and atomic flux flow, respectively, through the microchannel SS capillary. The temperature distribution in the capillary for its different heating configurations are simulated to obtain the desired temperature distribution distinguishing reservoir, collimator



Fig. 3.5: Snapshot of the COMSOL window showing simulation for temperature distribution in the oven at current 2.7 A. The model tree in model wizard shows the orderly sequence of operations including geometry, material, physics, mesh, study, plot groups, etc.

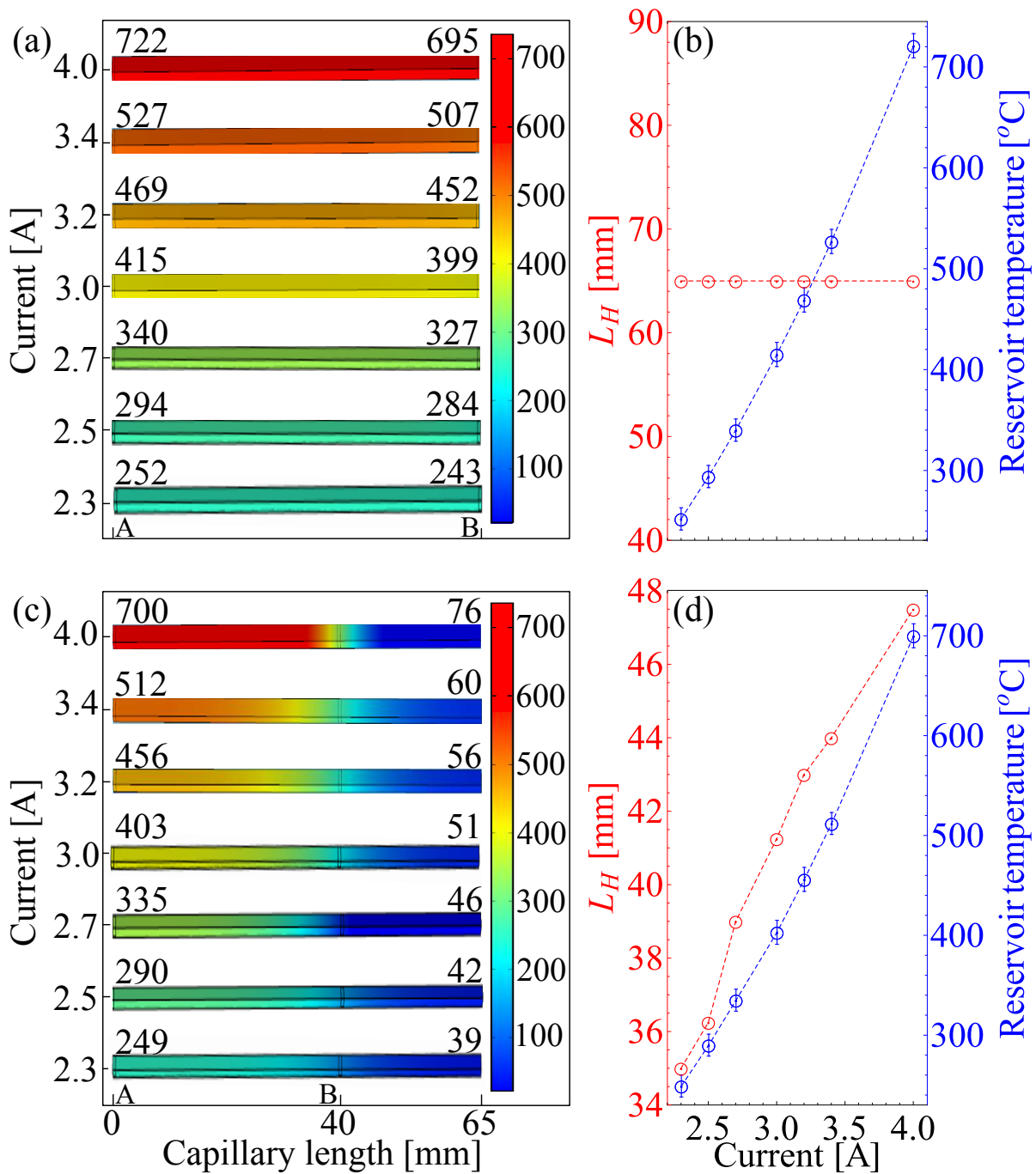


Fig. 3.6: Numerically simulated variation of temperature (in °C) along the length of the capillary for: (a) ovens with collimator and (c) in the presence of cold absorber. (b,d) show variation of the collimator's length L_H with current and corresponding reservoir temperature for a fixed operating voltage = 1.7 V.

and dark wall regions. The stepwise approach towards modelling the geometry and physics in COMSOL is already discussed in Chapter 2. Figure 3.5 displays the model builder and

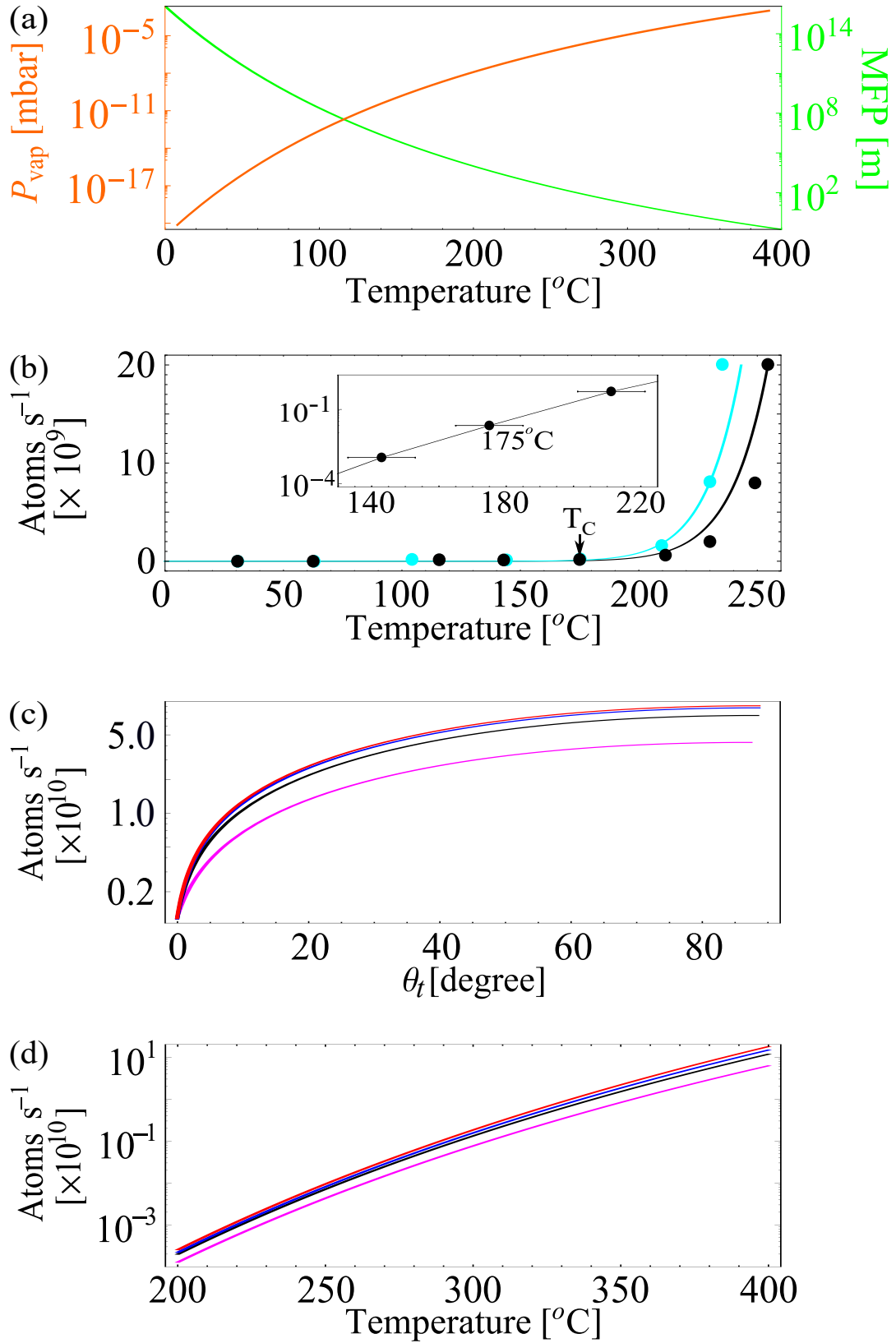


Fig. 3.7: (a) Variation of Yb vapor pressure (orange) and its mean free path (green) with temperature. (b) Output Yb flux with increasing temperature for bright oven with collimator (cyan) and dark wall oven (black) are shown. The discrete points in cyan and black are the corresponding numerical values, its inset emphasizes the critical temperature. Flux of atoms at different (c) cut off angles and (d) oven temperatures for fixed trap electrode voltage of 250 V (magenta), 350 V (black), 450 V (blue) and 550 V (red) that are available to be captured in our ion trap.

graphics window corresponding to reservoir temperature estimation at 2.7 A with the workflow details in the model tree. One needs to commence by selecting the space dimension, add required physics interface followed by stationary or time dependent study type. We define a critical oven temperature T_C at which output flow rate is negligible to use. In case of an inhomogeneously heated capillary, the point at T_C defines L_H . The capillary's length over which $T > T_C$ acts as the collimator and rest of it acts as the dark wall. Although we considered a wide variety of capillary geometry for simulations to identify the suitable one, we report here the results obtained for $L = 65$ mm, $a = 0.45$ mm and $L_E = 40$ mm giving variety of L_H and L_C at different currents, that we finally used to construct the oven. In case of heating the entire capillary, *i.e.* $L_E = L = L_H$ and $L_C=0$, inhomogeneity of the temperature distribution is within the accuracy of the simulation, as shown in Fig. 3.6(a) for different currents. In this case, the entire capillary acts as the collimator and the current regulated reservoir temperature is shown in Fig. 3.6(b). Partial heating of the capillary from reservoir end upto some intermediate point, as an example $L_E = 40$ mm, at different currents are shown in Fig. 3.6(c). Figure 3.6(d) clearly shows that for a fixed L_E , collimator's length L_H increases with stronger heating. Thus, a proper choice of the electrical contact points and current results to a desired length of the dark wall. As obtained from the FEM analysis, we consider $T_C \approx 175^\circ\text{C}$ at which output flux is two orders of magnitude smaller than the desired and this matches well with our experimental observation as described later. The response times of the dark wall oven to reach to 250°C and 350°C from the room temperature are 378 s and 402 s, respectively, as obtained by using the FEM analysis, whereas it takes only 94 s and 171 s to reach to these temperatures from the T_C . Thus, rather than reducing the reservoir temperature to room temperature, it may be set near to T_C while the oven is in frequent use.

Figure 3.7(a) shows temperature dependency of vapor pressure and MFP of ^{171}Yb atoms that satisfies $K_n > 1$ at $T > 127^\circ\text{C}$. The temperature dependent output flow rate of atoms following Eqn. 3.5 and their simulated values are shown in Fig. 3.7(b). The abrupt increase of the flow rate at $T_C = 175^\circ\text{C}$ is highlighted in the figure. As expected, the dark wall oven produces lower flow rate owing to the truncation of off-axis atoms. Figure 3.7(c,d) show capturable atoms for different θ_t and oven temperatures, respectively, estimated using Eqn. 5.3. Typically, ions upto a velocity v_{cap} corresponding to 10% of the trap depth can be captured in an ion trap. Considering our ion trap, that captures all atoms upto θ_t and operates at $\Omega=2\pi \times 15$ MHz and with 45% RF transfer efficiency to the trap electrodes [165], we have estimated D_{trap} and hence the maximum capture velocity. As an example, for the oven operating at 300°C and $v_{cap} \approx 535$ m/s, in case the ion trap operates at 1000 V RF, about 1.6×10^9 ions/s will be available for capturing, assuming 100% ionization of the atoms.

3.3.2 Experimental results

We have tested performance of our dark wall oven to produce ^{171}Yb atomic beam and compared the obtained flux distribution with that obtained through our model. The oven is tested at different currents as the simulation shown in Fig. 3.6 while heating the entire capillary and also for different cold end lengths during dark wall mode of its operation. For all the measurements, the oven was housed inside a vacuum chamber maintained at a pressure of 10^{-9} mbar vacuum, $L=65$ mm and for a fixed run time of 36 hours while the spots were recorded on a glass plate kept at a distance of 30 mm from the end tip of the oven. Deposition of Yb atoms on the glass plate is confirmed through chemical reaction. The glass plate with Yb in metallic silver color deposited on it is exposed to gaseous iodine and after few hours, it turns to white YbI_3 confirming presence of Yb. Yb spots deposited on glass slides are imaged through a digital microscope (Model No. 44308, Celestron) for different operating currents as shown in Fig. 3.8. As is evident, with increasing oven currents, axial beam width increases. With increasing current, the cold end temperature rises, thus permitting a fraction of the off-axis atoms to exit the tube. Figure 3.9(a) shows spatial distribution of atoms while the oven is entirely heated at $T = 252$ °C without any dark wall. Profile of the spot sizes are measured by Stylus profilometer which has a spatial resolution of $0.5 \mu\text{m}$ [166]. The profilometer has a probe which moves across a surface acquiring its height. In the dark wall mode of operation, at 2.1 A corresponding to $179(10)$ °C, a circular spot of Yb atoms deposited on the glass plate was barely detected by the Stylus. This temperature is good in agreement with the numerically estimated T_C within its accuracy. Truncated spatial distribution of atoms, as shown in Fig. 3.9(b), clearly indicates that spot size increases with higher current due to decrease of L_C [Fig. 3.6(c)]. Truncation extends to higher θ_t with increasing current together with increase of centreline intensity and the total flux following Eqn. 5.3. Assuming radially symmetric deposition of atoms in a circular profile, Stylus data along several diametric direction of it were averaged. The relative angular profiles corresponding to varying currents obtained from measured spatial distributions are

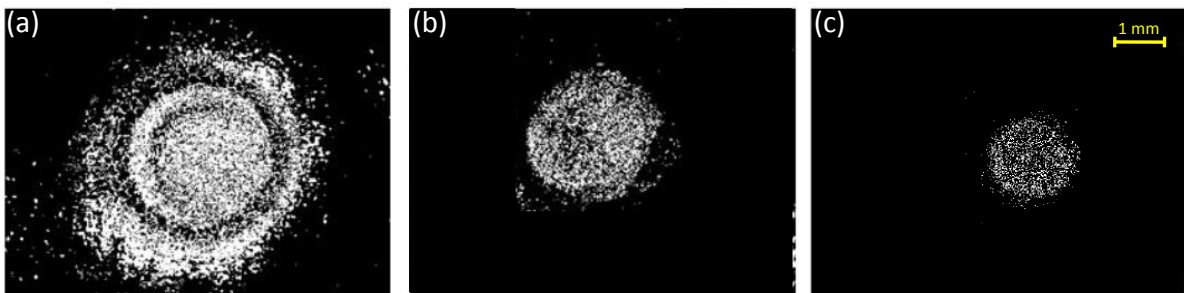


Fig. 3.8: Images of the Yb atoms, deposited on a glass sample, taken from Digital Microscope at (a) 4 A, (b) 3.2 A and (c) 2.3 A, respectively.

shown in Fig. 3.9(c), which are well described by the distribution function as given in Eqn. 3.11. Steep off axial decrease of atom's density and truncation as described in Fig. 3.4 are clearly visible at lower current *i.e.* longer L_C . The fitted values of L_H , as given in Eqn. 3.11, are in agreement with the numerical simulations [Fig. 3.6(d)] considering $T_C = 175$ °C. Figure 3.9(d) depicts experimental θ_t values obtained from distributions as shown in Fig. 3.9(c) for varying cold end lengths. The data matches well with the theoretical model following Eqn. 3.2. This reconfirms that with decreasing L_C at higher operating current, θ_t increases. Pointing nature of atoms' distribution towards centre of the spot [Fig. 3.9(b)] matches very well to the theoretical predictions Fig. 3.4. The minimum spot size produced by our dark wall oven has $1.2(1)^\circ$ divergence at 2.3 A and 1.7 V. The corresponding oven temperature $250(10)$ °C produces a flux of 7.9×10^9 atoms s^{-1} that is good enough for most of the experiments where higher divergence is not tolerable. Figure 3.10 shows the numerically calculated atomic flux using COMSOL by employing Eqn. 3.5 and those estimated using experimentally obtained

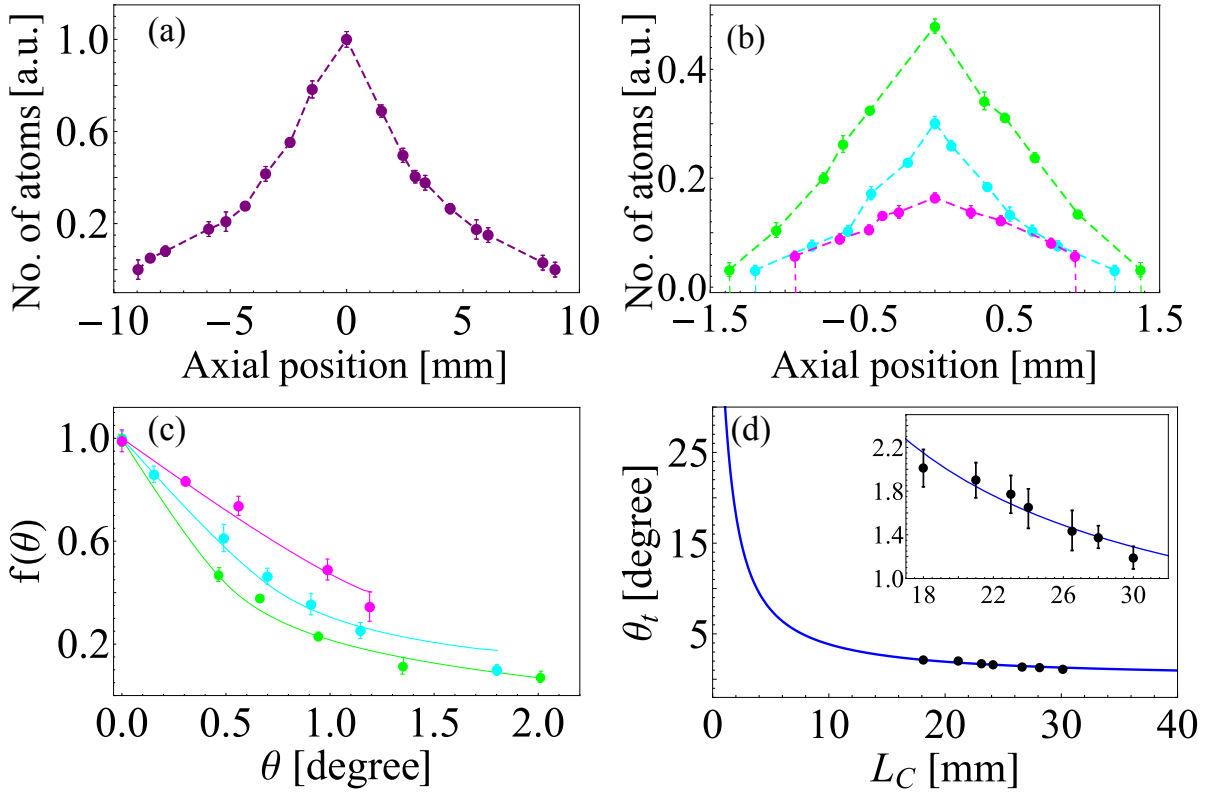


Fig. 3.9: Measured spatial profiles of Yb spot for: (a) end-to-end heating of the capillary at 2.3 A, (b) dark wall oven operated at 2.3 A (magenta), 3.2 A (cyan) and 4 A (green). (c) Relative angular profiles along with the fitted curves. (d) Variation of experimentally obtained truncated angle values for varying cold end length along with the fitted model.

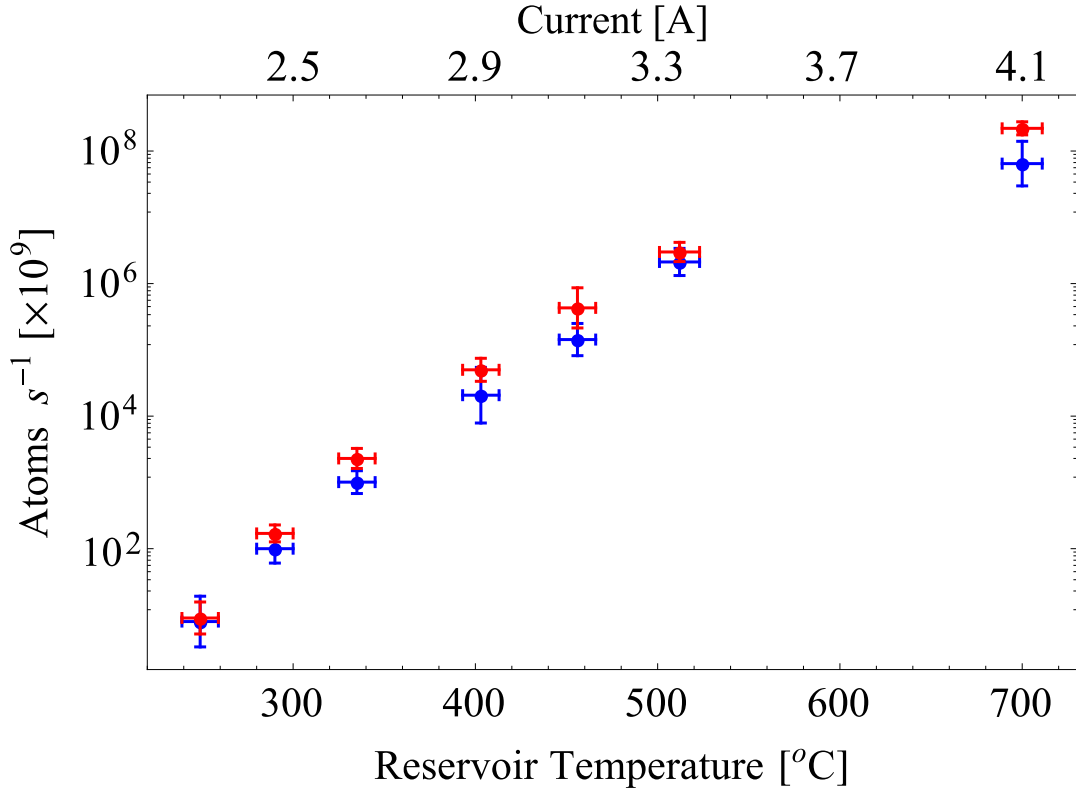


Fig. 3.10: Temperature dependence of the atomic flux coming out of the dark wall oven, as estimated numerically using COMSOL (blue) and using the measured $f(\theta)$ distribution function (red).

distribution function. Atomic flux upto a θ_t can be estimated as,

$$F_{\theta_t} = P_{vap}(T)a^2\sqrt{8kT} \int_0^{\theta_t} \frac{2\pi}{4kT\sqrt{\pi m}} f(\theta) d\theta, \quad (3.14)$$

where 2π arises due to radial symmetry of the distribution. Here, at a particular temperature T , $P_{vap}(T)$ is estimated as shown in Fig. 3.7(a) and fitted function of $f(\theta)$ at different temperatures as shown in Fig. 3.9(c) are used to estimate the atomic flux. In this case, uncertainties are estimated considering inaccuracies of $f(\theta)$, θ_t and our confidence on estimating oven temperature. Both the results are comparable to each other within their uncertainties.

3.4. Conclusion

A novel design of a simple dark wall oven is presented which is easy to operate for controlling the atomic beam divergence by proper choice of the capillary geometry and the contact points of resistive heating. Modified spatial distribution of atomic flux coming out from the designed

and developed oven is studied in detail and its high degree of collimation than that of a bright oven with collimator is obtained. We performed finite element analysis of the oven heating and atomic flux flow through it, theoretically modelled distribution function of the atomic flux and verified that via experimental measurements. The measured critical temperature 179(10) °C at which the atomic flux flow of ^{171}Yb atoms for our oven geometry is negligible to use, matches well with the numerically simulated value of 175 °C. Also, theoretically obtained distribution function is well characterized with the experimental observations, as shown for different operating conditions. Atomic flux as estimated using our measured spatial distribution of atoms matches to the numerically simulated values. Using a 65 mm capillary of fine diameter of 0.9 mm including a cold exit end of length 35 mm operating at 2.3 A and 1.7 V, we are able to generate an atomic beam with minimum divergence of $1.2(1)^\circ$ corresponding to $\theta_{\frac{1}{2}} = 0.8(1)^\circ$. This is better than many other complicated oven designs reported earlier. A dark wall oven, as described here, with multichannel array could be a way for producing high intensity, nearly collimated atomic beam.

Chapter 4

An imaging system with sub-micron resolution for detecting fluorescence from a single trapped ion

Publication: Lakhi Sharma, A. Roy, S. Panja, and S. De, An easy to construct sub-micron resolution imaging system, *Scientific Reports* **10**, 21796 (2020).

4.1. Introduction

In ion trap experiments, detection technique plays a crucial role in confirming the trapping of the desired species accompanied with extracting precise information regarding its state and other characteristics. Most commonly, two types of detection techniques are used: electronic (destructive) technique and fluorescence (non-destructive) technique. Electronic technique depends on expulsion of trapped ions so that these can be tracked by an external detector whereas the fluorescence technique relies on interaction of the trapped ions with electromagnetic radiation to monitor the emitted photons. The electronic technique is generally employed in cases where the trapped species do not have a closed fluorescence cycle or if the fluorescence wavelength is difficult to be generated and destroys any information related to the trapped sample. The fluorescence technique, on the other hand, involves detection of the ion's fluorescence based on a strong transition and ensures to preserve additional details of the ion. Since, we are aiming to retrieve information about the trapped sample, we chose the non-destructive technique. Neutral Yb beam produced by the atomic oven for trap loading needs to be further ionized by a combination of 399 nm and 369.5 nm lasers, thus preparing them for the trap. The 369 nm laser which probes the transition $^2S_{1/2} \rightarrow ^2P_{1/2}$ of $^{171}\text{Yb}^+$ also aids in cooling the trapped ion and induces a fluorescence which can be collected for imaging the trapped ion/ions.

The emitted photons are the main source of information regarding the trapped ion's dynamics and other parameters like its temperature, heating rate, secular frequency, *etc.* [212, 213]. For employing the fluorescence detection technique, a high resolution optical system is to be designed which can improve image quality by correcting the wavefront deformations that are introduced as the fluorescence photons travel from the source to image plane.

Studying molecular dynamics, many body physics, quantum simulation by detecting individual atoms and ions rely on high resolution and minimally aberrated optical system which can form a magnified image of the object. Such imaging systems are used in fluorescence microscopy and mass spectroscopy, which gained immense interest particularly for detection of biological molecules and other chemical compounds. Micron level resolution in such cases allows direct study of the molecular dynamics [167, 168]. Precision spectroscopy for parity non-conservation (PNC), electric dipole moment, optical clock *etc.*, which uses single atom [169–171] or ion [172–176], rely on high resolution imaging as the detection technique. Quantum phase transitions, quantum simulations and quantum information processing (QIP) by using atoms in an optical lattice or array of ions in an electrodynamic trap demands imaging of the individual particles.

In particular to the rapidly progressing QIP, (i) scaling up of the qubit and (ii) their individual addressing are the present challenges for which reading the individual atoms or ions is important [177]. These applications demand sub-micron resolution for detection of trapped ions [178–183] and atoms in optical lattices [184–188]. Different approaches, such as, by measuring the current produced upon impinging of a focussed electron beam on to the sample [189] and most commonly by setting up of a high quality imaging system are being used. In the latter case, the signal photons either from fluorescence or from absorption imaging are collected by different customized optical systems such as micro fabricated Phase Fresnel lenses (PFLs) or by using high NA diffraction limited objectives. W. Alt reported an objective with NA 0.29 covering 2.1% of 4π solid angle to detect a single atom in a magneto optical trap [190]. Y. R. P. Sortais *et al.* reported imaging with objective of NA 0.5 and magnification of 25 [191]. K. D. Nelson *et al.* first reported direct observation of individual atoms in lattice sites and imaging different lattice planes using a lens of NA 0.55 and magnification 32 [188], which then became a powerful tool for such systems to study quantum dynamics. M. Karski *et al.* reported an objective with NA 0.29 and magnification of 54 to resolve atoms separated by 433 nm [192]. Using customized lenses and wavefront corrector plate, A. S. Bakr *et al.* achieved the highest effective NA 0.8 so far and resolution 0.6 μm , which was pathbreaking for quantum gas microscopy [193]. For high resolution detection over large volume, A. Jechow *et al.* demonstrated use of microfabricated PFLs that obtained NA of 0.64 covering 12% of 4π solid angle and a magnification of 615 ± 9 [194]. Due to small size, PFLs can be placed close to

the sample which results to higher NA and they can also be arranged in an array to extend the viewing region further [179]. J. D. Wong-Campos *et al.* reported the least aberrated imaging and NA 0.6 to detect ions confined in a microfabricated trap [181].

A trapped single ion yields about a few hundreds of photons per second. For its detection, these photons are to be collected and imaged and this calls for a very efficient and high resolution imaging system. Based on experimental requirements, we have therefore designed and discussed the performance of an easy to construct imaging system using off-the-shelf available aspheric lenses and aberration corrector plates. The design can be adapted over visible to near-infrared wavelengths in different applications which require sub-micron spatial resolution and high quality images. Section 4.2 describes details of the design of the imaging system and related parameters which define its performance while the results and associated discussions are presented in Section 4.3.

4.2. Design of the lens system

This section discusses the process of lens design, experimental constraints, various parameters to be studied based upon which the best suitable design will be opted and the tolerancing analysis.

4.2.1 Aberration theory

The wavefronts propagating with photons get deformed due to inhomogeneous refractive index of the medium. As a result, the quality of image formed by an optical system is degraded. This can be minimized, if not eliminated [195], by proper choices of lenses and optimization of the design parameters. For quantitative analysis, let's consider (y, z) and (Y, Z) as the coordinates for exit pupil and its image, respectively, while the source is at the origin and the imaging system is along the x axis, as illustrated in Fig. 4.1. Introducing polar coordinates (ρ, θ) and (r, ϕ) in the exit pupil and image planes, respectively, the wave aberration $W(h, \rho, \theta)$ at the exit pupil for a rotationally symmetric optical system in its image plane (yz plane), can be written as [196, 197]:

$$W(h, \rho, \theta) = \sum_{j,m,n} W_{klm} h^k \rho^l \cos^m \theta, \quad (4.1)$$

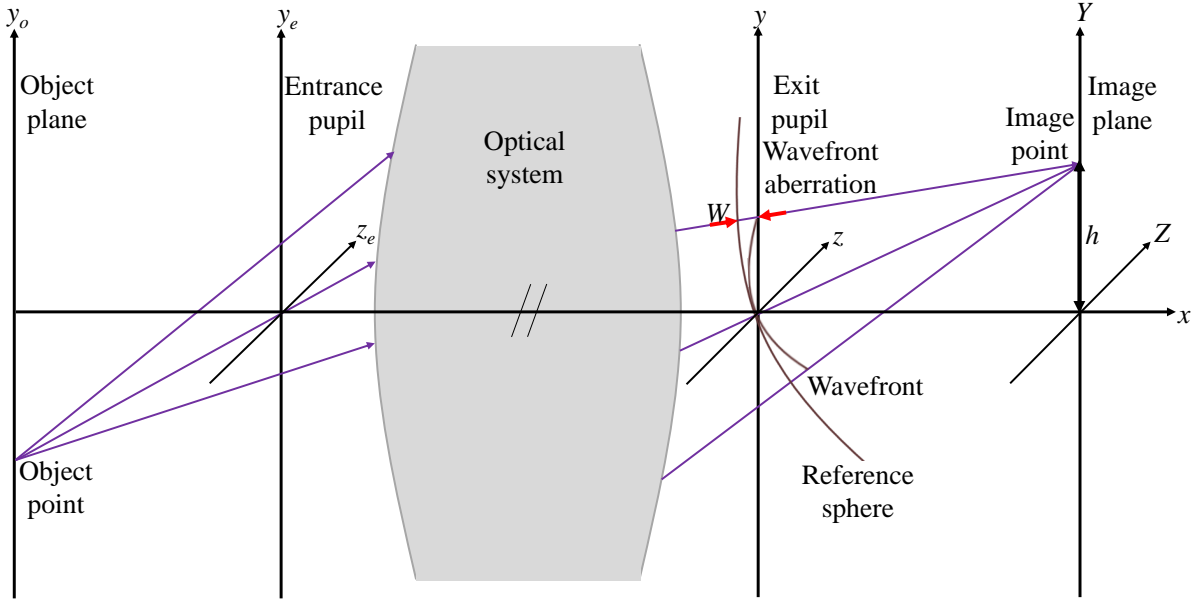


Fig. 4.1: A wave from a point at a distance h from the origin in the object plane is incident on the entrance pupil from which it then propagates through an optical system towards the exit pupil. The entrance pupil, exit pupil and the image point are referred to by (y_e, z_e) , (y, z) and (Y, Z) , respectively.

where aperture size $\rho = \sqrt{y^2 + z^2}$, θ is the azimuthal angle in the pupil plane, h is the image height, j, k, l, m, n are integers satisfying the condition $k = 2j + m$, $l = 2n + m$ and W_{klm} are the aberration coefficients. Upon expanding Eqn. (4.1), the terms associated to coefficients W_{200} , W_{111} and W_{020} represent piston, tilt and defocus, respectively, which do not contribute in case of monochromatic light source. Terms associated to W_{040} , W_{131} , W_{222} , W_{220} and W_{311} represent Seidel aberrations such as spherical, coma, astigmatism, field curvature and distortion, respectively and the remaining represents higher order distortions [196]. In case of monochromatic photons emitted by a point source located close to the imaging axis, coma and astigmatism do not play major role. Spherical aberration results from meridional rays failing to follow paraxial approximation. It dominates in case of imaging fluorescence that is isotropically emitted in all directions, hence Eqn. (4.1) simplifies to

$$W(\rho) = \sum_{n=2}^p W_{02n0} \rho^{2n}, \quad (4.2)$$

where $k = 0, l = 2n, m = 0$ and p and n are integers. The spatial profile of an image corresponding to a point source is given by the PSF as

$$S(r, \phi) = A(r, \phi)A^*(r, \phi), \quad (4.3)$$

which is in the form of an Airy pattern for a nearly perfect optical system, which is actually the Fraunhofer diffraction pattern obtained for a circular pupil [198]. Here, A and A^* are amplitude distribution of the image and its complex conjugate, respectively. The deformation of amplitude distribution during propagation can be obtained from pupil function as,

$$P(\rho, \theta) = E(\rho, \theta) \exp[ikW(\rho)], \quad (4.4)$$

where k is the wave vector and $E(\rho, \theta)$ is the transmittance amplitude of the optical system. Hence, the amplitude distribution is,

$$A(r, \phi) \approx C \int_0^{2\pi} \int_0^1 P(\rho, \theta) \exp[-i\rho\beta \cos(\theta - \phi)] \rho d\rho d\theta, \quad (4.5)$$

with $\beta = \frac{\pi r}{\lambda F}$ and $C = \frac{-i}{4\lambda F^2} \exp\left(ik \frac{r^2}{r_W}\right)$, where $r = \sqrt{Y^2 + Z^2}$, λ is photon's wavelength, F is effective focal number and r_W is radius of curvature of the wavefront at the exit pupil. Considering fully transmissive pupil *i.e.* $E(\rho, \theta) = 1$ and using Eqns. (4.4, 4.5), the PSF reduces to [196, 197, 199]

$$S(r, \lambda, F) \approx \frac{\pi}{\lambda^2 F^2} \left| V_0 + ikV_1 - \frac{k^2}{2} V_2 \right|^2, \quad (4.6)$$

where,

$$\begin{aligned} V_0 &= 2 \int_0^1 J_0(\beta\rho) \rho d\rho = 2 \frac{J_1(\beta)}{\beta}, \\ V_1 &= 2 \int_0^1 W(\rho) J_0(\beta\rho) \rho d\rho, \\ V_2 &= 2 \int_0^1 W^2(\rho) J_0(\beta\rho) \rho d\rho, \end{aligned}$$

where J_0 and J_1 are Bessel functions of first kind of order 0 and 1, respectively. The normalized PSF reduces to

$$S(r, \lambda, F) \approx V_0^2 - k^2(V_0V_2 - V_1^2) + 0.25k^4V_2^2, \quad (4.7)$$

which we shall use throughout this chapter. Here, the term V_0^2 represents ideal Airy pattern for an aberration free optical system whereas the remaining terms are associated with the optical system being affected by spherical aberration of higher orders.

4.2.2 Methodology

Probable solution to minimization of aberrations is to design the optics in such a way that one lens or combination of lenses corrects or lessens the distorted wavefronts created by another. The Optics Software for Layout and Optimization (OSLO) has been used for design optimization of the imaging system. It is capable of performing ray tracing and estimating the mentioned quality assurance parameters of an optical assembly upon proper feeding of its components [200]. OSLO considers upto 7th order of $W(\rho)$ as given in Eqn. (4.2) for its analysis using sequential ray tracing method [200]. Using OSLO, different combinations of lenses are iteratively altered and checked for best performance based on certain optical excellence deciding parameters which specify characteristics of an imaging system.

Our aim is to find optical solution to image a single Ytterbium ion (Yb^+) which is a point like source emitting fluorescence at wavelength 369.5 nm. The imaging system for such cases should have efficient fluorescence collection, adequate resolution l_R and magnification M to distinguish individual ions and minimized aberration. Here, we consider transverse spherical aberration (SA) owing to the fact that all rays fall within the magnified image eventhough longitudinally they are not focussed at a single point. The resolution should be either same as object size or more preferably lesser than that or else two objects will appear as one. Other than SA, Strehl ratio SR and root mean square wavefront deformation σ are some of the parameters to be taken care of. SR is the ratio of illumination at the center of the Airy disk for an aberrated system to that for its corresponding perfect system and it is related to σ following [201–204],

$$SR = \exp(-2\pi\sigma)^2, \quad (4.8)$$

which can be approximated to $SR = 1 - (2\pi\sigma)^2$ for diffraction limited optics. For resolving two ions, diameter of central spot of the image A_{image} which reduces to Airy disc diameter A_D for a nearly perfect image should follow

$$A_{image} < l_R \times M, \quad (4.9)$$

so that images do not overlap. Following the Maréchal's Strehl approximation [205], $SR \geq 0.8$ is acceptable, which corresponds to $\sigma \leq \lambda/14$. Thus, the optics of surface roughness $\simeq \lambda/20$ are recommended for constructing the imaging system. Positioning the collection lens nearer to the source ensures larger NA and hence enhances fluorescence collection, but that freedom is limited by available geometry which in our experiment is 31.5 mm to avoid any obstruction with incoming laser beams. In an ensemble of N trapped ions, minimum separation between

two consecutive central ions is [206],

$$l_o = \left(\frac{e^2}{4\pi\epsilon_o m\omega_s^2} \right)^{\frac{1}{3}} \frac{2.018}{N^{0.559}}, \quad (4.10)$$

where e , ϵ_o , m and ω_s are the electron charge, free space permittivity, mass of the ion and secular frequency, respectively. The minimum separation between two species that can be resolved by a lens system is $l_R = 0.61\lambda/NA$. In case of five ions confined in our Paul trap geometry [?, 207], as an example, $l_o = 1.4 \mu\text{m}$ that demands $NA \geq 0.16$ and as per Nyquist criterion, a magnification ≥ 11 for a pixel size of $8 \mu\text{m} \times 8 \mu\text{m}$ [208].

4.2.3 Design

The schematic of imaging system(s) considered in our analysis is shown in Fig. 4.2. An aspheric lens L_o of focal length $f_o = 40 \text{ mm}$ and 25.4 mm diameter is placed inside the vacuum chamber at a working distance $X_o = 31.6 \text{ mm}$ from the source. It collects 2.8% of the fluorescence, covering 0.36 sr solid angle and nearly collimates them towards the chamber window. This is followed by an objective O_i outside the vacuum chamber, where i represents different variants, which forms an intermediate image of $A_{image} = 1.3 \mu\text{m}$ at a distance X_2 from the window. The magnifier M_i is placed at a spacing X_3 from the intermediate image, which forms a magnified image on the charge coupled detector (CCD) (Model: Andor iXon Ultra 897) at a distance X_4 from it. After the magnifier, we use a flip mirror to route the fluorescence either towards a Photo Multiplier Tube (PMT) (Model: Hamamatsu C8855-01) or to the CCD. In both cases, it passes through an appropriate bandpass filter to transmit the desired wavelength. Distances between source and L_o ; and O_i to M_i are critical to form the best image. An iris mounted on a YZ translation stage is placed after the viewport to obstruct the unwanted photons scattered from surface of the vacuum chamber and knife edges. Another precision iris is mounted on a three axes translation stage and placed at the intermediate image position for its spatial isolation from others. A third iris mounted on YZ translation stage is placed immediately after O_i for second stage elimination of scattered photons that is useful for optical alignment of the imaging system as well.

4.3. Results and Discussions

This section discusses the design and performance of lens systems based on OSLO simulations along with detailed description of specifications of system chosen for our experiment.

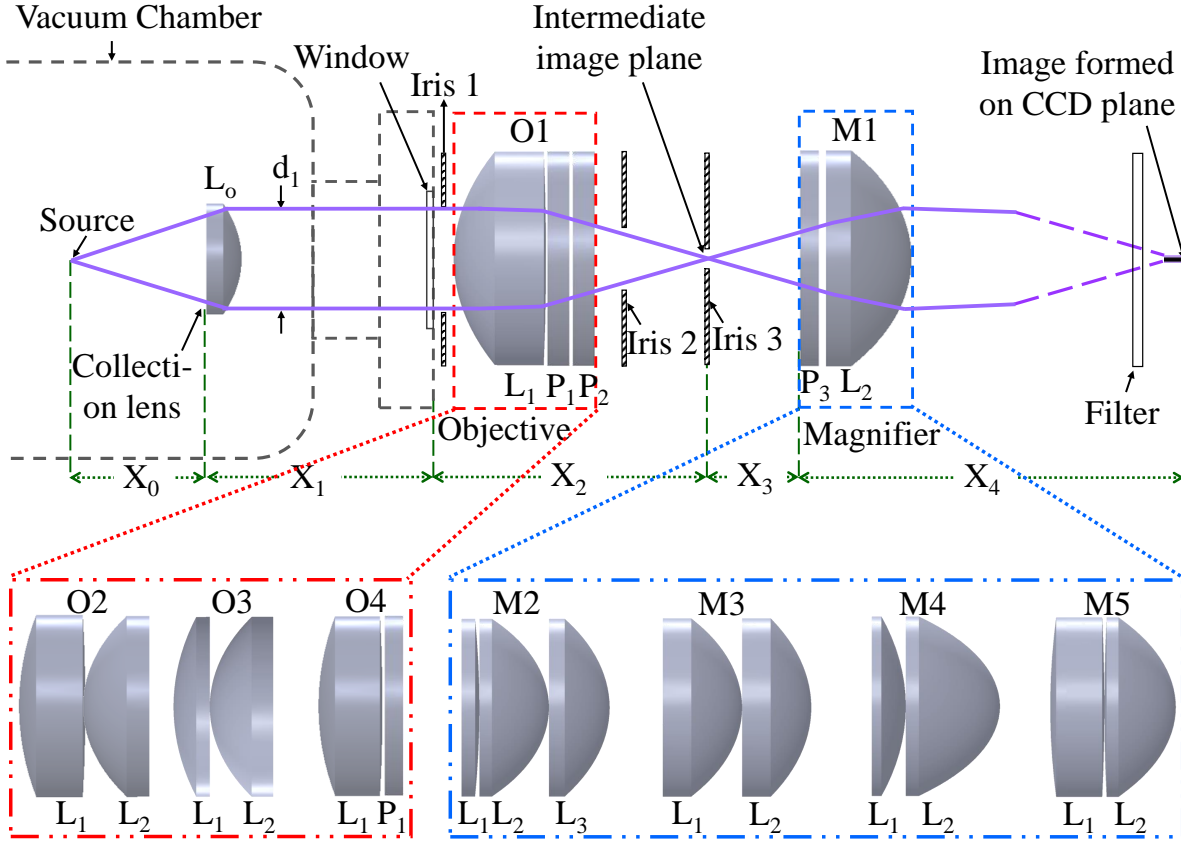


Fig. 4.2: Schematic of the imaging system considering a variety of objectives O1 - O4 and magnifiers M1 - M5. Lenses and wavefront corrector plates (WCP) are indicated as L_i and P_i , respectively, where i is their numbers. The collection lens L_o , and optics in objective, magnifier are of standard 25 mm and 50 mm diameter, respectively. For the L_o -O1-M1 combination, indicated length scales are $X_o = 31.6$ mm, $X_1 = 60.4$ mm, $X_2 = 58.2$ mm, $X_3 = 34$ mm and $X_4 = 4154$ mm.

4.3.1 Choosing the desirable lens system

In this section, we discuss performances of different imaging systems that we have studied. Table 4.1 lists values of parameters that we obtained for different objectives and magnifiers along with simulated ion images. Throughout our analysis, the collection lens L_o of $f_o = 40$ mm, its position $X_o = 31.6$ mm and $\lambda = 369.5$ nm is fixed. To resolve the species, the imaging system should satisfy *in-situ* interspecies separation $l_o \gg SA$ at the intermediate image and

$$l_o \times M > SA, \quad (4.11)$$

at the final image. Among the different objectives, O1 and O2 satisfy Maréchal's criterion [205] and have σ , l_R and SA values within the acceptable range. With the available commercial lenses, O3 gives a better resolution and an acceptable SA but $SR = 0.74$ does not satisfy Maréchal's

criterion. O4 does not minimize SA to the acceptable limit, results to a poor SR and has a low resolving power. The resultant SR and SA for all twenty combinations between objective-magnifier pairs are shown in Fig. 4.3(a,b), respectively. Combination of O1 with M1, M2, M3, M4 and O2 with M1, M4 results to $SR > 0.8$, among them O1-M1 gives the best results with $SR = 0.92$, $l_R = 0.68 \mu\text{m}$ and a diffraction limited performance over $M = 73$ to 238; whereas O2-M1 with $SR = 0.87$ and $l_R = 0.7 \mu\text{m}$ is also a probable choice but offers a comparatively lower magnification ranging from 51 to 65. For our experiment, we opt for O1-M1 combination which consists of only one aspheric lens together with two $+1\lambda$ spherical aberration compensation plates, making the imaging system simple to construct. Using off-the-shelf SA corrector plates enhances the performance of the system, thus producing better images. The results presented in this section are corresponding to the L_o -O1-M1 system. The component and air spacing details of the system is catalogued in Table 4.2. Estimated photon transfer efficiency due to reflections from its multiple optical surfaces without any band-pass filter is 0.91 and on passing through a $370 \pm 2 \text{ nm}$ commercial bandpass filter with 25% transmissivity is 0.23.

4.3.2 Optical performance of L_o -O1-M1 system

Figure 4.4(a) shows PSF as simulated using OSLO and compares it to the theoretical calculation following Eqn. (4.7) for the L_o -O1-M1 system, where the aberration coefficients as given in Eqn. (4.2) are obtained from OSLO. This gives confidence to understand the imaging system and

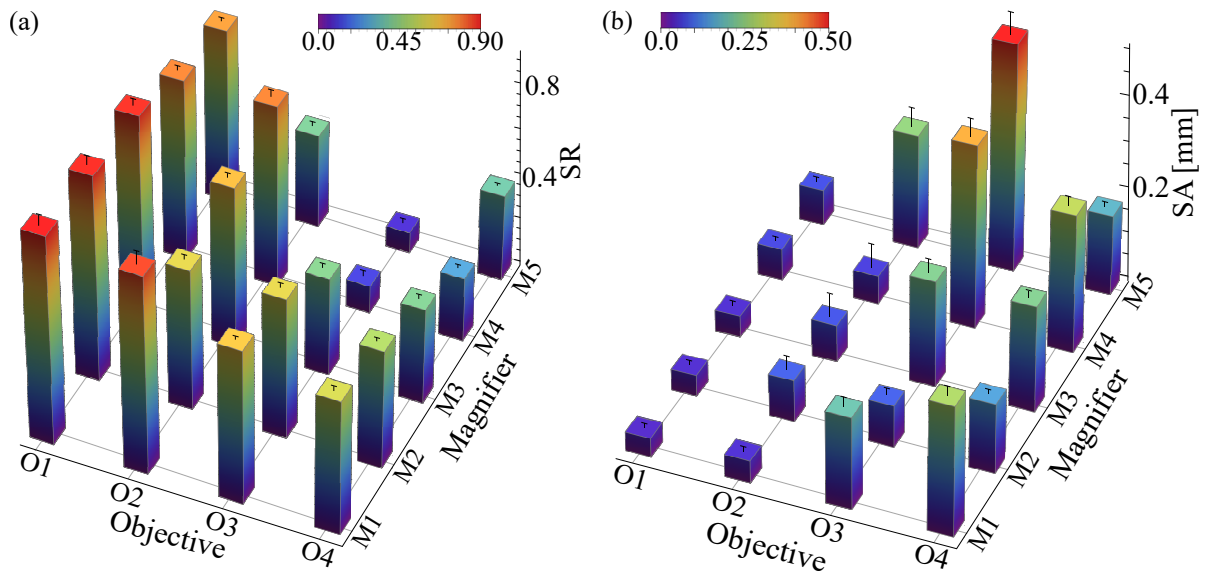


Fig. 4.3: (a) Strehl ratio (SR) and (b) spherical aberration (SA) for all possible combinations of objectives (O1 - O4) and magnifiers (M1 - M5) those we have studied.

Tab. 4.1: Estimated values of parameters for different lens combinations that we studied, where the magnifiers in conjunction with O1 are shown here. Abbreviations are Asp: asphere, WCP: Wavefront corrector plate, Ach: achromat, and PC: plano convex lens.

Objective [f in mm]	A_{image} (μm)	SR	SA (μm)	l_R (μm)	Image (2.5×2.5) μm^2
O1: 1 Asp [50], 2 WCP	1.3(2)	0.93(1)	0.7(1)	0.68(3)	
O2: 1 Asp [60], 1 Ach [100]	1.2(1)	0.84(3)	0.7(1)	0.71(1)	
O3: 1 Asp [100], 1 Asp [60]	1.2(3)	0.74(3)	0.7(1)	0.67(3)	
O4: 1 Ach [100], 1 WCP	1.8(5)	0.59(5)	2.4(3)	1.9(1)	
Magnifier [f in mm]	A_{image} (mm)	SR	SA (mm)	M	Image (0.5×0.5) mm^2
M1: 1 Asp [37.5], 1 WCP	0.06(3)	0.92(2)	0.05(1)	110(4)	
M2: 1 Asp [50], 1 Asp [60] 1 PC [500]	0.01(1)	0.91(1)	0.02(1)	15(1)	
M3: 1 Asp [50], 1 Asp [60]	0.04(3)	0.89(1)	0.04(3)	62(2)	
M4: 1 Asp [37.5], 1 PC [125]	0.07(3)	0.81(1)	0.05(3)	77(3)	
M5: 1 Asp [60], 1 Ach [100]	0.03(2)	0.76(2)	0.03(1)	33(1)	

thereby helps to model a measurable PSF for a real case. PSF in the intermediate image plane is also shown, which has $A_{image} = 1.3 \mu\text{m}$. The insets show the corresponding ion images obtained by simulation. Considering Yb ion as the source, the L_o -O1-M1 system diffracts 77% of the total collected photons into the central Airy disc. Figure 4.4(b) shows tunability of M1 to vary magnification of the final image and corresponding SR and SA. Mounting the magnifier on a precision translation stage is required to tune its position at micron accuracy across its focus f_{L3} . Tunability of $600 \mu\text{m}$ across f_{L3} varies the magnification from 73 to 238 within the acceptable SR and SA, beyond that focussing of marginal and axial rays do not coincide, which results into greater SA and hence poorer quality, as shown in the insets of the figure.

Tab. 4.2: Specifications of the L_o-O1-M1 lens system

Optics	Surface No.	Radius (mm)	Spacing (mm)	Component	Material (Placement)
L _o	1	∞	8.0	AFL-25-40	CROWN
	2	-19.7	43.7	(Asphericon)	(Vacuum)
Window	3	∞	1.5	VPZ38SVAR-NM	Sapphire
	4	∞	0	(Torr Scientific)	(Air)
L ₁ of O1	5	30.8	19.4	66316	LBAL35
	6	-500.0	0	(Edmund Optics)	(Air)
P ₁ of O1	7	∞	4.0	66765	NBK7
	8	∞	0	(Edmund Optics)	(Air)
P ₂ of O1	9	∞	4.0	66765	NBK7
	10	∞	65.5	(Edmund Optics)	(Air)
P ₃ of M1	11	∞	4.0	66765	NBK7
	12	∞	0	(Edmund Optics)	(Air)
L ₂ of M1	13	∞	19.4	69144	LBAL35
	14	-29.4	4.2×10^3	(Edmund Optics)	(Air)

Depth of Field (DOF) and Field of View (FOV) are the acceptable radial and axial ranges (with respect to trap's axis *i.e.* z-axis), respectively, over which images with $SR \geq 0.8$ are formed [209]. These also determine number of trapped species which can be imaged at a time. In case of 19 ions trapped along a particular direction, $l_o = 0.69 \mu\text{m}$ for our trap conditions, and hence they can be resolved as $l_R = 0.68 \mu\text{m}$. Considering this, we show planar visualisation with simulated images of 19 ions in our trap in Fig. 4.5(a,c) for radial and axial planes, respectively. Figure 4.5(b,d) show SR and SA corresponding to these images and indicate DOF and FOV. Actual spacing between consecutive ions is considered in this analysis, which increases as they are further away from the radio-frequency nullpoint of the trap (trap centre). That together

with source at out of focus results to steep change in SR and SA for the ions away from the trap centre. The L_o-O1 combination gives a DOF of 280 μm and FOV of 94 μm , whereas in conjunction with the magnifier these values reduce to 142 μm and 56 μm , respectively.

4.3.3 Fabrication tolerance

The performance discussed is for the nominal system but the fabrication tolerance is also to be taken into account. The Peak-to-Valley (P-V) optical path difference (OPD) corresponding to an SR of 0.8 is 0.25 waves. The P-V OPD for the system, OPD_s as obtained from the simulation is 0.19 waves; hence, to satisfy Maréchal's criterion, the P-V OPD from fabrication tolerance, OPD_t should be ≤ 0.16 waves. We determined the overall fabrication tolerance of the system considering different sources and their contributions within bracket are as: radius of curvature (0.022 λ), surface irregularity (0.002 λ), element thickness/ air space (0.116 λ), refractive index (0.085 λ) and surface tilt (5×10^{-5} λ), which results to $OPD_t = 0.14$ waves. This results to an effective $OPD_{total} = \sqrt{OPD_s^2 + OPD_t^2} = 0.24$ waves that corresponds to SR of 0.83 which is well within the limit. Apart from this, we have also calculated the allowable decenter and tilt tolerances for the 2 inch optics assembly to be mounted in optics tube. To maintain an SR ≥ 0.8 , estimated tolerances in decentration and tilt are ≤ 450 μm and $\leq 0.22^\circ$, respectively.

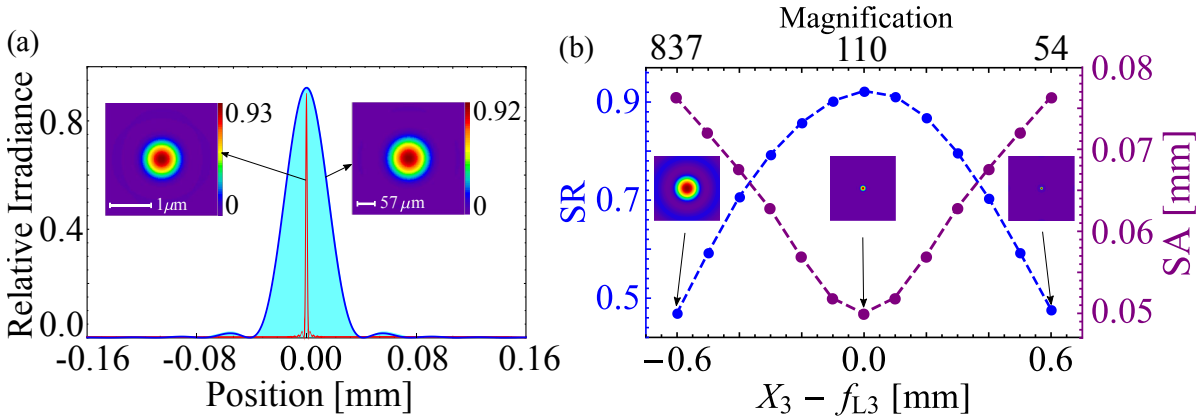


Fig. 4.4: (a) Point spread functions (PSF) simulated by OSLO (blue), and calculated from analytical relation (filled with cyan) at the final image of the L_o-O1-M1 combination. The PSF at the intermediate image plane (red) is shown for comparison. (b) Variations of SR (blue) and SA (purple) due to deviation of magnifier M1 from its ideal position *i.e.* $X_3 = f_{L3}$ is shown, which tunes the magnification. Images are shown in the insets for a glance quality comparison.

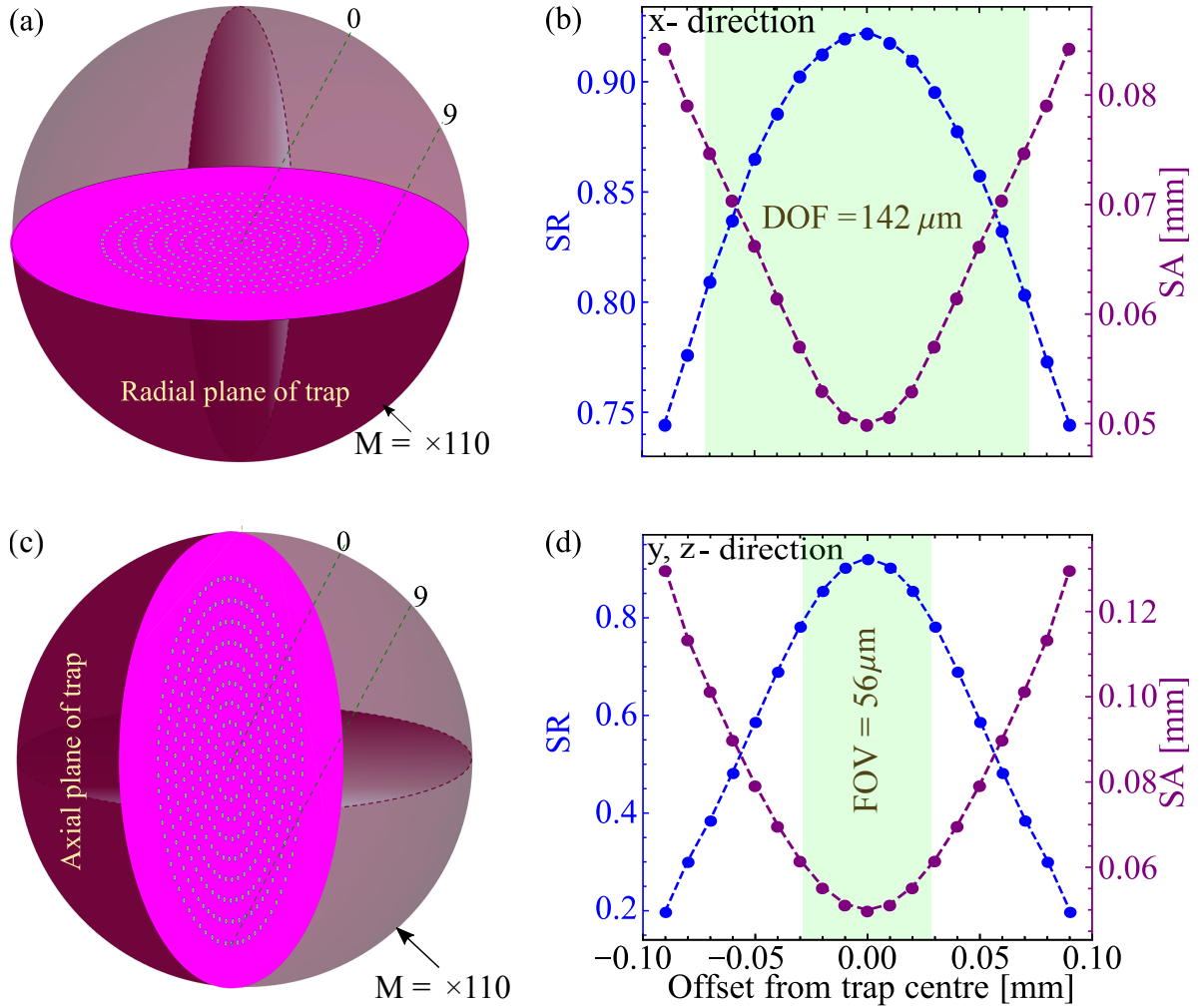


Fig. 4.5: Images of trapped ions on (a) xy (c) yz planes. Corresponding variation of SR and SA as the ion's position deviates from best focus. Depth of field (DOF) and Field of View (FOV) are indicated.

4.3.4 Mounting

Proper mounting of the lens assembly is crucial to ensure shielding of the optics from scattered light, easy change in distance between the optics whenever required and minimized aberration by aligning the outgoing beam to be parallel to the optic axis. Figure 4.6 shows an illustration of the mounting scheme. A lens tube with rotating optic adjustment (SM2V15, Thorlabs) is used for housing the objective O1 and magnifier M1. The adjustable part helps in tuning the optics position. The iris is mounted on an XYZ translation mount (LP-2A-XYZ, Newport) in between two bellow tubes (SM2B45, Thorlabs) to allow adjustment of the iris position. Simple 2 inch lens tubes are used for further extensions to PMT (HH8259, Hamamatsu) and EMCCD

(Ixon Ultra 897, Andor). A right angle mirror is installed in a beam turning cube mount (DFM1-M01, Thorlabs) to direct the collected light to PMT whenever required. The PMT is mounted on an in-house designed mount as shown in Fig. 4.7. For mounting all the tubes, SM2TC clamps from Thorlabs are used.

4.3.5 Method for performance analysis

Prior to using the optimized final lens assembly in the experiment, we decided to carry out an experimental analysis of a simple test setup in order to evaluate the consistency of the imaging properties of the lens assembly with OSLO simulations. Performance of a lens system can be determined experimentally using test targets such as the USAF 1951 target (shown in Fig. 4.8(d)) which consists of black and white line pairs of different sizes. These line pairs form an element E and many elements collectively form a group G . To find the resolution of an imaging system using the USAF target, the elements of the target is imaged with light of the desired wavelength onto a detector using the lens combination. In this way, the best visual resolution that can be obtained is identified. If at best, the system can resolve element E of group G , then resolution of the system in lp/mm (line pairs/mm) is given by,

$$l_R = 2^{G + \frac{E-1}{6}}. \quad (4.12)$$

The test set-up we chose consists of an aspheric lens of focal length 25 mm spaced 17.8 mm apart from the resolution target, followed by a biconvex lens of focal length 500 mm for further magnification. As per OSLO simulations, numerical aperture of the objective lens is 0.4 which

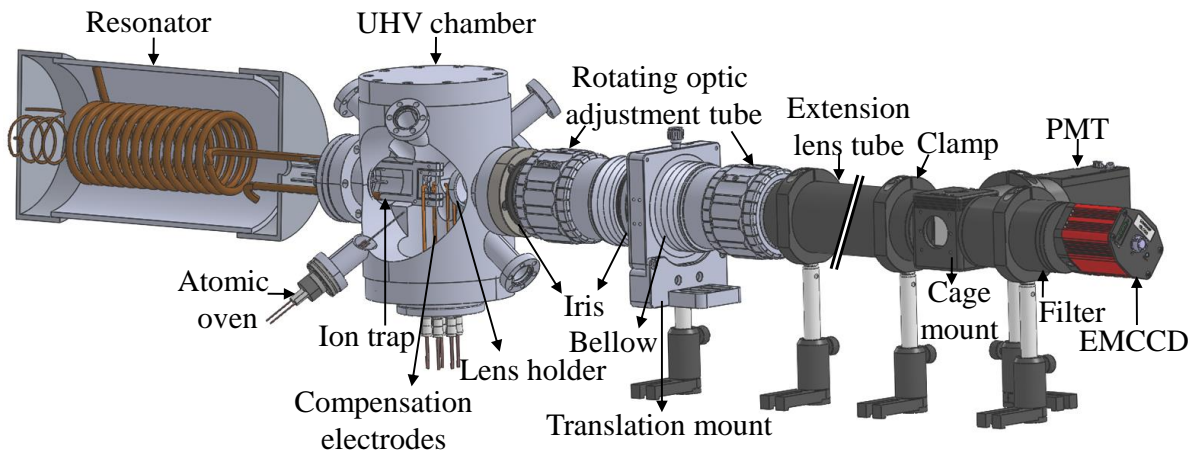


Fig. 4.6: A 3D drawing showing the planned scheme for mounting the lens assembly with appropriate optics tube and accessories for easy position adjustment to avoid misalignment.

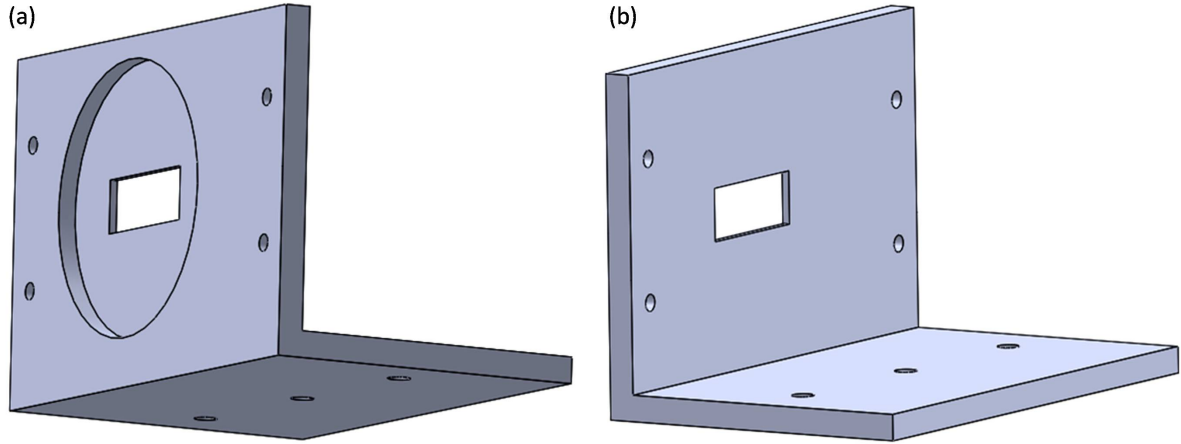


Fig. 4.7: SolidWorks drawing of the (a) front and (b) rear view of the PMT mount. The 2 inch circular grooving at front side is to hold a SM2 lens tube. The holes at the front and bottom planes are to secure the PMT and the optics post.

at a working wavelength of 780 nm gives a resolution of $1.18(3)\mu\text{m}$. The lens system and the simulation parameters are shown in Fig. 4.8(a-c). The images obtained from the Web Camera (C525, Logitech) are presented in Fig. 4.8(e) illustrating that it could clearly resolve each set of six elements of groups 1 to 6 and the first element of group 7 of the target using which as per Eqn. (4.12) gives a resolution of 128 lp/mm, *i.e.* $7.8\ \mu\text{m}$. The remaining elements of Group 7 are visible but blurred and so not clearly resolvable. The probable reasons behind the error in result is the poor image quality arising due to chromatic aberration from white light added up by wavefront distortion caused by the extra lens mounted on the detector.

4.4. Advantages of L_o -O1-M1 system

The position of aspheric lens L_o cannot be optimized or altered during the experiment as it is placed inside the UHV chamber. Deviation of X_o from f_{L_o} occurring due to inaccurate positioning of L_o or shifting of the trap centre will lead to a poor image quality and hence difficulty in detecting trapped ion/ions. Since L_o is inaccessible on regular basis, we studied dynamic range of its position over which SA and SR can be corrected by the external objective-magnifier combination. Figure 4.9(a) shows the change of SR and SA due to deviation of X_o from f_{L_o} and their post corrected values incorporated by tuning distance between O1-M1. We found, SA and SR can be significantly corrected for deviation of $X_o - f_{L_o}$ from -0.4 mm to 2.6 mm, which is better than the other objective-magnifier combinations. Thus, the designed optical system allows for correcting the image even if the collection lens is displaced by its best

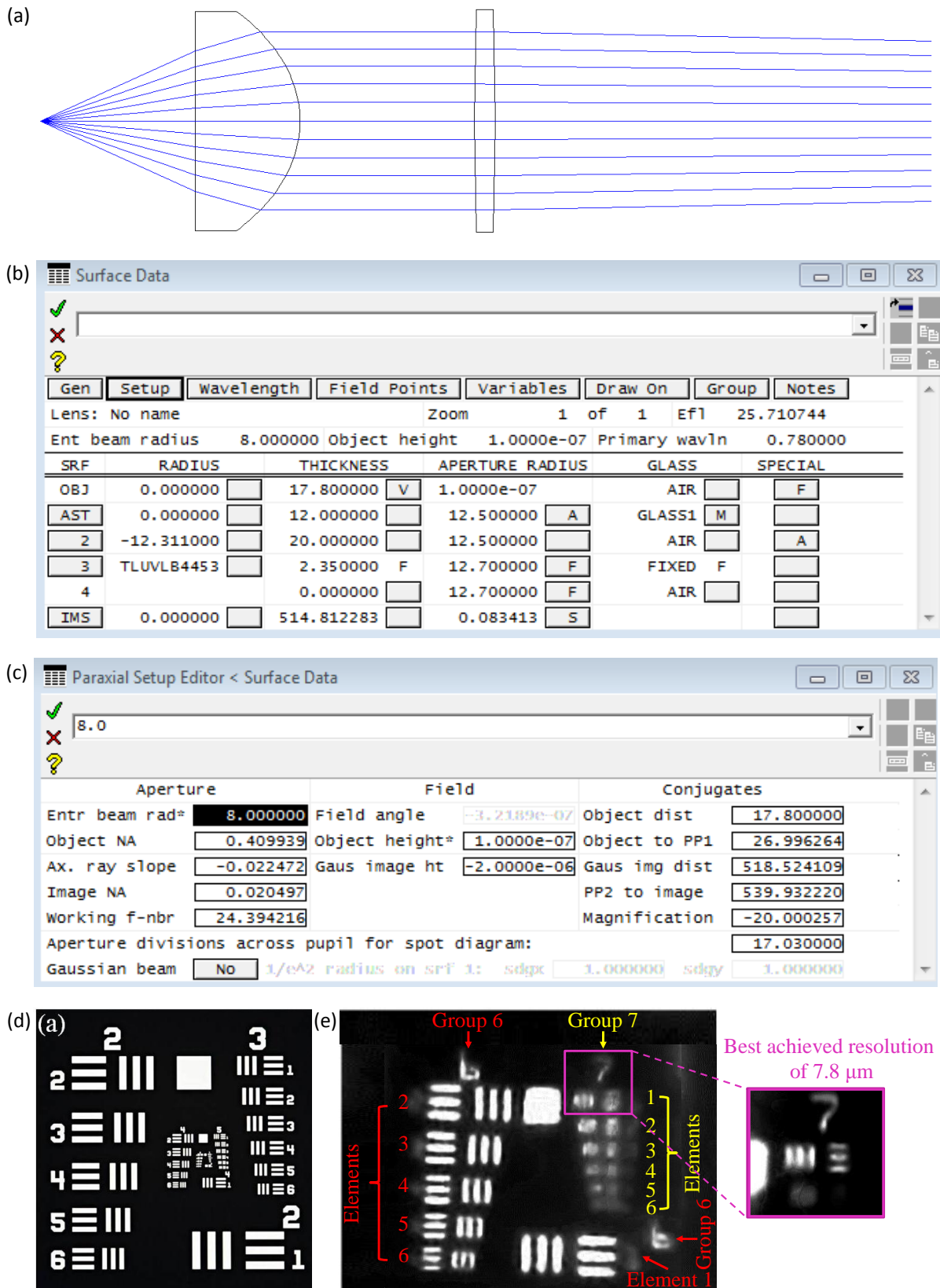


Fig. 4.8: (a) OSLO drawing of lens system used for testing using USAF target (b) Surface Data sheet of the OSLO simulation showing the input parameters for the displayed lens combination system and (c) the Paraxial setup editor giving the resultant parameters as numerical aperture and magnification. (d) A USAF 1951 resolution test target consisting of groups 2 to 7 of elements of different resolutions. (e) Images obtained from the detector for elements of Group 6 and Group 7 of a USAF-1951 resolution target. The inset shows the resolved first element of Group 7.

position. Additionally, we show that on optimization of X_o and X_3 , the described imaging system gives favorable results for SR and SA at different wavelengths covering from visible to near infrared corresponding to the elements Yb^+ , Ra^+ , Ca^+ , Sr^+ , Sr , Ba^+ , Lu^+ and Cs ; the result is displayed in Fig. 4.9(b). Values of other parameters describing the optical performance are stated in Table 4.3. Values of $\sigma < 0.07\lambda$ in all cases and a good magnification range confirms an acceptable performance of the system for a variety of wavelengths. Hence, the design can be adapted for applications other than Yb^+ as well.

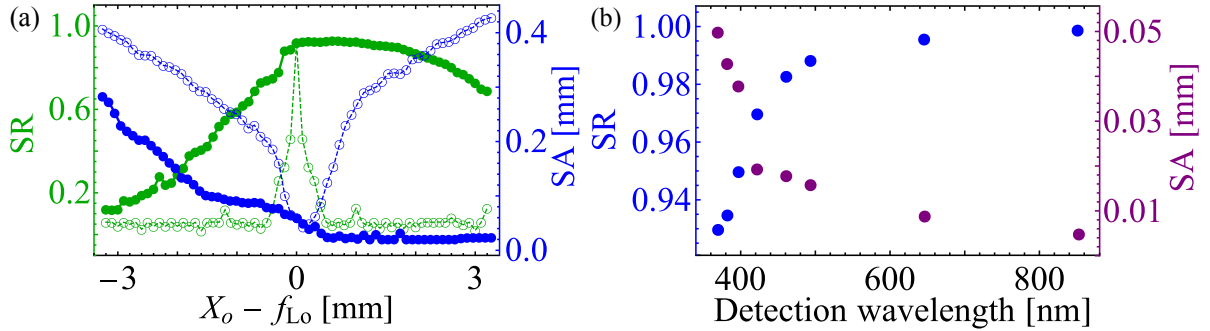


Fig. 4.9: (a) Change in SR (green empty circle) and SA (blue empty circle) values of the images due to inaccurate positioning of the collection lens L_o with respect to its focus f_{L_o} . Corresponding SR (green full circle) and SA (blue full circle) after incorporating corrections by tuning the magnifier's position are also shown. (b) SR and SA at different wavelengths (corresponding to different species), *e.g.*, 369.5 nm (Yb^+), 382 nm (Ra^+), 397 nm (Ca^+), 422 nm (Sr^+), 461 nm (Sr), 493.5 nm (Ba^+), 646 nm (Lu^+) and 852 nm (Cs).

Tab. 4.3: Estimated values of various optical excellence parameters obtained using OSLO for wavelengths corresponding to different atom/ion species.

λ (nm)	Species	σ (λ)	l_R (μm)	X_o (mm)	M	FOV (μm)
369.5	Yb^+	0.042(2)	0.68(3)	31.60(1)	73(1) - 238(3)	56(2)
382	Ra^+	0.039(2)	0.71(1)	31.81(1)	72(1) - 289(3)	58(2)
397	Ca^+	0.034(1)	0.74(1)	31.99(3)	65(1) - 243(2)	62(2)
422	Sr^+	0.029(3)	0.79(1)	32.28(3)	62(2) - 311(1)	66(2)
461	Sr	0.023(1)	0.87(1)	32.61(1)	56(3) - 310(1)	74(3)
493.5	Ba^+	0.019(2)	0.94(3)	32.82(2)	52(1) - 328(5)	78(2)
646	Lu^+	0.011(1)	1.25(3)	33.45(3)	45(3) - 982(7)	99(3)
852	Cs	0.006(1)	1.67(2)	33.87(3)	38(4) - 1192(9)	128(3)

4.5. Applications of an imaging system

The PSF being the image of a point source carries information related to the wavefronts forming the image as well as various dynamics of the source itself. It therefore not only aids in analysing the resulting aberration but helps in characterization of the trapped sample as well. PSF gives information on temperature of trapped ion, its heating rate, and monitoring the PSF helps in monitoring ion's position for efficient cooling, determination of secular frequency and identification of other trapped Yb isotopes [212–214]. In this regard, we have made a different and very simple approach to temperature determination based on PSF analysis.

4.5.1 Spatial thermometry of ions

Let us consider an ion of mass m confined along the z axis in a harmonic potential. The trapped ion exhibits a harmonic oscillation (called secular motion) at frequency ω_s (called secular frequency), which is typically thermal *i.e.*, the ion's kinetic energy is characterized by its temperature T . Hence, amplitude of this motion or the spatial spread, $2A_s$ is proportional

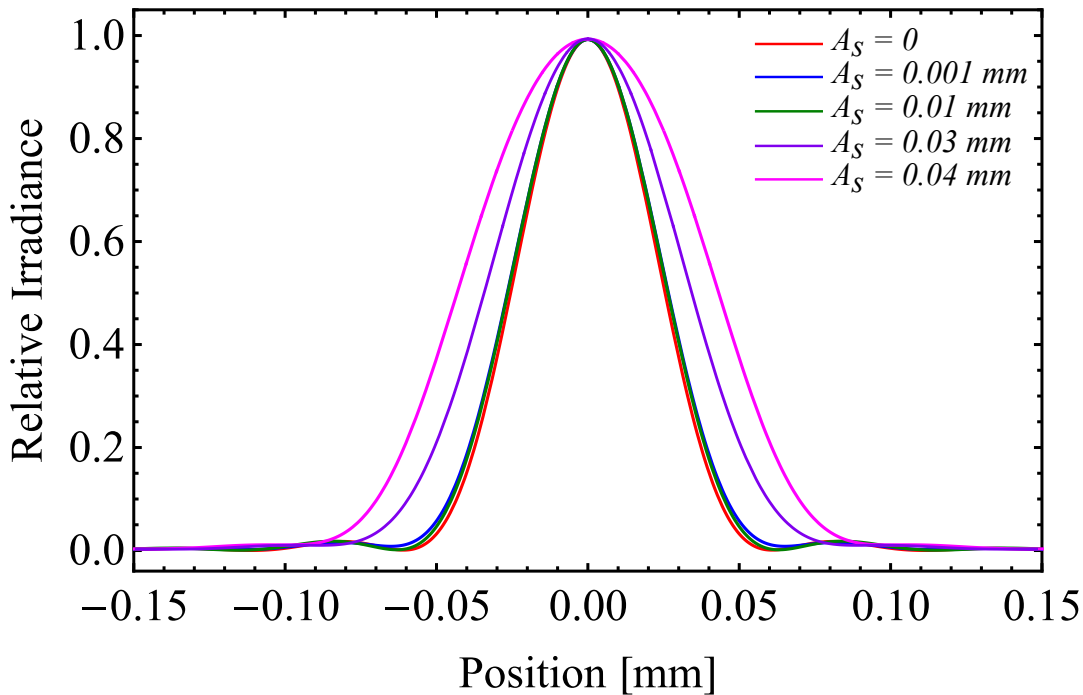


Fig. 4.10: Broadening of point spread function as modelled for different spatial extents resulting from ion's thermal motion.

to \sqrt{T} . Thus, ion's temperature can be determined from accurate measurement of its spatial occupancy with the help of a high resolution imaging system. The intensity distribution of the acquired image integrated over a certain duration $\gg \tau$ will be broadened than the PSF of a stationary point source (given by Eq. (4.6)) due to dynamicity of ion's position. Thus, instead of recording an ideal PSF, the detectors record a spatially broadened PSF similar to the sum of PSFs, as if a linear chain of ions were trapped. Based on this simplest assumption, we can consider an alternative approach for modelling the measurable distribution function in terms of A , *i.e.* a modified PSF. For this, we are considering the sum of PSFs for n number of trapped ions. Hence, the modified PSF for a single ion getting displaced to A from its mean position due to its temperature T can be written as,

$$S(r, \lambda, F, A) = \sum_{n=-A}^A S(r + n, \lambda, F). \quad (4.13)$$

Distribution of the modified PSF is shown in Fig. 4.10 where the effect of secular motion is depicted by its broadening.

4.6. Conclusion

The design criteria together with its detailed performance of an easy to build imaging system that can resolve particles at sub-micron level is investigated among a wide variety in this chapter. The finally opted lens system consists of standard catalog optics: aspheres and aberration corrector plates which makes the system user friendly. In comparison to designs from previous works those use multiple lenses, we achieved higher NA of 0.33 with only one asphere and two corrector plates. The system is advantageous as the image quality due to the axial misalignment of the collection lens by -0.4 mm to +2.6 mm can be corrected by readjustment in the later optics. The diffraction limited optics is able to recollect 77% photons to the central disc within a solid angle of 0.36 sr and produce images upto $\times 238$ magnification for the objects that are separated by as minimum as 0.68 μm with minimum spherical aberrations. Multiple particles confined within the trapping potential can be detected by this system as it has depth of field and field of view of 142 μm and 56 μm , respectively. Acceptable values of decentration and tilt in the optical system are $\leq 450 \mu\text{m}$ and $\leq 0.22^\circ$. The imaging system with the said specifications is therefore suitable for detecting a single trapped Yb^+ ion. In addition, the system is usable over wider wavelength range thus making it suitable to be opt for similar experiments too.

Chapter 5

Frequency stabilization of a diode laser to a hyperfine transition of molecular iodine for trapped Yb ion

Publication: Lakhi Sharma, A. Roy, S. Panja, and S. De, Saturated Absorption Spectroscopy of Molecular Iodine for frequency stabilization of 739 nm laser, *Conference Proceedings of 8th Topical conference on Atomic and Molecular Collisions for Plasma Applications*, IIT Rorkee (2020).

5.1. Introduction

The over all expansive experimental setup for building an optical frequency standard based on the interrogation of $4f^{14}6s\ ^2S_{1/2}|F = 0, m_F = 0\rangle \rightarrow 4f^{13}6s^2\ ^2F_{7/2}|F = 3, m_F = 0\rangle$ transition of a trapped single Yb-171 ion at 467 nm, has already been described in the previous chapters. A total of five lasers at wavelengths around 399 nm, 369.5 nm, 760 nm, 935 nm and 467 nm for probing transitions related to photoionization, cooling, repumping and clock state probing, are indispensable for its realization. External Cavity Diode Lasers (ECDL) are capable of providing linewidths of about tens to hundreds of kHz with excellent frequency stabilities. They are therefore expected to work over long period of time with frequency precision of tens of MHz, however, their output frequencies drift hundreds of MHz from a desired setpoint or resonance point within a few hours. On a longer time scale, frequency drifts are susceptible to ambient condition variation such as, thermal drift resulting from numerous causes, such as, nearby power supplies, heating ovens, lab temperature fluctuations, *etc.* Another probable cause is mechanical drifts like misalignment of optics or other parts within the laser enclosure with time. Such drifts are inadmissible in high-precision frequency measurement based optical clock experiment as the quality of the developed clock is destined by stability of the lasers

employed in interrogating the various transitions. Stable frequencies ensure good repeatability of the measurands and good statistical analysis. Such a state-of-the-art experiment demands accurate and precise regulation of all its components, hence, all the involved lasers need to be stabilized in the frequency domain so that desired transitions are probed effectively.

Frequency stabilization of lasers is consequently a stringent pre-requisite to perform high resolution spectroscopy in most of today's metrology and other precision based experiments. A significant advancement has indeed been achieved in this field and at present, several techniques for locking laser's frequency are attainable. One of the locking techniques is based on frequency stabilization with respect to a reference atomic/molecular transition. In this regard, most commonly used method is locking with respect to a Doppler free peak obtained by saturated absorption spectroscopy (SAS) of an atomic/molecular transition [215–217]. This technique comes with the disadvantage of non-availability of a reference atomic transition frequency at exactly desired setpoint to be locked or inadequacy of atomic vapor cell for certain elements. Another widespread technique is frequency locking to a high finesse and highly stable Fabry-Perot cavity [115, 218, 219] locked to another laser stabilized with respect to an atomic reference, by virtue of the Pound-Drever-Hall frequency stabilization scheme [221, 222]. This is known as transfer cavity technique and can be used for locking multiple lasers simultaneously [89]. It can also be utilized when no atomic reference line for desired laser frequency is accessible. Lasers are also stabilized using a high-finesse ultra-low expansion (ULE) optical cavity placed in ultra-high vacuum [220]. Commercially available wavelength meters are also an approach in this field and are in use in various spectroscopic, trapping and cooling experiments [223–225]. Furthermore, optical frequency combs provide accurate reference for optical frequencies, specifically in cases where signal-to-noise ratio is too low to employ any other method [226, 227]. Choice of a locking technique depends on experimental demand for level of accuracy. As for example, precision spectroscopy or high accuracy metrology related experiments demand relative frequency instabilities of 10^{-15} or below whereas other agenda such as atomic spectroscopy or atom cooling can be performed with laser frequencies of short-term instabilities $\leq 10^{-10}$. In our experiment, photoionizing laser at 399 nm is required for a short time to probe the strong dipole transition of linewidth of tens of MHz. ECDL used for this purpose has a low short-term instability and so its frequency is locked using a wavelength meter. The cooling laser at 369.5 nm laser, on the other hand, which is achieved through frequency doubling of 739 nm, is employed to probe the $^2S_{1/2} \rightarrow ^2P_{1/2}$ transition of natural linewidth of 19.6 MHz [228] for ion cooling. Hence, it is used for a longer time and along with its shifted frequencies, it is also used for imaging, optical pumping, state preparation, studying ion dynamics, *etc.* A long-term frequency stability of the cooling laser is therefore essential and is achieved by frequency stabilization with respect to an atomic reference. The re-pump lasers are vital for conserving ion's presence within the cooling cycle and hence has to function for a

longer time. To achieve this, stability of locked cooling laser is transferred to a transfer cavity with respect to which the repump lasers are then stabilized. The clock transition of linewidth 3 nHz is to be interrogated with a laser of ultra-narrow linewidth and ultrastable frequency; and so, the clock laser is stabilized to a ULE cavity which gives sub-Hz linewidth. This chapter discusses locking of the cooling laser via stabilization of its fundamental frequency at 739 nm using SAS technique.

5.2. Theory

Let us consider a laser beam propagating along z direction through a vapor cell of length L and population density n and consisting of two-level atoms with ω_0 as the central frequency of a transition with E_i and E_f as the initial and final energy states. A photon emitted in a transition from this level to the ground state will have a range of possible frequencies, $\Delta\omega$. If γ_0 be the natural linewidth of the transition, then the absorption line has a Lorentzian profile. However, in reality, the obtained profile is broadened due to factors such as Doppler velocities of the atoms, power of the laser beam, collisions (elastic and non-elastic) between atoms, *etc.* Most dominant one is the Doppler broadening and all such broadenings affect precision measurements. Consider atoms traversing along z -axis of the cell with velocity v_z . Due to relative motion with respect to incoming laser beam, a moving entity sees Doppler shifted light. Depending on whether it is moving along or opposite to the beam direction, its absorption frequency ω_a in the laboratory frame either increases or decreases by $\omega_0 v_z/c$, respectively. This results in Doppler broadening of Lorentzian lineshape and such broadening affects the resolution of spectroscopy we wish to perform to stabilize the laser's frequency with respect to an atomic line. To minimize the Doppler effects, Saturated Absorption Spectroscopy (SAS) is employed or in other word, we perform velocity selection. A counterpropagating pair of laser beams, one more intense (pump beam) than the other (probe beam) but of the same frequency are allowed to interact with the molecules of the vapor cell, while being swept over a frequency range including ω_0 . Both probe and pump beams will interact with the gas molecules over a certain velocity range. The overlap between these two velocity ranges gives a subset of molecules which will interact with both the beams. The pump beam being more intense will excite a greater population of these molecules leaving them unavailable for the probe beam to interact with. The Doppler broadened absorption signal will therefore encounter Doppler free dips corresponding to this velocity class range. Thus, instead of locking a laser's frequency to an absorption spectrum of some hundreds of MHz, it can be stabilized with respect to that of a few tens of MHz.

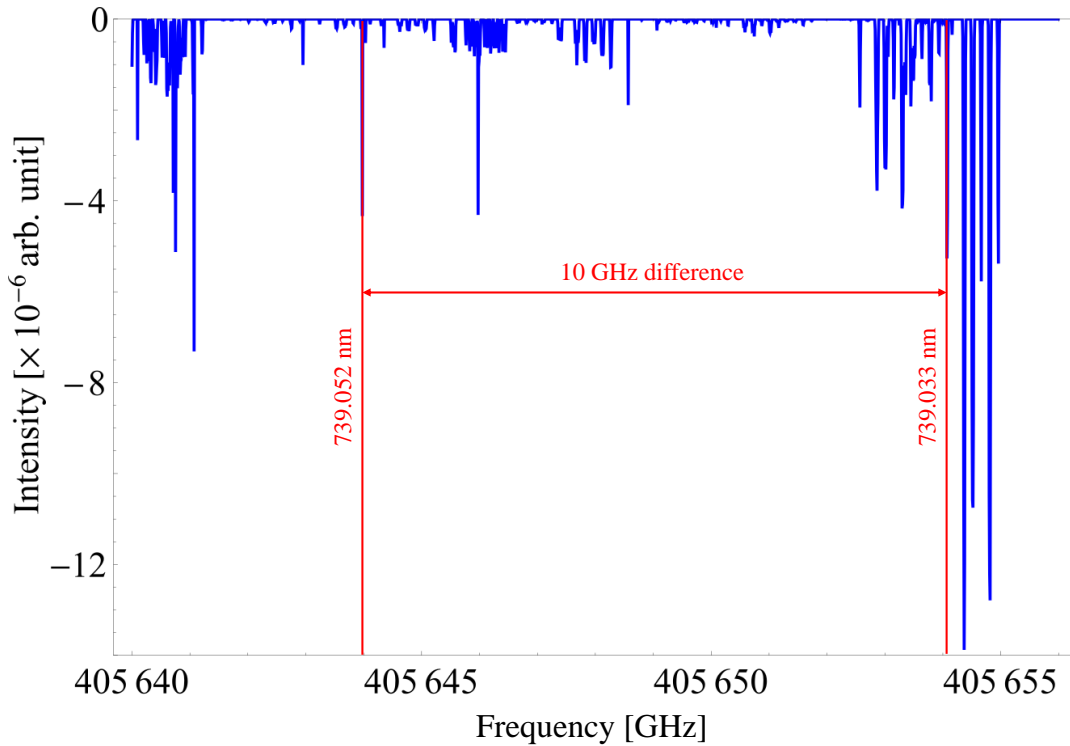


Fig. 5.1: Absorption Spectra of hyperfine transitions of molecular iodine from 739.03 nm to 739.06 nm at 450 °C. Difference in frequencies between the desired setpoint and available hyperfine transition is shown.

The 369.526 nm laser used primarily for imaging purpose and for cooling the trapped ion by probing $^2S_{1/2} \rightarrow ^2P_{1/2}$ is produced by generating the second harmonic of a 739.052 nm laser. Stabilization of the 739.052 nm laser will subsequently lead to locking of 369.526 nm. Iodine molecule is the most frequently used species for reference absorption lines as these have been extensively studied by various groups [229–234]. It has densely populated, narrow absorption lines extensively ranging from visible to near infrared region [234, 235] as can be seen in Fig. 5.1. As is discernible from Fig. 5.1, the iodine spectrum consists of an absorption line at 405654 GHz corresponding to 739.033 nm which is 10 GHz away from the frequency of our interest [236]. Hence, by coupling the cooling laser to an electro-optical modulator (EOM), an offset of 10 GHz can be employed to shift it to 739.033 nm for its further locking with respect to SAS of iodine. The resonance lines of iodine around 739 nm are a result of R(78) (1-11) line which is a hot band transition implying transition from a non-ground vibrational level. As per Boltzmann distribution, at any temperature T , population at an upper state n_u is given by,

$$n_u = \exp\left(\frac{-\Delta E}{k_B T}\right)n_l, \quad (5.1)$$

where k_B , n_l and ΔE are Boltzmann constant, lower state and separation between the energy

levels, respectively. This implies that only the ground state is heavily populated at room temperature. So, at lower temperatures, hot transitions have negligible or lower signal intensities. It is therefore necessary to heat the iodine cell to about 500 °C to sufficiently populate the desired higher vibrational level to achieve appreciable signal intensity [242].

As the Doppler free signals which we are trying to detect are a result of temperature-dependent transition, resulting signal is weak. For its effective detection, we plan to perform Modulation Transfer Spectroscopy (MTS) gives derivative of saturation absorption signals with better signal to noise ratio [237–240]. In this method, the frequency of pump beam is modulated whereas that of probe remains unmodulated. Their interaction in the cell transfers the frequency modulated sidebands to the probe beam [237]. After modulation, a phase sensitive detector or a Lock-in amplifier is used to demodulate the photodiode signal [241]. The signal is first smoothed by a band pass filter which removes the low frequency terms. This signal is passed through a mixer where it gets multiplied to a reference signal of frequency same as that of the high frequency modulation and then passed through a low pass filter to cutoff high frequency noises.

5.3. Experimental setup

In this section, the arrangements for carrying out the experiment and optimizing the desired signal will be discussed. The successful establishment and success of the SAS experiment involves optics for spectroscopy part and electronics for signal detection.

5.3.1 *Setting up the Iodine cell*

The iodine cell used in our experiment is bought from Precision Glassblowing and has a path length of 30 cm, an optical diameter of 25 mm with fused silica Brewster's angle windows and a 15 cm long cold finger at the rear end of the cell. Any polarized light entering the cell is perfectly transmitted owing to the windows tapered at Brewster's angle. Both silica and quartz possess high melting points and so can bear being heated to higher temperatures. However, to avoid any damages it is advisable not to heat them beyond 750 °C. The iodine cell is first wrapped around with a fiber glass insulated heat tape (Model No. FGS052-060, Omega) followed by numerous layers of aluminium foil and glass wool as is shown in Fig. 5.2(a,b). These layers ensure uniform heating of the cell as uneven heating would result rupture in the cell. The glass wool used for wounding the cell is an insulating material made from fiber glass and has many

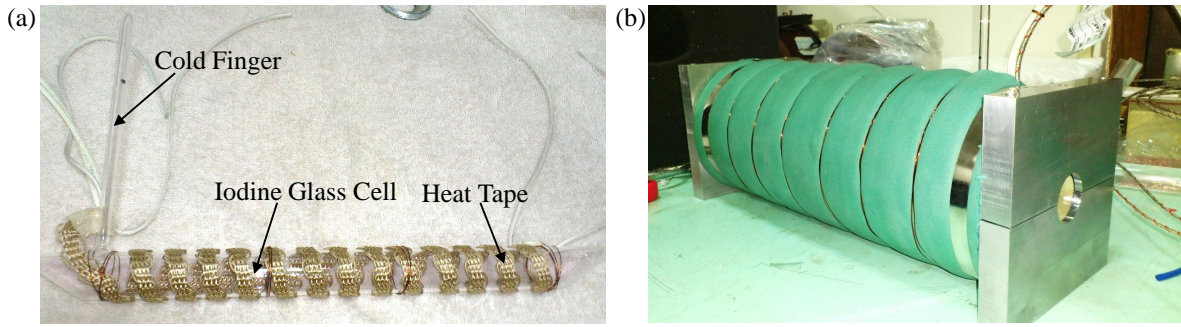


Fig. 5.2: Arrangement for heating the Iodine cell: (a) Iodine cell with the cold finger. A heating tape is wrapped round the cell for its uniform heating. (b) Layers of aluminium foil and fibre glass wool wound around the vapor cell for insulation so that surrounding optics remain unaffected.

small air pockets between the glass resulting in high thermal insulation properties. It therefore reduces heat radiation to avoid impairing the surrounding optics. Glass wool is to be handled properly by wearing hand gloves as it causes superficial itching. To keep a trail of the cell temperature, a pair of J-type thermocouple connected to a digital thermometer (Model No. 54 II B, Fluke) are kept in contact to either ends of the cell.

The purpose of a cold finger in the iodine cell is to minimize pressure/collisional broadening. The cell is maintained at a very high temperature to populate the higher vibrational level. Increased temperature escalates internal energy of the molecules in terms of kinetic energy and with increased populations, this enhances pressure broadening. To minimize that, the cold finger is kept at room temperature so that due to huge difference in temperatures of the cell and the finger, pressure difference would result in pushing some iodine molecules towards the cold finger where they would eventually crystallize. This narrows down collisional probability between molecules and hence reduces pressure broadening. A copper mesh is wrapped around the cold finger to conduct heat away to the surroundings.

5.3.2 Optics and electronics setup

A schematic of the optical setup and the actual experimental setup for achieving SAS of iodine molecules is demonstrated in Fig. 5.3(a,b), respectively. The second harmonic generation (SHG) laser (Model No. TA-SHG Pro, Toptica) with 739 nm as its fundamental output has three laser output ports: 30 mW fundamental, 3 mW fundamental and 10 mW frequency doubled output. The 3 mW fundamental output is coupled to a collimator and then to a wavelength meter (Model No. WS7, High Finesse) via a multimode optical fiber. The 30 mW

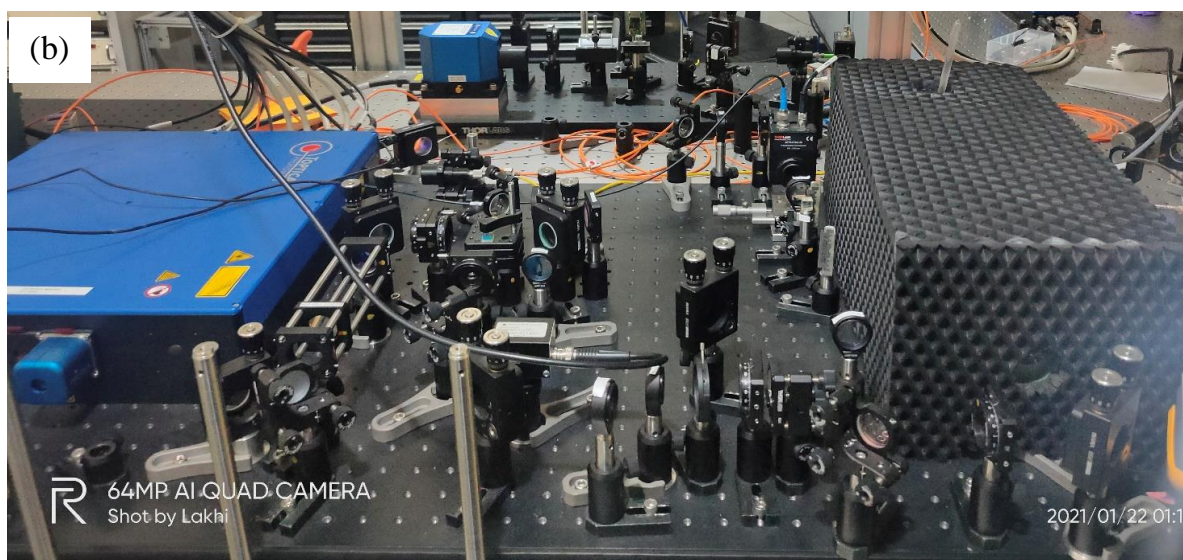
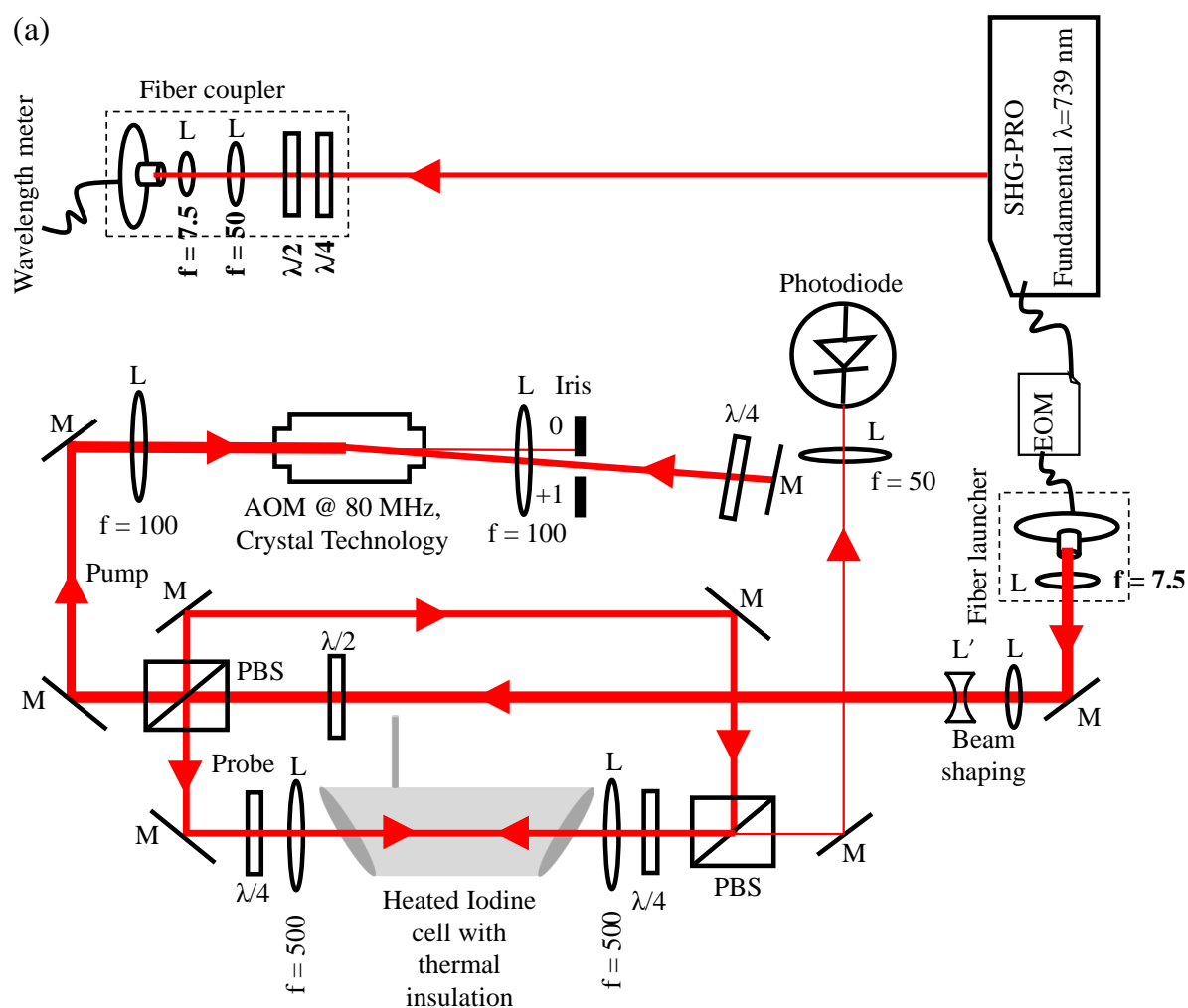


Fig. 5.3: (a) Schematic and (b) Experimental set-up for carrying out SAS of iodine. Here, M: mirror, L: convex lens, L' : concave lens, f : focal length of lens, PBS: polarizing beam splitter, $\lambda/2$: half waveplate, $\lambda/4$: quarter waveplate, EOM: electro optic modulator and AOM: acousto optic modulator.

is used for the SAS setup. It is coupled to a fiber EOM (Model No. NIR-MPX800, Photline) the output of which is splitted into probe (reflected part) and pump (transmitted part) beams using a polarizing beam splitter (PBS) (Model No. PBS102, Thorlabs). A half waveplate before the PBS adjusts the power distribution between probe and pump beams. For carrying out SAS, the pump beam is further frequency modulated using an AOM (Model No. R46080-1-LTD, Gooch & Housego) arranged in double-pass configuration and operated at 80 MHz and 1 W RF power. The external frequency modulation is performed by feeding the AOM driver with a 60 kHz, 30 mV peak to peak sinusoidal wave, which modulates the first order diffracted light, all provided by in-house designed AOM driver. The diffraction efficiency of AOM depends on good optics alignment. In double pass configuration, the first order output from the AOM is reflected back into it as an input. The first order output of the second input is now used as the pump beam for the SAS experiment; the pump beam is therefore shifted by 160 MHz than the probe beam frequency. This configuration exterminates requirement of re-aligning the optics on varying operating frequency of the AOM. On passing twice the quarter waveplate placed behind AOM, the polarization of the pump beam changes and so while retracing back the path to PBS, it now gets reflected. The power of pump and probe beams are kept at a ratio of 10:1 and finally sent into the cell in a counter-propagating direction.

The success of an SAS experiment depends on efficient overlapping of probe and pump beams and an excellent beam alignment inside and outside the cell, otherwise depletion of a particular velocity-class atoms caused by the pump beam will not affect the probe beam, resulting in no Doppler free signal. In an attempt to achieve maximum overlapping, we decided to use larger beam diameter for the spectroscopy and so, we used beam expanders. This, however, proved to be a complete failure as we observed that smaller beam diameters are more effective as larger ones cannot saturate the iodine. Two bi-convex lenses of focal length 50 cm are used to focus both the beams into the cell such that maximum overlapping of their Rayleigh ranges is achieved ensuring maximum interaction between the laser and the iodine molecules. Within the spatial region of Rayleigh range, the laser intensity is high. The probe beam after crossing the cell is focussed onto a fast photodiode (Model No. APD430A/M, Thorlabs) for signal detection. For signal demodulation, we use Digital laser locking module (Model No. DigiLock 110, Toptica) to which the photodiode signal is fed and error signal is obtained. For sweeping the laser frequency over a certain range, the laser controller supplied with the laser is used.

5.4. Results and Discussions

5.4.1 SAS signal

This section presents and discusses the relevant outcomes of the experiment. The 739 nm is scanned over a wavelength scan range of ≈ 1 GHz from 739.0332 nm to 739.0349 nm to probe the R(78) (1-11) line containing 15 components a_1 to a_{15} . Figure 5.4(a) shows the theoretical and experimental Doppler broadened signal as well as the experimental SAS signal. For obtaining theoretical signal, we used the program IodineSpec5 [243] which is based on iodine atlas published by Gerstenkorn and Luc [230–233], works of Bacis and coworkers [244,245]; H. Knöckel and E. Tiemann [242,246,247] and other available literature [248,249]. The theoretical Doppler broadened signal has a full width at half maximum (FWHM) of ≈ 856 MHz and that obtained from experiment is 903(3) MHz. The experimental signals are obtained with 1 mW probe power and 10 mW pump power, the pump power should be maintained at lesser values to avoid power broadening. A view of the hyperfine transitions within the mentioned wavelength range as obtained from IodineSpec5 is presented in Fig. 5.4(b). For a better identification of the Doppler free dips and comparison with the theoretical hyperfine lines, the experimental Doppler free spectra is subtracted from the Doppler broadened one (shown in Fig. 5.4) and the same is also illustrated in Fig. 5.4(b). Analysis of the obtained spectra shows a total of six Doppler free features of R(78) (1-11) line as labelled in the figure and detailed in Tab. 5.1. Additionally, all the observed peaks are in perfect alignment to their corresponding first derivatives in the lock signal. As per IodineSpec5, peaks 2, 3 and 5 are results of unresolved four, four and three hyperfine peaks, respectively. The SAS spectra and more evidently, the error signal clearly shows that in the experiment all the hyperfine lines are resolved for feature 3 and three and two of them are resolved for peaks 2 and 5, respectively. The details of all the six features are mentioned in Tab. 5.1 along with the measured FWHM. The cooling laser can preferably be locked to any of peaks 1, 4 or 6 having an FWHM of 23(3) MHz, 21(2) MHz and 23(4) MHz, respectively as compared to hundreds of MHz of a Doppler broadened signal.

We have also studied the effect of temperature and pump beam power on the peak amplitude of the Doppler free peak labelled as 4 and presented the variation in Fig. 5.5. Keeping the pump and probe power fixed to 10 mW and 1 mW, respectively, the temperature is set at different points from 264 °C to 560 °C and the corresponding data for peak 6 is noted. On changing the cell temperature, readings are noted only after ensuring that thermal equilibrium has reached. Also, we do not go beyond 600 °C to avoid causing any damage to the cell. As is apparent from Fig. 5.5(a), peak amplitude increases with rise in temperature which is obvious as increased temperature heavily populates the desired state with more iodine molecules. The equation of

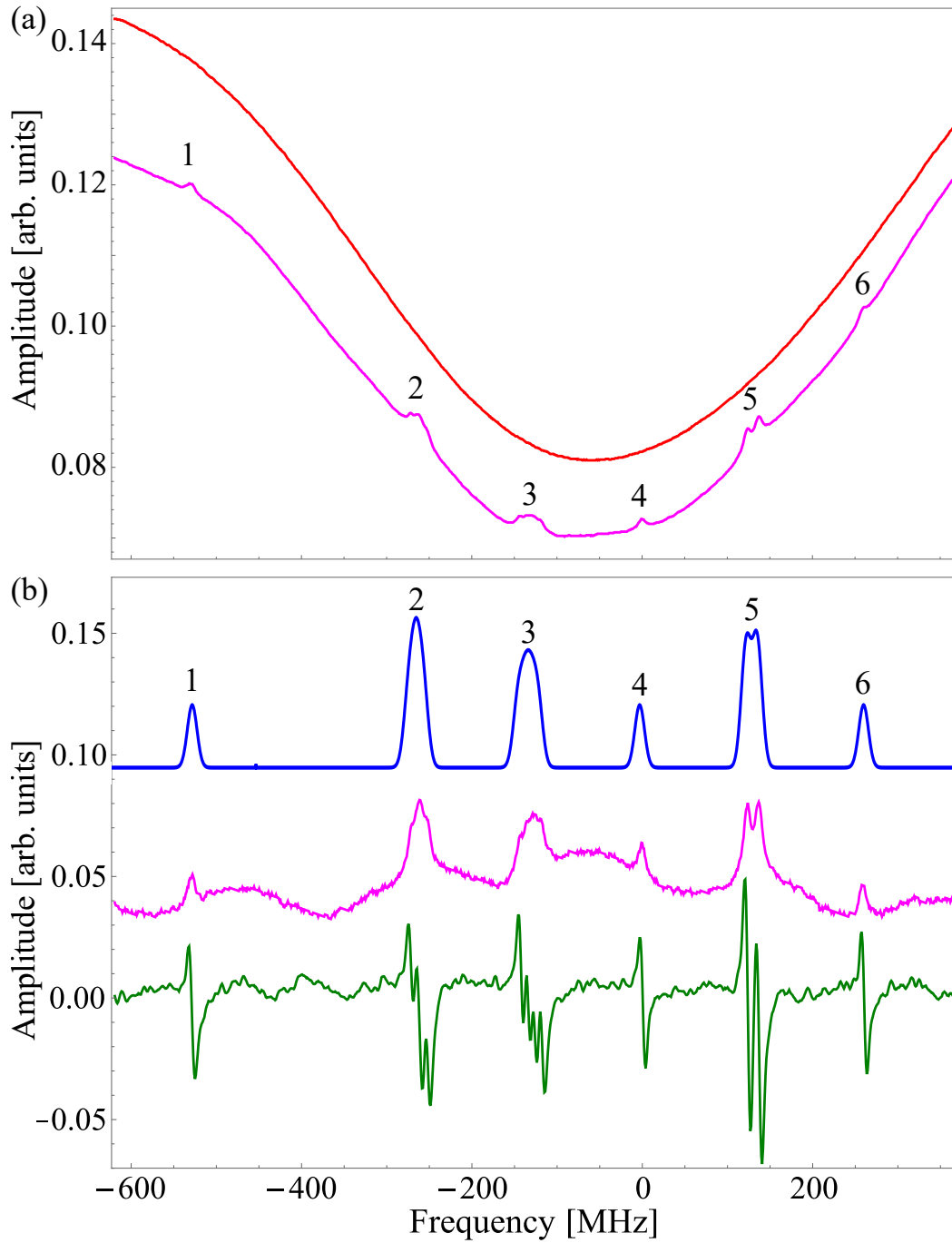


Fig. 5.4: (a) Doppler broadened absorption spectrum (red) and Doppler free spectrum (magenta) of molecular iodine obtained experimentally, (b) positions of hyperfine transitions obtained from IodineSpec5 (blue) and from SAS experiment (magenta) and their corresponding error signals (green) for a wavelength scan from 739.0332 nm to 739.0349 nm with vapor cell heated to 450 °C. A total of six Doppler free peaks are observed which are labelled as 1-6; almost all of them are resolved.

Tab. 5.1: Details of the hyperfine transitions observed in R(78) (1-11) line of molecular iodine.

Peak	Component of R(78) (1-11)	Frequency (MHz) (from IodineSpec5) (offset: 405654000 MHz)	Frequency (MHz) (from experiment) (offset: 405654000 MHz)	FWHM (MHz) (from IodineSpec5)	FWHM (MHz) (from experiment)
1	a ₁	74	189(60)	15(2)	23(3)
2	a ₂ - a ₅	368	218(60)	25(4)	35(4)
3	a ₆ - a ₉	516	396(60)	31(5)	40(6)
4	a ₁₀	662	584(60)	15(2)	21(2)
5	a ₁₁ - a ₁₄	811	749(60)	26(4)	39(5)
6	a ₁₅	957	923(60)	15(3)	23(4)

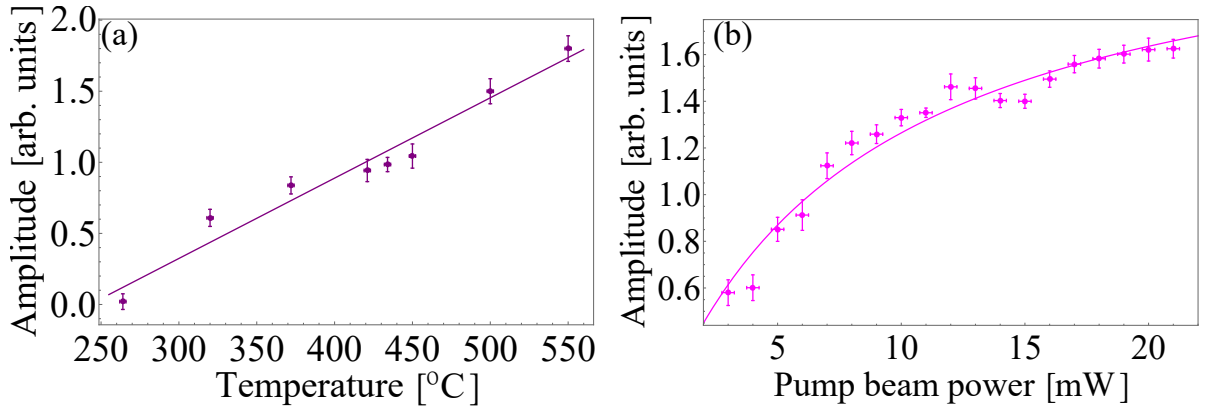


Fig. 5.5: Variation of peak amplitude of Doppler free feature labelled 4 with increasing (a) cell temperature and (b) pump beam power, along with the fits.

line fitted to the data is $-1.37143 + 0.00565 x$ which implies that at temperatures below 243 °C, there will be negligible peak intensity. Furthermore, keeping probe power fixed at 1 mW and cell temperature at 450 °C, the pump power is varied. The corresponding observation is shown in Fig. 5.5(b) from which we infer that peak amplitude of the Doppler free feature increases. This occurs because increased pump power implies increased intensity within Rayleigh range and hence better interaction with the iodine molecules within that spatial range. If γ_s , I_p and I_s be the light scattered from the population in the excited state, peak intensity and saturation intensity of the corresponding signal, respectively, then we have,

$$\gamma_s \propto I_p, \quad (5.2)$$

$$\gamma_s = \frac{\gamma_o}{2} \frac{I}{I + I_s}, \quad (5.3)$$

where γ_0 and I are natural linewidth and pump power, respectively. The fit function for the data points shown in Fig. 5.5(b) therefore takes the form

$$\gamma_s = A \frac{x/B}{1 + x/B}, \quad (5.4)$$

with A and B being the fit parameters with $B = I_s$. The solid line in Fig. 5.5(b) is the fitted plot obtained using Eqn. 5.4 which gives $I_s = 8.3 \pm 0.9$ mW.

5.4.2 Lock signal

The aim behind the molecular iodine SAS is frequency stabilization of cooling laser at 369.5 nm with respect to one of the Doppler free peaks, we chose Doppler free feature 4 or component a_{10} for this purpose. For stabilizing the laser frequency to the desired peak, the widely used approach Pound–Drever–Hall technique is employed [221,222]. The amplitude of laser scanning is first reduced so that only a_{10} is scanned. For locking the laser with respect to peak of the fringe, an error signal is required. The pump signal is therefore modulated with a sine wave of frequency 60 kHz and amplitude 1.9 V. The probe beam interacts with the frequency modulated pump and the resulting signal on the photodiode is fed to the lock-in-amplifier where a mixer multiplies the carrier signal with a reference signal of same frequency. The resultant is the error signal which is further passed through a low pass filter of cutoff at 60 kHz. The phase difference between the reference and modulated signal in the lock-in amplifier is optimized to achieve maximum peak amplitude for the error signal for a tight locking. A proportional-integral-derivative (PID) controller takes in the error signal, generates a feedback signal which

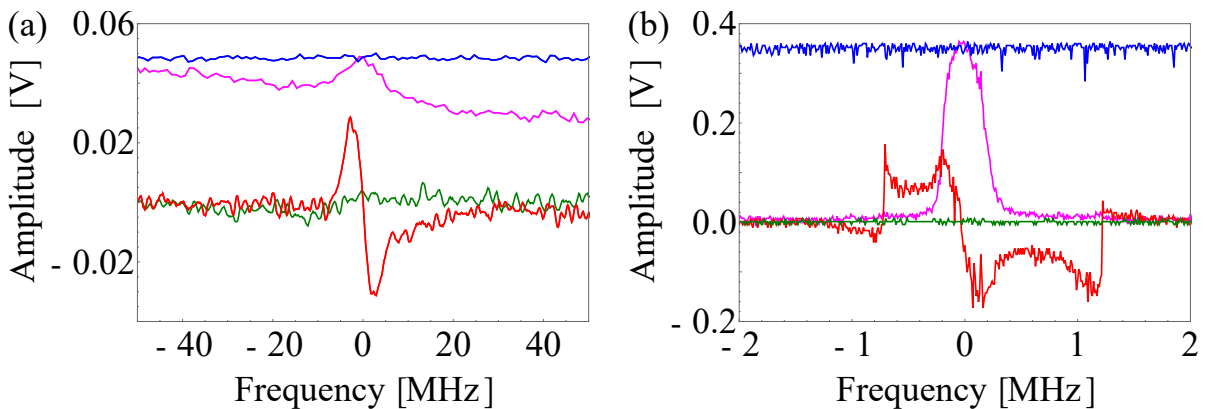


Fig. 5.6: Error signal (red) for peak (magenta) and their corresponding lock signals (green and blue, respectively) when laser is stabilized to top of the peaks for (a) experimentally obtained saturation absorption peak of a_{10} component and (b) SHG cavity peak of the laser system.

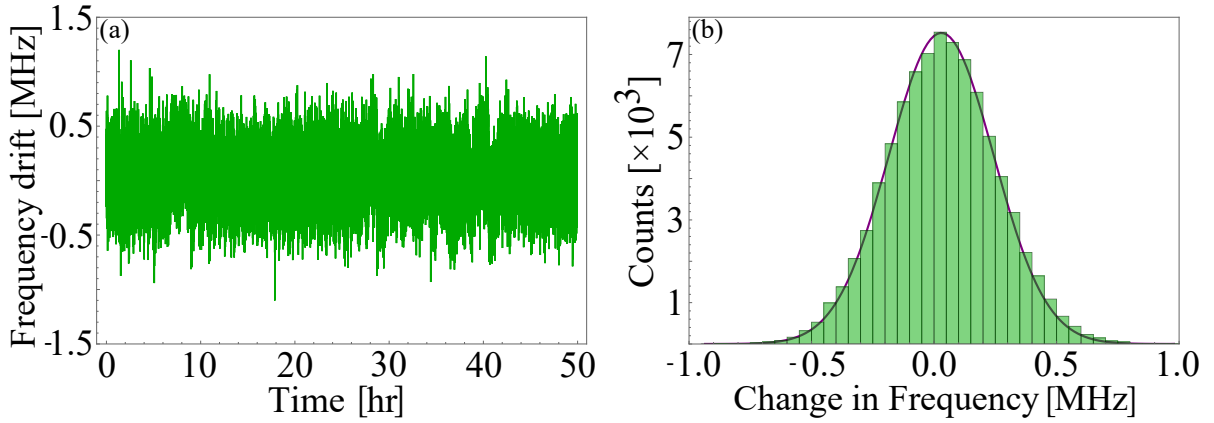


Fig. 5.7: (a) Frequency drift of the fundamental frequency of the cooling laser when locked to SAS peak no. 4 over 50 hours and (b) the corresponding histogram with the Gaussian fit for linewidth determination.

is consigned to the piezo driver of the laser for its active stabilization. The photodiode signal for a_{10} , its error signal and the corresponding lock signals are shown in Fig. 5.6(a). After stabilizing the fundamental frequency of the laser, the SHG cavity is locked using commercial PDH and PID module in-built in the laser controller. Figure 5.6(b) shows the SHG cavity peak, corresponding error signal obtained by PDH technique via applying a sine wave modulation of frequency 19 MHz to the laser current and their respective lock signals. In order to study the long-term instabilities in the locked frequency, data corresponding to laser stabilized over for 50 hours is collected and its histogram is obtained as represented in Fig. 5.7. From the histogram, we find that the long-term linewidth of the laser is 0.5(2) MHz with a drift of 0.028(7) kHz/hr.

5.4.3 Noise density profile

To measure the short-term stability of the locked laser, we have obtained the Fast Fourier transform (FFT) of the locked error signals corresponding to the SHG cavity peak and the Doppler free peak no. 4. The data is collected using a spectrum analyzer (Model No. FSV 40, Rohde & Schwarz) using which the power spectral density of the noise is acquired and shown in Fig. 5.8. Analysis of the noise spectrum using rectangular noise spectrum approximation gives information on laser linewidth as well as its short-term stability. Area under the curves shown in Fig. 5.8 are integrated to evaluate the V_{rms} for the shown locked error signals; and after subtraction from V_{rms} of the noise floor of the spectrum analyser, these are found to be 0.16(3) V and 0.0125(4) V with corresponding laser linewidths of 9(2) MHz and 0.75(3) MHz, when locked with respect to SHG cavity peak and the Doppler free peak, respectively. The respective noise density is measured to be $3.3 \mu\text{V}/\sqrt{\text{Hz}}$ @ 16 kHz and $1.8 \mu\text{V}/\sqrt{\text{Hz}}$ @ 4 kHz.

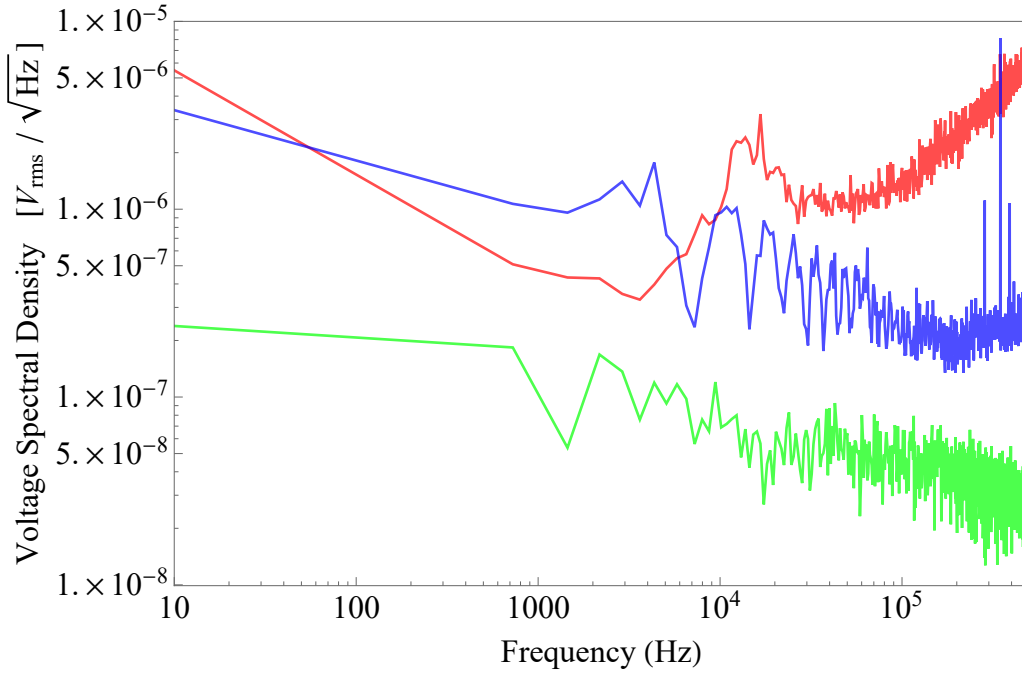


Fig. 5.8: Voltage spectral density of noise floor of the spectrum analyser (green), error signal when locked to the top of SAS signal (blue) and SHG cavity peak (red).

The noise density corresponding to SHG cavity is the sum of instabilities of frequency noise of the fundamental frequency of laser diode, tapered amplifier and length of the SHG cavity whereas the noise density of the SAS generated error signal of iodine is sole contribution of frequency noise of the fundamental frequency of laser diode. As a result, the noise density of the locked error signal of the SHG cavity peak is more than that of the SAS peak.

5.5. Conclusion

We have stabilized an ECDL laser at 739 nm, the frequency doubled output of which at 369.5 nm is used for ion production, laser cooling and imaging of the trapped $^{171}\text{Yb}^+$ experiment for developing an optical frequency standard. The hyperfine transitions of molecular iodine around 739 nm within a frequency span of 1 GHz have been observed by performing Saturated absorption spectroscopy. A total of six hyperfine transitions are found to be centred at 739.03321 nm, 739.03352 nm, 739.03382 nm, 739.03416 nm, 739.03448 nm and 739.03454 nm. The intensities of the peaks are found to increase with increasing pump beam power as well as with cell temperature. Using the SAS generated error signal from the lock-in amplifier as the feedback signal to the laser piezo, the cooling laser is locked on the a_{10} component of R(78)

(1-11) transition corresponding to 739.03382 nm. Its short-term and long-term linewidths are measured to be 0.75(3) MHz and 0.5(2) MHz, respectively. The locked laser is checked for a period of over 50 hours and is found to be stable even under external perturbations. Its noise density is measured to be $1.8 \mu\text{V}/\sqrt{\text{Hz}}$ @ 4 kHz. Hence, the locked laser is ready to probe the cooling transition of the ion-trap experiment.

Chapter 6

Absolute frequency measurement for $^1S_0 \rightarrow ^1P_1$ transition of Yb atoms and its isotope-selective photoionization

Publication: Lakhi Sharma, H. Rathore, S. Utreja, Neelam, A. Roy, S. De, S. Panja, Optical Atomic Clocks for Redefining SI Units of Time and Frequency, *MAPAN* **35**, 531 (2020).

6.1. Introduction

Electrical load analysis for delivering desired radiofrequency for creation of trapping potential, estimation of dominant BBR shift, design and development of a low-divergent atomic oven to deliver neutral Yb atoms, design and performance analysis of an optics assembly constructed for single trapped ion imaging and stabilization of cooling laser have been worked out towards establishing $^{171}\text{Yb}^+$ based optical clock. Once the ion trap and the atomic oven are installed within the vacuum chamber and ultra high vacuum condition is achieved, next step towards instigating the experiment is ionization of the neutral atoms emerging from the oven as only ionized species can perceive the harmonic potential and get trapped for further experimentation. Naturally occurring Yb shows presence of seven stable isotopes: ^{168}Yb (0.13%), ^{170}Yb (3.05%), ^{171}Yb (14.3%), ^{172}Yb (21.9%), ^{173}Yb (16.12%), ^{174}Yb (31.8%) and ^{176}Yb (12.7%) of which we are fixated on ^{171}Yb . This chapter deals with a method for selective ionization of desirable isotopes for creating ^{171}Yb ions. Trapped Ytterbium atom and ion (Yb^+) are potential candidates [48,250–252] for building an optical frequency standard. Till date, the best achieved fractional uncertainty of an Yb atom based optical clock is 1.4×10^{-18} [48] and that for an Yb

ion optical clock is 3.2×10^{-18} [253]. It is also advantageous for various applications in atomic physics. They are used by many research groups for carrying out experiments in the fields of quantum information processing [254, 255], measurement of physical properties of ultra-cold quantum gas [251], parity violation in atoms [256], precision measurements [257], *etc.* For all such experiments, the ion is trapped and for trapping ions, an important step is production of ions or ionization of neutral atoms. Various methods have been adopted for production of ions, prominently, by bombardment of electrons [258, 259] or photons [260, 261] on a weak atomic flux outcoming from an atomic oven or the photoelectric ionization method [262]. The electron impact ionization method requires strong atomic flux and strong current leading to deposition of metallic Yb on the trap electrodes [263, 264]. As described earlier in Chapter 3, such deposition leads to differential work function resulting in unwanted potential difference or patch potential. Such source of excess electric field shifts the confining potential's minima causing increased micromotion over time, thus deteriorating trap's performance. Photoelectric ionization accompanies similar disadvantages [262]. However, photoionization method mitigates the drawbacks of these two methods. Photoionization method is effective for reduced atomic flux too, thus reducing chances of atom deposition on electrodes [265]. It allows for isotope selectivity by implementing fluorescence spectroscopy of the neutral species. In this way, experiment can be carried out with naturally available Yb metal instead of isotopically enriched element. So, on account of its high efficiency, no patch effects and isotope selectivity, experimental society has turned to trap loading by photoionization, specifically in precision measurement experiments.

Photoionization of neutral atomic flux for loading trap with ions in ion clock experiments has been reported numerous times by several research groups [261, 265–269]. Borisov *et. al.* first developed the atomic-vapor laser isotope separation method based on isotopically selective photoionization of atoms. They employed it to study the selectivity of various isotopes of Ytterbium both theoretically and experimentally [270]. Later, M. Sankari and M. V. Suryanarayana proposed and computationally studied and compared different schemes of Yb photoionization based on various parameters such as laser power and laser linewidth [271]. Neutral calcium atoms are also ionized by two-step photoionization process using 423 nm and 390 nm lasers, for precision ion-trapping experiments [272]. A study by M. Brownnutt *et. al.* compares the electron bombardment and photoionization processes for loading $^{88}\text{Sr}^+$ in trap and found out that Sr vapor pressure required to load the trap reduces by four orders of magnitude when ionized by photons [273]. As shown by Meyer and group, photoionization also aids in calculating isotopic shifts from which mass shift and field shift can be measured [274]. Thus, most of the atomic ions being used as the candidate for clock transition are produced through photoionization of their neutral atoms.

In this chapter, we discuss atom-photon interaction for selective photoionization of ^{171}Yb . The absolute frequencies of $^1\text{S}_0 \rightarrow ^1\text{P}_1$ transition for each isotopes of Yb, their isotopic shifts and linewidths are reported. Section 6.2 discusses the Yb photoionization scheme whereas the experimental details are presented in Section 6.3. The outcome of the experimental studies are reported in Section 6.4.

6.2. Schemes for photoionization loading of Yb ions

The interaction of atoms with light has proved to be one of the most advantageous tools developed in trapped-ion experiments. Atom-light interaction assists in production of ions [270,274], ion-trapping [169,275,276], ion cooling [277,278], state preparation of ions and also in detecting them [179,181]. The difference in energy levels *i.e.*, the absorption frequencies of the isotopes of an element is utilized in measuring the absolute frequency of a transition of the desired isotope, in our case, ^{171}Yb . Figure 6.1 shows energy level diagrams corresponding to two possible schemes for photoionization of Ytterbium. The first ionization potential of Yb *i.e.* amount of energy required to knock out one valence electron from the outermost shell, is

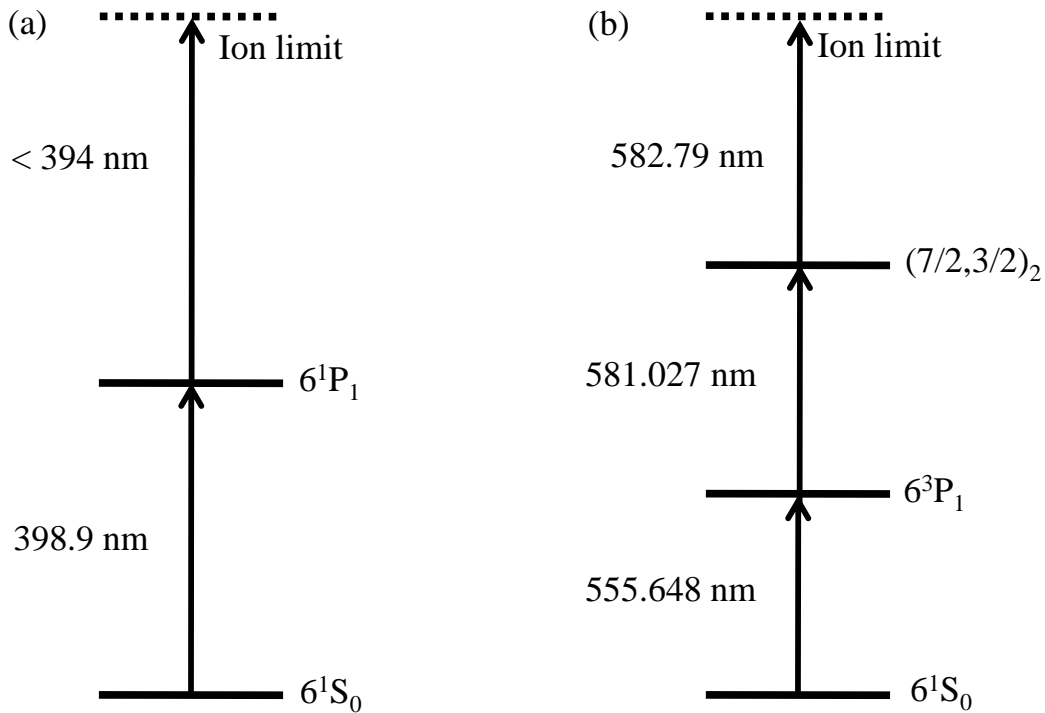


Fig. 6.1: Energy level diagram for Yb relevant to its photoionization. (a) Scheme 1: a 2-photon ionization process (b) Scheme 2: a 3-photon ionization process.

6.25 eV *i.e.* 50443.5 cm^{-1} . Hence, photoionization by a single photon requires radiation with wavelength $< 198 \text{ nm}$ in the vacuum ultraviolet region. Producing laser beam in this wavelength domain as well as developing optical set-up for navigating it is comparatively difficult. Also, since we are aiming at isotope selective photoionization, excitation using a single high energy photon will desist taking advantage of the bound levels of Yb. Scheme 1 (Fig. 6.1(a)) depicts a two-photon ionization process [271] in which the first stage included excitation to 1P_1 from ground state 1S_0 followed by shining by any laser of wavelength $< 394 \text{ nm}$ to strip off one of its valence electron. Scheme 2 (Fig. 6.1(b)), on the other hand is a three-photon ionization process [270] where the Yb atom is first excited from the ground level to 3P_1 using laser at 555.648 nm . In the next step, the atom is further excited to $(7/2, 3/2)_2$ state using second laser tuned to 581.027 nm followed by excitation to an auto-ionization level using 582.79 nm , where it is eventually ionized.

Isotope selectivity depends on photoionization scheme used, its resonance ionization transitions, the isotopic shift and natural linewidth of the transition [279–281]. Optical selectivity for a transition is higher provided its isotopic shift is larger. Laser bandwidth and other inhomogeneous broadenings also lead to decreased isotope selectivity. Scheme 1 was proposed by Sankari *et. al.*; he compared both the above-mentioned schemes and concluded that for broader laser linewidths ($\sim 1000 \text{ MHz}$), Scheme 2 gives higher selectivity whereas Scheme 1 yields higher selectivity when performed with narrow linewidth ($< 500 \text{ MHz}$) laser. The first stage of Scheme 1 is based on the strong $^1S_0 \rightarrow ^1P_1$ transition compared to the weak inter-combination line in Scheme 2; hence the former produces more ions even with low energy laser beam. We, therefore plan to use Scheme 1 in our experiment. Also, Scheme 1 being a 2-photon ionization process includes less experimental complexity in comparison to Scheme 1. Besides, step 2 of the scheme requires a laser of wavelength $< 394 \text{ nm}$ and as mentioned earlier, the experiment uses a 369 nm laser for laser cooling as well as for single ion detection technique. Use of the same laser for completing the ionization process is therefore an advantage. Transformation of the desired experimental species to its gaseous state is important for realization of the photoionization method. The indigenously designed and developed atomic oven, discussed in Chapter 3 serves for this purpose.

6.3. Experimental set-up

For demonstration of photoionization of Yb, we built a vacuum set-up with a test chamber having a total of six viewports. The chamber is pumped down to pressure $1.8 \times 10^{-8} \text{ mbar}$ by a turbomolecular pump (HiClassic 80, Pfeiffer). The schematic of the optical set-up is shown in

Fig. 6.2. The atomic oven made of stainless steel capillary and resistively heated by tungsten wire, is filled with either Yb ingot (ALF-000407-14, Alfa Aesar) or Yb foil (ALF-012437-FF, Alfa Aesar) and housed inside the test vacuum chamber. The 399 nm radiation used for probing the $^1S_0 \rightarrow ^1P_1$ transition comes from a tunable, grating-stabilized, external-cavity diode laser (ECDL) from Toptica, whereas 369 nm is accomplished with a frequency-doubled ECDL system from Toptica, the fundamental output of which is at 739 nm. Both the laser systems are set in Littrow configuration and have a linewidth of hundreds of kHz. With the help of beam splitters, both the light beams are splitted into two parts. For 399 nm, one part goes into the experimental chamber and the remaining ($\sim 50\mu\text{W}$) to the wavelengthmeter (WS7, High Finesse) for further monitoring of frequency scanning or locking. Two outputs of 739 nm laser at 40 mW and 3 mW are available; a fraction of the 40 mW is utilized for the current experiment, while remaining is used for performing Iodine SAS to carry out laser locking as mentioned in the previous chapter. The 3 mW coupled to a multimode optical fibre and fed to the wavelengthmeter to keep a track. Both the laser lights are guided to the chamber via mirrors and coupled using a Polarizing Beam Splitter (PBS) before launching them into the experimental point of interaction with the neutral Yb beam. The laser and the Yb beam are kept orthogonal to each other to minimize Doppler shifts. The 399 nm and 369 nm beams used for the experiment are kept at 1 mW and 2.5 mW, respectively. The oven current is maintained at a power of 3.9 W for which the reservoir temperature is about 250°C and atomic flux is estimated to be $7.9 \times 10^9 \text{ atoms s}^{-1}$, as indicated in Chapter 3. The absolute frequency

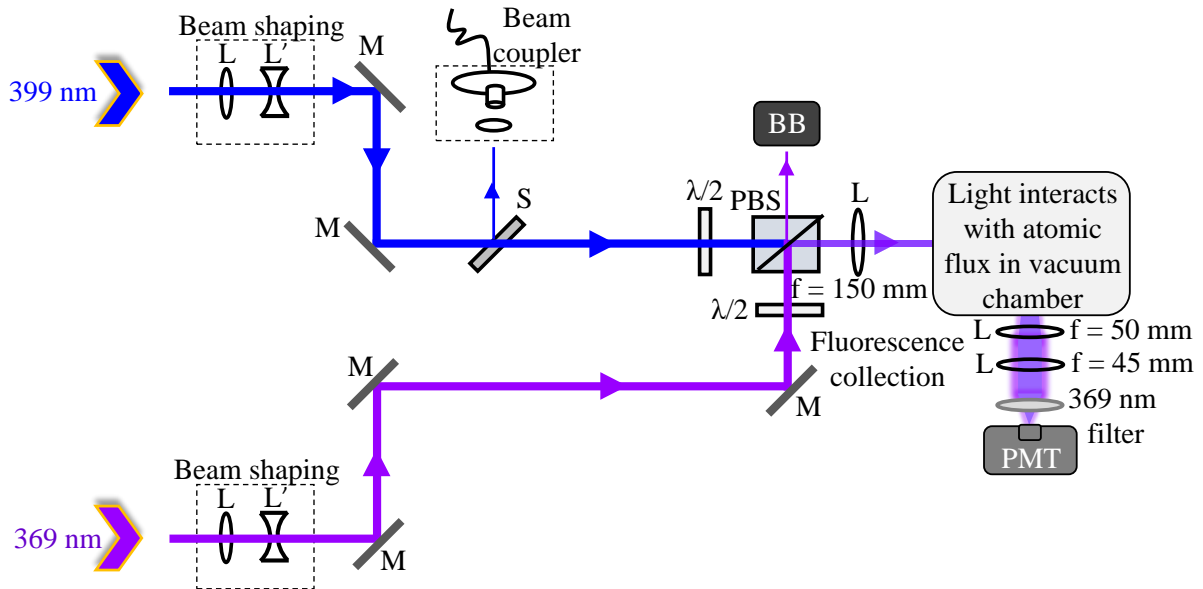


Fig. 6.2: Schematic of the optical set-up for carrying out isotope selective fluorescence spectroscopy followed by ionization. Here, M: mirror, L: convex lens, L': concave lens, S: beam sampler, $\lambda/2$: half waveplate, BB: beam blocker and PBS: polarizing beam splitter.

corresponding to the desired $S \rightarrow P$ transition of the Yb isotopes is searched by slow scan of the frequency of 399 nm laser over a range of 2.5 GHz. For collecting the fluorescence photons, a high numerical aperture, 2 inch diameter lens of focal length 75 mm is used, followed by another lens of focal length 40 mm which converges the collected photons onto a PMT (H8259, Hamamatsu) for signal detection. The PMT's output is transferred to a counting unit (C8855-01, Hamamatsu). The counting unit comes with a sample software and so the measurement can be started as soon as the unit is connected to a PC. The entire set-up, specifically the chamber and the photon collection optics is efficiently housed inside a dark environment to minimize background counts as well as to protect the PMT from any damages.

6.4. Results and Discussions

Once the experimental setup is equipped with all requisites as shown in Fig. 6.3(a), the oven is heated resistively by applying a power of 4.6 W. With the assistance of the laser controller, the 399 nm laser is scanned over 2.5 GHz from 398.90960 nm to 398.91250 nm. The outcoming atomic flux interacts with the scanning 399 laser beam forthcoming along a direction orthogonal to atomic beam propagation direction. When the laser frequency is in resonance with $S \rightarrow P$ transition of any of the isotopes of the Yb sample, photons are emitted, as a result of which the blue fluorescence is visible as shown in Fig. 6.3(c) in contrast to no such trace when the interacting frequency is in off-resonance condition (Fig. 6.3(b)). The red light is of the glowing tungsten to which a high current is applied for resistive heating. At 2.7 A, reservoir temperature is 335°C and so, a high atomic flux of 5.8×10^{12} results due to which the fluorescence is visible

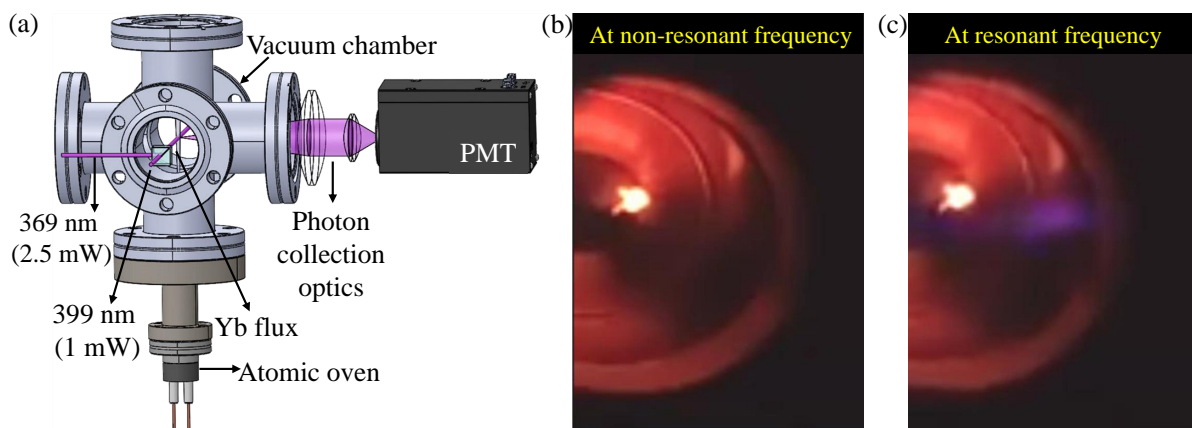


Fig. 6.3: (a) A 3D illustration of Yb atomic beam interacting orthogonally with coupled 399 nm and 369 nm laser beams, Snapshot of oven operating inside the test chamber when the laser frequency is scanned: (b) At non-resonant condition (c) At resonant condition.

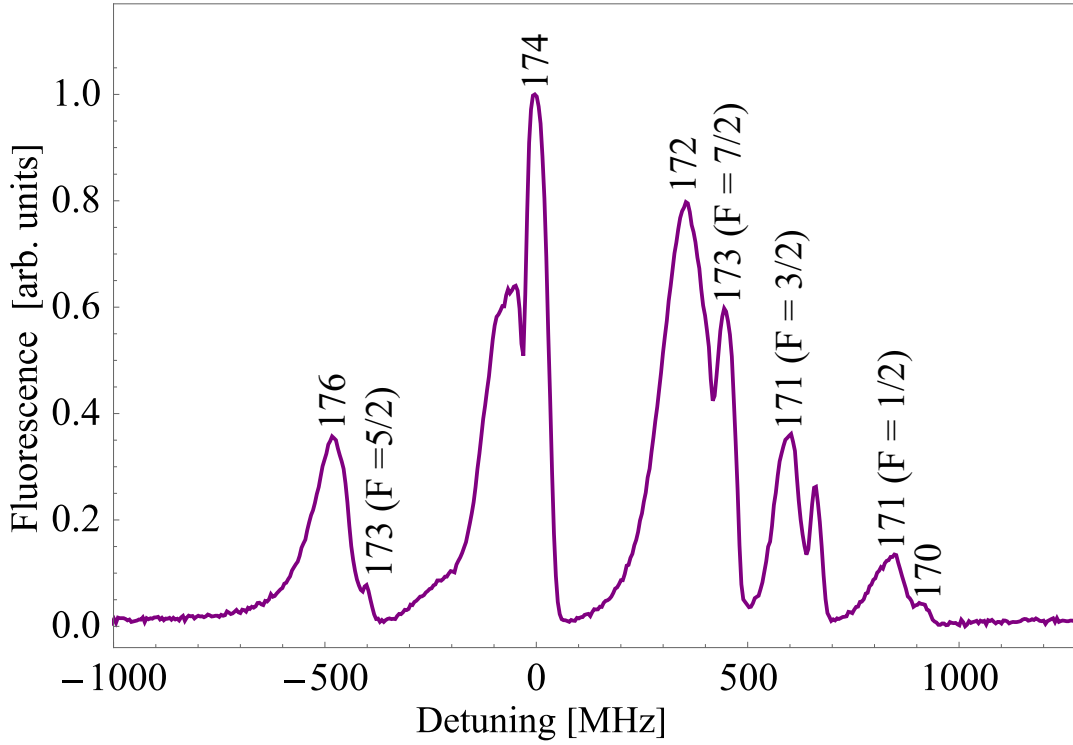


Fig. 6.4: Fluorescence excitation spectra of Yb isotopes. Different isotopes are labelled and their excitation frequencies are plotted relative to that of ^{174}Yb .

through naked eye too. For further experimental analysis, the oven current is fixed at 2.3 A at 1.7 V *i.e.* at 3.9 W so that the oven welds for a longer time.

The laser induced photo-excitation spectra within the mentioned wavelength range, recorded by the PMT for Yb atoms is shown in Fig. 6.4. The abscissa of the graph depicts laser frequency relative to the resonant value ($\Delta\nu = \nu - \nu_{174}$) for exciting $^1\text{S}_0 \rightarrow ^1\text{P}_1$ transition in ^{174}Yb which is found to be at a vacuum wavelength near 398.91129 nm; the ordinate represents the normalized photon counts. As can be seen, trace of a total of 8 isotopes are obtained at a frequency spread of 1930 MHz. The experimental data is fitted to a sum of eight Lorentz profiles to extract the transition frequency values corresponding to different isotopes and their hyperfine transitions which are listed in Tab. 6.1. Same values are reported for ^{171}Yb ($F = 1/2$) and ^{170}Yb as the two peaks are not clearly distinguishable due to very small difference between the two. The extracted values are useful for selective ionization of any isotope as well as for subsequent trapping. The resonance frequency of ^{171}Yb , isotope of our experimental interest, is measured to be 751527138 ± 60 MHz *i.e.* 398.91102 nm. It is at a difference of 157 MHz and 238 MHz with respect to its adjacent isotopes ^{173}Yb ($F = 7/2$) and ^{171}Yb ($F = 1/2$). Since, the first stage transition frequencies are now known, the second stage of selective excitation of

Tab. 6.1: Absolute frequency measurement of the $^1S_0 \rightarrow ^1P_1$ transition for the naturally occurring isotopes of Yb

Isotope	Frequency (MHz)	$\Delta\nu$ (MHz)	FWHM
^{176}Yb	751526985(60)	-489(60)	91(5)
^{173}Yb (F = 5/2)	751526206(60)	-82(60)	92(4)
^{174}Yb	751526614(60)	0	42(1)
^{172}Yb	751526695(60)	359(60)	46(3)
^{173}Yb (F = 7/2)	751527055(60)	443(60)	50(1)
^{171}Yb (F = 3/2)	751527138(60)	600(60)	65(5)
^{171}Yb (F = 1/2)	751527296(60)	838(60)	82(14)
^{170}Yb	751527296(60)	838(60)	82(14)

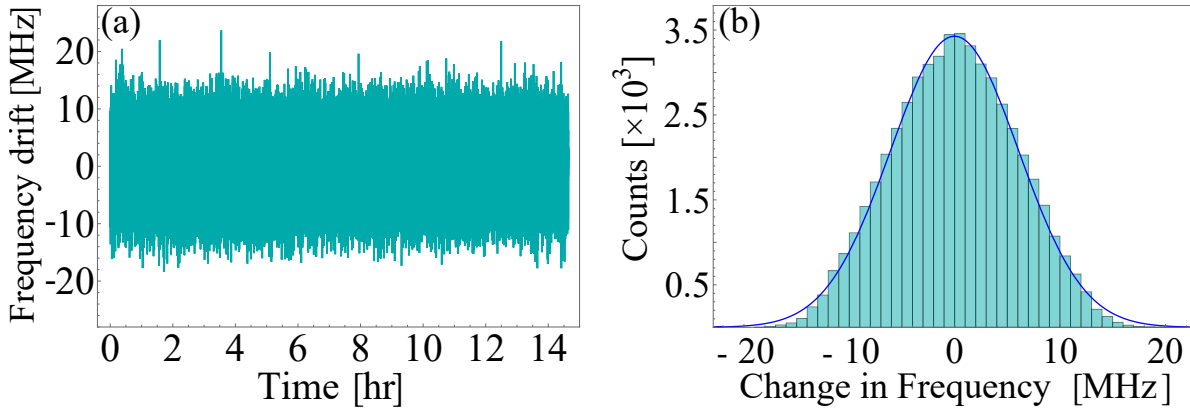


Fig. 6.5: (a) Frequency drift of the 399 nm when locked using WS7 wavelength meter over 14 hours and (b) the corresponding histogram with the Gaussian fit for linewidth determination.

a certain isotope out of a mixture of natural abundance material becomes easier. ECDLs have a spectral linewidth of a few tens of kHz and so, they are excellent to probe the excitation of desired isotope. However, as mentioned in Chapter 5, due to mechanical as well as thermal drifts, frequency drifts result with time in such lasers. Locking the frequency of 399 nm laser therefore becomes essential to avoid probing of any other isotope. As the photoionizing laser is required for a short span of time, locking technique giving a good short-term stability is adequate for the purpose. We therefore opt for laser locking via the wavelength meter. The optical unit of WS7 from High Finesse consists of Fizeau-based interferometers read out by photodiode arrays. An optical fiber couples light from the laser into the instrument and then collimates it onto the interferometer via a pair of mirrors. A cylindrical lens sends the formed interference pattern onto the CCD photodiode arrays. The final output is sent to a computer

via USB communication where the relevant software fits and compares the interferogram to a previously recorded and stored interference pattern obtained from a reference laser's signal. For occasional calibration of the reference pattern, we are using the signal of a 780 nm laser, the frequency of which is stabilized with respect to D₂ transition of rubidium obtained using SAS. We are choosing 780 nm laser as calibration source as it is closer to wavelengths of major lasers used in the experiment *i.e.* repump lasers 760 nm and 935 nm and fundamental wavelength of the cooling laser 739 nm, and hence, will give reliable wavelength measurements. For frequency locking, its software based proportional-integral-derivative (PID) controller is utilized which calculates the difference between measured and desired values of wavelength and exports it as a voltage signal to the piezo of the laser. The output of the PID controller depends on the values of control terms: P (proportional), I (integral) and D (derivative) and so these are to be set appropriately to have a good measuring and locking system. The associated PID simulator (PIDSIM2) of the instrument assists in finding the best matches for P, I and D. Therefore, using the PID control and PID simulator feature of the wavelength meter, the 399 nm laser is locked at 398.91065 nm, corresponding locked data over 14 hours and histogram plot is shown in Fig. 6.5(a,b). A probability distribution function fitting to the histogram data indicates that the locked 399 nm laser has a long-term spectral width of 14.7(3) MHz which is acceptable for our case as the adjacent isotopes are far apart by hundreds of MHz. This is followed by excitation to the continuum level by means of 369 nm laser. To find the resonant frequency for ionizing

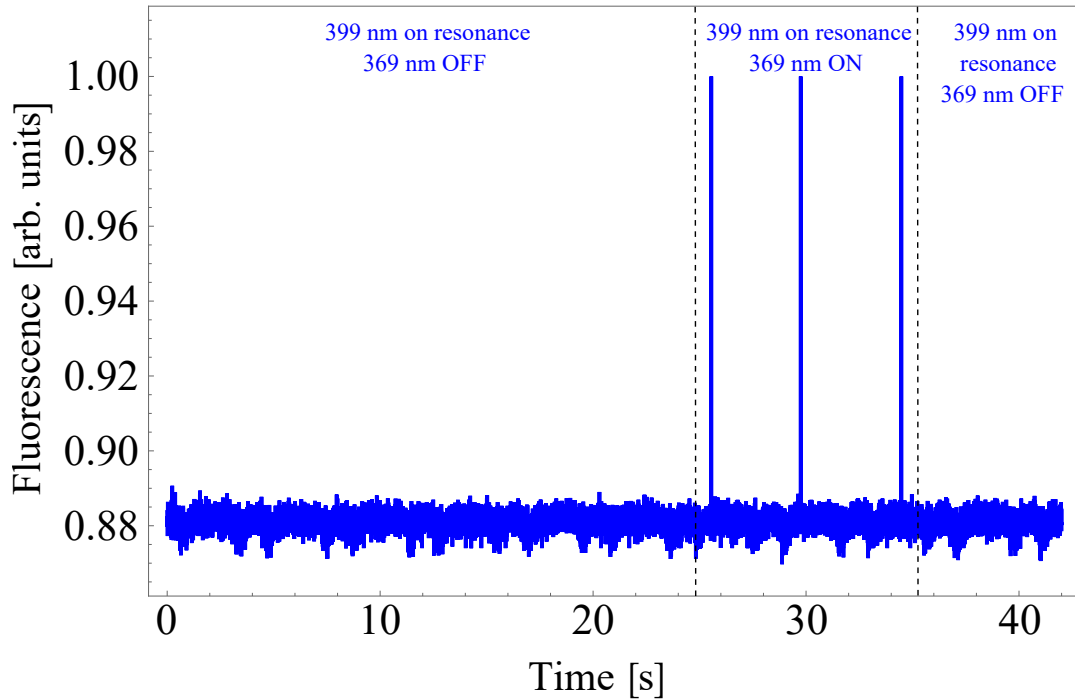


Fig. 6.6: Signal trace for two-photon ionization of ^{171}Yb at oven current of 2.3 A.

^{171}Yb , the 369 nm laser is scanned across 100 MHz about 369.5249 nm while keeping the 399 nm laser locked. As shown in Fig. 6.6, traces of photoionization are noticed at this stage, while when 369 nm laser is OFF, no such peaks are observed. For further more strong confirmation, the Yb ion is to be trapped for which work is currently going on in the laboratory.

6.5. Conclusion

We performed fluorescence spectroscopy of neutral Yb atoms emerging from an in-house developed atomic oven, using 399 nm laser. This aids in identification of various isotopes present in the Yb ingot used for the experiment as well as measurements of their corresponding transition frequencies for $^1S_0 \rightarrow ^1P_1$. The reported frequency values are useful in selectively ionizing the desired isotope in ion trapping experiments for building clock or any other quantum technology based experiments. The resonant frequency for exciting ^{171}Yb relevant to our experiment is measured to be 751527138 ± 60 MHz *i.e.* 398.91065 nm. We locked the 399 nm laser at this wavelength using the wavelengthmeter and the measured long-term linewidth is found to be 14.7(3) MHz. Consequently, using 369.5 nm laser, we performed the second step towards photoionizing ^{171}Yb and reported ionization proof for the same. The ions are therefore ready to be loaded in the trap, hence an initial but prime step towards achieving the bigger picture is accomplished.

Chapter 7

Conclusion

Trapped atomic ions have become one of the most enthralling areas of research for various aspects as mass spectrometry, spectroscopy, probing fundamental physics problems, quantum information, *etc.* All these studies require or aim for precise and accurate measurements which demand isolation of the experimental species from its surroundings to avoid external perturbations that may give an erroneous result. Invention of ion traps has eased this requirement as it allows for manipulation of charged particles by confining and alienating them.

At CSIR-National Physical Laboratory, New Delhi, we are working towards trapping and laser cooling a single Ytterbium-171 ion ($^{171}\text{Yb}^+$) within a specially designed end-cap type radio-frequency trap or Paul trap for developing an optical clock. At present, amongst all the measurable physical quantities, time and frequency is the most accurately measured one and an optical clock is expected to provide orders of magnitude better stability and accuracy than the microwave Cs clock, the present primary standard of time and frequency. Measuring time with highest level of accuracy is of utmost importance as measurement of some of the physical quantities, directly or indirectly, depends on time. Besides, accurate time also finds applications in banking, telecommunications, internet communication, navigation, power grids, basic sciences, *etc.* The primary requisites of an optical frequency standard are an atomic frequency reference, its trapping and cooling at ultra-high vacuum condition, ultra-narrow linewidth laser for probing the clock transition and a frequency counter for measuring absolute optical frequencies. Transitions of neutral atoms and atomic ions are used as a reference frequency of optical clocks. In case of ion optical clock, ions are confined and cooled within radio frequency (RF) ion trap; and only a single ion is preferred to be interrogated in the field free region of the trap centre in order to avoid any perturbation of the ionic clock transition due to Columbic interaction among the charged particles. RF ion traps provide unperturbed

environment for confining and cooling, thus providing longer interaction time and hence reduced instability.

Developing such a state-of-the-art ion trap experiment demands plethora of components which involves prior computation, theoretical and numerical analysis, fabrication of indigenously designed electrical, electronics and vacuum components, optical set-ups, precision measurements, *etc.* The accomplishment of this experiment depends on the successful establishment of its smaller building blocks, such as, fabrication of ion trap and vacuum chamber, creation of a trapping potential, atomic beam production, optical set-up and frequency stabilization of involved lasers, computer controlled electronic devices, single ion fluorescence detection and various relevant theoretical calculations like systematic shifts estimations. Various such requisites and theoretical estimations have been worked upon as a part of this doctoral work which are presented in this thesis.

The kernel of the experiment revolves around trapping and cooling of single $^{171}\text{Yb}^+$ and measuring its clock transition frequency. The trapping potential is created by applying a high voltage RF and a DC signal to the inner and outer pair of trap electrodes, respectively. The RF delivery to the trap is achieved via a helical resonator whose working parameters change at loaded and unloaded conditions. This necessitates accurate estimation of capacitive, inductive and resistive loads related to the ion trap-resonator assembly for constructing the helical resonator at the correct resonant frequency for supplying the desired RF to the ion trap. The said loads are estimated analytically using pre-existing formulae, numerically using finite element analysis via COMSOL MultiPhysics software and then verified experimentally. The constructed resonator delivers a resonant frequency of 27.04(7) MHz and quality factor of 600(8) at unloaded condition. The RF voltage transfer factor is estimated to be 0.45. The discussed load analysis is extended to estimation of BBR shift resulting from any excess capacitive load introduced by machining inaccuracy. An RF amplitude of 1 kV at $2\pi \times 15$ MHz and with ± 10 μm machining inaccuracy is found to result to ± 0.42 K heating of the trap and ∓ 43 mHz BBR shift for the Yb ion E3-clock transition corresponding to fractional frequency uncertainty of 6.6×10^{-17} . Such pre-evaluation of shifts in energy level is necessary for error budget estimation.

Once the harmonic potential is ready, it can be loaded with Yb ions for which a collimated source is required for delivering neutral Yb atomic flux. A very minute spacing of 0.7 mm between the trap electrodes in our experiment demands a low-divergent atomic beam source to avoid any atomic deposition which may disturb the harmonic trapping potential. We have therefore designed a dark wall oven consisting of a reservoir, a collimating tube, and a cold part at the exit, all made out of a single 316L stainless steel (SS) capillary of inner diameter 0.9 mm. It is operated in the transparent mode and gives a divergence as minimum as $1.2(1)^\circ$

at an oven temperature of 250 °C that produces an atomic flux of about 8×10^9 atoms s^{-1} . The spatial distribution of atomic flux of the oven has been estimated theoretically and also verified experimentally.

Single-ion based clock has an advantage of offering longer interaction time but it has to compromise with lower signal-to-noise ratio. Hence, it requires a very high resolution and diffraction limited imaging system for detection of cooling laser-induced fluorescence and for characterization of the trapped species. A 3-lens optical system has been designed after optimization using Optics Software for Layout and Optimization (OSLO), for ion imaging purpose that can resolve particles separated by $0.68(3) \mu\text{m}$ with minimum aberrations, recollects 77% of the incoming photons, magnifies by 238 times, and has a depth of field of $142 \mu\text{m}$ and a field of view of $56 \mu\text{m}$. It gives a diffraction limited performance over visible to near-infrared wavelengths, thus making it suitable to opt for different experiments.

Laser frequency stabilization is an necessitous requirement in such experiments to ensure high probability of desired atomic transitions throughout the experiment. The 369.5 nm laser and its shifted frequencies are used in the experiment for laser cooling, in second stage of photoionization process and also in single ion detection purpose. Its frequency is therefore stabilized to a Doppler free spectroscopic line of molecular iodine using saturated absorption spectroscopy (SAS) technique. A total of six Doppler free features of molecular iodine are resolved and their Full width at half maxima (FWHM) are measured to be approximately 13 MHz, 24 MHz, 31 MHz, 17 MHz, 29 MHz and 16 MHz. As compared to the measured Doppler broadened width of $\sim 903(3)$ MHz at 450°C, the Doppler free spectra obtained is of the order of a few tens of MHz. Using Pound-Drever Hall technique, the cooling laser's frequency is locked to one of the Doppler free features to avoid any drift in the used laser frequency and the short-term and long-term locked laser's linewidth are measured to be $0.75(3)$ MHz and $0.5(2)$ MHz, respectively and its noise density is measured to be $1.8 \mu\text{V}/\sqrt{\text{Hz}}$ @ 4 kHz.

Additionally, the neutral Yb atoms released from the oven are to be ionized for subsequent trapping and cooling for which a two step photo ionization scheme has been adopted combining lasers of wavelength 399 nm and 369.5 nm. The $^1\text{S}_0 \rightarrow ^1\text{P}_1$ transition in neutral Yb is the first isotopic-selective stage in 2-photon ionization of Yb for which the absolute frequency of this transition corresponding to Yb-171 isotope is to be measured. We have carried out the photo-excitation spectroscopy of neutral Yb atoms and obtained atomic resonance fluorescence spectra for its different isotopes. Total eight emission peaks are obtained corresponding to different isotopes of Yb: 176Yb, 173Yb ($F = 5/2$), 174Yb, 173Yb ($F = 3/2$), 172Yb, 173Yb ($F = 7/2$), 171Yb ($F = 3/2$), 171Yb ($F = 1/2$) and 170Yb. From the obtained spectrum, the transition frequency of 171Yb ($F = 3/2$) is measured to be $751527365(28)$ MHz. These

measurements are crucial as Yb atom is widely used in many fields of atomic physics. Locking the laser wavelength to 398.91102 nm, the cooling laser is scanned to ionize ^{171}Yb isotope required for our experiment.

In the field of time and frequency metrology, ultra-narrow atomic transition in the optical domain as a source of stable and accurate frequency standard is of great importance to Physics. This thesis discusses in details the development of various components which are very crucial towards developing one such optical clock based on a singly trapped $^{171}\text{Yb}^+$. The developed components and theoretical analysis leaps us forward towards achieving the main experiment which aims to measure 1 second precisely and accurately. Since ionization of Yb atoms has already been tested, we have cleaned, baked and assembled various vacuum components and assembled the main vacuum chamber along with the resonator and atomic oven. Nearby optical set-ups for sending light into the chamber is also ready. Various vacuum pumps as turbo molecular pump, ion pump and Ti-sublimation pump have already been connected to the chamber and a pressure of 6.9×10^{-10} mbar is achieved and we are currently working on attaining ultra-high vacuum so that the ion trapping can be performed.

Bibliography

- [1] O. W. Osberghaus, E. Fischer, *Forschungsbe.Wirtsch. – Verkehrsminist.Nordrhein – Westfalen*, 415 (1958).
- [2] F. M. Penning, Die glimmentladung bei niedrigem druck zwischen koaxialen zylindern in einem axialen magnetfeld. *Physica* **3**, 873-894 (1936).
- [3] W. Paul, Electromagnetic traps for charged and neutral particles, *Rev. Mod. Phys.* **62**, 531-540 (1990).
- [4] H. G. Dehmelt, Radiofrequency spectroscopy of stored ions. I. Storage, *Adv. At. Mol. Phys.* **3**, 53-72 (1967).
- [5] H. G. Dehmelt, Radiofrequency spectroscopy of stored ions. II. Spectroscopy, *Adv. At. Mol. Phys.* **5**, 109–154 (1969).
- [6] J. Byrne and P. S. Farago, On the production of polarized electrons by spin-exchange collisions, *Proc. Phys. Soc.* **86**, 801–815 (1965).
- [7] G. Gräff and E. Klempt, Messung der Zyklotronfrequenz im Vierpolkäfig, *Zeitschrift für Naturforschung* **22a**, 1960–1962 (1967).
- [8] A. A. Sokolov and Yu. G. Pavlenko, *Opt. Spectrosc.* **22**, 1–3 (1967).
- [9] F. M. Penning, Introduction of an axial magnetic field in the discharge between two coaxial cylinders, *Physica* **3**, 873–894 (1936).
- [10] K. Blaum, Yu. N. Novikov and G. Werth, Penning traps as a versatile tool for precise experiments in fundamental physics, *Contemp. Phys.* **51**, 149–175 (2010).
- [11] D. M. Segal and Ch. Wunderlich, “Cooling techniques for trapped ions” in M. Knoop, N. Madsen and R. C. Thompson (eds), *Physics with Trapped Charged Particles* (Imperial College Press, London, 2013).
- [12] F. Anderegg, “Waves in non-neutral plasma” in M. Knoop, N. Madsen and R. C. Thompson (eds), *Physics with Trapped Charged Particles* (Imperial College Press, London, (2013).

- [13] J. Fajans and C. M. Surko, Plasma and trap-based techniques for science with antimatter featured, *Phys. Plasmas* **27**, 030601 (2020).
- [14] W. M. Itano, External-field shifts of the $^{199}\text{Hg}^+$ optical frequency standard, *J. Res. Nat. Inst. Stand. Tech.* **105(6)**, 829–837 (2000).
- [15] C. Audoin and B. Guinot, *The Measurement of Time: Time, Frequency and the Atomic Clock*, Cambridge, Cambridge University Press, (2001).
- [16] F. Riehle, *Frequency Standards: Basics and Applications*, in *Freq. Stand. Basics Appl.*, Weinheim : Wiley-VCH, 2005.
- [17] A. D. Ludlow, M. M. Boyd, J. Ye, E. Peik and P. O. Schmidt, Optical atomic clocks, *Rev. Mod. Phys.* **87**, 637-701 (2015).
- [18] A. Bjerhammar, On a relativistic geodesy, *Bull. Géodésique* **59**, 207 (1985).
- [19] W. Shen, J. Ning, J. Liu, J. Li and D. Chao, Determination of the geopotential and orthometric height based on frequency shift equation, *Nat. Sci.* **3**, 388 (2011).
- [20] F. G. Major, The quantum beat: principles and applications of atomic clocks, *Choice Rev. Online* **45**, 45-1523 (2007).
- [21] M. S. Grewal, L. R. Weill and A. P. Andrews, *Global Positioning Systems, Inertial Navigation, and Integration*, 2nd ed., in *Glob. Position. Syst. Inert. Navig. Integr.*, 2nd ed., M. S. Grewal, L. R. Weill, and A. P. Andrews, Eds., John Wiley & Sons, Inc, Hoboken, NJ, USA, (2006).
- [22] M. J. Rycroft, Understanding GPS. Principles and applications, *J. Atmos. Solar-Terrestrial Phys.* **59**, (1997) 598.
- [23] S. G. Dittus, Hansjörg, Lämmerzahl, Claus, Turyshev, Ed., *Lasers, Clocks and Drag-Free Control - Exploration of Relativistic Gravity in Space — Hansjörg Dittus — Springer*, 1st ed., Springer-Verlag, Heidelberg, Germany, (2008).
- [24] L. Maleki and J. Prestage, Applications of clocks and frequency standards: from the routine to tests of fundamental models, *Metrologia* **42**, S145-S153 (2005).
- [25] D. W. Allan, Statistics of Atomic Frequency Standards, *Proc. IEEE* **54**, 221-230 (1966).
- [26] D. W. Allan, Time and Frequency (Time-Domain) Characterization, Estimation, and Prediction of Precision Clocks and Oscillators, *IEEE Trans. Ultrason. Ferroelectr. Freq. Control* **34**, 647-654 (1987).

- [27] W. M. Itano, J. C. Bergquist, J. J. Bollinger, J. M. Gilligan, D. J. Heinzen, F. L. Moore, M. G. Raizen and D. J. Wineland, Quantum projection noise: Population fluctuations in two-level systems, *Phys. Rev. A* **47**, 169-183 (1993).
- [28] N. Ramsey, *Molecular Beams*, Oxford University Press, 1985.
- [29] L. Essen and J. V. L. Parry, An Atomic Standard of Frequency and Time Interval: A Caesium Resonator, *Nature* **4476**, 280-282 (1955).
- [30] D. J. Wineland and W. M. Itano, Laser cooling of atoms, *Phys. Rev. A* **20**, 1521-1540 (1979).
- [31] N. F. Ramsey, History of early atomic clocks, *Metrologia* **42**, S1-S3 (2005).
- [32] B. Guinot and E. F. Arias, Atomic time-keeping from 1955 to the present, *Metrologia* **42**, S20-S30 (2005).
- [33] S. Weyers, V. Gerginov, M. Kazda, J. Rahm, B. Lipphardt, G. Dobrev and K. Gibble, Advances in the accuracy, stability, and reliability of the PTB primary fountain clocks, *Metrologia* **55**, 789-805 (2018).
- [34] S. G. Turyshev, *From Quantum to Cosmos: Fundamental Physics Research in Space*, Scientific Publishing Company, 2009.
- [35] C. W. Chou, D. B. Hume, T. Rosenband and D. J. Wineland, Optical clocks and relativity, *Science* **329**, 1630-1633 (2010).
- [36] N. Poli, C. W. Oates, P. Gill and G. M. Tino, Optical atomic clocks, *Riv. del Nuovo Cim.*, (2013).
- [37] N. Batra, A. Roy, S. Majhi, S. Panja and S. De, Singly charged ions for optical clocks, *Asian J. Phys.* **25**, 1069 (2016).
- [38] H. Katori, T. Ido and M. Kuwata-Gonokami, Optimal design of dipole potentials for efficient loading of Sr atoms, *J. Phys. Soc. Japan* **68**, 2479 (1999).
- [39] J. McKeever, J. R. Buck, A. D. Boozer, A. Kuzmich, H. C. Nägerl, D. M. Stamper-Kurn and H. J. Kimble, State-Insensitive Cooling and Trapping of Single Atoms in an Optical Cavity, *Phys. Rev. Lett.* **90**, 4 (2003).
- [40] T. Udem, R. Holzwarth and T. W. Hänsch, Optical frequency metrology, *Nature* **416**, 233-237 (2002).
- [41] J. L. Hall, M. Zhu and P. Buch, Prospects for using laser-prepared atomic fountains for optical frequency standards applications, *J. Opt. Soc. Am. B* **6**, 2194-2205 (1989).

- [42] K. Gibble and S. Chu, Laser-cooled Cs frequency standard and a measurement of the frequency shift due to ultracold collisions, *Phys. Rev. Lett.* **70**, 1771-1774 (1993).
- [43] J. Friebe, A. Pape, M. Riedmann, K. Moldenhauer, T. Mehlstäubler, N. Rehbein, C. Lisdat, E. M. Rasel, W. Ertmer, *et al.*, Absolute frequency measurement of the magnesium intercombination transition $^1S_0 \rightarrow ^3P_1$, *Phys. Rev. A - At. Mol. Opt. Phys.* **78**, 033830 (2008).
- [44] K. Sengstock, U. Sterr, J. H. Müller, V. Rieger, D. Bettermann and W. Ertmer, Optical Ramsey spectroscopy on laser-trapped and thermal Mg atoms, *Appl. Phys. B Lasers Opt.* **59**, 99-115 (1994).
- [45] W. Paul and M. Raether, Das elektrische Massenfilter, *Zeitschrift für Phys.* **140**, 262-273 (1955).
- [46] T. Kurosu, M. Morinaga and F. Shimizu, Observation of the Ca 4s $1S_0$ -4p $3P_1$ transition in continuous free-falling cold atomic flow from an atom trap, *Jpn. J. Appl. Phys.* **31**, L273-L275 (1992).
- [47] H. Katori, M. Takamoto, V. G. Pal'chikov and V. D. Ovsiannikov, Ultrastable optical clock with neutral atoms in an engineered light shift trap, *Phys. Rev. Lett.* **91**, 173005 (2003).
- [48] W. F. McGrew, X. Zhang, R. J. Fasano, S. A. Schäffer, K. Beloy, D. Nicolodi, R. C. Brown, N. Hinkley, G. Milani, *et al.*, Atomic clock performance enabling geodesy below the centimetre level, *Nature* **564**, 87-90(2018).
- [49] K. Beloy, D. R. Leibbrandt and W. M. Itano, Hyperfine-mediated electric quadrupole shifts in Al^+ and In^+ ion clocks, *Phys. Rev. A* **95**, 043405 (2017).
- [50] M. Takamoto, F. L. Hong, R. Higashi and H. Katori, An optical lattice clock, *Nature* **435**, 321-324 (2005).
- [51] G. E. Marti, R. B. Hutson, A. Goban, S. L. Campbell, N. Poli and J. Ye, Imaging Optical Frequencies with 100 μ Hz Precision and 1.1 μ m Resolution, *Phys. Rev. Lett.* **120**, 103201 (2018).
- [52] H. Dehmelt, Experiments with an isolated subatomic particle at rest, *Rev. Mod. Phys.* **62**, 525-530 (1990).
- [53] D. Wineland and H. Dehmelt, Proposed 1014 $\delta\nu/\nu$ laser fluorescence spectroscopy on Tl^+ mono-ion oscillator III (side band cooling), *Bull. Am. Phys. Soc.* **20**, 637 (1975).

- [54] F. L. Hong, Optical frequency standards for time and length applications, *Meas. Sci. Technol.* **28**, 012002 (2017).
- [55] C. W. Chou, D. B. Hume, J. C. J. Koelemeij, D. J. Wineland and T. Rosenband, Frequency comparison of two high-accuracy Al optical clocks, *Phys. Rev. Lett.* **104**, 070802 (2010).
- [56] M. S. Safronova, M. G. Kozlov and C. W. Clark, Precision calculation of black-body radiation shifts for optical frequency metrology, *Phys. Rev. Lett.* **107**, 143006 (2011).
- [57] R. Maiwald, A. Golla, M. Fischer, M. Bader, S. Heugel, B. Chalopin, M. Sondermann and G. Leuchs, Collecting more than half the fluorescence photons from a single ion, *Phys. Rev. A - At. Mol. Opt. Phys.* **86**, 043431 (2012).
- [58] H. G. Dehmelt, Mono-ion oscillator as potential ultimate laser frequency standard, *IEEE Trans. Instrum. Meas.* **IM-31**, 83–87 (1982).
- [59] Berkeland D. J., Miller, J. D., Bergquist, J. C., Itano W. M. & Wineland, D. J. Minimization of ion micromotion in a Paul trap. *J. Appl. Phys.* **83**, 5025 (1998).
- [60] J.D. Jackson: Classical Electrodynamics 2nd edn. (Wiley, New York 1975) p. 132.
- [61] R. Weinstock, On a fallacious proof of Earnshaw's theorem, *Am. J. Phys.* **44**, 392 (1976).
- [62] F. M. Arscott, Periodic Differential Equations: An introduction to Mathieu, Lamé and Allied Functions, Pergamon press, New York, 66 (1964).
- [63] M. Abramowitz and I. A. Stegun, Handbook of Mathematical Functions, NBS Applied Mathematics Series No. 55 (1972).
- [64] N. W. McLachlan, (Theory and Applications of Mathieu Functions(Clarendon, Oxford)) (1947).
- [65] Ghosh, P. K., Ion Traps, Clarendon Press, Oxford, (1995), p. 12 – 18.
- [66] BIPM - Recommended values of standard frequencies, <https://www.bipm.org/en/publications/mises-en-pratique/standard-frequencies.html>.
- [67] F. Riehle, P. Gill, F. Arias and L. Robertsson, The CIPM list of recommended frequency standard values: Guidelines and procedures, *Metrologia* **55**, 188-200 (2018).
- [68] K. Sugiyama and J. Yoda, Production of YbH⁺ by chemical reaction of Yb⁺ in excited states with H₂ gas, *Phys. Rev. A* **55**, 10 (1997).

- [69] K. Tsigutkin, D. Dounas-Frazer, A. Family, J. E. Stalnaker, V. V. Yashchuk and D. Budker, Observation of a large atomic parity violation effect in ytterbium, *Phys. Rev. Lett.* **103**, 071601 (2009).
- [70] V. A. Dzuba and V. V. Flambaum, Relativistic corrections to transition frequencies of Ag I, Dy I, Ho I, Yb II, Yb III, Au I, and Hg II and search for variation of the finestructure constant, *Phys. Rev. A* **77**, 012515 (2008).
- [71] A. Arvanitaki, J. Huang and K. Van Tilburg, Searching for dilaton dark matter with atomic clocks, *Phys. Rev. D* **91**, 01501 (2015)5.
- [72] S. Falke, N. Lemke, C. Grebing, B. Lipphardt, S. Weyers, V. Gerginov, N. Huntemann, C. Hagemann, A. Al-Masoudi, et al., A strontium lattice clock with 3×10^{-17} inaccuracy and its frequency, *New J. Phys.* **16**, 073023 (2014).
- [73] S. A. King, R. M. Godun, S. A. Webster, H. S. Margolis, L. A. M. Johnson, K. Szymaniec, P. E. G. Baird and P. Gill, Absolute frequency measurement of the $2S_{1/2}$ - $2F_{7/2}$ electric octupole transition in a single ion of $^{171}\text{Yb}^+$ with 10^{-15} fractional uncertainty, *New J. Phys.* **14**, 013045 (2012).
- [74] N. Huntemann, C. Sanner, B. Lipphardt, C. Tamm and E. Peik, Single-Ion Atomic Clock with 3×10^{-18} Systematic Uncertainty, *Phys. Rev. Lett.* **116**, 063001 (2016).
- [75] E. C. Beaty, Simple electrodes for quadrupole ion traps, *J. Appl. Phys.* **61**, 2118-2122 (1987).
- [76] C. A. Schrama, E. Peik, W. W. Smith and H. Walther, Novel miniature ion traps, *Opt. Commun.* **101**, 32-36 (1993).
- [77] N. Batra, Ph.D. Thesis, Computations, Design & Instrumentation for Precision Ion Trap Experiment, Academy of Scientific and Innovative Research, New Delhi, India.
- [78] S. De, N. Batra, S. Chakraborty, S. Panja and A. Sen Gupta, Design of an ion trap for trapping single $^{171}\text{Yb}^+$, *Curr. Sci.* **106**, 1348-1352 (2014).
- [79] A. Rastogi, N. Batra, A. Roy, J. Thangjam, V. P. S. Kalsi, S. Panja and S. De, Design of the Ion Trap and Vacuum System for ^{171}Yb -ion Optical Frequency Standard, *Mapan - J. Metrol. Soc. of India* **30**, 169-174(2015).
- [80] N. Batra, B. K. Sahoo and S. De, An optimized ion trap geometry to measure quadrupole shifts of $^{171}\text{Yb}^+$ clocks, *Chinese Phys. B* **25**, 113703 (2016).
- [81] J. Stenger, H. Schnatz, C. Tamm and H. R. Telle, Ultraprecise Measurement of Optical Frequency Ratios, *Phys. Rev. Lett.* **88**, 073601 (2002).

- [82] S. T. Cundiff and J. Ye, Colloquium: Femtosecond optical frequency combs, *Rev. Mod. Phys.* **75**, 325-342 (2003).
- [83] J. L. Hall, Nobel lecture: Defining and measuring optical frequencies, *Rev. Mod. Phys.* **78**, 1279-1295 (2006).
- [84] T. W. Hänsch, Nobel lecture: Passion for precision, *Rev. Mod. Phys.* **78**, 1297-1309 (2006).
- [85] J. L. Hall, Nobel lecture: Defining and measuring optical frequencies, *Rev. Mod. Phys.* **78**, 1279-1295 (2006).
- [86] J. L. Hall, J. Ye, S. A. Diddams, L. S. Ma, S. T. Cundiff and D. J. Jones, Ultra-sensitive spectroscopy, the ultrastable lasers, the ultrafast lasers, and the seriously nonlinear fiber: A new alliance for physics and metrology, *IEEE J. Quantum Electron.* **37**, 1482-1492 (2001).
- [87] N. Batra, A. Roy, C. Samal, S. Majhi, S. Panja, and S. De, Automation of an optical frequency standard experiment, in *2nd International Conference on Control, Instrumentation, Energy and Communication*, (India, 2016), p. 78.
- [88] A. Roy, N. Batra, S. Majhi, S. Panja, A. Sen Gupta and S. De, Design of a Stable DC Voltage Source and Computer Controlling of It Using an Indigenously Developed All-Digital Addressing-Cum-Control Hardware, *Mapan - J. Metrol. Soc.* **33**, 139-145 (2018).
- [89] A. Roy, Ph.D. Thesis, Developing Experimental setup for Trapped Ion based Optical Atomic Clock, Academy of Scientific and Innovative Research, New Delhi, India.
- [90] M. Knoop, N. Madsen, and R. C. Thompson, Trapped Charged Particles, ISBN: 978-1-78634-011-5, <https://doi.org/10.1142/q0004>, World Scientific Publishing Europe Limited, 2016 - Science.
- [91] E. Tely, & D. Gerlich, Integral cross sections for ion–molecule reactions. I. The guided beam technique, *Chem. Phys.* **4**, 417-427 (1974).
- [92] D. Gerlich, Inhomogeneous RF fields: A versatile tool for the study of processes with slow ions, *Adv. Chem. Phys.* **1**, 82 (1992).
- [93] Q. A. Turchette, D. Kielpinski, B. E. King, D. Leibfried, D. M. Meekhof, C. J. Myatt, M. A. Rowe, C. A. Sackett, C. S. Wood, W. M. Itano, C. Monroe, and D. J. Wineland, Heating of trapped ions from the quantum ground state, *Phys. Rev. A: At., Mol., Opt. Phys.* **61(6)**, 063418 (2000).

- [94] M. G. Raizen, J. M. Gilligan, J. C. Bergquist, W. M. Itano & D. J. Wineland, Ionic crystals in a linear Paul trap, *Phys. Rev. A* **45**, 6493 (1992).
- [95] J. D. Siverns, L. R. Simkins, S. Weidt, & W.K. Hensinger, On the application of radio frequency voltages to ion traps via helical resonators, *J. Appl. Phys. B* **107**, 921-934 (2012).
- [96] R. M. Jones, D. Gerlich, & S. L. Anderson, Simple radio-frequency power source for ion guides and ion traps, *Rev. Sci. Instrum.* **68**, 3357-3362 (1997).
- [97] R. M. Jones, & S. L. Anderson, Simplified radio-frequency generator for driving ion guides, traps, and other capacitive loads, *Rev. Sci. Instrum.* **71**, 4335 (2000).
- [98] A. Reza, *etal.*, An in situ trap capacitance measurement and ion-trapping detection scheme for a Penning ion trap facility, *Rev. Sci. Instrum.* **88**, 034705 (2017).
- [99] J. R. Noriega, L. A. García-Delgado, R. Gómez-Fuentes, & A. García-Juárez, Low power RF amplifier circuit for ion trap, *Rev. Sci. Instrum.* **87**, 094704 (2016).
- [100] W. W. Macalpine and R. O. Schildknecht, Coaxial resonators with helical inner conductor, *Proceedings of the IRE*, 47(12):2099–2105, December 1959.
- [101] K.G Johnson, Active stabilization of ion trap radiofrequency potentials, *Rev. Sci. Instrum.* **87**, 053110 (2016).
- [102] Y. Jau, F. M. Benito, H. Partner & P. D. D. Schwindt, Low power high-performance radio frequency oscillator for driving ion traps, *Rev. Sci. Instrum.* **82**, 023118-1–023118-5 (2011).
- [103] P. Marmillod, S. Antonioni, & U. J. Lorenz, A radio frequency/high voltage pulse generator for the operation of a planar multipole ion trap/time-of-flight mass spectrometer, *Rev. Sci. Instrum.* **84**, 044707 (2013).
- [104] I. Cermak, Compact radio-frequency power supply for ion and particle guides and traps, *Rev. Sci. Instrum.* **76**, 063302 (2005).
- [105] N. Batra, S. Panja, S. De, A. Roy, S. Majhi, S. Yadav & A. Sen Gupta, Design and Construction of a Helical Resonator for Delivering Radio Frequency to an Ion Trap, *MAPAN – Journal of Metrology Society of India*, DOI 10.1007/s12647-017-0209-5123 (2017).
- [106] S. Panja, S. De, S. Yadav, and A. Sen Gupta, Measuring capacitance and inductance of a helical resonator and improving its quality factor by mutual inductance alteration, *Rev. Sci. Instrum.* **86**, 056104 (2015).

- [107] R. G. Medhurst, H. F. Resistance and Self-Capacitance of Single Layer Solenoids, *Wireless Engineer* **24**, 80 (1947).
- [108] D. Knight, The self-resonance and self-capacitance of solenoid coils: applicable theory, models and calculation methods, *G3YNH info* DOI 10.13140/RG.2.1.1472.0887 (2016).
- [109] D. C. Roper, & L. J. Briggs, Radio Instruments and Measurements, *Bureau of Standards circular C74, U. S. Government Printing Office , Washington, D. C. , 252* (1937).
- [110] A. N. Payne, The HF Resistance of Single Layer Solenoids. <http://g3rbj.co.uk/wp-content/uploads/2013/08/The-HF-Resistance-of-Single-Layer-Solenoids2.pdf>.
- [111] A. N. Payne, The ac Resistance of Rectangular Conductors. <http://g3rbj.co.uk/wp-content/uploads/2017/06/The-ac-Resistance-of-Rectangular-Conductors-PayneIssue3.pdf>.
- [112] M. Doležal, *et al.*, Analysis of thermal radiation in ion traps for optical frequency standards, *Metrologia* **52**, 842 (2015).
- [113] J. Keller, T. Burgermeister, D. Kalincev, J. Kiethe, & T. E. Mehlstäubler, Evaluation of trap-induced systematic frequency shifts for a multi-ion optical clock at the 10^{-19} level, *J. Phys. Conf. Ser.* **723**, 012027 (2016).
- [114] P. Zhang, *et al.*, Evaluation of blackbody radiation shift with temperature-associated fractional uncertainty at 10^{-18} level for ${}_{40}\text{Ca}^+$ ion optical clock, *J. Appl. Phys. B* **50**, 015002 (2016).
- [115] A. Roy, S. De, Bindiya Arora, & B. K. Sahoo, Accurate determination of blackbody radiation shift, magic and tune-out wavelengths for the ${}^6\text{S}_{1/2} \rightarrow {}^5\text{D}_{3/2}$ clock transition in Yb^+ , *J. Appl. Phys. B* **50**, 205201 (2017).
- [116] J. W. Farley, & W. H. Wing, Accurate calculation of dynamic Stark shifts and depopulation rates of Rydberg energy levels induced by blackbody radiation, Hydrogen, helium and alkali-metal atoms, *Phys. Rev. A* **23**, 2397 (1981).
- [117] C. F. A. Baynham, *et al.*, Measurement of differential polarizabilities at a mid-infrared wavelength in ${}^{171}\text{Yb}^+$, Preprint at arXiv:1801.10134v2 (2018).
- [118] M. O. Krause, Th. A. Carlson, and R R. Woodruff, Angular distribution of photoelectrons of Xe 5p spin-orbit components between 20 and 105 eV, *Phys. Rev. A* **24**, 1374 (1981).

- [119] C. Dzionk, W. Fiedler, M. V. Liicke, and P. Zimmermann, Photoion Spectroscopy in the 4d Giant Resonances of the Lanthanides, *Phys. Rev. Lett.* **62**, 878 (1989).
- [120] C. Dzionk, W. Fiedler, M. V. Liicke, and P. Zimmermann, Photoion yield spectra of the lanthanides in the region of the 5p excitation: The elements Gd, Tb, Dy, Ho, Er, Tm, and Yb, *Phys. Rev. A* **41**, 3572 (1990).
- [121] S. Aksela, M. Harkoma, M. Pahjola, and H. Aksela, $N_{6,7}O_{4,5}O_{4,5}$ Auger spectrum of free Au atoms, *J. Phys. B* **17**, 2227 (1984).
- [122] E. Forrest, G. K. James, K. J. Ross, and M. Wilson, An experimental and theoretical study of the ejected-electron spectrum of Sn I and Sn II autoionising levels between 0 and 20 eV resulting from 20-1000 eV electron impact excitation, *J. Phys. B* **18**, 3123 (1985).
- [123] J. P. Gordon, H. J. Zeiger, and C. H. Townes, The Maser—New Type of Microwave Amplifier, Frequency Standard, and Spectrometer, *Phys. Rev.* **99**, 1264 (1955).
- [124] S. Stellmer, M. K. Tey, B. Huang, R. Grimm, and F. Schreck, Bose-Einstein Condensation of Strontium, *Phys. Rev. Lett.* **103**, 200401 (2009).
- [125] M. Schioppo, N. Poli, M. Prevedelli, St. Falke, Ch. Lisdat, U. Sterr, and G. M. Tino, A compact and efficient strontium oven for laser-cooling experiments, *Rev. Sci. Instrum.* **83**, 103101 (2012).
- [126] R. Senaratne, S. V. Rajagopal, Z. A. Geiger, K. M. Fujiwara, V. Lebedev, and D. M. Weld, Effusive atomic oven nozzle design using an aligned microcapillary array, *Rev. Sci. Instrum.* **86**, 023105 (2015).
- [127] S. H. W. Wouters, G. Haaf, P. H. A. Mutsaers, and Edgar J. D. Vredenburg, Design and experimental validation of a compact collimated Knudsen source, *Rev. Sci. Instrum.* **87**, 083305 (2016).
- [128] S. C. Bell, M. Junker, M. Jasperse, L. D. Turner, Y.-J. Lin, I. B. Spielman, and R. E. Scholten, A slow atom source using a collimated effusive oven and a single-layer variable pitch coil Zeeman slower, *Rev. Sci. Instrum.* **81**, 013105 (2010).
- [129] A. J. Murray, M. J. Hussey, and M. Needham, Design and characterization of an atomic beam source with narrow angular divergence for alkali-earth targets, *Meas. Sci. Technol.* **17**, 3094-3101 (2006).
- [130] W. DeGraffenreid, J. R. Serrano, Y. M. Liu, and J. Weiner, Continuous, dense, highly collimated sodium beam, *Rev. Sci. Instrum.* **71**, 3668 (2000).

- [131] H. Lew, in *Methods of Experimental Physics*, edited by V. W. Hughes and H. L. Schultz (Academic, New York, 1967), Vol. 4A, p. 155.
- [132] P. Kusch and V. W. Hughes, in *Handbuch der Physik*, edited by Fliigge (Springer, Berlin, 1959), Vol. 37, p. 1.
- [133] L V. Hertel and K. J. Ross, An atomic beam oven with very low associated magnetic field, *J. Sci. Instrum.* **1**, 1245 (1968).
- [134] K. J. Ross and B. Sonntag, High temperature metal atom beam sources, *Rev. Sci. Instrum.* **66**, 4409 (1995).
- [135] D. M. P. Holland, K. Codling, and R. N. Chamberlain, Double ionisation in the region of the 5p thresholds of Ba and Yb, *J. Phys. B* **14**, 839 (1981).
- [136] C. Vishwakarma, J. Mangaonkar, K. Patel, G. Verma, S. Sarkar, U. D. Rapol, A simple atomic beam oven with a metal thermal break, *Rev. Sci. Instrum.* **90**, 053106 (2019).
- [137] J. G. Ring and J. R. Zacharias, Some New Applications and Techniques of Molecular Beams, *Adv. Electron. Electron. Phys.* **8**, 1 (1956).
- [138] U. Becker, in *X-Ray and Inner Shell Physics*, edited by Th. A. Carlson. M. O. Krause and S. T. Manson (AJP Conf. Proc.,1990), Vol. 125, p. 621.
- [139] P. H. Kobrin, U. Becker, S. Southworth, C. M. Truesdale, D. W. Lindle, and D. A. Shirley, Autoionizing resonance profiles in the photoelectron spectra of atomic cadmium, *Phys. Rev. A* **26**, 842 (1982).
- [140] A. Hausmann, B. Kimmerling, H. Kossmann, and V. Schmidt, New approach for a perfect experiment: 2p photoionization in atomic magnesium, *Phys. Rev. Lett.* **23**, 2669 (1988).
- [141] H. C. W. Beijerinck and N. F. Verster, Velocity distribution and angular distribution of molecular beams from multichannel arrays, *J. App. Phys.* **46**, 2083 (1975).
- [142] D. R. Olander and V. R. Kruger, Molecular Beam Sources Fabricated from Multichannel Arrays. III. The Exit Density Problem, *J. App. Phys.* **41**, 2769 (1970).
- [143] N. Cooper, E. D. Ros, J. Nute, D. Baldolini, P. Jouve, L. Hackermüller, M. Langer, Collimated dual species oven source and its characterisation via spatially resolved fluorescence spectroscopy, *J. Phys. D: Appl. Phys.* **51**, 105602 (2018).
- [144] M. Richter, M. Meyer, M. Pahler, T. Prescher, E. V. Raven, B. Sonntag, and H. E. Wetzal, Experimental study of atomic 4d giant resonances by photoabsorption and photoelectron spectroscopy: Ba, La, and Ce, *Phys. Rev. A* **39**, 5666 (1989).

- [145] Bulgin, J. Dyke, J. Goodfellow, N. Jonathan, E. Lee, and A. J. Morris, A high temperature furnace for use in photoelectron spectroscopy, *Electron Spectrosc.* **12**, 67 (1977).
- [146] P. R. Willmott and J. R. Huber, Pulsed laser vaporization and deposition, *Rev. Mod. Phys.* **72(1)**, 315–328 (2000).
- [147] R. D. Knight, Storage of ions from laser produced plasmas, *Appl. Phys. Lett.* **38(4)**, 221–223 (1981).
- [148] R.E. Drullinger, D.J. Glaze, and D.B. Sullivan, A Recirculating Oven for Atomic Beam Frequency Standards in *Proceedings of the 39th Annual Symposium on Frequency Control*, (USA, 1985), p. 13.
- [149] W. M. I. M. E. Poitzsch, J. C. Bergquist and D. J. Wineland, Cryogenic linear ion trap for accurate spectroscopy, *Rev. Sci. Instrum.* **67**, 129 (1996).
- [150] A. D. Ludlow, M. M. Boyd, J. Ye, and P. O. Schmidt, Optical atomic clocks, *Rev. Mod. Phys.* **87**, 637 (2015).
- [151] P. Clausing, Über die Strahlformung bei der Molekularströmung, *Z. Phys.* **66**, 471 (1930).
- [152] B. B. Dayton, in *1956 National Vacuum Technology Transactions*, edited by E. Perry and J. Durant (Pergamon, London, 1957).
- [153] J. A. Giordmaine and T. C. Wang, Molecular Beam Formation by Long Parallel Tubes, *J. App. Phys.* **31**, 463 (1960).
- [154] R. H. Jones, D. R. Olander, and V. R. Kruger, Molecular-Beam Sources Fabricated from Multichannel Arrays. I. Angular Distributions and Peaking Factors, *J. App. Phys.* **40**, 4641 (1969).
- [155] D. R. Olander, Molecular-Beam Sources Fabricated from Multichannel Arrays. II. Effect of Source Size and Alignment, *J. Appl. Phys.* **40**, 4650 (1969).
- [156] D. R. Olander, R. H. Jones, and W. J. Siekhaus, Molecular Beam Sources Fabricated from Multichannel Arrays. IV. Speed Distribution in the Centerline Beam, *J. Appl. Phys.* **41**, 4388 (1970).
- [157] W. J. Siekhaus, R. H. Jones, and D. R. Olander, Molecular Beam Sources Fabricated from Multichannel Arrays. V. Measurement of the Speed Distribution, *J. Appl. Phys.* **41**, 4392 (1970).
- [158] P. Krasuski, Angular distribution of flux at the exit of cylindrical tubes, *J. Vac. Sci. Technol. A* **5**, 2488 (1987).

- [159] D. Halwidl, *Development of an Effusive Molecular Beam Apparatus* (Springer Spektrum, Wiesbaden, 2016), Chap. 1, p. 5
- [160] D. O. Sabulsky, Ph. D. Thesis, The University of Chicago, (2014).
- [161] D. E. Kuhl and R. G. Tobin, On the design of capillary and effusive gas dosers for surface science, *Rev. of Sci. Instrum.* **66**, 3016 (1995).
- [162] A. Roy, S. De, B. Arora, and B. K. Sahoo, Accurate determination of black-body radiation shift, magic and tune-out wavelengths for the ${}^6\text{S}_{1/2} \rightarrow {}^5\text{D}_{3/2}$ clock transition in Yb^+ , *J. Phys. B* **50**, 205201 (2017).
- [163] S. De, N. Batra, S. Chakraborty, S. Panja, and A. Sen Gupta, Design of an ion trap for trapping single ${}^{171}\text{Yb}^+$, *Curr. Sci.* **106**, 1348 (2014).
- [164] N. Batra, S. Panja, S. De, A. Roy, S. Majhi, S. Yadav, and A. Sen Gupta, Design and Construction of a Helical Resonator for Delivering Radio Frequency to an Ion Trap, *MAPAN- J. Met. Soc. India* **32**, 193 (2017).
- [165] L. Sharma, A. Roy, S. Panja, V. N. Ojha, and S. De, Estimation of the ion-trap assisted electrical loads and resulting BBR shift, *Sci. Rep.* **8**, 16884 (2018).
- [166] K. J. Stout, L. Blunt, *Three-Dimensional Surface Topography 2nd ed.* (Penton Press, 2000), Chap 2, p. 22..
- [167] E. R. Amstalden van Hove, D. F. Smith, & R. M. A. Heeren, A concise review of mass spectrometry imaging, *J. Chromatogr. A.* **1217**, 3946 (2010).
- [168] A. D. Feenstra, M. E. Dueñas, & Y. J. Lee, Five Micron High Resolution MALDI Mass Spectrometry Imaging with Simple, Interchangeable, Multi-Resolution Optical System, *J. Am. Soc. Mass Spectrom.* **28**, 434 (2017).
- [169] P. W. H. Pinkse, T. Fischer, P. Maunz, & P. Rempe, Trapping an atom with single photons, *Nature* **404**, 365 (2000).
- [170] A. Boca, *et al.*, Observation of the Vacuum Rabi Spectrum for One Trapped Atom, *Phys. Rev. Lett.* **93**, 233603 (2004).
- [171] J. Volz, *et al.*, Observation of Entanglement of a Single Photon with a Trapped Atom, *Phys. Rev. Lett.* **96**, 030404 (2006).
- [172] N. Fortson, Possibility of measuring parity nonconservation with a single trapped atomic ion, *Phy. Rev. Lett.* **70**, 2383 (1993).
- [173] B. B. Blinov, D. L. Moehring, L. M. Duan, & C. Monroe, Observation of entanglement between a single trapped atom and a single photon, *Nature* **428**, 153 (2004).

- [174] N. Huntemann, C. Sanner, B. Lipphardt, C. Tamm, & E. Peik, Single-Ion Atomic Clock with 3×10^{-18} Systematic Uncertainty, *Phys. Rev. Lett.* **116**, 063001 (2016).
- [175] S. M. Brewer, *et al.*, $^{27}\text{Al}^+$ Quantum-Logic Clock with a Systematic Uncertainty below 10^{-18} , *Phys. Rev. Lett.* **123**, 033201 (2019).
- [176] G. Shu, N. Kurz, M. R. Dietrich, & B. B. Blinov, Efficient fluorescence collection from trapped ions with an integrated spherical mirror, *Phys. Rev. A* **81**, 042321 (2010).
- [177] D. Kielpinski, C. Monroe, & D. J. Wineland, Architecture for a large-scale ion-trap quantum computer, *Nature* **417**, 709 (2002).
- [178] D. Leibfried, R. Blatt, C. Monroe, & D. J. Wineland, Quantum dynamics of single trapped ions, *Rev. Mod. Phys.* **75**, 281 (2003).
- [179] E. W. Streed, B. G. Norton, A. Jechow, T. J. Weinhold, & D. Kielpinski, Imaging of Trapped Ions with a Microfabricated Optic for Quantum Information Processing, *Phys. Rev. Lett.* **106**, 010502 (2011).
- [180] G. S. Agarwal, G. O. Ariunbold, J. von Zanthier, & H. Walther, Nonclassical imaging for a quantum search of trapped ions, *Phys. Rev. A* **70**, 063816 (2004).
- [181] J. D. Wong-Campos, K. G. Johnson, B. Neyenhuis, J. Mizrahi, & C. Monroe, High-resolution adaptive imaging of a single atom, *Nat. Photonics* **10**, 606 (2016).
- [182] K. A. Landsman, Verified quantum information scrambling, *Nature* **567**, 61 (2019).
- [183] K. Wright *et al.*, Benchmarking an 11-qubit quantum computer, *Nat. Commun.* **10**, 5464 (2019).
- [184] R. Raussendorf, & H. J. Briegel, A One-Way Quantum Computer, *Phys. Rev. Lett.* **86**, 5188 (2001).
- [185] R. N. Palmer, C. Moura Alves, & D. Jaksch, Detection and characterization of multipartite entanglement in optical lattices, *Phys. Rev. A* **72**, 042335 (2005).
- [186] J. Cho, Addressing Individual Atoms in Optical Lattices with Standing-Wave Driving Fields, *Phys. Rev. Lett.* **99**, 020502 (2007).
- [187] A. V. Gorshkov, L. Jiang, M. Greiner, P. Zoller, & M. D. Lukin, Coherent Quantum Optical Control with Subwavelength Resolution, *Phys. Rev. Lett.* **100**, 093005 (2008).
- [188] K. D. Nelson, X. Li, & D. S. Weiss, Imaging single atoms in a three-dimensional array, *Nature Phys.* **3**, 556 (2007).

- [189] T. Gericke, P. Würtz, D. Reitz, T. Langen, & H. Ott, High-resolution scanning electron microscopy of an ultracold quantum gas, *Nature Phys.* **4**, 949 (2008).
- [190] W. Alt, An objective lens for efficient fluorescence detection of single atoms, *Optik* **113**, 142 (2002).
- [191] Y. R. P. Sortais, *et al.*, Diffraction-limited optics for single-atom manipulation, *Phys. Rev. A* **75**, 013406 (2007).
- [192] M. Karski, Nearest-Neighbor Detection of Atoms in a 1D Optical Lattice by Fluorescence Imaging, *Phys. Rev. Lett.* **102**, 053001 (2009).
- [193] W. S. Bakr, J. I. Gillen, A. Peng, S. Fölling, & M. Greiner, A quantum gas microscope for detecting single atoms in a Hubbard-regime optical lattice, *Nature* **462**, 74 (2009).
- [194] S. Hu, K. Maslo, & L. V. Wang, Second-generation optical-resolution photoacoustic microscopy with improved sensitivity and speed, *Opt. Lett.* **36**, 1371 (2011).
- [195] R. G. González-Acuña, & H. A. Chaparro-Romo, General formula for bi-aspheric singlet lens design free of spherical aberration, *App. Optics* **57**, 9341 (2018).
- [196] W. J. Smith, *Modern Optical Engineering* (McGraw-Hill, 2008).
- [197] J. C. Wyant, & K. Creath, *Applied Optics and Optical Engineering* (Academic press Inc, 1992).
- [198] I. Gris-Sánchez, D. Van Ras, & T. A. Birks, The Airy fiber: an optical fiber that guides light diffracted by a circular aperture, *Optica* **3**, 270 (2016).
- [199] A. Miks, & J. Novak, Point spread function of an optical system with defocus and spherical aberration — analytical formulas, *App. Optics* **58**, 5823 (2019).
- [200] OSLO Premium Edition, Revision 7.0.2, Copyright[®] 2001 - 2017 Lambda Research Corporation, <http://www.lambdares.com/wp-content/uploads/support/oslo/osloedu/oslouserguide>.
- [201] K. Strehl, Aplanatische und fehlerhafte Abbildung im Fernrohr, *Z. Instrumentenkunde* **15**, 362 (1895).
- [202] K. Strehl, Ueber Luftschlieren und Zoenfehler, *Z. Instrumentenkunde* **22**, 213 (1902).
- [203] V. N. Mahajan, Strehl ratio for primary aberrations: some analytical results for circular and annular pupils, *J. Opt. Soc. Am.* **72**, 1258 (1982).

- [204] V. N. Mahajan, Strehl ratio for primary aberrations in terms of their aberration variance, *J. Opt. Soc. Am.* **73**, 860 (1983).
- [205] Maréchal, A. Study of the combined effects of diffraction and geometrical aberrations on the image of a luminous point, *Rev. Opt. Theor. Instrum.* **26**, 257 (1947).
- [206] D. F. V. James, Quantum dynamics of cold trapped ions with application to quantum computation, *Appl. Phys. B* **66**, 181 (1998).
- [207] A. Rastogi *et al.* Design of the Ion Trap and Vacuum System for ^{171}Yb -ion Optical Frequency Standard, *MAPAN- J. Met. Soc. India* **30**, 169 (2015).
- [208] <https://www.photometrics.com/learn/imaging-topics/matching-resolution>
- [209] H. Gross, H. Zügge, M. Peschka, & F. Blechinger, *Handbook of Optical Systems, Aberration Theory and Correction of Optical Systems* (Wiley-VCH, 2015), pp. 1–756.
- [210] M. S. Herbane, H. Berriche, A. A. El-hady, G. Al Shahrani, G. Band, X. Fléchardd, and E. Liénard, Simulation of ion behavior in an open three-dimensional Paul trap using a power series method, *Nucl. Instrum. Methods in Phys. Res. A* **751**, 11 (2014).
- [211] M. S. Herbane, Minimized computational time method for the dynamics of ions trapped in an ideal quadrupole ion trap, *Int. J. Mass Spectrometry* **303**, 73 (2011).
- [212] S. Knünz, M. Herrmann, V. Batteiger, G. Saathoff, T. W. Hänsch, and Th. Udem, Sub-millikelvin spatial thermometry of a single Doppler-cooled ion in a Paul trap, *Phys. Rev. A* **85**, 023427 (2012).
- [213] B. Srivathsan, M. Fischer, L. Alber, M. Weber, M. Sondermann, and G. Leuchs, Measuring the temperature and heating rate of a single ion by imaging, <https://arxiv.org/abs/1905.09011>.
- [214] B. G. Norton, E. W. Streed, M. J. Petراسiunas, A. Jechow, and D. Kielpinski, Millikelvin spatial thermometry of trapped ions, *New J. Phys.* **13**, 113022 (2011).
- [215] Daryl W. Preston, Doppler-free saturated absorption: Laser Spectroscopy, *Am. J. Phys.* **64**, 1432 (1996).
- [216] J. E. Debs, N. P. Robins, A. Lance, M. B. Kruger, and J. D. Close, Piezo-locking a diode laser with saturated absorption spectroscopy, *Applied Optics* **47**, 5163 (2008).
- [217] J. L. Hall, C. J. Bordé, and K. Uehara, Direct optical resolution of recoil effect using saturated absorption spectroscopy, *Phys. Rev. Lett.* **37**, 1339–1342 (1976).

- [218] J. Alnis, A. Matveev, N. Kolachevsky, T. Udem, and T. W. Hänsch, Subhertz linewidth diode lasers by stabilization to vibrationally and thermally compensated ultralow-expansion glass Fabry–Perot cavities, *Phys. Rev. A* **77**, 053809 (2008).
- [219] Peng Yang and Sheng Feng, Fabry–Perot cavity locking with phase-locked frequency-synthesized light, *Journal of the Optical Society of America B* **34**, 533–537 (2017).
- [220] N. Arias, L. J. González, V. Abediyeh, and E. Gomez, Frequency locking of multiple lasers to an optical cavity, *Journal of the Optical Society of America B* **35**, 2394–2398 (2018).
- [221] R. W. P. Drever, J. L. Hall, F. V. Kowalski, J. Hough, G. M. Ford, A. J. Munley, H. Ward, Laser phase and frequency stabilization using an optical resonator, *Appl. Phys. B* **31** (1983) 97–105.
- [222] E. D. Black, An introduction to Pound–Drever–Hall laser frequency stabilization, *Am. J. Phys.* **69**, 79–87 (2001).
- [223] Luc Couturier, Ingo Nosske, Fachao Hu, Canzhu Tan, Chang Qiao, Y. H. Jiang, Peng Chen, and Matthias Weidemüller, Laser frequency stabilization using a commercial wavelength meter, *Rev. Sci. Instrum.* **89**, 043103 (2018).
- [224] Khaldoun Saleh, Jacques Millo, Alexandre Didier, Yann Kersale, and Clement Lacroute, Frequency stability of a wavelength meter and applications to laser frequency stabilization, *Appl. Opt.* **32**, 9446–9449 (2015).
- [225] S. Kobtsev, S. Kandrushin, and A. Potekhin, Long-term frequency stabilization of a continuous-wave tunable laser with the help of a precision wavelengthmeter, *Appl. Opt.* **46**, 5840–5843 (2007).
- [226] C. Guo, M. Favier, N. Galland, V. Cambier, H. Álvarez-Martínez, M. Lours, L. De Sarlo, M. Andia, R. Le Targat, and S. Bize, Accurate laser frequency locking to optical frequency combs under low-signal-to-noise-ratio conditions, *Rev. Sci. Instrum.* **91**, 033202 (2020).
- [227] T. Fordell, A. E. Wallin, T. Lindvall, M. Vainio, and M. Merimaa, Frequency comb-referenced tunable diode laser spectroscopy and laser stabilization applied to laser cooling, *Appl. Opt.* **53**, 7476–7482 (2014).
- [228] E. Biemont, J. F. Dutrieux, I. I. Martin, and P. Quinet, Lifetime Calculations in Yb II, *J. Phys. B: At. Mol. Opt. Phys.* **31**, 3321 (1998).
- [229] J. Cariou and P. Luc. Atlas du spectre d’absorption de la molécule d’iode 21100 cm^{-1} - 23800 cm^{-1} 1980.

- [230] S. Gerstenkorn and P. Luc. Atlas du spectre d'absorption de la molécule d'iode 15600 cm^{-1} - 17600 cm^{-1} 1977.
- [231] S. Gerstenkorn and P. Luc. Atlas du spectre d'absorption de la molécule d'iode 17500 cm^{-1} - 20000 cm^{-1} 1977.
- [232] S. Gerstenkorn and P. Luc. Atlas du spectre d'absorption de la molécule d'iode 14000 cm^{-1} - 15600 cm^{-1} 1978.
- [233] S. Gerstenkorn and P. Luc. Atlas du spectre d'absorption de la molécule d'iode 19700 cm^{-1} - 20035 cm^{-1} 1983.
- [234] S. Gerstenkorn and J. Verges. Atlas du spectre d'absorption de la molécule d'iode 7220 cm^{-1} - 11200 cm^{-1} 1982.
- [235] G. Herzberg. Molecular Spectra and Molecular Structure I. Spectra of Diatomic Molecules. D. Van Nostrand Company, Inc., 2nd edition, 1950.
- [236] S. Olmschenk, K. Younge, D. Moehring, D. Matsukevich, P. Maunz, and C. Monroe, Manipulation and detection of a trapped Yb^+ hyperfine qubit, *Phys. Rev. A* **76**, 052314 (2007).
- [237] J. H. Shirley, Modulation transfer processes in optical heterodyne saturation spectroscopy, *Opt. Lett.* 1982 (11) 540.
- [238] E. Jaatinen and N. Brown, Sequential frequency locking of three He-Ne lasers with an external iodine stabilizer, *Metrologia* 1997 34 309.
- [239] E. Jaatinen and J. M. Chartier Possible influence of residual amplitude modulation when using modulation transfer with iodine transitions at 543 nm, *Metrologia* 1998 35 75
- [240] D. McCarron, S. King, and S. Cornish, Modulation transfer spectroscopy in atomic rubidium, *Meas. Sci. Technol.* 19 (2008).
- [241] W. Demtröder. Laser Spectroscopy. Springer-Verlag, 3rd edition, 2002.
- [242] H. Knöckel, B. Bodermann, E. Tiemann, High precision description of the rovibronic structure of the I_2 B - X spectrum, *Eur. Phys. J. D* **28**, 199 (2004).
- [243] <https://www.researchgate.net/deref/http://www.iqo.uni-hannover.de>
- [244] F. Martin, R. Bacis, S. Churassy, J. Vergés, Laser-induced-fluorescence Fourier transform spectrometry of the X0^+_g state of I_2 : Extensive analysis of the B0^+_u - X0^+_g fluorescence spectrum of $^{127}\text{I}_2$, *J. Mol. Spectr.* **116**, 71 (1986)

- [245] D. Cerny, R. Bacis, J. Vergés, Laser-induced-fluorescence Fourier transform spectrometry of the $X0^+_g$ state of I_2 : Extensive analysis of the $B0^+_u - X0^+_g$ fluorescence spectrum of ^{127}I , ^{129}I and $^{129}I_2$, *J. Mol. Spectr.* **116**, 458 (1986).
- [246] H. Bodermann, E. Knöckel, E. Tiemann, Widely usable interpolation formulae for hyperfine splittings in the $^{127}I_2$ spectrum *Eur. Phys. J. D* **19**, 31 (2002).
- [247] B. Bodermann, Thesis, Universitat Hannover, 1998.
- [248] E.J. Salumbides, K.S.E. Eikema, W. Ubachs, U. Hollenstein, H. Knöckel, E. Tiemann, The hyperfine structure of $^{129}I_2$ and ^{127}I ^{129}I in the $B^3\Pi_{0u^+} - X^1\Sigma^+_g$ band system, *Mol. Phys.* **104**, 2641 (2006).
- [249] E.J. Salumbides, K.S.E. Eikema, W. Ubachs, U. Hollenstein, H. Knöckel, E. Tiemann, Improved potentials and Born-Oppenheimer corrections by new measurements of transitions of $^{129}I_2$ and ^{127}I ^{129}I in the $B^3\Pi_{0u^+} - X^1\Sigma^+_g$ band system, *Eur. Phys. J. D* **47**, 171 (2008).
- [250] C. Tamm, N. Huntemann, B. Lipphardt, V. Gerginov, N. Nemitz, M. Kazda, S. Weyers and E. Peik, Cs-based optical frequency measurement using cross-linked optical and microwave oscillators, *Phys. Rev. A - At. Mol. Opt. Phys.* **89**, 023820 (2014).
- [251] N. Huntemann, C. Sanner, B. Lipphardt, C. Tamm and E. Peik, Single-Ion Atomic Clock with 3×10^{-18} Systematic Uncertainty, *Phys. Rev. Lett.* **116**, 063001 (2016).
- [252] N. Hinkley, J. A. Sherman, N. B. Phillips, M. Schioppo, N. D. Lemke, K. Beloy, M. Pizzocaro, C. W. Oates and A. D. Ludlow, An Atomic Clock with 10^{-18} Instability, *Science* **341**, 1215 (2013).
- [253] N. Huntemann, C. Sanner, B. Lipphardt, C. Tamm and E. Peik, Single-Ion Atomic Clock with 39×10^{-18} Systematic Uncertainty, *Phys. Rev. Lett.* **116**, 063001 (2016).
- [254] K. Kim, M.-S. Chang, S. Korenblit, R. Islam, E. E. Edwards, J. K. Freericks, G.-D. Lin, L.-M. Duan, and C. Monroe, Quantum simulation of frustrated Ising spins with trapped ions, *Nature* **465**, 590 (2010).
- [255] N. Timoney, I. Baumgart, M. Johanning, A. F. Varon, M. B. Plenio, A. Retzker, and C. Wunderlich, Quantum Gates and Memory using Microwave Dressed States, *Nature* **476**, 185 (2011).
- [256] V. Natarajan, Proposed search for an electric-dipole moment using laser-cooled ^{171}Yb atoms, *Eur. Phys. J. D* **32**, 33 (2005).

- [257] M. Roberts, P. Taylor, G. P. Barwood, W. R. C. Rowley, and P. Gill, Observation of the $^2S_{1/2}$ - $^2F_{7/2}$ electric octupole transition in a single $^{171}\text{Yb}^+$ ion, *Phys. Rev. A* **62**, 020501 (2000).
- [258] Oleg Kornienko, Peter T. A. Reilly, William B. Whitten, and J. Michael Ramsey, Electron impact ionization in a microion trap mass spectrometer, *Rev. Sci. Instrum.* **70**, 3907 (1999).
- [259] R. G. DeVoe and C. Kurtsiefer, Experimental study of anomalous heating and trap instabilities in a microscopic ^{137}Ba ion trap, *Phys. Rev. A* **65**, 063407 (2002).
- [260] A. Mortensen, J. J. T. Lindballe, I. S. Jensen, P. Staantum, D. Voigt, and M. Drewsen, Isotope shifts of the $4s^2^1S_0 \rightarrow 4s5p^1P_1$ transition and hyperfine splitting of the $4s5p^1P_1$ state in calcium, *Phys. Rev. A* **69**(4), 042502 (2004).
- [261] D. M. Lucas, A. Ramos, J. P. Home, M. J. McDonnell, S. Nakayama, J.-P. Stacey, S. C. Webster, D. N. Stacey, and A. M. Steane, Isotope-selective photoionization for calcium ion trapping, *Phys. Rev. A* **69**, 012711 (2004).
- [262] A. V. Steele, L. R. Churchill, P. F. Griffin, and M. S. Chapman, Photoionization and photoelectric loading of barium ion traps, *Phys. Rev. A* **75**, 053404 (2005).
- [263] A. Keil, H. Hernandez-Soto, R. J. Noll, M. Fico, L. Gao, Z. Ouyang, and R. G. Cooks, Monitoring of toxic compounds in air using a handheld rectilinear ion trap mass spectrometer, *Anal. Chem.* **80**, 734–741 (2008).
- [264] A.N. Vilkov, C.M. Gamage, A.S. Misharin, V.M. Doroshenko, D.A. Tolmachev, I.A. Tarasova, O.N. Kharybin, K.P. Novoselov, and M.V. Gorshkov, Atmospheric pressure ionization permanent magnet Fourier transform ion cyclotron resonance mass spectrometry, *J. Am. Soc. Mass Spectrom.* **18**, 1552–1558 (2007).
- [265] L. Deslauriers, M. Acton, B. B. Blinov, K. A. Brickman, P. C. Haljan, W. K. Hensinger *et al.*, Efficient photoionization loading of trapped ions with ultrafast pulses, *Phys. Rev. A* **74**, 063421 (2006).
- [266] D. N. Madsen, S. Balslev, M. Drewsen, N. Kjærgaard, Z. Videsen, and J. W. Thomsen, Measurements on photo-ionization of $3s3p^1P_1$ magnesium atoms, *J. Phys. B* **33**, 4981 (2000).
- [267] K. Hosaka, S. A. Webster, P. J. Blythe, A. Stannard, D. Beaton, H. S. Margolis, S. N. Lea, and P. Gill, Optical Frequency Standards and Clocks Based On Single Trapped Ions, *IEEE Trans. Instrum. Meas.* **54**, 759 (2005).

- [268] N. Kjærgaard, L. Hornekær, A. M. Thommesen, Z. Videsen, and M. Drewsen, Isotope selective loading of an ion trap using resonance-enhanced two-photon ionization, *Appl. Phys. B: Lasers Opt.* **71**, 207 (2000).
- [269] U. Tanaka, H. Matsunishi, I. Morita, and S. Urabe, Isotope-selective trapping of rare calcium ions using high-power incoherent light sources for the second step of photo-ionization, *Appl. Phys. B* **81**, 795 (2005).
- [270] S. K. Borisov, M. A. Kuz'mina, and V. A. Mishin, A Study of isotopically selective photoionization of Ytterbium atoms for laser isotope separation, *J. Russ. Laser Res.* **17**, 332-345 (1996).
- [271] M Sankari and M V Suryanarayana, Studies on the isotope selective photoionization of the low-abundant ^{168}Yb isotope, *J. Phys. B: At. Mol. Opt. Phys.* **31**, 261 (1998).
- [272] S. Gulde, D. Rotter, P. Barton, F. Schmidt-Kaler, R. Blatt & W. Hogervorst, Simple and efficient photo-ionization loading of ions for precision ion-trapping experiments, *Appl. Phys. B* **73**, 861-863 (2001).
- [273] M. Brownnutt, V. Letchumanan, G. Wilpers, R.C. Thompson, P. Gill & A.G. Sinclair, Controlled photoionization loading of $^{88}\text{Sr}^+$ for precision ion-trap experiments, *Appl. Phys. B* **87**, 411 (2007).
- [274] Hendrik M. Meyer, Matthias Steiner, Lothar Ratschbacher, Christoph Zipkes, and Michael Kohl, Laser spectroscopy and cooling of Yb^+ ions on a deep-UV transition, *Phys. Rev. A* **85**, 012502 (2012).
- [275] A. Ashkin, J. M. Dziedzic, J. E. Bjorkholm, & S. Chu, Observation of a single beam gradientforce optical trap for dielectric partices, *Opt. Lett.* **11**, 288–290 (1976).
- [276] Julian Schmidt, Alexander Lambrecht, Pascal Weckesser, Markus Debatin, Leon Karpa, and Tobias Schaetz, Optical Trapping of Ion Coulomb Crystals, *Phys. Rev. X* **8**, 021028 (2018).
- [277] W. D. Phillips, Laser cooling and trapping of neutral atoms, Nobel Lecture: Laser cooling and trapping of neutral atoms, *Rev. Mod. Phys.* **70**, 721 (1998).
- [278] Timo A. Nieminen, Trapping Ions, *Nat. Photonics* **4**, 737 (2010).
- [279] M. Sankari and M. V. Suryanarayana, Effect of ^{87}Sr hyperfine structure on the isotope selective excitation of ^{89}Sr and ^{90}Sr isotopes in collinear resonance ionization spectroscopy, *J. Phys. B: At. Mol. Opt. Phys.* **35**, 983–995 (2002).
- [280] Y. A. Kudriavtsev and V. S. Letokhov, *Appl. Phys. B* **29**, 219 (1982).

- [281] L. Monz, R. Hohmann, H. J. Kluge *et al.*, Fast, low-level detection of strontium-90 and strontium-89 in environmental samples by collinear resonance ionization spectroscopy, *Spectrochim. Acta* **48**, 1655–1671 (1993).

ABSTRACT

Name of the Student: Lakhi Sharma

Registration No. : 10PP16A32021

Faculty of Study: Physical Sciences

Year of Submission: 2021

AcSIR academic centre/CSIR Lab: CSIR - NPL

Name of the Supervisor(s): Dr. Subhasis Panja
Dr. Subhadeep De

Title of the thesis: Ion production and optical set-up for single Ytterbium ion trap experiment

The enrapturing field of trapped ions has paved the way to fundamental as well as application-based research in many arenas of physics such as high-precision measurements of fundamental constants, frequency metrology, quantum information, quantum optics, atomic spectroscopy, plasma physics, etc. Ion traps, development of laser stabilization techniques, invention of frequency combs etc. are some of the fantastic tools which emanated manipulation of individual ions. At CSIR – National Physical Laboratory, India, we are working on a single trapped, laser cooled Ytterbium-171 ion to develop an optical frequency standard – an ultraprecise time measuring device. Such a state-of-the-art experiment involves theoretical, experimental, technological challenges and a plethora of integrants for its accomplishment. This thesis expounds several such pre-requisites such as trap potential generation, atomic beam production and its subsequent ionization, laser frequency stabilization, trapped ion detection, systematic shifts calculation, etc. For delivering the desired amplitude and frequency via a resonator for creation of trap potential, various ion trap-resonator assembly assisted electrical loads are analytically and numerically calculated and experimentally verified. The Black Body Radiation (BBR) shift induced by the excess capacitive load arising due to machining inaccuracy in the radiofrequency (RF) carrying parts has been accurately estimated, which results to a fractional frequency shift of 6.6×10^{-17} for an RF of 1 kV at $2\pi \times 15$ MHz and with $\pm 10 \mu\text{m}$ machining inaccuracy. This needs to be considered in the total systematic uncertainty budget of a frequency standard as it is about an order of magnitude higher than the present reach of the trapped ion optical clocks. A low-divergent atomic oven is required in such precision metrology experiments to avoid atomic deposition on the ion trap, which leads to patch potential. Based on inhomogeneous thermal distribution along a capillary resulting due to its partial resistive heating, a dark wall atomic oven is thus

designed and developed using a seamless stainless-steel capillary heated by tungsten wire. The nearly collimated spatial distribution of the atoms resulting due to the absorber eliminating the atoms diverging above a certain angle is modeled and experimentally verified. A divergence as minimum as $1.2(1)^\circ$ corresponding to a half angle of $0.9(1)^\circ$ is measured at an oven temperature of 250°C that produces an atomic flux of about 8×10^9 atoms s^{-1} . For trapped ion's fluorescence detection, an imaging system has been designed that resolves particles separated by $\geq 0.68 \mu\text{m}$ with minimum aberrations, magnifies upto 238 times, recollects 77% photons within a solid angle of 0.36 sr, has a depth of field of $142 \mu\text{m}$ and a field of view of $56 \mu\text{m}$ which images a large ensemble of atoms and gives a diffraction limited performance over visible to near-infrared wavelengths. The frequency of External Cavity Diode Lasers (ECDL) used in the experiment drift over longer times owing to thermal and mechanical changes. The cooling laser is operated for a longer time and so its fundamental frequency at 739 nm is stabilized to one of the hyperfine transitions of R(78) (1-11) line of molecular iodine resolved via Saturated absorption spectroscopy. The short-term and long-term linewidths of the locked laser are measured to be $0.75(3)$ MHz and $0.5(2)$ MHz, respectively with a noise density of $1.8 \mu\text{V}/\sqrt{\text{Hz}}$ @ 4 kHz. For carrying out selective ionization of Yb-171 isotope, frequency corresponding to $^1\text{S}_0 \rightarrow ^1\text{P}_1$ transition is to be known for which fluorescence spectroscopy of neutral Yb atoms using 399 nm is carried out. The resonant frequency for exciting ^{171}Yb is measured 751527138 ± 60 MHz i.e., 398.91065 nm. It is further ionized, traces for which are found by detecting fluorescence corresponding to $^2\text{S}_{1/2} \rightarrow ^2\text{P}_{1/2}$ at 369.52602(3) nm. Thus, many building blocks of the experiment are worked upon within the scope of my doctoral thesis which contributes towards CSIR-NPL's mission mode project "Indigenous development of the state-of-the-art quantum standard of time".

List of publication(s) in SCI Journal(s) (published & accepted) emanating from the thesis work, with complete bibliographic details

1. **Lakhi Sharma**, A. Roy, S. Panja, V. N. Ojha and S. De, Estimation of the ion-trap assisted electrical loads and resulting BBR shift, *Scientific Reports* **8**, 16884 (2018).
2. **Lakhi Sharma**, A. Roy, S. Panja, and S. De, Atomic flux distribution from a low-divergent dark wall oven, *Review of Scientific Instruments* **90**, 053201 (2019).
3. **Lakhi Sharma**, H. Rathore, S. Utreja, Neelam, A. Roy, S. De, S. Panja, Optical Atomic Clocks for Redefining SI Units of Time and Frequency, *MAPAN* **35**, 531 (2020).
4. **Lakhi Sharma**, A. Roy, S. Panja, and S. De, An easy to construct sub-micron resolution imaging system, *Scientific Reports* **10**, 21796 (2020).

List of Papers with abstract presented (oral/poster) at national/international conferences/seminars with complete details

1. **Lakhi Sharma**, N. Batra, A. Roy, S. Majhi, S. Panja, V.N. Ojha and S. De, An Optimized Imaging System for Fluorescence Detection of a Single Ytterbium-ion, in 5th National Conference Proceedings on Advances in Metrology (AdMet), NorthCap University, Gurugram, March 2017.

Abstract

At CSIR-NPL, we are developing an optical frequency standard based on trapped and laser cooled single Ytterbium ion ($^{171}\text{Yb}^+$). The fluorescence emitted at 369.5 nm by the single Yb^+ will be detected. A high-resolution imaging system incorporated with a high numerical aperture (NA) fluorescence collection lens is required for that. In this paper, we present the preliminary design of the optical arrangement which shows diffraction limited performance for imaging single Yb^+ . The fluorescence collection lens is fixed inside of the vacuum vessel and is only ~ 23 mm away from the trapped ion position. This has NA of 0.48 and can collect fluorescence over a solid angle of 0.79 steradian. The objective giving a numerical aperture of 0.17 with effective focal length of 64.31 mm consists of three lenses out of which two are spherical lenses and the third one is an aspheric lens. This reduces spherical aberrations, coma, astigmatism and other wavefront errors. Using these off the shelf standard lenses we have achieved relatively high Strehl ratio of 0.98.

2. **Lakhi Sharma**, A. Roy, S. Panja, V. N. Ojha and S. De, Black Body Radiation Shift induced by Resistive Heating of an Ion Trap, in Proceedings of the 13th Asian International Seminar on Atomic and Molecular Physics, IIT Bombay, Mumbai, December 2018.

Abstract

At CSIR-National Physical Laboratory (NPL), the National Measurement Institute (NMI) of India, we are developing an optical frequency standard based on a laser cooled and singly trapped Ytterbium ion. The end-cap Paul type ion-trap which is indigenously designed and developed for this purpose requires a high voltage, narrow-band radio frequency (RF) for generation of the trapping potential. The ion-trap forms an LCR circuit which has impedance different from that of the RF source delivering the said potential. So, following the standard

technique of using a directional device after an RF source to avoid unwanted power reflection, a helical resonator is utilized. The intermediate resonator delivers the RF to the trap via inductive coupling. The resonant frequency and quality factor of the helical resonator that efficiently delivers high voltage RF to any electrodynamic ion-trap depends on its capacitive, resistive and inductive loads and are different at unloaded and loaded conditions. Hence, accurate estimation of the loads of the resonator as well as those of the parts that are attached to the resonator is a requisite for delivering desired radio frequency (RF) to the trap. We have identified different sources of these loads and estimated their values using analytical and finite element analysis methods, which are found to be well in agreement with the experimentally measured values. For our trap geometry, we obtained values of the effective inductive, capacitive and resistive loads as: 3.1 μH , 3.71 μH , 3.68(6) μH ; 50.4 pF, 51.4(7) pF, 40.7(2) pF; and 1.373 Ω , 1.273(3) Ω , 1.183(9) Ω by using analytical, numerical and experimental methods, respectively.

In particular to high precision frequency standard experiments like the trapped ion optical atomic clock, various systematic shifts arise which alters the measured clock frequency [4]; it is therefore important to determine these systematic shifts precisely in order to improve the accuracy of the realized frequency standard. One such dominant systematic shift is the Black Body Radiation (BBR) shift [4]. Estimation of the loads also lead to accurate estimation of the Black-Body Radiation (BBR) shift resulting from excess capacitance arising due to inaccurate machining of the ion-trap. We have estimated that for our trap, for an RF of 1 kV at $2\pi \times 15$ MHz and with ± 10 μm machining inaccuracy, the induced BBR shift results a fractional frequency shift of 6.6×10^{-17} .

3. **Lakhi Sharma**, A. Roy, S. Panja and S. De, Design and construction of a simple dark wall atomic oven, in Proceedings of the 10th International Conference for Advances in Metrology (AdMet), CSIR-NPL, New Delhi, February 2019.

Abstract

Many of the ion trapped experiments for various scientific investigations require low divergent atomic oven. Using a single capillary tube, we have developed a compact, easy to fabricate and inexpensive dark wall atomic oven working in the molecular flow regime, which gives narrow-divergent and less-intense atomic flux. Inhomogeneous thermal distribution along a capillary arises due to partial heating at one of the ends and an intermediate point of the capillary. Based on this, we have designed the oven which consists of a reservoir, collimator and cold absorber fabricated out of a single stainless-steel capillary, resistively heated by Tungsten wire. The absorber truncates the unwanted off divergent atoms above a certain truncation angle, thus giving narrowed beam divergence. Using finite element analysis method, the performance of the oven is studied for Ytterbium-171 which shows that with decreasing current, the effective absorber length increases which gives decreased output flow rates of atoms and decreased beam widths which has been confirmed experimentally too. A minimum divergence of 1.2° has been achieved by operating the oven at 250°C . The discussed oven retains directionality, gives less atomic concentration in the interaction region, is well apt for frequency standard experiments and can be utilized for other experimental species too.

4. **Lakhi Sharma**, A. Roy, S. Panja and S. De, Frequency stabilization of 739 nm diode laser using Doppler Free Spectroscopy of Molecular Iodine, in Proceedings of the 6th National Conference on “Advances in Metrology” (AdMet), New Delhi, January 2020.

Abstract

Frequency stabilization of laser light is essential in many atomic, molecular and optical physics experiments. At CSIR – National Physical Laboratory, New Delhi, we are engaged in developing a frequency standard based on the $|^2S_{1/2}, F = 0\rangle \rightarrow |^2F_{7/2}, F = 3\rangle$ electric octupole transition of a trapped Ytterbium ion ($^{171}\text{Yb}^+$) at 467 nm. This state-of-the-art precision experiment requires lasers at different frequencies which need to be stabilized with respect to a stable reference frequency. In this work, we discuss the stabilization of a 739 nm laser, the frequency doubled output of which serves for laser cooling the trapped ion at 369.5 nm. We are employing standard saturated absorption spectroscopy of molecular iodine (I_2) since it has a density of narrow absorption lines in the infrared region to be chosen as the reference frequency. Half the frequency of the cooling transition $^2S_{1/2} \rightarrow ^2P_{1/2}$ of $^{171}\text{Yb}^+$ with an offset of 10 GHz (using fibre based electro-optic modulator) corresponds to a hyperfine structure of the iodine absorption line (739.05 nm). The (B \rightarrow X) transition of I_2 involved in producing this line is scarce at room temperature and so the I_2 cell is heated to about 400 °C and counter propagating pump and probe beams with 9:1 power ratio are focused into the cell. For both the beams addressing the same velocity class atoms, a sharp peak (narrower than Doppler broadened profile) in the probe beam spectrum is observed as those atoms have already been saturated by the pump beam. As compared to the Doppler broadened width of ≈ 670 MHz, the Doppler free spectra obtained by this technique is of the order of a few MHz which is very less than the natural linewidth of cooling transition *i.e.*, 19.8 MHz. Once the Doppler free peak is achieved, the laser’s frequency can be locked at its peak using Pound-Drever Hall technique. Since, signal to noise ratio for Doppler free spectra at 739 nm is very low, we have also developed a balanced photo-detector to be used in the experiment.

5. **Lakhi Sharma**, A. Roy, S. Panja and S. De, Saturated Absorption Spectroscopy of Molecular Iodine for frequency stabilization of 739 nm laser, in Proceedings of the 8th Topical Conference on Atomic and Molecular Collisions for Plasma Applications, IIT Roorkee, March 2020.

Abstract

Frequency stabilization of lasers is essential in many atomic, molecular and optical physics experiments. Our experiment aims at developing a singly trapped, laser cooled Ytterbium ion ($^{171}\text{Yb}^+$) based optical frequency standard at 467 nm. Ion cooling is obtained by driving the $^2S_{1/2} \rightarrow ^2P_{1/2}$ transition using 369.5 nm (vc) beam which is obtained from a second harmonic generation (SHG) laser at fundamental frequency of 739 nm. Additionally, $\text{vc} + 2.1$ GHz and $\text{vc} + 14.7$ GHz are also used in the process. For probing the said transition, the 739 nm laser therefore has to be frequency stabilized which is done with respect to molecular iodine (I_2) reference. In this work, we discuss the saturated absorption spectroscopy (SAS) of I_2 for stabilization of the 739 nm ECDL laser. The SAS optical set-up is shown in Figure 1(a). On focusing counter-propagating pump and probe beams of power 10.6 mW and 1.5 mW respectively into a 30 cm long Iodine (I_2) vapor cell heated to 420 °C with a cold finger at 30 °C, and scanning the laser frequency from 405.65395 THz to 405.65518 THz, we obtain the molecular iodine Doppler free spectroscopy as shown in Figure 1(b). The pump beam double

passed through an 80 MHz AOM before entering the vapor cell. For effective detection of the weak signals, the pump is frequency modulated at 60 kHz using the AOM and the signal from the photodiode is demodulated using a Lock-in Amplifier. As can be seen, six Doppler free features are present in this region centered at 739.03475 nm, 739.03421 nm, 739.03394 nm, 739.03367 nm, 739.03341 nm and 739.03314 nm and they overlap well with their derivatives in the lock signal. The Full width at half maximum (FWHM) for these peaks are approximately 13 MHz, 24 MHz, 31 MHz, 17 MHz, 29 MHz and 16 MHz, respectively. As compared to the measured Doppler broadened width of ≈ 930 MHz at 420 °C, the Doppler free spectra obtained by this technique is of the order of a few tens of MHz. Using Pound- Drever Hall technique, the laser's frequency can be locked with respect to the Doppler free features 1, 4 or 6, which is in progress.

6. **Lakhi Sharma**, A. Roy, S. Panja and S. De, Diffraction Limited Optics Giving Sub-micron Resolution for Single Ion Imaging, in Proceedings of the Fundamental Sciences & Quantum Technologies using Atomic Systems (FSQT), Online mode, September 2020.

Abstract

At CSIR – National Physical Laboratory, India, we are developing an optical clock based on trapped and laser-cooled single Ytterbium ion ($^{171}\text{Yb}^+$). The single ion is monitored by detecting its fluorescence induced by the cooling laser at 369 nm. Detecting a low level of fluorescence emitted by a single ion necessitates a high resolution, diffraction limited imaging system with a good collection efficiency. We therefore report the design of an imaging system built from off-the-shelf optics; optimizations of various parameters for its best performance is done using Optics Software for Layout and Optimization (OSLO). From the several studied choices for objectives and magnifiers, the best designed imaging system consists of three aspheres, an achromat and an aberration corrector plate. The collection lens is a 1” diameter asphere of focal length 40 mm, having a collection efficiency of 2.7 % and covering a solid angle of 0.34 sr. It is followed by an asphere and achromat, which collectively gives a numerical aperture of 0.32 and can resolve ions separated by $\geq 0.7 \mu\text{m}$; the magnifier consisting of a wavefront corrector plate and an Asphere. The diffraction limited optics with a Strehl ratio (SR) of 0.87 is able to recollect 73% photons, produces images upto a magnification of $\times 65$ and has a transverse spherical aberration of 0.06 mm. The system has a depth of focus of $\pm 60 \mu\text{m}$ and a field of view of $\pm 20 \mu\text{m}$ which facilitates to readout over a large ensemble of atoms. With manufacturing tolerances, the SR reduces to 0.81, which still satisfies the Maréchal's criterion. The lens system is advantageous from the viewpoint that it gives a favorable performance at different wavelengths covering from visible to near infrared region; thus it can be adapted in other applications as well where high resolution imaging system is an indispensable requirement.

SCIENTIFIC REPORTS

OPEN

Estimation of the ion-trap assisted electrical loads and resulting BBR shift

Lakhi Sharma^{1,2}, A. Roy^{1,2}, S. Panja^{1,2}, V. N. Ojha^{1,2} & S. De^{1,2}

Capacitive, inductive and resistive loads of an ion-trap system, which can be modelled as LCR circuits, are important to know for building a high accuracy experiment. Accurate estimation of these loads is necessary for delivering the desired radio frequency (RF) signal to an ion trap via an RF resonator. Of particular relevance to the trapped ion optical atomic clock, determination of these loads lead to accurate evaluation of the Black-Body Radiation (BBR) shift resulting from the inaccurate machining of the ion-trap itself. We have identified different sources of these loads and estimated their values using analytical and finite element analysis methods, which are found to be well in agreement with the experimentally measured values. For our trap geometry, we obtained values of the effective inductive, capacitive and resistive loads as: 3.1 μH , 3.71 (1) μH , 3.68 (6) μH ; 50.4 pF, 51.4 (7) pF, 40.7 (2) pF; and 1.373 Ω , 1.273 (3) Ω , 1.183 (9) Ω by using analytical, numerical and experimental methods, respectively. The BBR shift induced by the excess capacitive load arising due to machining inaccuracy in the RF carrying parts has been accurately estimated, which results to a fractional frequency shift of 6.6×10^{-17} for an RF of 1 kV at $2\pi \times 15$ MHz and with $\pm 10 \mu\text{m}$ machining inaccuracy. This needs to be incorporated into the total systematic uncertainty budget of a frequency standard as it is about one order of magnitude higher than the present precision of the trapped ion optical clocks.

An ion-trap system either for guiding^{1,2} or for trapping^{3,4} of ions requires narrow band radio frequency (RF) at the desired parameters. It is equivalent to an LCR-circuit having different impedance than the 50 Ω output impedance of an RF source. Using a directional device following an RF source is a standard technique to avoid unwanted power reflection due to impedance mismatching. So, the RF is generally delivered via inductive coupling through an intermediate resonator whose resonant condition is tuned to obtain the desired RF parameters. Over the last few decades, increasing application of the ion-traps for mass spectrometry, precision measurements, generating ion-qubit for quantum computation, development of optical clocks, *etc.* has been demanding high quality RF oscillator and resonator together with improvement in all the associated technologies to achieve an overall high performance.

Focussing on the objectives of this article, here, we briefly review the relevant work on the RF resonator and oscillator. Jones *et al.* reported novel design of an RF generator that allows for tuning of the resonant frequency which varies with the external capacitive loads^{5,6}. Recently, Reza *et al.* reported a tunable Colpitts oscillator that also tunes the RF at a desired frequency⁷. In many cases, the resonant frequency of an RF generator is adjusted by adding extra capacitor in parallel to the ion-trap's intrinsic capacitance but that degrades the quality factor (*Q*-factor) and efficiency of the power transferred to the trap electrodes. As reported in ref.⁸, the operating frequency of their indigenously developed RF amplifier got shifted by about 13.6% than it was designed for, which is due to the lack of prior knowledge on the load of their ion-trap. In all these above-mentioned cases, prior analysis and accurate estimation of the electrical loads will help in proper designing of the RF oscillator. In some applications, feedback controlled RF oscillators are used to enhance the stability⁹. There, a Phase-Lock-Loop locks the resonant frequency, which depends on the extra phase added to the RF due to the propagation delay¹⁰. Estimation of the loads that are attached to the RF generator and their electrical equivalent circuitry analysis helps in proper designing of the feedback system. For ion ejections, fast discharge of the RF after switching it off is required, otherwise the ions are deflected due to residual oscillations¹¹. As the characteristic discharge time of a RF source depends on the effective inductive and capacitive loads¹², estimation of these is required prior to designing of the RF supply.

¹CSIR-National Physical Laboratory, Dr. K. S. Krishnan Marg, New Delhi, 110012, India. ²Academy of Scientific and Innovative Research (AcSIR), Ghaziabad, 201002, India. Correspondence and requests for materials should be addressed to S.D. (email: subhadeep@npl.in)

So far, efforts have been made for novel designing of the RF generator and oscillator for developing high performance ion-traps. In this article, we show a pathway for accurate estimation of the capacitive, inductive and resistive loads resulting from an ion-trap and its associated system. Towards designing of a precision ion trap that will be used for building of a Yb-ion optical clock^{13,14}, we have estimated electrical equivalent loads resulting from different sources and verified them experimentally. This helps us to build a desired helical resonator^{15,16} and to estimate the BBR shift resulting from resistive heating of the ion-trap.

Methodology

The equivalent inductances, L_i ; capacitances, C_i and resistances, R_i resulting from various components, as indicated by the subscript (i), of an ion-trap appear as loads. Due to impedance mismatch, direct connection of the RF source to an ion-trap not only leads to back reflection but also injects intrinsic noise of the RF source to the confining potential, which results to instability of the ions trapped in it. To overcome these, a helical coil resonator is generally used for applying the RF to the ion-trap^{17,18}. This also acts as a bandpass filter and suppresses the noise. The resonant frequency, f_0 and Q-factor, Q_0 of a helical resonator itself can be estimated as,

$$f_0 = \frac{1}{2\pi} \sqrt{\frac{1}{L_R C_R}}, \quad (1)$$

$$Q_0 = \frac{1}{R_R} \sqrt{\frac{L_R}{C_R}}, \quad (2)$$

where L_R , C_R and R_R are the inductance, capacitance and resistance of the resonator, respectively¹⁸. In a loaded condition, *i.e.*, when the ion-trap is attached to the resonator via a connector, the f_0 and Q_0 changes as,

$$f' = \frac{1}{2\pi} \sqrt{\frac{1}{(L_R + L_L)(C_R + C_L)}}, \quad (3)$$

$$Q' = \frac{1}{R_R + R_L} \sqrt{\frac{L_R + L_L}{C_R + C_L}}, \quad (4)$$

where L_L , C_L and R_L are the inductive, capacitive and resistive loads, respectively. The ratio of the effective RF voltage, V' at the trap electrode relative to the input voltage, V is given as,

$$k_{RF} = \frac{V'}{V} = \sqrt{\frac{R_R C_R}{(R_R + R_L)(C_R + C_L)}}. \quad (5)$$

Our ion-trap system, which is attached to an amplified RF source, consists of three parts: a helical resonator **R**, a connector **C** and the end cap type Paul trap **T**. Their arrangements are shown in Fig. 1. Here, we have identified as well as estimated possible sources of loads that contribute to L_L , C_L and R_L which are then validated through experiment.

Helical Resonator (R). The design parameters of our helical resonator are described in the earlier publications^{15,16}. The antenna and the secondary coil have self inductances, L_{R1} and L_{R2} ; resistances, R_{R1} and R_{R2} and a parasitic capacitance, C_{R1} . Capacitance C_{R2} results from the shield-air-coil combination. In the present design, the copper enclosure is silver coated to reduce the electromagnetic radiation loss, which introduces a resistance R_{R3} . Electrical circuitry comprising of these loads are shown in Fig. 2(a). For calculation of the self capacitance of a helical coil of height h_c and outer diameter d_c , the modified Medhurst equation¹⁹ as given by D. W. Knight²⁰ is,

$$C_{coil} = \frac{4\varepsilon_0\varepsilon_x}{\pi} \left[1 + \frac{k_c}{2} \left(1 + \frac{\varepsilon_i}{\varepsilon_x} \right) \right] \frac{h_c}{\cos^2\Psi}, \quad (6)$$

where ε_0 , ε_i and ε_x are permittivities of free space, inside and outside mediums of the coil, respectively and Ψ is the pitch angle. The coefficient k_c is expressed as,

$$k_c = 0.717439 \frac{d_c}{h_c} + 0.933048 \left(\frac{d_c}{h_c} \right)^{\frac{3}{2}} + 0.106 \left(\frac{d_c}{h_c} \right)^2, \quad (7)$$

where the numerical pre-factors are the empirical coefficients²⁰. Assuming the shield and the coil as coaxial cylinders, the shield-to-coil (s-c) capacitance is calculated using the relation,

$$C_{s-c} = 2\pi\varepsilon_0\varepsilon_r h_c \left(\ln \frac{d_s}{d_c} \right)^{-1}, \quad (8)$$

where d_s is the inner diameter of the shield and ε_r is the relative permittivity of any dielectric material in between. For proper positioning of the coil, the space between the shield and coil is partially filled with polyethylene foam of permittivity 2.22. Hence, following the Eqns (6–8), the capacitances of the coil and shield-to-coil are,

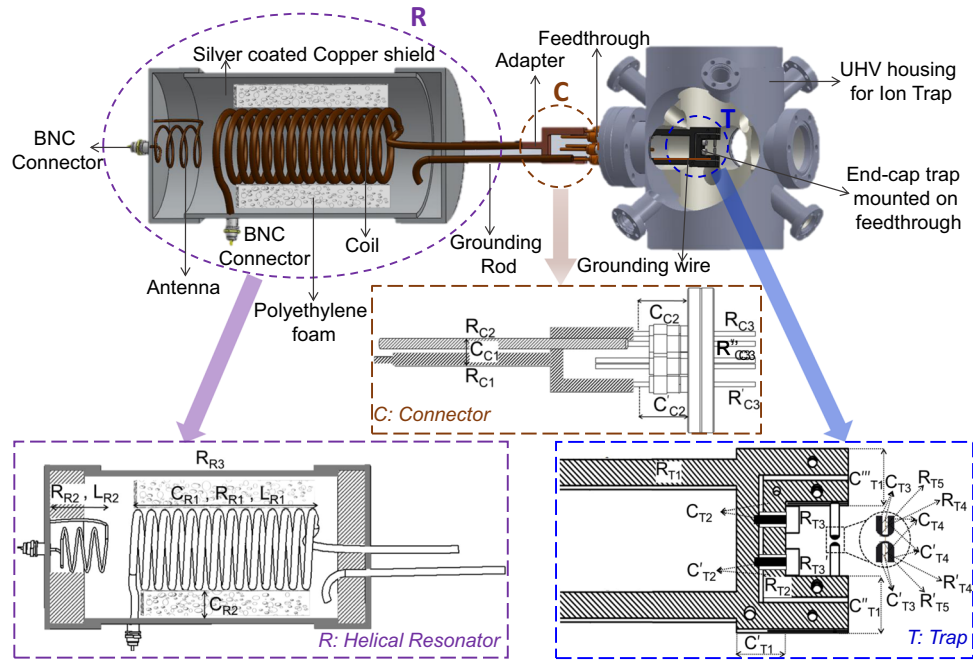


Figure 1. Ion-trap system of our experiment where the resonator (R) and ion-trap (T) are connected via a connector (C). The inserts show schematics of each part R, C and T where sources of the loads are indicated.

$$C'_{coil} = m C_{coil}|_{\epsilon_r, \epsilon_x=1} + n C_{coil}|_{\epsilon_r=1, \epsilon_x=2.22}, \tag{9}$$

$$C'_{s-c} = m C_{s-c}|_{\epsilon_r=1} + n C_{s-c}|_{\epsilon_r=2.22}, \tag{10}$$

here $m = 0.46$ and $n = 0.54$ are the filling factors for air and foam, respectively. Inductance of the coil is estimated as,

$$L_{coil} = 39.37 \frac{\mu_0}{16\pi} \frac{h_c d_c^2}{\tau^2} \left[1 - \left(\frac{d_c}{d_s} \right)^2 \right], \tag{11}$$

where τ is the winding pitch of the coil and the numerical term arises from unit conversion of the formula, as given in ref.²¹ to the SI. The DC resistance of a part of length l and cross-sectional area A is given by,

$$R_{dc} = \frac{\rho l}{A}, \tag{12}$$

where ρ is the resistivity of the material. AC resistances for the RF carrying parts are different and those are important to be calculated. For a cylindrical rod of diameter D , the AC resistance²² is,

$$R_{ac}^c = \frac{R_{dc}}{\pi} \frac{A}{D\delta}, \tag{13}$$

where the skin depth of the material is $\delta = 503 \sqrt{\rho / \omega_{RF} \mu}$ with ω_{RF} and μ being the applied frequency and the relative permeability of the material, respectively. R_{R1} and R_{R2} are calculated using Eqns (12) and (13).

Connector (C). A connector is used to interface the helical resonator with the ion-trap, which is assembly of a Y-shaped copper adapter, a grounding rod and an electrical feedthrough (Fig. 1). The Y-shaped adapter is used for symmetric distribution of the RF to the ion-trap electrode pair. The trap is screwed to two radially symmetric electrical pins of the feedthrough for firm and stable mounting. The capacitance, C_{C1} arises between the adapter and the grounding rod along with the feedthrough pins whereas C_{C2} and C'_{C2} results from the feedthrough pins and its flange. The adapter, grounding rod, feedthrough pins also carry resistances R_{C1} , R_{C2} and R_{C3} , respectively. The rectangular parts of the connector of width w and thickness t carrying RF has an AC resistance²³ which is given as,

$$R_{ac}^r = R_{dc} \frac{K_c}{1 - e^{-x}}, \tag{14}$$

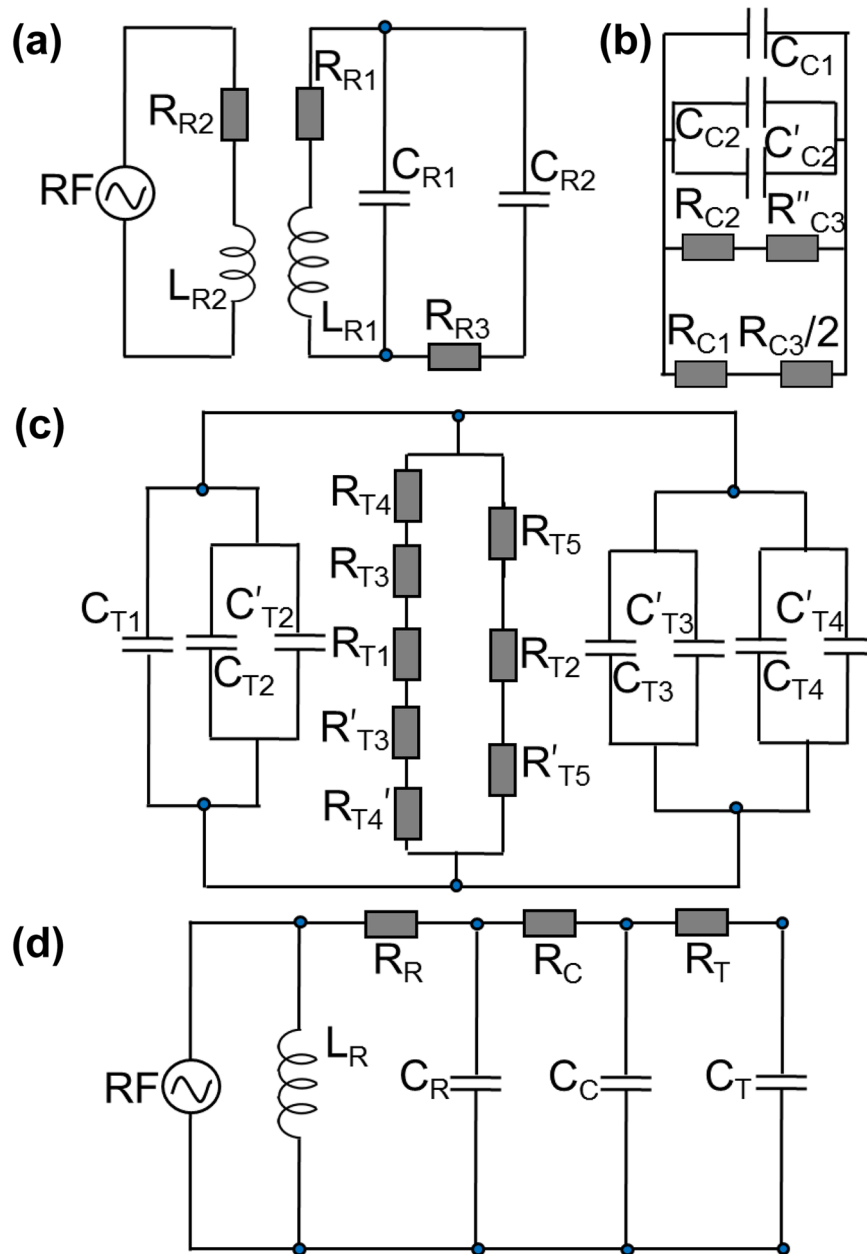


Figure 2. Electrical circuitry of (a) resonator (R), (b) connector (C), (c) ion trap (T) and (d) equivalent (E) of all three components. C_p , R_i and L_i as shown in the circuits denote capacitance, resistance and inductance, respectively, where the subscript i refers to R, C and T, respectively.

where $x = 2(1 + t/w) \delta/t$, current crowding factor $K_c = 1 + (1 - e^{-0.048p}) [0.06 + 0.22 \ln(w/t) + 0.28 (t^2/w^2)]$ and $p = \sqrt{A}/1.26 \delta$. Equivalent electrical circuitry of all the loads described in this section are shown in Fig. 2(b).

Trap (T). The ion-trap electrodes are made of Tantalum, whereas its holding structure is made of Molybdenum and Macor²⁴. The holder mounts the ion-trap inside an Ultra High Vacuum (UHV) chamber via an electrical feedthrough. Capacitances in the trap arise out of the inner electrode holder to outer electrode holder with dielectric macor in between. This capacitance, C_{T1} is estimated part-by-part as C'_{T1} , C''_{T1} and C'''_{T1} as shown in Fig. 1. The capacitances resulting from the mounting bolts and the electrode holders are C_{T2} and C'_{T2} , respectively and from the inner-to-outer electrodes are C_{T3} , C'_{T2} , C_{T4} and C'_{T4} . Resistances result from the inner electrode holder, R_{T1} ; outer electrode holder, R_{T2} ; bolts, R_{T3} ; inner and outer electrode, R_{T4} , R_{T5} and R'_{T4} and R'_{T5} , respectively. Trap's inner and outer electrode holders can be considered as parallel plates spaced apart by macor of thickness d . In that case, the capacitances are calculated as,

$$C = \varepsilon_0 \varepsilon_r \frac{A}{d}. \quad (15)$$

Since, the trap electrodes are cylindrical in shape, their in-between capacitance is calculated from Eqn. (8) by replacing h , d_i and d_o with the length, inner and outer diameters of the outer and inner electrodes, respectively. Equation (14) gives R_{T1} whereas Eqn. (13) is utilized for calculating R_{T3} and R_{T4} . The electrical equivalent circuitry of the loads associated to the ion-trap is shown in Fig. 2(c).

Numerical and Analytical methods. We perform finite element analysis via COMSOL Multiphysics software (COMSOL) for numerical estimation of various L , C and R values. The geometric designs of the parts are fed into the COMSOL and subdivided into finite size elements as per the user's choice. The software analyzes them and generates a final solution using variational method. The computational time increases dramatically with finer mesh size, however, after a certain mesh size, the incremental change of the computed value is well within the limit of our desired accuracy. We use the AC/DC electromagnetics module of COMSOL as the subnodes: electrostatics interface, electric current and magnetostatics allow direct computation of capacitances, resistances and inductances, respectively.

For analytical estimation, we use the formulae as described in the Sec. III A-C, which rely on certain assumptions. As for example, C_i values are estimated assuming parallel plate capacitors. Thus, we do not expect them to be as accurate as for the numerical techniques but this shows inaccuracy of the estimation in case it is done only analytically.

Experiment. Experimental verification of the estimated values are obtained through an indirect measurement as well as via a direct measurement of the loads using an LCR meter. For indirect measurement, the resonant condition is obtained by scanning the RF frequency across f_0 and f' as given in Eqns (1 and 3). A small fraction of the RF ($\leq 3\%$) gets reflected from the resonator. Using a directional coupler, this reflected signal is outcoupled to a spectrum analyzer for further analysis. The resonance condition is ensured by minimum reflection of the RF while tuning its frequency. The outcoupled RF is measured in a spectrum analyzer at different values of fixed capacitive loads and also in the unloaded condition of the resonator.

Results and Discussions

Simple circuitry analysis using Kirchoff's current law leads to estimation of the effective loads as following, for the Resonator **R**:

$$\begin{aligned} C_R &= C_{R1} + C_{R2}, \\ R_R &= R_{R1} + R_{R2} + R_{R3}, \\ L_R &= \frac{L_{R1}L_{R2}}{L_{R1} + L_{R2}}, \end{aligned} \quad (16)$$

for the Connector **C**:

$$\begin{aligned} C_C &= C_{C1} + C_{C2}, \\ R_C &= \frac{(2R_{C1} + R_{C3})(R_{C2} + R_{C3})}{2(R_{C1} + R_{C2}) + 3R_{C3}}, \end{aligned} \quad (17)$$

for the Trap **T**:

$$\begin{aligned} C_T &= C_{T1} + 2(C_{T2} + C_{T3} + C_{T4}), \\ R_T &= \frac{AB}{A + B}, \end{aligned} \quad (18)$$

where, $C_{T1} = (C_{T1}' + C_{T1}'' + C_{T1}''')$ as indicated in Fig. 1, $A = (R_{T2} + 2R_{T5})$ and $B = (R_{T1} + 2R_{T3} + 2R_{T4})$, for total effective loads **E**:

$$\begin{aligned} C_E &= C_R + C_T + C_C, \\ R_E &= R_R + R_T + R_C, \\ L_E &= L_R. \end{aligned} \quad (19)$$

The wire that is used for grounding of the trap inside of the UHV chamber results in a resistive load. The extra compensation electrodes, that are generally used for precise positioning of the ion at the trap centre, also results to finite capacitance. These values have been estimated to be orders of magnitude lower than the rest, which are therefore neglected.

The values of the loads as given in Eqns (16–18), estimated via analytical and numerical techniques are given in Table 1. Source of errors in the numerically calculated values are two fold: accuracy a that is obtained from COMSOL for a certain mesh size and their inaccuracy b for $\pm 10 \mu\text{m}$ machining tolerance. Hence, the total error is estimated to be $\pm \sqrt{a^2 + b^2}$, which is dominated by b .

In the experiment, we measure resonant frequencies and Q -factors when: (i) the resonator is attached to capacitors and (ii) the resonator is attached to the connector and capacitors. For this purpose, we use capacitors

Parts	Analytical	Numerical
Resonator (R)		
C_{R1}	3.7 pF	2.067 (5) pF
C_{R2}	5.7 pF	10.72 (1) pF
R_{R1}	7 m Ω	8 (1) m Ω
	351 m Ω^{ac}	450 (5) m Ω^{ac}
R_{R2}	18 m Ω	10 (4) m Ω
	820 m Ω^{ac}	610 (9) m Ω^{ac}
R_{R3}	5.2 $\mu\Omega$	5.83 (3) $\mu\Omega$
L_{R1}	3.1 μH	3.71 (6) μH
L_{R2}	0.3 μH	0.242 (5) μH
Connector (C)		
C_{C1}	8.2 pF	9.8 (2) pF
C_{C2}	0.04 pF	0.038 (7) pF
R_{C1}	0.22 m Ω	0.222 (1) m Ω
	6 m Ω^{ac}	7 (1) m Ω^{ac}
R_{C2}	454.55 $\mu\Omega$	455.8 (4) $\mu\Omega$
R_{C3}, R'_{C3}	347.6 $\mu\Omega$	348.35 (3) $\mu\Omega$
	10 m Ω^{ac}	9 (2) m Ω^{ac}
Trap (T)		
C_{T1}	22.5 pF	22.1 (3) pF
C_{T2}, C'_{T2}	0.8 pF	0.71 (2) pF
C_{T3}, C'_{T3}	1.6 pF	1.5 (1) pF
C_{T4}, C'_{T4}	0 pF	0.042 (4) pF
R_{T1}	0.073 m Ω	0.078 (1) m Ω
	70 m Ω^{ac}	85 (3) m Ω^{ac}
R_{T2}	80.1 $\mu\Omega$	81.1 (3) $\mu\Omega$
R_{T3}, R'_{T3}	189.44 $\mu\Omega$	197.8 (3) $\mu\Omega$
	3.2 m Ω^{ac}	3.4 (2) m Ω^{ac}
R_{T4}, R'_{T4}	2.816 m Ω	2.790 (2) m Ω
	15 m Ω^{ac}	14 (1) m Ω^{ac}
R_{T5}, R'_{T5}	780.3 $\mu\Omega$	788.6 (1) $\mu\Omega$

Table 1. Estimated values of the loads resulting from different parts of the ion-trap system. AC resistances are indicated by superscript ‘ac’.

with different values that are calibrated at 0.3% uncertainty. As shown in Fig. 3, the characteristic change of the resonant frequency and Q -factor due to additional capacitive load are fitted to $f(C_L) = f_0 \sqrt{C_R/(C_L + C_R)}$ and $Q(C_L) = Q_0 \sqrt{C_R/(C_L + C_R)}$, respectively, where f_0 , Q_0 and C_R are used as the fit parameters. Capacitive load resulting from a component attached to the resonator is obtained by measuring shift of the resonant frequency or Q -factor from the unloaded f_0 , Q_0 values and obtaining change of capacitance corresponding to that shift from their respective characteristic curves, as given in Fig. 3. With the known values of f_0 and f' for any attached capacitance C_p , its unknown value of L_i can be estimated by using Eqns (1) and (3). Further, as the Q_0 and Q' values are also known from experiments, using the estimated L_i values, the unknown R_i values can be obtained using the Eqns (2) and (4). The experimental values are obtained by taking mean of the values taken from different techniques and their variance is quoted as the uncertainty. We measure $f_0 = 27.04$ (7) MHz and $Q_0 = 600$ (8), estimate them as 25.85 (5) MHz and 508 (1) using the numerically estimated loads in Eqns (1–2) and also extract them as 27.5 (1.0) MHz and 590 (7) from the fits. Mutual agreement of these values also validates our calculation in an independent way. The analytical, numerical and experimental values of different loads are compared in Table 2. Using the numerical and experimental values of the loads in Eqn. (5), we estimate the RF voltage transfer factor, $k_{RF} \approx 0.45$ and 0.46, respectively. Therefore, voltage at the trap is about half of that is at the output of RF resonator.

The described electrical load analysis also leads to estimation of the excess BBR shift that results from heating of the ion-trap. The resistive heating of the ion-trap electrodes due to absorption of the RF power propagating through it has already been reported elsewhere^{25–27}. Here, we are estimating the BBR shift associated to heating of the trap due to current flowing through it, which originates due to finite capacitance introduced by inaccurate machining of the trap parts. The RF appears at a different phase with a relative phase difference ϕ on the trap electrodes, that are aligned axially facing each other, due to a path difference x resulting from non-negligible machining tolerances. Due to this, at any instant of time, the RF, $V_0 \sin \omega_{RF} t$, appears at different voltage level, which can be modelled as a parallel plate capacitor with an unwanted excess capacitance C_{ex} kept at a potential $V_0 \phi^{28}$. The phase difference, resulting from the inaccurate machining, is

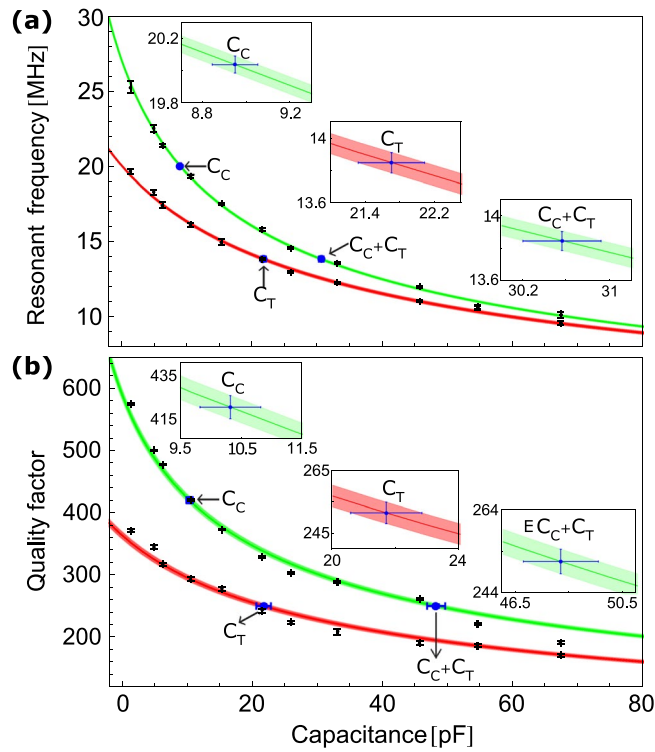


Figure 3. Variation of the (a) resonant frequency and (b) quality factor with capacitance for the resonator itself (green) and for the resonator + connector without the ion-trap connected to it (red). The experimental data (black) and theoretically fitted lines to it are shown, where the width of the lines depict fitting inaccuracy. The measured capacitance (blue) of connector and the combination of connector and trap are indicated on the fitted curves and also shown in the inserts.

Parts	Analytical	Numerical	Experimental
C_R	9.4 pF	12.78 (2) pF	10.6 (1) pF
C_C	8.24 pF	9.9 (2) pF	8.6 (4) pF
C_T	27.3 pF	26.7 (5) pF	21.5 (9) pF
R_R	1241 mΩ	1062 (1) mΩ	981 (5) mΩ
R_C	28 mΩ	29 (9) mΩ	44 (2) mΩ
R_T	174 mΩ	182 (3) mΩ	162 (2) mΩ
L_R	3.1 μH	3.71 (1) μH	3.68 (6) μH
C_E	50.4 pF	51.4 (7) pF	40.7 (2) pF
R_E	1373 mΩ	1273 (3) mΩ	1183 (9) mΩ
L_E	3.1 μH	3.71 (1) μH	3.68 (6) μH

Table 2. Values of the loads obtained through different methods.

$$\phi = 2\pi \left(\frac{x}{\lambda_{RF}} - p \right), \tag{20}$$

where p is the integer number of RF wavelength λ_{RF} that gets accommodated within x . Figure 4(a) shows numerically estimated values of C_{ex} for our ion-trap and calculated ϕ following the Eqn. (20) as a function of the machining inaccuracy. Even though there is no direct relation, the capacity factor in our ion-trap geometry is $\alpha_c = C_{ex} \phi = 1.9$, where C_{ex} and ϕ are in fF and milli-degree, respectively. Although, in an ideal condition ($\phi = 0$), the RF electrodes stay in an open circuit condition, a finite current $I_{ex} = V_o \phi / R_{RF}$ flows through in a real trap that has certain capacity factor. A simple minded physical picture to understand this is by considering a voltage source of $V_o \phi$ V that is present in between the electrodes. In that case, the resulting I_{ex} flows through the resistance R_{RF} that is present in the RF path of the ion-trap system. In a thermal equilibrium, the resistive heating due to I_{ex} will elevate temperature of the trap, which is non-negligible in many precision experiments particularly in case of an optical clock as that significantly contributes to the BBR shift²⁹. The amount of temperature rise during the time

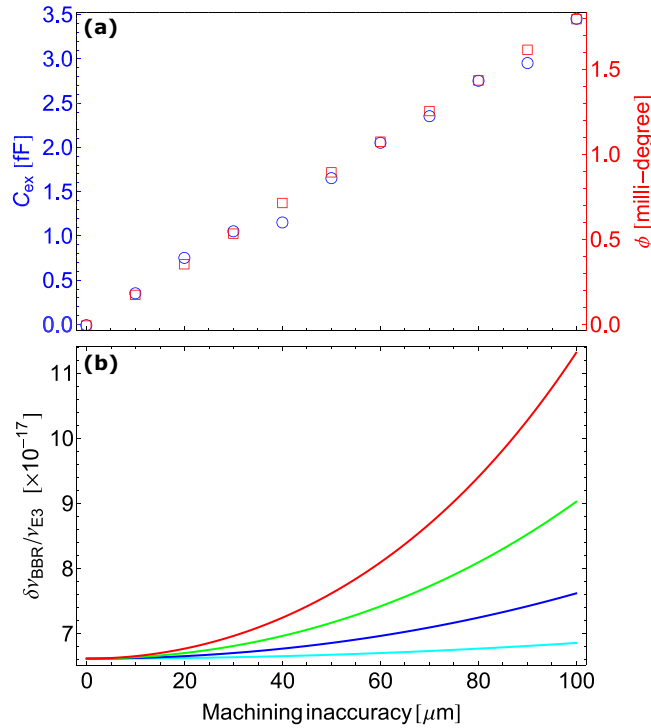


Figure 4. (a) Excess capacitance, C_{ex} , and phase difference, ϕ and (b) the BBR shift, at RF amplitudes 250 V (cyan), 500 V (blue), 750 V (green) and 1000 V (red) at the trap electrodes; resulting from the machining inaccuracy are shown.

of current flow (*i.e.* cycle time of the experiment and we have considered that to be 1 s just for simplicity) can be estimated following the conservation of energy as

$$\begin{aligned} \Delta T &= \frac{V_o^2 \phi^2}{R_{RF} \sum_j m_j s_j} \\ &= \frac{C_{ex}^2 V_o^2}{\alpha_c^2 R_{RF} \sum_j m_j s_j}, \end{aligned} \tag{21}$$

where m_j and s_j are masses and specific heats of the elements j , respectively. Corresponding BBR shift due to the electromagnetic radiation at an elevated temperature T^{30} can be estimated as,

$$\Delta\nu^{BBR} = - \frac{(831.945)^2}{2h} \delta\alpha_o \left(\frac{T}{300} \right)^4 [1 + \eta(T)], \tag{22}$$

where h is the Planck's constant, $\delta\alpha_o$ is differential scalar polarizability of the transition and $\eta(T)$ is the dynamic correction since atomic transitions other than the E1-transitions are neglected in $\delta\alpha_o$. Here, we have neglected this factor since $\eta < 0.01$ at room temperature. As an example, here we estimate $\Delta\nu^{BBR}$ at $T = (296 + \Delta T)$ that is from the machining inaccuracy for the Ytterbium-ion ($^{171}\text{Yb}^+$) octupole (E3) clock transition at frequency $\nu_{E3} = 642121496772645.150 \text{ Hz}^{31}$ and having $\delta\alpha_o = 0.859 \times 10^{-40} \text{ Jm}^2\text{V}^{-2}^{32}$. We use our estimated values of resistances, as given in Table 1, to get $R_{RF} = (R_{T1} + R_{T3} + R'_{T3} + R_{T4} + R'_{T4} + R_{C1} + R_{C3} + R'_{C3})$. Figure 4(b) shows expected fractional BBR-shift $\Delta\nu^{BBR}/\nu_{E3}$ resulting from the machining inaccuracy of the electrodes at different amplitudes of RF of $\omega_{RF} = 2\pi \times 15 \text{ MHz}$. Accurate estimation of this systematic shift carries merit for developing optical clocks with increasing accuracies as it is about two orders of magnitude higher than the present best trapped ion optical frequency standard³¹.

Conclusion

We made detailed analysis of the resistive, inductive and capacitive loads that results from each part of the ion-trap system. We also performed an experiment to measure the effective loads to validate our theoretical estimations. Considering the estimated load values, the design parameters of the resonator can be chosen such that it operates as desired. This analysis shows a pathway for predicting output values, *e.g.*, resonant frequency, Q -factor of an RF resonator both in loaded and unloaded conditions prior to its construction. The RF phase difference at the tip of the electrodes resulting from the unignorable machining inaccuracy, has been estimated accurately. Its relation with one of the dominant systematic shifts in the atomic clock experiments: BBR shift is obtained, which

is important to be considered in the overall systematic budget. As for example, at an RF amplitude of 1 kV at $2\pi \times 15$ MHz and with $\pm 10 \mu\text{m}$ machining inaccuracy will result to ± 0.42 K heating of the trap. A temperature increase (decrease) will result to -43 ($+43$) mHz shift for the Yb ion E3-clock transition that corresponds to fractional frequency uncertainty 6.6×10^{-17} due to the BBR effect. This exercise for precise estimation of the machining inaccuracy assisted BBR shift helps in building highly accurate optical frequency standards that are approaching to 10^{-18} level even without any cryogenic environment.

References

1. Teloy, E. & Gerlich, D. Integral cross sections for ion–molecule reactions. I. The guided beam technique. *Chem. Phys.* **4**, 417–427 (1974).
2. Gerlich, D. Inhomogeneous RF fields. A versatile tool for the study of processes with slow ions. *Adv. Chem. Phys.* **1**, 82 (1992).
3. Paul, W. Electromagnetic traps for charged and neutral particles. *Rev. Mod. Phys.* **62**, 531–540 (1990).
4. Penning, F. M. Die glimmentladung bei niedrigem druck zwischen koaxialen zylindern in einem axialen magnetfeld. *Physica* **3**, 873–894 (1936).
5. Jones, R. M., Gerlich, D. & Anderson, S. L. Simple radio-frequency power source for ion guides and ion traps. *Rev. Sci. Instrum.* **68**, 3357–3362 (1997).
6. Jones, R. M. & Anderson, S. L. Simplified radio-frequency generator for driving ion guides, traps, and other capacitive loads. *Rev. Sci. Instrum.* **71**, 4335 (2000).
7. Reza, A. *et al.* An *in situ* trap capacitance measurement and ion-trapping detection scheme for a Penning ion trap facility. *Rev. Sci. Instrum.* **88**, 034705 (2017).
8. Noriega, J. R., García-Delgado, L. A., Gómez-Fuentes, R. & García-Juárez, A. Low power RF amplifier circuit for ion trap applications. *Rev. Sci. Instrum.* **87**, 094704 (2016).
9. Johnson, K. G. Active stabilization of ion trap radiofrequency potentials. *Rev. Sci. Instrum.* **87**, 053110 (2016).
10. Jau, Y., Benito, F. M., Partner, H. & Schwindt, P. D. D. Low power high-performance radio frequency oscillator for driving ion traps. *Rev. Sci. Instrum.* **82**, 023118-1–023118-5 (2011).
11. Marmillod, P., Antonioni, S. & Lorenz, U. J. A radio frequency/high voltage pulse generator for the operation of a planar multipole ion trap/time-of-flight mass spectrometer. *Rev. Sci. Instrum.* **84**, 044707 (2013).
12. Cermak, I. Compact radio-frequency power supply for ion and particle guides and traps. *Rev. Sci. Instrum.* **76**, 063302 (2005).
13. De, S., Batra, N., Chakraborty, S., Panja, S. & Gupta, A. Sen. Design of an ion trap for trapping single $^{171}\text{Yb}^+$. *Curr. Sci.* **106**, 1348–1352 (2014).
14. Batra, N., Sahoo, B. K. & De, S. An optimized ion trap geometry to measure quadrupole shifts of $^{171}\text{Yb}^+$ clocks. *Chin. Phys. B* **25**, 11 (2016).
15. Batra, N. Design and Construction of a Helical Resonator for Delivering Radio Frequency to an Ion Trap. *MAPAN - Journal of Metrology Society of India*, <https://doi.org/10.1007/s12647-017-0209-5123> (2017).
16. Panja, S., De, S., Yadav, S. & Sen Gupta, A. Measuring capacitance and inductance of a helical resonator and improving its quality factor by mutual inductance alteration. *Rev. Sci. Instrum.* **86**, 056104 (2015).
17. Raizen, M. G., Gilligan, J. M., Bergquist, J. C., Itano, W. M. & Wineland, D. J. Ionic crystals in a linear Paul trap. *Phys. Rev. A* **45**, 6493 (1992).
18. Siverns, J. D., Simkins, L. R., Weidt, S. & Hensinger, W. K. On the application of radio frequency voltages to ion traps via helical resonators. *J. Appl. Phys. B* **107**, 921–934 (2012).
19. Medhurst, R. G. H. F. R. and Self-Capacitance of Single Layer Solenoids. *Wireless. Engineer* **24**, 80 (1947).
20. Knight, D. The self-resonance and self-capacitance of solenoid coils. applicable theory, models and calculation methods. *G3YNH info*, <https://doi.org/10.13140/RG.2.1.1472.0887> (2016).
21. Roper, D. C. & Briggs, L. J. Radio Instruments and Measurements. *Bureau of Standards circular C74; U.S. Government Printing Office; Washington; D.C.*, 252 (1937).
22. Payne, A. N. The HF Resistance of Single Layer Coils. *G3RBJ*, <http://g3rbj.co.uk/> (2013).
23. Payne, A. N. The AC Resistance of Rectangular Conductors. *G3RBJ*, <http://g3rbj.co.uk/> (2017).
24. Rastogi, A. *et al.* Design of the Ion Trap and Vacuum System for ^{171}Yb -ion Optical Frequency Standard. *MAPAN - Journal of Metrology Society of India* **30**, 169–174 (2015).
25. Doležal, M. *et al.* Analysis of thermal radiation in ion traps for optical frequency standards. *Metrologia* **52**, 842 (2015).
26. Keller, J., Burgermeister, T., Kalincev, D., Kiethe, J. & Mehlstäubler, T. E. Evaluation of trap-induced systematic frequency shifts for a multi-ion optical clock at the 10^{-19} level. *J. Phys. Conf. Ser.* **723**, 012027 (2016).
27. Zhang, P. *et al.* Evaluation of blackbody radiation shift with temperature-associated fractional uncertainty at 10^{-18} level for $^{40}\text{Ca}^+$ ion optical clock. *J. Appl. Phys. B* **50**, 015002 (2016).
28. Berkeland, D. J., Miller, J. D., Bergquist, J. C., Itano, W. M. & Wineland, D. J. Minimization of ion micromotion in a Paul trap. *J. Appl. Phys.* **83**, 502 (1998).
29. Roy, A., De, S., Bindiya, A. & Sahoo, B. K. Accurate determination of black-body radiation shift, magic and tune-out wavelengths for the $^6\text{S}_{1/2} \rightarrow ^5\text{D}_{3/2}$ clock transition in Yb^+ . *J. Appl. Phys. B* **50**, 205201 (2017).
30. Farley, J. W. & Wing, W. H. Accurate calculation of dynamic Stark shifts and depopulation rates of Rydberg energy levels induced by blackbody radiation. Hydrogen, helium and alkali-metal atoms. *Phys. Rev. A* **23**, 2397 (1981).
31. Hüntemann, N., Sanner, C., Lipphardt, B., Tamm, C. & Peik, E. Single-Ion Atomic Clock with 3×10^{-18} Systematic Uncertainty. *Phys. Rev. Lett.* **116**, 063001–063006 (2016).
32. Baynham, C. F. A. *et al.* Measurement of differential polarizabilities at a mid-infrared wavelength in $^{171}\text{Yb}^+$ Preprint at *arXiv:1801.10134v2* (2018).

Acknowledgements

Authors thank Tanja Mehlstäubler for fruitful discussions. We acknowledge CSIR-National Physical Laboratory, Department of Science and Technology (DST) grant no. SB/S2/LOP/033/2013 and Board of Research in Nuclear Sciences grant no. 34/14/19/2014-BRNS/0309 for supporting this work. LS and AR thank DST and CSIR for providing Inspire fellowship and Senior research fellowship, respectively.

Author Contributions

S.D. was conceptualizing the entire work reported here. L.S. and S.D. was performing the theoretical analysis. L.S. has performed the numerical simulations using COMSOL Multiphysics software. L.S., A.R., S.P. and S.D. designed and performed the experimental work reported here. L.S., A.R., S.P., V.N.O. and S.D. discussed the result altogether, interpreted the physics behind it and contributed for writing the paper. S.D. supervised the reported work.

Additional Information

Competing Interests: The authors declare no competing interests.

Publisher's note: Springer Nature remains neutral with regard to jurisdictional claims in published maps and institutional affiliations.



Open Access This article is licensed under a Creative Commons Attribution 4.0 International License, which permits use, sharing, adaptation, distribution and reproduction in any medium or format, as long as you give appropriate credit to the original author(s) and the source, provide a link to the Creative Commons license, and indicate if changes were made. The images or other third party material in this article are included in the article's Creative Commons license, unless indicated otherwise in a credit line to the material. If material is not included in the article's Creative Commons license and your intended use is not permitted by statutory regulation or exceeds the permitted use, you will need to obtain permission directly from the copyright holder. To view a copy of this license, visit <http://creativecommons.org/licenses/by/4.0/>.

© The Author(s) 2018

Atomic flux distribution from a low-divergent dark wall oven

Cite as: Rev. Sci. Instrum. **90**, 053202 (2019); <https://doi.org/10.1063/1.5090199>
Submitted: 25 January 2019 . Accepted: 20 April 2019 . Published Online: 10 May 2019

 Lakhi Sharma,  A. Roy,  S. Panja, and  S. De



View Online



Export Citation



CrossMark

ARTICLES YOU MAY BE INTERESTED IN

[A simple atomic beam oven with a metal thermal break](#)

Review of Scientific Instruments **90**, 053106 (2019); <https://doi.org/10.1063/1.5067306>

[Effusive atomic oven nozzle design using an aligned microcapillary array](#)

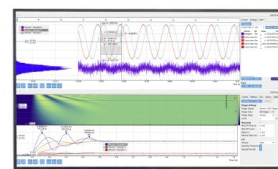
Review of Scientific Instruments **86**, 023105 (2015); <https://doi.org/10.1063/1.4907401>

[A compact and efficient strontium oven for laser-cooling experiments](#)

Review of Scientific Instruments **83**, 103101 (2012); <https://doi.org/10.1063/1.4756936>

Challenge us.

What are your needs for
periodic signal detection?



Zurich
Instruments

Atomic flux distribution from a low-divergent dark wall oven

Cite as: Rev. Sci. Instrum. 90, 053202 (2019); doi: 10.1063/1.5090199

Submitted: 25 January 2019 • Accepted: 20 April 2019 •

Published Online: 10 May 2019



View Online



Export Citation



CrossMark

Lakhi Sharma,^{1,2}  A. Roy,^{1,2}  S. Panja,^{1,2}  and S. De^{1,2,a)} 

AFFILIATIONS

¹CSIR–National Physical Laboratory, Dr. K. S. Krishnan Marg, New Delhi 110012, India

²Academy of Scientific and Innovative Research (AcSIR), Ghaziabad 201002, India

^{a)}Electronic mail: subhadeep@nplindia.org.

ABSTRACT

Nearly collimated atomic beam is of interest for a variety of experiments. This article reports a simple way of modifying the atomic beam distribution using a dark wall oven and describes detailed study of outgoing atoms' spatial distribution. A simple design is obtained by employing the fact that inhomogeneous thermal distribution along a capillary results due to its partial resistive heating. Based on this phenomenon, we have designed a dark wall oven consisting of a reservoir, collimator, and cold absorber at the exit end of atoms, where all three are fabricated out of a single stainless steel capillary. The nearly collimated spatial distribution of the atoms resulting due to the absorber eliminating the atoms diverging above a certain angle is modeled and experimentally verified. A divergence as minimum as $1.2(1)^\circ$ corresponding to a half angle $\theta_{1/2} = 0.9(1)^\circ$ is measured at an oven temperature of 250°C that produces an atomic flux of about 8×10^9 atoms s^{-1} . Total flux as estimated using our measured spatial distribution of atoms matches well with the numerically simulated values of it for the dark wall oven.

Published under license by AIP Publishing. <https://doi.org/10.1063/1.5090199>

I. INTRODUCTION

Atoms are the basis of many advanced techniques aiming for scientific investigations as well as for state-of-the-art technologies. An atomic source is a common requisite in all such techniques where high flux, collimated beam, and unwanted deposition in the vicinity of the experimental volume are specific to the experiment. Depending on the atomic species, oven temperature varies; hence, different heating methods such as resistive,¹ electron bombardment,^{2,3} and inductive^{4,5} are being used. Along with that, different oven geometries are used to produce intense^{6–9} and collimated^{10–13} sources. Resistive heating is widely used up to 1200°C ^{14–19} as temperature control becomes easy by regulating the current flow.^{18,20–23} For collimation, a long tube is used which is further modified with multi-channel^{24,25} and microcapillary arrays^{9,26} to increase the atomic flux. Electron bombardment and inductive heating methods are widely used for heating up to 1800°C ²⁷ and above 2000°C ,^{28,29} respectively. The ovens can have complex designs depending on specific requisites or choice of samples. Spatial distribution of atoms depends on the oven geometry, whereas their velocity distribution depends on the temperature. In case it is required, velocity distribution of

the atoms is modified by the laser cooling technique, as an example, whereas controlling of its spatial distribution can be achieved by proper choice of the oven geometry; dark wall oven³⁰ is one such example.

In order to restrict deposition of the unused atoms at the experimental region of interest as that introduces certain systematics,^{13,31,32} many efforts are made to produce nearly collimated atomic beam.^{8,9,12} Thus, studying atoms' distribution pattern is always a subject of interest.^{25,33–39} Clausing modeled the angular distribution of molecules emerging from cylindrical tubes and analyzed their dimensional dependency,³³ which was later experimentally verified by Dayton.³⁴ Giordmaine and Wang studied peak beam intensities and beam widths from array of long tubes stacked in different shapes.³⁵ The predicted theory justifies only the centerline intensity since it assumed zero number density at the nozzle end of the tube. Olander and Kruger modified that with finite number density at the nozzle end.²⁵ Furthermore, they experimentally verified their model for a multichannel source³⁶ and demonstrated its dependency on the source size.³⁷ Beijerinck and Verster measured the velocity and angular distribution of the atomic beam produced from multichannel arrays in both transparent and opaque modes.²⁴ Krasuski

studied the shapes of angular distribution at different exit zones of a tube which leads to better understanding of the atomic flux pattern.⁴⁰

In this article, we studied the modified spatial distribution of atomic flux coming out of a dark wall oven: theoretically modeled the distribution function, experimentally verified it, and compared it with bright collimating ovens. For this purpose, we developed a simple dark wall oven resulting from nonhomogeneous thermal distribution due to partial heating of a single capillary. This delivers a low-divergent atomic flux that has been tested to produce an Ytterbium (Yb) atomic beam. Due to the dark wall at the exit end, spatial distribution is truncated above an angle. The Finite Element Method (FEM) by using COMSOL Multiphysics® software is performed for studying the thermal distribution throughout of the capillary. This facilitates to choose the suitable oven design parameters. Section II of this article describes details of the oven design and theoretical model of the outgoing atoms' angular distribution pattern. Experimental results and associated discussions are given in Sec. III.

II. OVEN DESIGN AND ITS ATOMIC FLUX DISTRIBUTION

The design of the oven and theoretical model of its expected atomic flux distribution are described in this section. The oven, as shown in Fig. 1(a), consists of a reservoir, a collimating tube, and a cold part at the exit. The oven is operated in the transparent mode, i.e., the ratio of Mean Free Path (MFP) $\lambda = kT/\sqrt{2}\pi d^2 P_{\text{vap}}$ to diameter of the collimating tube $2a$, i.e., the Knudsen number $K_n > 1$.⁴¹ Here, d is the atom's diameter and the vapor pressure is

$$\log P_{\text{vap}} = A + BT^{-1} + C \log T + DT^{-3}, \quad (1)$$

with A , B , C , and D being coefficients for a particular species. In this mode, $\lambda > L > 2a$ leads to free molecular flow in which majority of particles move along a straight path until hitting the wall since atom-atom collisions are suppressed. The aspect ratio of the collimating tube $2a/L$ defines the atomic beam flux as well as its angular divergence. Atoms are stored at the starting end of the capillary which acts as a reservoir where atomic vapor is produced and that propagates through the collimating tube. At the end of the collimating tube, the capillary is partially used as a dark wall, i.e., a cold

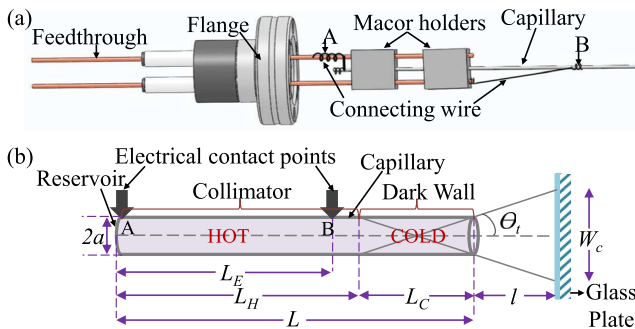


FIG. 1. (a) Drawing of the dark wall oven and its holders for UHV mounting. (b) Schematic of the capillary consisting of three regions: reservoir, collimator, and dark wall.

absorber to truncate the off-axis atoms above a certain angle. In the previously reported dark wall ovens, the reservoir, collimator, and absorber are separate units and assembled together.^{17,18,42} In our simple design, these are made out of a single 316L stainless steel (SS) capillary of inner diameter 0.9 mm and the regions are distinguishable by temperature. Thus, it is easy to mount the oven inside a vacuum chamber. The reservoir end of the capillary is spot welded to a heating wire and closed to stop atoms from exiting. The other electrical contact is separated by a length L_E ($L_E < L$) so that current flows partially through the capillary and the end part of it stays at lower temperature since thermal loss is dominating there [Fig. 1(b)]. By controlling the current's path, the capillary is inhomogeneously heated to create three regions widely separated in temperature. A tungsten wire of AWG 27 is used for electrical contacting of the capillary to the feedthrough pins owing to its high tensile strength of 100 000–500 000 psi at room temperature, a good thermal conductivity of 173 W/m·K, and a high melting point of 3422 °C. Two Macor blocks of dimensions 12 mm × 8 mm × 10 mm are used for holding the capillary along their midway and also for firm mounting of it to the conducting pins of a standard CF16 electrical feedthrough. The cold end truncates the angular distribution at $\theta_i = \tan^{-1}(2a/L_C)$ since atoms traveling beyond that stick to the dark wall at a rate $2\pi a L_C n_o \bar{v}/4$, where $\bar{v} = \sqrt{8kT/\pi m}$ is average thermal velocity. Thus, the expected atomic beam width on a plane, e.g., glass plate placed at a distance l from the exit end of the capillary is,

$$W_c = 2a \left(1 + \frac{2l}{L_C}\right). \quad (2)$$

This assumes that atoms that do not collide the wall are only coming out, which is correct for the atoms having a negligible effusion coefficient at the cold end's temperature.

The vaporized atoms with density n_o within the reservoir are equally probable to move along any direction with a flow rate

$$d^3 \dot{N} = I(\theta) P(v) d^2 \Omega dv, \quad (3)$$

within a solid angle $d\Omega$. Here, $I(\theta)$ and $P(v) = 32v^3 \exp(-4v^2/\pi\bar{v}^2)/\pi^2\bar{v}^4$ are the angular intensity and the normalized velocity distributions, respectively, for the atoms moving at a speed v along θ relative to the tube's axis. The angular distribution follows

$$\dot{N} = \int_{-\pi}^{\pi} I(\theta) d^2 \Omega = \frac{2\pi n_o \bar{v} a^3}{3L}, \quad (4)$$

where \dot{N} is the flow rate of atoms through a transparent tube.²⁴ Angular distribution of atoms exiting a wall strip of width dz situated at a distance z from the reservoir end is given as³⁵

$$dI(\theta) = \frac{n_o z \bar{v}}{4\pi L_H} 2a \sin \theta \left[1 - \left(\frac{z \tan \theta}{2a}\right)^2\right]^{\frac{1}{2}} dz, \quad (5)$$

where $n(z)$ is the atom's density. The centerline atomic intensity is $I(0) = n_o \bar{v} a^2/4$. The critical angle $\theta_C = \tan^{-1}(2a/L_H)$ is obtained from the geometry [Fig. 1(b)], up to which atoms exit from the collimation tube without colliding with its wall. At half angle $\theta_{\frac{1}{2}} = 1.68a/L_H$, the atomic intensity becomes $I(\theta_{\frac{1}{2}}) = I(0)/2$. The angular distribution has two components: (i) atoms that are flowing with and without hitting the wall $I_u(\theta)$, which dominates up to θ_C , and (ii) atoms effusing out after hitting the wall $I_w(\theta)$, which

dominates at $\theta > \theta_C$. The distribution functions as given in Ref. 35 are

$$\begin{aligned}
 I_u(\theta) &= \frac{n_0 \bar{v}}{4\pi} 2a^2 \cos \theta \left[\cos^{-1}(p) - p\sqrt{1-p^2} \right] \\
 &+ \int_0^{L_H} \frac{n(z) \bar{v}}{4\pi} 2a \sin \theta \left[1 - \left(\frac{z \tan \theta}{2a} \right)^2 \right]^{\frac{1}{2}} dz \\
 &= \frac{a^2 n_0 \bar{v}}{2\pi} \left[R(\theta) + \frac{2}{3} P(\theta) \right] \cos \theta, \quad 0 < \theta \leq \theta_C, \\
 I_w(\theta) &= \int_0^{2a/\tan \theta} \frac{n(z) \bar{v}}{4\pi} 2a \sin \theta \left[1 - \left(\frac{z \tan \theta}{2a} \right)^2 \right]^{\frac{1}{2}} dz \\
 &= \frac{2a^3 \bar{v} n_0 \cos^2 \theta}{3\pi L_H \sin \theta}, \quad \theta_C < \theta < \pi/2,
 \end{aligned} \tag{6}$$

where $R(\theta) = \cos^{-1}(p) - p\sqrt{1-p^2}$, $P(\theta) = [1 - (1-p^2)^{\frac{3}{2}}]/p$, and $p = L_H \tan \theta / 2a$. Thus, the relative angular profiles, i.e., $f(\theta) = I(\theta)/I(0)$, are

$$\begin{aligned}
 f_u(\theta) &= \frac{2}{\pi} \left[R(\theta) + \frac{2}{3} P(\theta) \right] \cos \theta, \quad 0 \leq \theta \leq \theta_C, \\
 f_w(\theta) &= \frac{8a}{3\pi L_H} \frac{\cos^2 \theta}{\sin \theta}, \quad \theta_C \leq \theta \leq \pi/2,
 \end{aligned} \tag{7}$$

which are obtained following Giordmaine and Wang's approach.^{24,35,43} The modified equation following the Olander and Kruger model²⁵ considering nonzero number densities at the source and exit ends of the tube is

$$\begin{aligned}
 f'_u(\theta) &= \zeta_0 \cos \theta + \frac{2}{\pi} \cos \theta \left[\zeta_1 R(\theta) + \frac{2}{3} (\zeta_1 - \zeta_0) P(\theta) \right], \\
 &0 < \theta \leq \theta_C, \\
 f'_w(\theta) &= \zeta_0 \cos \theta + \frac{8a}{3\pi L_H} (\zeta_1 - \zeta_0) \frac{\cos^2 \theta}{\sin \theta}, \quad \theta_C \leq \theta \leq \pi/2.
 \end{aligned} \tag{8}$$

Here, dimensionless parameters $\zeta_0 = 4a/3L$ and $\zeta_1 = (1 - \zeta_0)$ are related to the wall collision rates at the entrance and exit of the capillary, respectively. Figure 2 compares angular profiles of outgoing atoms from effusive ovens with and without collimation, following $L \gg 2a$ and $L < 2a$, respectively. For comparison, truncated distribution from a dark wall oven is also shown there. The angles θ_C , θ_t , and $\theta_{\frac{1}{2}}$ for different aspect ratios of the collimator and the dark wall tubes are shown in the inset, which suggests that stronger collimation can be obtained at longer collimator lengths but at a cost of lower throughput. It is to be noted that the truncated angular distribution expected from a collimator followed by a dark wall has similar nature like θ_C , but they operate at different length scales defined by values of L_H and L_C . Atoms at the tail of the distribution are mostly not useful since they are beyond the capturing capability of a trapped atom experiment; hence, truncation is not inefficient for the atom loading. The rate of flow of atoms up to a velocity v and angle θ can be obtained as

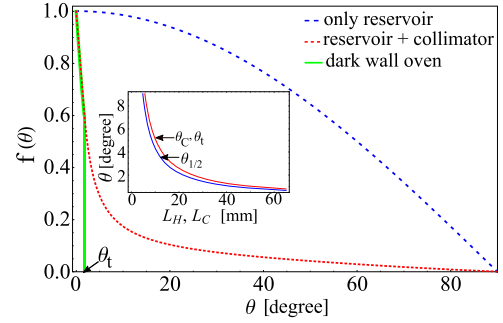


FIG. 2. Angular profile of atoms for different ovens such as reservoir (blue), reservoir attached to a collimator (red), and dark wall oven (green). The inset shows the critical and truncated angle (red) and half-width angle (blue) for different lengths of the capillary. Here, we consider $T = 249$ °C, $L = 65$ mm, $L_H = 35$ mm, $L_C = 30$ mm, and $a = 0.45$ mm.

$$\begin{aligned}
 F_v^\theta \left(\frac{a}{L}, \frac{a}{L_H}, T \right) &= \dot{N} \int_0^\theta F(\theta) 2\pi \sin \theta d\theta \int_0^v P(v) dv \\
 &= \frac{\dot{N}}{2\pi} \left[\pi \sin^2 \theta + (\zeta_1 - \zeta_0) (\sin 2\theta - 2\theta_C - 2\theta) \right] \\
 &\quad \times \left[1 - \exp \left(-\frac{4v^2}{\pi \bar{v}^2} \right) \left(1 + \frac{4v^2}{\pi \bar{v}^2} \right) \right].
 \end{aligned} \tag{9}$$

Here, $F(\theta) = \kappa f'(\theta)/\pi$ is the normalized angular distribution function where $\kappa = \pi I(0)/\dot{N} = 3L/8a^{24}$ is the “peaking factor” that characterizes the degree of collimation. In the spirit of our trapped Ytterbium (Yb^+) optical clock experiment,^{44–50} as an example, the maximum velocity v_{cap} that can be captured in the ion trap is defined by its depth $D_{trap} = a^2 Q r^2 V^2 / (4mR^4 \Omega^2)$, which depends on the trapping voltage, V . Here, a and z are trap geometry specific parameters, V is the applied voltage at radio-frequency Ω , Q is the charge, and R is the radius of the trapping volume. The maximum θ can be either θ_t or the maximum capturing angle by the trap depending on whichever is smaller.

III. EXPERIMENTAL RESULT AND DISCUSSION

We used “Electric Currents” and “Fluid Flow” submodules of COMSOL to study the steady state temperature variation and atomic flux flow, respectively, through the microchannel SS capillary. The temperature distribution in the capillary for its different heating configurations is simulated to obtain the desired temperature distribution distinguishing the reservoir, collimator, and dark wall regions. We define a critical oven temperature T_C at which the output flow rate is negligible to use. In the case of an inhomogeneously heated capillary, the point at T_C defines L_H . The capillary's length over which $T > T_C$ acts as the collimator, and the rest of it acts as the dark wall. Although we considered a wide variety of capillary geometries for simulations to identify the suitable one, we report here the results obtained for $L = 65$ mm, $a = 0.45$ mm, and $L_E = 40$ mm giving a variety of L_H and L_C at different currents that we finally used to construct the oven. In the case of heating the entire capillary, i.e., $L_E = L = L_H$ and $L_C = 0$, inhomogeneity

of the temperature distribution is within the accuracy of the simulation, as shown in Fig. 3(a) for different currents. In this case, the entire capillary acts as the collimator, and the current regulated reservoir temperature is shown in Fig. 3(b). Partial heating of the capillary from the reservoir end up to some intermediate point, as an example $L_E = 40$ mm, at different currents is shown in Fig. 3(c). Figure 3(d) clearly shows that for a fixed L_E , the collimator's length L_H increases with stronger heating. Thus, a proper choice of the electrical contact points and current results in a desired length of the dark wall. As obtained from the FEM analysis, we consider $T_C \approx 175^\circ\text{C}$ at which output flux is two orders of magnitude smaller than the desired and this matches well with our experimental observation as described later. The response times of the dark wall oven to reach 250°C and 350°C from the room temperature are 378 s and 402 s, respectively, as obtained by using the FEM analysis, whereas it takes 94 s and 171 s to reach these temperatures from T_C . Thus, rather than reducing the reservoir temperature to room temperature, it may be set near to T_C while the oven is in frequent use. Figure 4(a) shows temperature dependency of vapor pressure and MFP of ^{171}Yb atoms that satisfy $K_n > 1$ at $T > 127^\circ\text{C}$. The temperature dependent output flow rate of atoms following Eq. (4) and their simulated values are shown in Fig. 4(b). The abrupt increase in the flow rate at $T_C = 175^\circ\text{C}$ is highlighted in the figure. As expected, the dark wall oven produces lower flow rate owing to the truncation of off-axis atoms. Figures 4(c) and 4(d) show capturable atoms

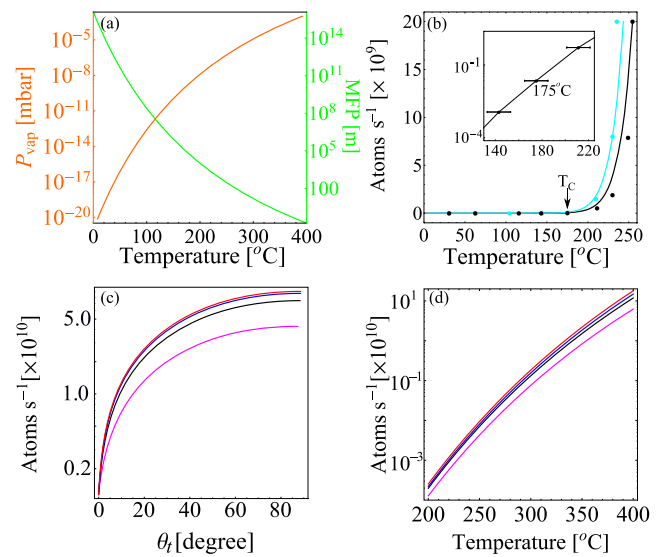


FIG. 4. (a) Variation of Yb vapor pressure (orange) and its mean free path (green) with temperature. (b) Output Yb flux with increasing temperature for a bright oven with collimator (cyan) and a dark wall oven (black) is shown. The discrete points in cyan and black are the corresponding numerical values the inset emphasizes the critical temperature. Flux of atoms at different (c) cutoff angles and (d) oven temperatures for a fixed trap electrode voltage of 250 V (magenta), 350 V (black), 450 V (blue), and 550 V (red) that are available to be captured in our ion trap.

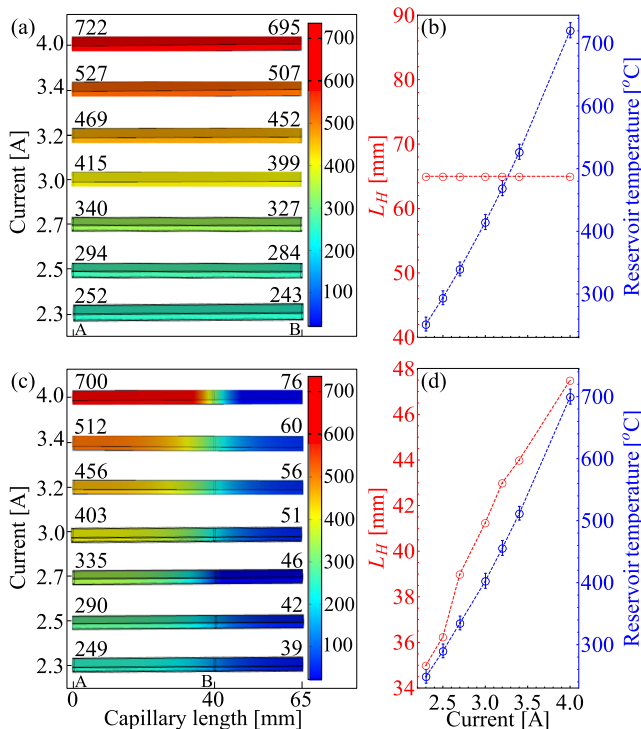


FIG. 3. Numerically simulated variation of temperature (in $^\circ\text{C}$) along the length of the capillary for ovens with a (a) collimator and (c) collimator and cold absorber. (b) and (d) show variation of the collimator's length L_H with current and corresponding reservoir temperature for a fixed operating voltage = 1.7 V.

for different θ_t and oven temperatures, respectively, estimated using Eq. (9). Typically, ions up to a velocity v_{cap} corresponding to 10% of the trap depth can be captured in an ion trap. Considering our ion trap, which captures all atoms up to θ_t and operates at $\Omega = 2\pi \times 15$ MHz and with 45% RF transfer efficiency to the trap electrodes,⁵⁰ we have estimated D_{trap} and hence the maximum capture velocity. As an example, for the oven operating at 300°C and $v_{\text{cap}} \approx 535$ m/s, in case the ion trap operates at 1000 V RF, about 1.6×10^9 ions/s will be available for capturing, assuming 100% ionization of the atoms.

We have tested the performance of our dark wall oven to produce a ^{171}Yb atomic beam and compared the obtained flux distribution with the predicted model. The oven is tested at different currents as the simulation shown in Fig. 3 while heating the entire capillary and also for different cold end lengths during the dark wall mode of its operation. For all the measurements, the oven was kept at 10^{-9} mbar vacuum, $L = 65$ mm and for a fixed run time of 36 h while the spots were recorded on a glass plate at $l = 30$ mm. Deposition of Yb atoms on the glass plate is confirmed through chemical reaction. The glass plate with Yb in metallic silver color deposited on it is exposed to gaseous iodine, and after few hours, it turns to white YbI_3 confirming the presence of Yb. Figure 5(a) shows spatial distribution of atoms while the oven is entirely heated at $T = 252^\circ\text{C}$ without any dark wall. The profile of the spot sizes is measured by STYLUS which has a spatial resolution of $0.5 \mu\text{m}$.⁵¹ In the dark wall mode of operation, at 2.1 A corresponding to $179(10)^\circ\text{C}$, a circular spot of Yb atoms deposited on the glass plate was barely detected by the STYLUS. This temperature is in good agreement

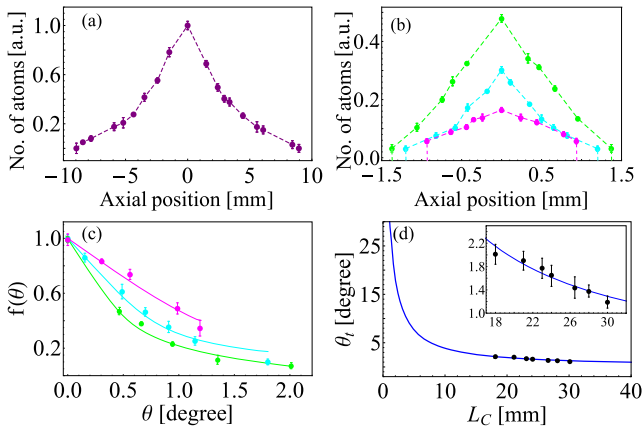


FIG. 5. Measured spatial profiles of the Yb spot for: (a) end-to-end heating of the capillary at 2.3 A and (b) dark wall oven operated at 2.3 A (magenta), 3.2 A (cyan), and 4 A (green). (c) Relative angular profiles along with the fitted curves. (d) Variation of experimentally obtained truncated angle values for varying cold end length along with the fitted model.

with the numerically estimated T_C within its accuracy. Truncated spatial distribution of atoms, as shown in Fig. 5(b), clearly indicates that the spot size increases with higher current due to the decrease in L_C [Fig. 3(c)]. Truncation extends to higher θ_t with increasing current together with the increase in centerline intensity and the total flux following Eq. (9). Assuming radially symmetric deposition of atoms in a circular profile, STYLUS data along several diametric directions were averaged. The relative angular profiles corresponding to varying currents obtained from measured spatial distributions are shown in Fig. 5(c), which are well described by the distribution function as given in Eq. (8). A steep off axial decrease in the atom's density and truncation as described in Fig. 2 is clearly visible at lower current, i.e., longer L_C . The fitted values of L_H , as given in Eq. (8), are in agreement with the numerical simulations [Fig. 3(d)] considering $T_C = 175^\circ\text{C}$. Figure 5(d) depicts experimental θ_t values obtained from distributions, as shown in Fig. 5(c) for varying cold end lengths. The data match well with the theoretical model following Eq. (2). This reconfirms that with decreasing L_C at higher operating current, θ_t increases. Pointing nature of the atoms' distribution toward the center of the spot [Fig. 5(b)] matches very well to the theoretical predictions (Fig. 2). The minimum spot size produced by our dark wall oven has $1.2(1)^\circ$ divergence at 2.3 A and 1.7 V. The corresponding oven temperature $250(10)^\circ\text{C}$ produces a flux of 7.9×10^9 atoms s^{-1} which is good enough for most of the experiments where higher divergence is not tolerable. Figure 6 shows the numerically calculated atomic flux using COMSOL by employing Eq. (4) and those estimated using the experimentally obtained distribution function. Atomic flux up to θ_t can be estimated as $P_{\text{vap}}(T) a^2 \sqrt{8kT} \int_0^{\theta_t} 2\pi f(\theta) d\theta / (4kT \sqrt{\pi m})$, where 2π arises due to the radial symmetry of the distribution. Here, at a particular temperature T , $P_{\text{vap}}(T)$ is estimated as shown in Fig. 4(a) and the fitted function of $f(\theta)$ at different temperatures as shown in Fig. 5(c) is used to estimate the atomic flux. In this case, uncertainties are estimated considering inaccuracies of $f(\theta)$, θ_t , and our confidence on estimating oven temperature. Both the results are comparable to each other within their uncertainties.

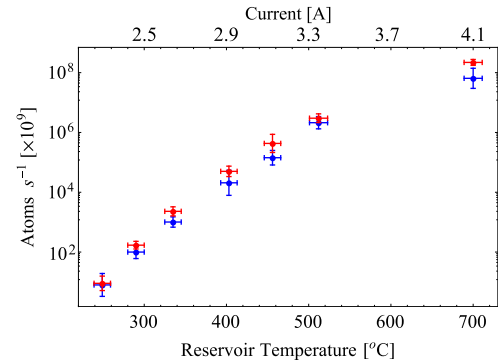


FIG. 6. Temperature dependence of the atomic flux coming out of the dark wall oven, as estimated numerically using COMSOL (blue) and using the measured $f(\theta)$ distribution function (red).

IV. CONCLUSION

Modified spatial distribution of atomic flux coming out of a dark-wall oven is studied in detail, and its high degree of collimation than that of a bright oven with collimator is obtained. A novel design of a simple dark wall oven is presented which is easy to operate for controlling the atomic beam divergence by proper choice of the capillary geometry and the contact points of resistive heating. We performed finite element analysis of the oven heating and atomic flux flow through it, theoretically modeled the distribution function of the atomic flux, and verified it via experimental measurements. The measured critical temperature $179(10)^\circ\text{C}$ at which the atomic flux flow of ^{171}Yb atoms for our oven geometry is negligible to use matches well with the numerically simulated value of 175°C . Also, theoretically obtained distribution function is well characterized with the experimental observations, as shown for different operating conditions. Atomic flux as estimated using our measured spatial distribution of atoms matches to the numerically simulated values. Using a 65 mm capillary of a fine diameter of 0.9 mm including a cold exit end of length 35 mm operating at 2.3 A and 1.7 V, we are able to generate an atomic beam with minimum divergence of $1.2(1)^\circ$ corresponding to $\theta_{\frac{1}{2}} = 0.8(1)^\circ$. This is better than many other complicated oven designs reported earlier. A dark wall oven, as described here, with a multichannel array could be a way for producing a high intensity, nearly collimated atomic beam.

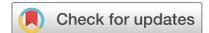
ACKNOWLEDGMENTS

We acknowledge CSIR-NPL, Department of Science and Technology (DST), Grant No. SB/S2/LOP/033/2013 for supporting this work. L.S. thanks DST for the INSPIRE fellowship, and A. Roy thanks CSIR for the SRF Fellowship. We thank Rajeev Rakshit, Manju Singh, and Preetam Singh of CSIR-NPL for allowing us to use their instrument STYLUS.

REFERENCES

- M. O. Krause, Th. A. Carlson, and R. R. Woodruff, *Phys. Rev. A* **24**, 1374 (1981).
- C. Dzionk, W. Fiedler, M. V. Liicke, and P. Zimmermann, *Phys. Rev. Lett.* **62**, 878 (1989).

- ³C. Dzionk, W. Fiedler, M. V. Liicke, and P. Zimmermann, *Phys. Rev. A* **41**, 3572 (1990).
- ⁴S. Aksela, M. Harkoma, M. Pahjola, and H. Aksela, *J. Phys. B: At. Mol. Phys.* **17**, 2227 (1984).
- ⁵E. Forrest, G. K. James, K. J. Ross, and M. Wilson, *J. Phys. B: At. Mol. Phys.* **18**, 3123 (1985).
- ⁶J. P. Gordon, H. J. Zeiger, and C. H. Townes, *Phys. Rev.* **99**, 1264 (1955).
- ⁷S. Stellmer, M. K. Tey, B. Huang, R. Grimm, and F. Schreck, *Phys. Rev. Lett.* **103**, 200401 (2009).
- ⁸M. Schioppo, N. Poli, M. Prevedelli, St. Falke, Ch. Lisdat, U. Sterr, and G. M. Tino, *Rev. Sci. Instrum.* **83**, 103101 (2012).
- ⁹R. Senaratne, S. V. Rajagopal, Z. A. Geiger, K. M. Fujiwara, V. Lebedev, and D. M. Weld, *Rev. Sci. Instrum.* **86**, 023105 (2015).
- ¹⁰S. H. W. Wouters, G. Haaf, P. H. A. Mutsaers, and E. J. D. Vredenburg, *Rev. Sci. Instrum.* **87**, 083305 (2016).
- ¹¹S. C. Bell, M. Junker, M. Jasperse, L. D. Turner, Y.-J. Lin, I. B. Spielman, and R. E. Scholten, *Rev. Sci. Instrum.* **81**, 013105 (2010).
- ¹²A. J. Murray, M. J. Hussey, and M. Needham, *Meas. Sci. Technol.* **17**, 3094–3101 (2006).
- ¹³W. DeGraffenreid, J. R. Serrano, Y. M. Liu, and J. Weiner, *Rev. Sci. Instrum.* **71**, 3668 (2000).
- ¹⁴H. Lew, in *Methods of Experimental Physics*, edited by V. W. Hughes and H. L. Schultz (Academic, New York, 1967), Vol. 4A, p. 155.
- ¹⁵P. Kusch and V. W. Hughes, in *Handbuch der Physik*, edited by Fliigge (Springer, Berlin, 1959), Vol. 37, p. 1.
- ¹⁶L. V. Hertel and K. J. Ross, *J. Sci. Instrum.* **1**, 1245 (1968).
- ¹⁷K. J. Ross and B. Sonntag, *Rev. Sci. Instrum.* **66**, 4409 (1995).
- ¹⁸D. M. P. Holland, K. Codling, and R. N. Chamberlain, *J. Phys. B: At. Mol. Phys.* **14**, 839 (1981).
- ¹⁹C. Vishwakarma, J. Mangaonkar, K. Patel, G. Verma, S. Sarkar, and U. D. Rapol, e-print [arXiv:1810.09090](https://arxiv.org/abs/1810.09090) (2018).
- ²⁰J. G. King and J. R. Zacharias, *Adv. Electron. Electron. Phys.* **8**, 1 (1956).
- ²¹U. Becker, in *X-Ray and Inner Shell Physics*, edited by Th. A. Carlson, M. O. Krause, and S. T. Manson (AJP Conf. Proc., 1990), Vol. 125, p. 621.
- ²²P. H. Kobrin, U. Becker, S. Southworth, C. M. Truesdale, D. W. Lindle, and D. A. Shirley, *Phys. Rev. A* **26**, 842 (1982).
- ²³A. Hausmann, B. Kimmerling, H. Kossmann, and V. Schmidt, *Phys. Rev. Lett.* **23**, 2669 (1988).
- ²⁴H. C. W. Beijerinck and N. F. Verster, *J. Appl. Phys.* **46**, 2083 (1975).
- ²⁵D. R. Olander and V. R. Kruger, *J. Appl. Phys.* **41**, 2769 (1970).
- ²⁶N. Cooper, E. D. Ros, J. Nute, D. Baldolini, P. Jouve, L. Hackermüller, and M. Langer, *J. Phys. D: Appl. Phys.* **51**, 105602 (2018).
- ²⁷M. Richter, M. Meyer, M. Pahler, T. Prescher, E. V. Raven, B. Sonntag, and H. E. Wetzel, *Phys. Rev. A* **39**, 5666 (1989).
- ²⁸L. Feher, Ph.D. thesis, Southampton University, 1987.
- ²⁹D. Bulgin, J. Dyke, J. Goodfellow, N. Jonathan, E. Lee, and A. Morris, *J. Electron Spectrosc.* **12**, 67 (1977).
- ³⁰R. E. Drullinger, D. J. Glaze, and D. B. Sullivan, “A recirculating oven for atomic beam frequency standards,” in *Proceedings of the 39th Annual Symposium on Frequency Control* (IEEE, USA, 1985), p. 13.
- ³¹M. E. Poitzsch, J. C. Bergquist, W. M. Itano, and D. J. Wineland, *Rev. Sci. Instrum.* **67**, 129 (1996).
- ³²A. D. Ludlow, M. M. Boyd, J. Ye, and P. O. Schmidt, *Rev. Mod. Phys.* **87**, 637 (2015).
- ³³P. Clausing, *Z. Phys.* **66**, 471 (1930).
- ³⁴B. B. Dayton, in *1956 National Vacuum Technology Transactions*, edited by E. Perry and J. Durant (Pergamon, London, 1957).
- ³⁵J. A. Giordmaine and T. C. Wang, *J. Appl. Phys.* **31**, 463 (1960).
- ³⁶R. H. Jones, D. R. Olander, and V. R. Kruger, *J. Appl. Phys.* **40**, 4641 (1969).
- ³⁷D. R. Olander, *J. Appl. Phys.* **40**, 4650 (1969).
- ³⁸D. R. Olander, R. H. Jones, and W. J. Siekhaus, *J. Appl. Phys.* **41**, 4388 (1970).
- ³⁹W. J. Siekhaus, R. H. Jones, and D. R. Olander, *J. Appl. Phys.* **41**, 4392 (1970).
- ⁴⁰P. Krasuski, *J. Vac. Sci. Technol. A* **5**, 2488 (1987).
- ⁴¹D. Halwidl, *Development of an Effusive Molecular Beam Apparatus* (Springer Spektrum, Wiesbaden, 2016), Chap. 1, p. 5.
- ⁴²D. O. Sabulsky, Ph.D. thesis, University of Chicago, 2014.
- ⁴³D. E. Kuhl and R. G. Tobin, *Rev. Sci. Instrum.* **66**, 3016 (1995).
- ⁴⁴A. Rastogi, N. Batra, A. Roy, J. Thangjam, V. P. S. Kalsi, S. Panja, and S. De, *MAPAN* **30**, 169 (2015).
- ⁴⁵N. Batra, B. K. Sahoo, and S. De, *Chin. Phys. B* **25**, 113703 (2016).
- ⁴⁶A. Roy, S. De, B. Arora, and B. K. Sahoo, *J. Phys. B: At. Mol. Opt. Phys.* **50**, 205201 (2017).
- ⁴⁷S. De, N. Batra, S. Chakraborty, S. Panja, and A. Sen Gupta, *Curr. Sci.* **106**, 1348 (2014), <https://www.currentscience.ac.in/php/toc.php?vol=106&issue=10>.
- ⁴⁸S. Panja, S. De, S. Yadav, and A. Sen Gupta, *Rev. Sci. Instrum.* **86**, 056104 (2015).
- ⁴⁹N. Batra, S. Panja, S. De, A. Roy, S. Majhi, S. Yadav, and A. Sen Gupta, *MAPAN* **32**, 193 (2017).
- ⁵⁰L. Sharma, A. Roy, S. Panja, V. N. Ojha, and S. De, *Sci. Rep.* **8**, 16884 (2018).
- ⁵¹K. J. Stout and L. Blunt, in *Three-Dimensional Surface Topography*, 2nd ed. (Penton Press, 2000), Chap 2, p. 22.



OPEN

An easy to construct sub-micron resolution imaging system

Lakhi Sharma^{1,2}, A. Roy^{1,2,3}, S. Panja^{1,2} & S. De⁴✉

We report an easy to construct imaging system that can resolve particles separated by $\geq 0.68 \mu\text{m}$ with minimum aberrations. Its first photon collecting lens is placed at a distance of 31.6 mm giving wide optical access. The microscope has a Numerical Aperture (NA) of 0.33, which is able to collect signal over 0.36 sr. The diffraction limited objective and magnifier recollects 77% photons into the central disc of the image with a transverse spherical aberration of 0.05 mm and magnification upto 238. The system has a depth of field of 142 μm and a field of view of 56 μm which images a large ensemble of atoms. The imaging system gives a diffraction limited performance over visible to near-infrared wavelengths on optimization of the working distance and the distance between the objective and magnifier.

Studying molecular dynamics, many body physics, quantum simulation by detecting individual atoms and ions rely on high resolution, minimally aberrated optical system to form a magnified image of the object. Imaging systems are used in fluorescence microscopy and mass spectroscopy, which gained immense interest particularly for detection of biological molecules and other chemical compounds. Micron level resolution in such cases allows direct study of the molecular dynamics^{1,2}. Precision spectroscopy for parity non-conservation (PNC), electric dipole moment, optical clock etc., which uses single atom³⁻⁵ or ion⁶⁻¹⁰, rely on high resolution imaging. Quantum phase transitions, quantum simulations and quantum information processing (QIP) by using atoms in an optical lattice or array of ions in an electrodynamic trap demands imaging of the individual particles.

In particular to the rapidly progressing QIP, (i) scaling up of the qubit and (ii) their individual addressing are the present challenges for which reading the individual atoms or ions is important¹¹. These applications demand sub-micron resolution for detection of trapped ions¹²⁻¹⁷ and atoms in optical lattices¹⁸⁻²². Different approaches, such as, by measuring the current produced upon impinging of a focussed electron beam on to the sample²³ and most commonly by setting up of a high quality imaging system are being used. In the latter case, the signal photons either from fluorescence or from absorption imaging are collected by different customized optical systems such as micro fabricated Phase Fresnel lenses (PFLs) or by using high NA diffraction limited objectives. Alt reported an objective with NA 0.29 covering 2.1% of 4π solid angle to detect a single atom in a magneto optical trap²⁴. Sortais et al. reported imaging with objective of NA 0.5 and magnification of 25²⁵. Nelson et al. first reported direct observation of individual atoms in lattice sites and imaging different lattice planes using a lens of NA 0.55 and magnification 32²², which then became a powerful tool for such systems to study quantum dynamics. Karski et al. reported an objective with NA 0.29 and magnification of 54 to resolve atoms separated by 433 nm²⁶. Using customized lenses and wavefront corrector plate, Bakr et al. achieved the highest effective NA 0.8 so far and resolution 0.6 μm , which was pathbreaking for quantum gas microscopy²⁷. For high resolution detection over large volume, Jechow et al. demonstrated use of microfabricated PFLs that obtained NA of 0.64 covering 12% of 4π solid angle and a magnification of 615 ± 9 ²⁸. Due to small size, PFLs can be placed close to the sample which results to higher NA and they can also be arranged in an array to extend the viewing region further¹³. Wong-Campos et al. reported the least aberrated imaging and NA 0.6 to detect ions confined in a microfabricated trap¹⁵.

In this article, we describe design geometry of an easy to construct imaging system using off-the-shelf optics where positions of only two lenses are critical and also obtain their important features. The design can be adapted over visible to near-infrared wavelengths in different applications which require sub-micron spatial resolution and high quality images. The described imaging system will be used to image single Ytterbium-ion using its $^2S_{1/2} \rightarrow ^2P_{1/2}$ fluorescence at the wavelength 369.5 nm in our optical clock experiment²⁹.

¹CSIR - National Physical Laboratory, Dr. K. S. Krishnan Marg, New Delhi 110012, India. ²Academy of Scientific and Innovative Research (AcSIR), Ghaziabad 201002, India. ³Max Planck Institute for the Science of Light, Staudtstrasse 2, Erlangen 91058, Germany. ⁴Inter-University Centre for Astronomy and Astrophysics (IUCAA), Post Bag 4, Ganeshkhind, Pune 411007, India. ✉email: subhadeep@iucaa.in

Design of the lens system

The wavefronts propagating with photons get deformed due to inhomogeneous refractive index of the medium. As a result, the image formed by an optical system is aberrated which can be minimized, if not cancelled³⁰, by proper choices of lenses and optimization of the design parameters. For quantitative analysis, let's consider (y, z) and (Y, Z) as the coordinates for exit pupil and its image, respectively, while the source is at the origin and the imaging system is along the x axis. Introducing polar coordinates (ρ, θ) and (r, ϕ) in the exit pupil and image planes, respectively, the wave aberration $W(h, \rho, \theta)$ at the exit pupil for a rotationally symmetric optical system in its image plane (yz plane), can be written as^{31,32}:

$$W(h, \rho, \theta) = \sum_{j,m,n} W_{klm} h^k \rho^l \cos^m \theta, \tag{1}$$

where aperture size $\rho = \sqrt{y^2 + z^2}$, θ is the azimuthal angle in the pupil plane, h is the image height, j, k, l, m, n are integers satisfying the condition $k = 2j + m, l = 2n + m$ and W_{klm} are the aberration coefficients. Upon expanding Eq. (1), the terms associated to coefficients W_{200}, W_{111} and W_{020} represent piston, tilt and defocus, respectively, which do not contribute in case of monochromatic light source. Terms associated to $W_{040}, W_{131}, W_{222}, W_{220}$ and W_{311} represent Seidel aberrations such as spherical, coma, astigmatism, field curvature and distortion, respectively and the remaining represents higher order distortions³¹. In case of monochromatic photons emitted by a point source located close to the imaging axis, coma and astigmatism do not play major role. Spherical aberration dominates in case of imaging fluorescence that is isotropically emitted in all directions, hence Eq. (1) simplifies to

$$W(\rho) = \sum_{n=2}^P W_{02n0} \rho^{2n}, \tag{2}$$

where $k = 0, l = 2n, m = 0$ and p and n are integers. The spatial profile of an image corresponding to a point source, given by the PSF $S(r, \phi) = A(r, \phi) A^*(r, \phi)$ is in the form of an Airy pattern for a nearly perfect optical system³³. Here, A and A^* are amplitude distribution of the image and its complex conjugate, respectively. The deformation of amplitude distribution during propagation can be obtained from pupil function as,

$$P(\rho, \theta) = E(\rho, \theta) \exp[ikW(\rho)], \tag{3}$$

where k is the wave vector and $E(\rho, \theta)$ is the transmittance amplitude of the optical system. Hence, the amplitude distribution is,

$$A(r, \phi) \approx C \int_0^{2\pi} \int_0^1 P(\rho, \theta) \exp[-i\rho\beta \cos(\theta - \phi)] \rho d\rho d\theta, \tag{4}$$

with $\beta = \frac{\pi r}{\lambda F}$ and $C = \frac{-i}{4\lambda F^2} \exp\left(ik \frac{r^2}{r_w}\right)$, where $r = \sqrt{Y^2 + Z^2}$, λ is photon's wavelength, F is effective focal number and r_w is radius of curvature of the wavefront at the exit pupil. Considering fully transmissive pupil i.e. $E(\rho, \theta) = 1$ and using Eqs. (3) and (4), the PSF reduces to^{31,32,34}

$$S(r, \lambda, F) \approx \frac{\pi}{\lambda^2 F^2} \left| V_0 + ikV_1 - \frac{k^2}{2} V_2 \right|^2, \tag{5}$$

where, $V_0 = 2 \frac{I_1(\beta)}{\beta}, V_1 = 2 \int_0^1 W(\rho) J_0(\beta\rho) \rho d\rho$ and $V_2 = 2 \int_0^1 W^2(\rho) J_0(\beta\rho) \rho d\rho$. The normalized PSF reduces to

$$S(r, \lambda, F) = V_0^2 - k^2(V_0 V_2 - V_1^2) + 0.25k^4 V_2^2, \tag{6}$$

which we shall use throughout this article.

The Optics Software for Layout and Optimization (OSLO) is used for design optimization of the imaging system. It is capable of performing ray tracing and estimating the mentioned quality assurance parameters of an optical assembly upon proper feeding of its components³⁵. OSLO considers upto 7th order of $W(\rho)$ as given in Eq. (2) for its analysis using sequential ray tracing method³⁵.

Optical solutions to image a single Ytterbium ion (Yb^+), as an example, which is a point like source emitting fluorescence at wavelength 369.5 nm is discussed here. The imaging system for such cases should have efficient fluorescence collection, adequate resolution I_R and magnification M to distinguish individual ions and minimized aberration. Here, we consider transverse spherical aberration (SA) owing to the fact that all rays fall within the magnified image eventhough longitudinally they are not focussed at a single point. Other than SA, Strehl ratio SR and root mean square wavefront deformation σ , specify characteristics of an imaging system following³⁶⁻³⁹,

$$SR = \exp(-2\pi\sigma)^2, \tag{7}$$

which can be approximated to $SR = 1 - (2\pi\sigma)^2$ for diffraction limited optics. For resolving two ions, diameter of central spot of the image A_{image} which reduces to Airy disc diameter A_D for a nearly perfect image should follow

$$A_{image} < I_R \times M, \tag{8}$$

so that images do not overlap. Following the Maréchal's Strehl approximation⁴⁰, $SR \geq 0.8$ is acceptable, which corresponds to $\sigma \leq \lambda/14$. Thus, the optics of surface roughness $\simeq \lambda/20$ are recommended for constructing the

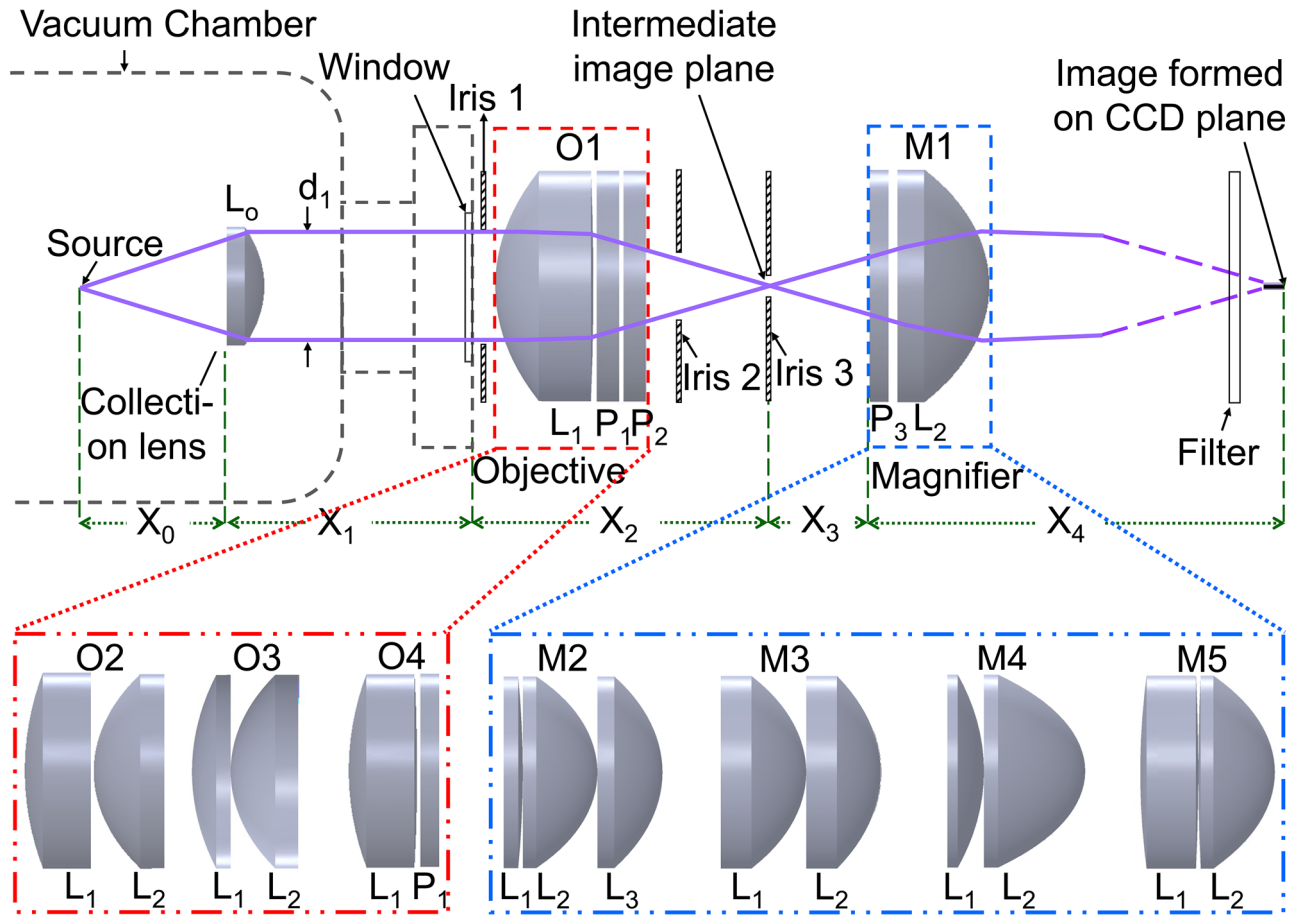


Figure 1. Schematic of the imaging system considering a variety of objectives O1–O4 and magnifiers M1–M5. Lenses and wavefront corrector plates (WCP) are indicated as L_i and P_i , respectively, where i is their numbers. The collection lens L_0 , and optics in objective, magnifier are of standard 25 mm and 50 mm diameter, respectively. For the L_0 –O1–M1 combination, indicated length scales are $X_0 = 31.6$ mm, $X_1 = 60.4$ mm, $X_2 = 58.2$ mm, $X_3 = 34$ mm and $X_4 = 4154$ mm.

imaging system. Positioning the collection lens nearer to the source enhances the fluorescence collection but that freedom is limited by available geometry which in our experiment is 31.5 mm to avoid any obstruction. In an ensemble of N trapped ions, minimum separation between two consecutive central ions is⁴¹,

$$l_o = \left(\frac{e^2}{4\pi\epsilon_0 m\omega_s^2} \right)^{\frac{1}{3}} \frac{2.018}{N^{0.559}}, \tag{9}$$

where e , ϵ_0 , m and ω_s are the electron charge, free space permittivity, mass of the ion and secular frequency, respectively. The minimum separation between two species that can be resolved by a lens system is $l_R = 0.61\lambda/NA$. In case of five ions confined in our Paul trap geometry^{42,43}, as an example, $l_o = 1.4 \mu\text{m}$ that demands $NA \geq 0.16$ and as per Nyquist criterion a magnification ≥ 11 for a pixel size of $8 \mu\text{m} \times 8 \mu\text{m}$.

The schematic of imaging system(s) considered in our analysis is shown in Fig. 1. An aspheric lens L_0 of focal length $f_o = 40$ mm and 25.4 mm diameter is placed inside the vacuum chamber at a working distance $X_0 = 31.6$ mm from the source. It collects 2.8% of the fluorescence, covering 0.36 sr solid angle and nearly collimates them towards the chamber window. This is followed by an objective O_i outside the vacuum chamber, where i represents different variants, which forms an intermediate image of $A_{\text{image}} = 1.3 \mu\text{m}$ at a distance X_2 from the window. The magnifier M_i is placed at a spacing X_3 from the intermediate image, which forms a magnified image on the charge coupled detector (CCD) at a distance X_4 from it. After the magnifier, we use a flipper mirror to route the fluorescence either towards a Photo Multiplier Tube (PMT) or to the CCD. In both cases, it passes through an appropriate bandpass filter to transmit the desired wavelength. Distances between source and L_0 ; and O_i to M_i are critical to form the best image. An iris mounted on a YZ translation stage is placed after the viewport to obstruct the unwanted photons scattered from surface of the vacuum chamber and knife edges. Another precision iris is mounted on a three axes translation stage and placed at the intermediate image position for its spatial isolation from others. A third iris mounted on YZ translation stage is placed immediately after O_i for second stage elimination of scattered photons that is useful for optical alignment of the imaging system as well.

Objective [<i>f</i> in mm]	A_{image} (μm)	SR	SA (μm)	l_R (μm)	Image (2.5×2.5) μm^2 
O1: 1 Asp [50], 2 WCP	1.3 (2)	0.93 (1)	0.7 (1)	0.68 (3)	
O2: 1 Asp [60], 1 Ach [100]	1.2 (1)	0.84 (3)	0.7 (1)	0.71 (1)	
O3: 1 Asp [100], 1 Asp [60]	1.2 (3)	0.74 (3)	0.7 (1)	0.67 (3)	
O4: 1 Ach [100], 1 WCP	1.8 (5)	0.59 (5)	2.4 (3)	1.9 (1)	
Magnifier [<i>f</i> in mm]	A_{image} (mm)	SR	SA (mm)	M	Image (0.5×0.5) mm^2 
M1: 1 Asp [37.5], 1 WCP	0.06 (3)	0.92 (2)	0.05 (1)	110 (4)	
M2: 1 Asp [50], 1 Asp [60] 1 PC [500]	0.01 (1)	0.91 (1)	0.02 (1)	15 (1)	
M3: 1 Asp [50], 1 Asp [60]	0.04 (3)	0.89 (1)	0.04 (3)	62 (2)	
M4: 1 Asp [37.5], 1 PC [125]	0.07 (3)	0.81 (1)	0.05 (3)	77 (3)	
M5: 1 Asp [60], 1 Ach [100]	0.03 (2)	0.76 (2)	0.03 (1)	33 (1)	

Table 1. Estimated values of parameters for different lens combinations that we studied, where the magnifiers in conjunction with O1 are shown here. *Asp* asphere, *WCP* wavefront corrector plate, *Ach* achromat, *PC* plano convex lens.

Results and discussions

In this section, we discuss performances of different imaging systems that we have studied. Table 1 lists values of parameters that we obtained for different objectives and magnifiers along with simulated ion images. Throughout our analysis, the collection lens L_o of $f_o = 40$ mm, its position $X_o = 31.6$ mm and $\lambda = 369.5$ nm is fixed. To resolve the species, the imaging system should satisfy in-situ interspecies separation $l_o \gg SA$ at the intermediate image and

$$l_o \times M > SA, \quad (10)$$

at the final image. Among the different objectives, O1 and O2 satisfy Maréchal's criterion⁴⁰ and have σ , l_R and SA values within the acceptable range. With the available commercial lenses, O3 gives a better resolution and an acceptable SA but SR = 0.74 does not satisfy Maréchal's criterion. O4 does not minimize SA to the acceptable limit, results to a poor SR and has a low resolving power. The resultant SR and SA for all twenty combinations between objective-magnifier pairs are shown in Fig. 2a,b, respectively. Combination of O1 with M1, M2, M3, M4 and O2 with M1, M4 results to SR > 0.8, among them O1–M1 gives the best results with SR = 0.92, $l_R = 0.68$ μm and a diffraction limited performance over M = 73 to 238; whereas O2–M1 with SR = 0.87 and $l_R = 0.7$ μm is also a probable choice but offers a comparatively lower magnification ranging from 51 to 65. For our experiment, we opt for O1–M1 combination which consists of only one aspheric lens together with two $+1\lambda$ spherical aberration compensation plates, making the imaging system simple to construct. Using off-the-shelf SA corrector plates enhances the performance of the system, thus producing better images. The results presented in this section are corresponding to the L_o –O1–M1 system. The component and air spacing details of the system is catalogued in Table 2 (see Supplementary Fig. S1 for more details). Estimated photon transfer efficiency due to reflections from its multiple optical surfaces without any band-pass filter is 0.91 and on passing through a 370 ± 2 nm commercial bandpass filter with 25% transmissivity is 0.23.

Figure 3a shows PSF as simulated using OSLO and compares it to the theoretical calculation following Eq. (6) for the L_o –O1–M1 system, where the aberration coefficients as given in Eq. (2) are obtained from OSLO. This gives confidence to understand the imaging system and thereby helps to model a measurable PSF for a real case. PSF in the intermediate image plane is also shown, which has $A_{image} = 1.3$ μm . The insets show the corresponding ion images obtained by simulation. Considering Yb ion as the source, the L_o –O1–M1 system diffracts 77% of the total collected photons into the central Airy disc. Figure 3b shows tunability of M1 to vary magnification

Optics	Surface no.	Radius (mm)	Spacing (mm)	Component	Material (placement)
L _o	1	∞	8.0	AFL-25-40 (Asphericon)	CROWN (Vacuum)
	2	-19.7	43.7		
Window	3	∞	1.5	VPZ38SVAR-NM (Torr scientific)	Sapphire (Air)
	4	∞	0		
L ₁ of O1	5	30.8	19.4	66316 (Edmund optics)	LBAL35 (Air)
	6	-500.0	0		
P ₁ of O1	7	∞	4.0	66765 (Edmund optics)	NBK7 (Air)
	8	∞	0		
P ₂ of O1	9	∞	4.0	66765 (Edmund optics)	NBK7 (Air)
	10	∞	65.5		
P ₃ of M1	11	∞	4.0	66765 (Edmund optics)	NBK7 (Air)
	12	∞	0		
L ₂ of M1	13	∞	19.4	69144 (Edmund optics)	LBAL35 (Air)
	14	-29.4	4.2 × 10 ³		

Table 2. Specifications of the L_o-O1-M1 lens system.

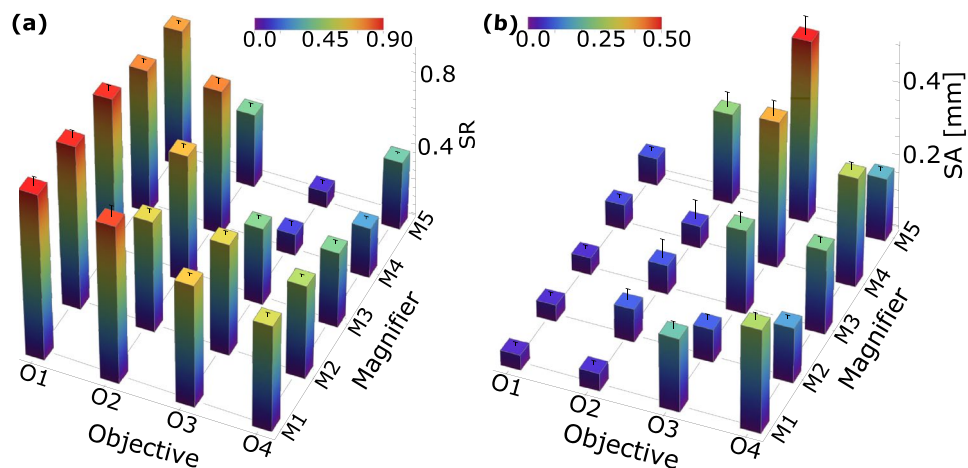


Figure 2. (a) Strehl ratio (SR) and (b) spherical aberration (SA) for all possible combinations of objectives (O1–O4) and magnifiers (M1–M5) those we have studied.

of the final image and corresponding SR and SA. Mounting the magnifier on a precision translation stage is required to tune its position at micron accuracy across its focus f_{L3} . Tunability of 600 μm across f_{L3} varies the magnification from 73 to 238 within the acceptable SR and SA, beyond that focussing of marginal and axial rays do not coincide, which results into greater SA and hence poorer quality, as shown in the insets of the figure.

Depth of Field (DOF) and Field of View (FOV) are the acceptable radial and axial ranges (with respect to trap's axis i.e. z-axis), respectively, over which images with $\text{SR} \geq 0.8$ are formed⁴⁴. These also determine number of trapped species which can be imaged at a time. In case of 19 ions trapped along a particular direction, $l_o = 0.69 \mu\text{m}$ for our trap conditions, and hence they can be resolved as $l_R = 0.68 \mu\text{m}$. Considering this, we show planar visualisation with simulated images of 19 ions in our trap in Fig. 4a,c for radial and axial planes, respectively. Figure 4b,d show SR and SA corresponding to these images and indicate DOF and FOV. Actual spacing between consecutive ions is considered in this analysis, which increases as they are further away from the radio-frequency nullpoint of the trap (trap centre). That together with source at out of focus results to steep change in SR and SA for the ions away from the trap centre. The L_o-O1 combination gives a DOF of 280 μm and FOV of 94 μm , whereas in conjunction with the magnifier these values reduce to 142 μm and 56 μm , respectively.

The performance discussed is for the nominal system but the fabrication tolerance is also to be taken into account. The Peak-to-Valley (P-V) optical path difference (OPD) corresponding to an SR of 0.8 is 0.25 waves. The P-V OPD for the system, OPD_s as obtained from the simulation is 0.19 waves; hence, to satisfy Maréchal's criterion, the P-V OPD from fabrication tolerance, OPD_t should be ≤ 0.16 waves. We determined the overall fabrication tolerance of the system considering different sources and their contributions within bracket are as: radius of curvature (0.022 λ), surface irregularity (0.002 λ), element thickness/ air space (0.116 λ), refractive index (0.085 λ) and surface tilt ($5 \times 10^{-5} \lambda$), which results to $\text{OPD}_t = 0.14$ waves. This results to an effective $\text{OPD}_{total} = \sqrt{\text{OPD}_s^2 + \text{OPD}_t^2} = 0.24$ waves that corresponds to SR of 0.83 which is well within the limit. Apart

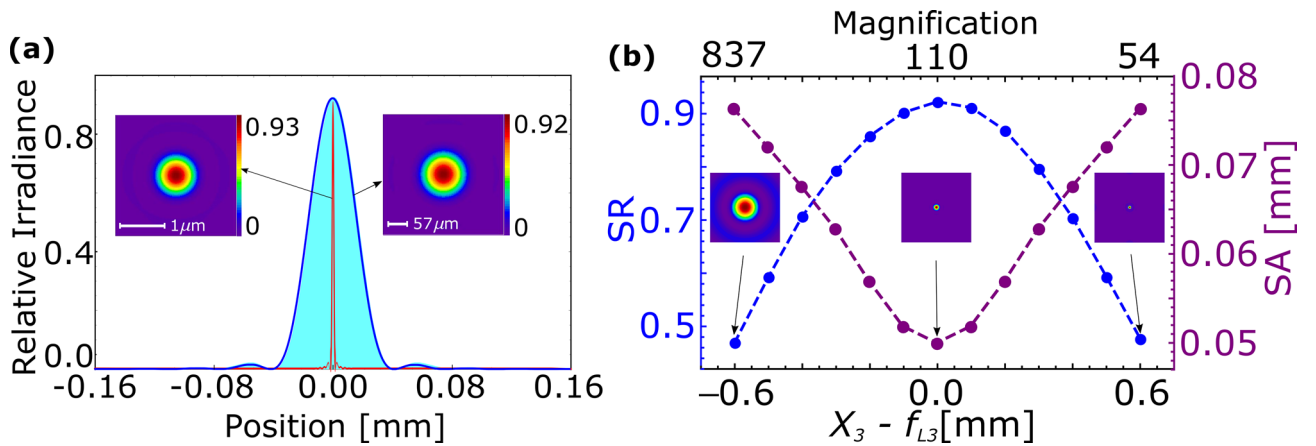


Figure 3. (a) Point spread functions (PSF) simulated by OSLO (blue), and calculated from analytical relation (filled with cyan) at the final image of the L_0 -O1-M1 combination. The PSF at the intermediate image plane (red) is shown for comparison. (b) Variations of SR (blue) and SA (purple) due to deviation of magnifier M1 from its ideal position i.e. $X_3 = f_{L3}$ is shown, which tunes the magnification. Images are shown in the insets for a glance quality comparison.

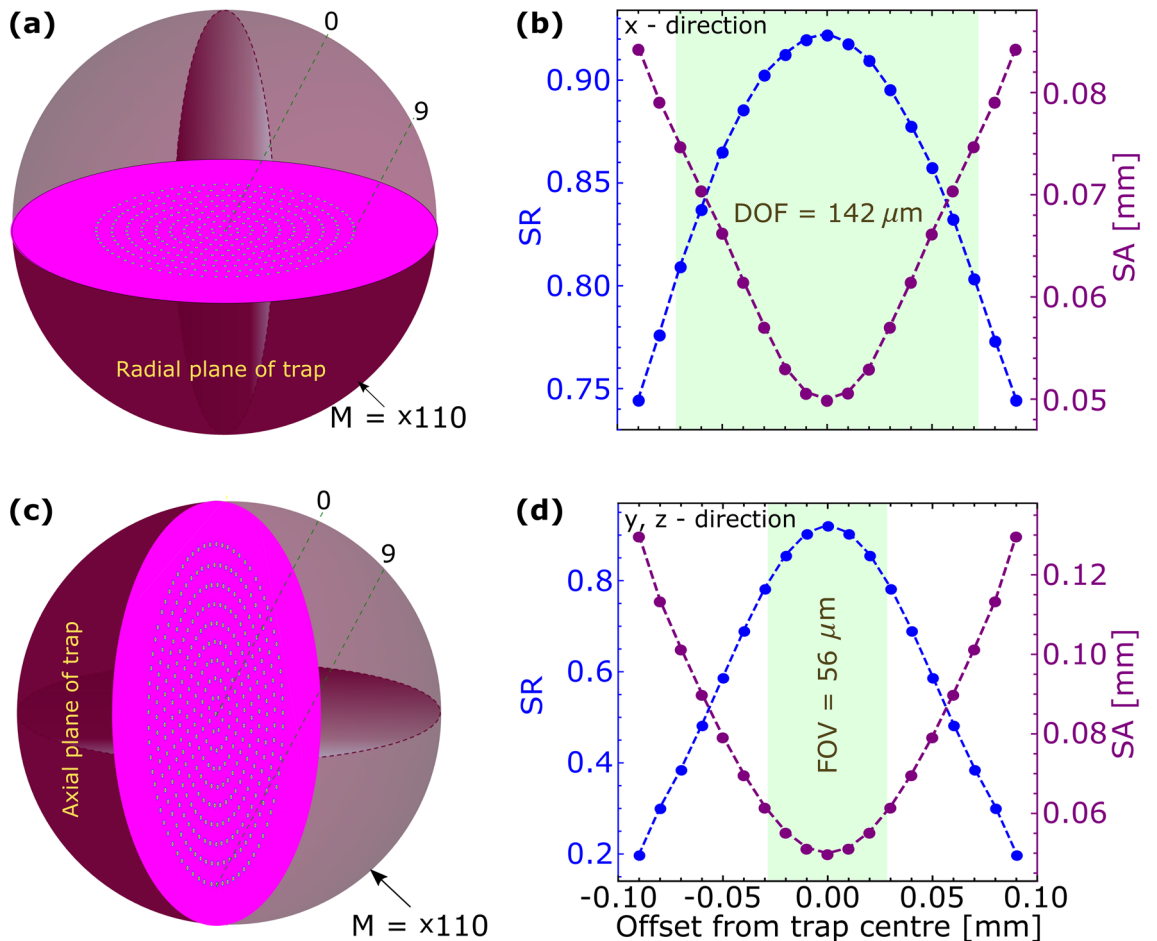


Figure 4. Images of trapped ions on (a) xy , (c) yz planes. (b) and (d) shows corresponding variation of SR and SA as the ion's position deviates from best focus. Depth of field (DOF) and Field of View (FOV) are indicated.

from this, we have also calculated the allowable decenter and tilt tolerances for the 2 inch optics assembly to be mounted in optics tube. To maintain an $SR \geq 0.8$, estimated tolerances in decentration and tilt are $\leq 450 \mu\text{m}$ and $\leq 0.22^\circ$, respectively. Deviation of X_0 from f_{L_0} occurs from inaccurate positioning of L_0 or shifting of the trap centre. Since L_0 is inaccessible on regular basis, we studied dynamic range of its position over which SA and SR can be corrected by the external objective-magnifier combination. Figure 5a shows the change of SR and SA due

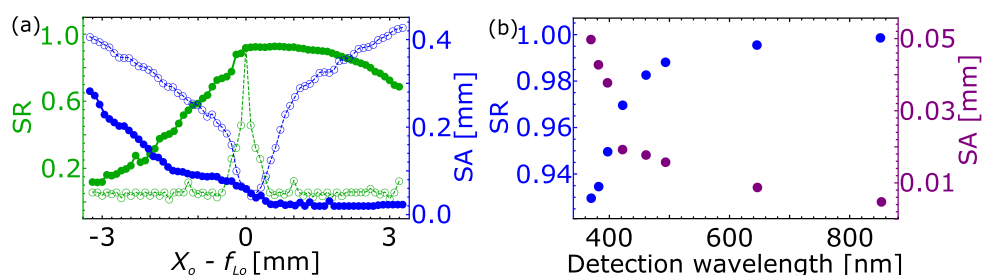


Figure 5. (a) Change in SR (green empty circle) and SA (blue empty circle) values of the images due to inaccurate positioning of the collection lens L_o with respect to its focus f_{L_o} . Corresponding SR (green full circle) and SA (blue full circle) after incorporating corrections by tuning the magnifier's position are also shown. (b) SR and SA at different wavelengths (corresponding to different species), e.g., 369.5 nm (Yb^+), 382 nm (Ra^+), 397 nm (Ca^+), 422 nm (Sr^+), 461 nm (Sr), 493.5 nm (Ba^+), 646 nm (Lu^+) and 852 nm (Cs).

λ (nm)	Species	σ (λ)	l_R (μm)	X_o (mm)	M	FOV (μm)
369.5	Yb^+	0.042 (2)	0.68 (3)	31.60 (1)	73 (1)–238 (3)	56 (2)
382	Ra^+	0.039 (2)	0.71 (1)	31.81 (1)	72 (1)–289 (3)	58 (2)
397	Ca^+	0.034 (1)	0.74 (1)	31.99 (3)	65 (1)–243 (2)	62 (2)
422	Sr^+	0.029 (3)	0.79 (1)	32.28 (3)	62 (2)–311 (1)	66 (2)
461	Sr	0.023 (1)	0.87 (1)	32.61 (1)	56 (3)–310 (1)	74 (3)
493.5	Ba^+	0.019 (2)	0.94 (3)	32.82 (2)	52 (1)–328 (5)	78 (2)
646	Lu^+	0.011 (1)	1.25 (3)	33.45 (3)	45 (3)–982 (7)	99 (3)
852	Cs	0.006 (1)	1.67 (2)	33.87 (3)	38 (4)–1192 (9)	128 (3)

Table 3. Estimated values of various optical excellence parameters obtained using OSLO for wavelengths corresponding to different atom/ion species.

to deviation of X_o from f_{L_o} and their post corrected values incorporated by tuning distance between O1–M1. We found, SA and SR can be significantly corrected for deviation of $X_o - f_{L_o}$ from -0.4 to 2.6 mm, which is better than the other objective-magnifier combinations and makes it user friendly. In Fig. 5b, we show that on optimization of X_o and X_3 , the described imaging system gives favorable results for SR and SA at different wavelengths covering from visible to near infrared corresponding to the elements Yb^+ , Ra^+ , Ca^+ , Sr^+ , Sr, Ba^+ , Lu^+ and Cs. Values of other parameters describing the optical performance are stated in Table 3. Values of $\sigma < 0.07\lambda$ in all cases and a good magnification range confirms an acceptable performance of the system. Hence, the design can be adapted for applications other than Yb^+ as well.

Conclusion

The design criteria together with its detailed performance of an easily buildable imaging system that can resolve particles at sub-micron level is investigated among a wide variety in this article. The finally opted lens system consists of standard catalog optics: aspheres and aberration corrector plates. This makes the system user friendly. In comparison to previous works those use multiple lenses, we achieved higher NA of 0.33 with only one asphere and two corrector plates. The system is advantageous as the image quality due to the axial misalignment of the collection lens by -0.4 mm to $+2.6$ mm can be corrected by readjustment in the later optics. The diffraction limited optics is able to recollect 77% photons to the central disc and produce images upto $\times 238$ magnification for the objects that are separated by as minimum as $0.68 \mu\text{m}$ with minimum spherical aberrations. Each particle in a large ensemble can be detected by this system as it has depth of field and field of view of $142 \mu\text{m}$ and $56 \mu\text{m}$, respectively. In addition, the system is usable over wider wavelength range thus making it suitable to opt for different experiments.

Data availability

The data generated or analysed during this study have been included in this paper.

Received: 13 July 2020; Accepted: 20 November 2020

Published online: 11 December 2020

References

1. van Amstalden, H. E. R., Smith, D. F. & Heeren, R. M. A. A concise review of mass spectrometry imaging. *J. Chromatogr. A* **1217**, 3946 (2010).

2. Feenstra, A. D., Dueñas, M. E. & Lee, Y. J. Five micron high resolution MALDI mass spectrometry imaging with simple, interchangeable, multi-resolution optical system. *J. Am. Soc. Mass Spectrom.* **28**, 434 (2017).
3. Pinkse, P. W. H., Fischer, T., Maunz, P. & Rempe, P. Trapping an atom with single photons. *Nature* **404**, 365 (2000).
4. Boca, A. *et al.* Observation of the vacuum rabi spectrum for one trapped atom. *Phys. Rev. Lett.* **93**, 233603 (2004).
5. Volz, J. *et al.* Observation of entanglement of a single photon with a trapped atom. *Phys. Rev. Lett.* **96**, 030404 (2006).
6. Fortson, N. Possibility of measuring parity nonconservation with a single trapped atomic ion. *Phys. Rev. Lett.* **70**, 2383 (1993).
7. Blinov, B. B., Moehring, D. L., Duan, L. M. & Monroe, C. Observation of entanglement between a single trapped atom and a single photon. *Nature* **428**, 153 (2004).
8. Huntemann, N., Sanner, C., Lipphardt, B., Tamm, C. & Peik, E. Single-ion atomic clock with 3×10^{-18} systematic uncertainty. *Phys. Rev. Lett.* **116**, 063001 (2016).
9. Brewer, S. M. *et al.* $^{27}\text{Al}^+$ quantum-logic clock with a systematic uncertainty below 10^{-18} . *Phys. Rev. Lett.* **123**, 033201 (2019).
10. Shu, G., Kurz, N., Dietrich, M. R. & Blinov, B. B. Efficient fluorescence collection from trapped ions with an integrated spherical mirror. *Phys. Rev. A* **81**, 042321 (2010).
11. Kielpinski, D., Monroe, C. & Wineland, D. J. Architecture for a large-scale ion-trap quantum computer. *Nature* **417**, 709 (2002).
12. Leibfried, D., Blatt, R., Monroe, C. & Wineland, D. J. Quantum dynamics of single trapped ions. *Rev. Mod. Phys.* **75**, 281 (2003).
13. Streed, E. W., Norton, B. G., Jechow, A., Weinhold, T. J. & Kielpinski, D. Imaging of trapped ions with a microfabricated optic for quantum information processing. *Phys. Rev. Lett.* **106**, 010502 (2011).
14. Agarwal, G. S., Ariunbold, G. O., von Zanthier, J. & Walther, H. Nonclassical imaging for a quantum search of trapped ions. *Phys. Rev. A* **70**, 063816 (2004).
15. Wong-Campos, J. D., Johnson, K. G., Neyenhuis, B., Mizrahi, J. & Monroe, C. High-resolution adaptive imaging of a single atom. *Nat. Photonics* **10**, 606 (2016).
16. Landsman, K. A. Verified quantum information scrambling. *Nature* **567**, 61 (2019).
17. Wright, K. *et al.* Benchmarking an 11-qubit quantum computer. *Nat. Commun.* **10**, 5464 (2019).
18. Raussendorf, R. & Briegel, H. J. A one-way quantum computer. *Phys. Rev. Lett.* **86**, 5188 (2001).
19. Palmer, R. N., Moura Alves, C. & Jaksch, D. Detection and characterization of multipartite entanglement in optical lattices. *Phys. Rev. A* **72**, 042335 (2005).
20. Cho, J. Addressing individual atoms in optical lattices with standing-wave driving fields. *Phys. Rev. Lett.* **99**, 020502 (2007).
21. Gorshkov, A. V., Jiang, L., Greiner, M., Zoller, P. & Lukin, M. D. Coherent quantum optical control with subwavelength resolution. *Phys. Rev. Lett.* **100**, 093005 (2008).
22. Nelson, K. D., Li, X. & Weiss, D. S. Imaging single atoms in a three-dimensional array. *Nat. Phys.* **3**, 556 (2007).
23. Gericke, T., Würtz, P., Reitz, D., Langen, T. & Ott, H. High-resolution scanning electron microscopy of an ultracold quantum gas. *Nat. Phys.* **4**, 949 (2008).
24. Alt, W. An objective lens for efficient fluorescence detection of single atoms. *Optik* **113**, 142 (2002).
25. Sortais, Y. R. P. *et al.* Diffraction-limited optics for single-atom manipulation. *Phys. Rev. A* **75**, 013406 (2007).
26. Karski, M. Nearest-neighbor detection of atoms in a 1D optical lattice by fluorescence imaging. *Phys. Rev. Lett.* **102**, 053001 (2009).
27. Bakr, W. S., Gillen, J. I., Peng, A., Fölling, S. & Greiner, M. A quantum gas microscope for detecting single atoms in a Hubbard-regime optical lattice. *Nature* **462**, 74 (2009).
28. Hu, S., Maslo, K. & Wang, L. V. Second-generation optical-resolution photoacoustic microscopy with improved sensitivity and speed. *Opt. Lett.* **36**, 1371 (2011).
29. Sharma, L., Roy, A., Panja, S., Ojha, V. N. & De, S. Estimation of the ion-trap assisted electrical loads and resulting BBR shift. *Sci. Rep.* **8**, 16884 (2018).
30. González-Acuña, R. G. & Chaparro-Romo, H. A. General formula for bi-aspheric singlet lens design free of spherical aberration. *App. Opt.* **57**, 9341 (2018).
31. Smith, W. J. *Modern Optical Engineering* (McGraw-Hill, New York, 2008).
32. Wyant, J. C. & Creath, K. *Applied Optics and Optical Engineering* (Academic press Inc, Cambridge, 1992).
33. Gris-Sanchez, I., van Ras, D. & Birks, T. A. The Airy fiber: an optical fiber that guides light diffracted by a circular aperture. *Optica* **3**, 2 (2016).
34. Mijs, A. & Novak, J. Point spread function of an optical system with defocus and spherical aberration—analytical formulas. *Appl. Opt.* **58**, 5823 (2019).
35. OSLO Premium Edition, Revision 7.0.2, Copyright© 2001–2017 Lambda Research Corporation. <http://www.lambdaresearch.com/wp-content/uploads/support/oslo/osloedu/oslouseruide>. Accessed 8 July 2019.
36. Strehl, K. Aplanatische und fehlerhafte Abbildung im Fernrohr. *Z. Instrum.* **15**, 362 (1895).
37. Strehl, K. Ueber Luftschlieren und Zoenfehler. *Z. Instrum.* **22**, 213 (1902).
38. Mahajan, V. N. Strehl ratio for primary aberrations: some analytical results for circular and annular pupils. *J. Opt. Soc. Am.* **72**, 1258 (1982).
39. Mahajan, V. N. Strehl ratio for primary aberrations in terms of their aberration variance. *J. Opt. Soc. Am.* **73**, 860 (1983).
40. Maréchal, A. Study of the combined effects of diffraction and geometrical aberrations on the image of a luminous point. *Rev. Opt. Theor. Instrum.* **26**, 257 (1947).
41. James, D. F. V. Quantum dynamics of cold trapped ions with application to quantum computation. *Appl. Phys. B* **66**, 181 (1998).
42. Rastogi, A. *et al.* Design of the ion trap and vacuum system for ^{171}Yb -ion optical frequency standard. *MAPAN J. Met. Soc. India* **30**, 169 (2015).
43. Batra, N., Sahoo, B. K. & De, S. An optimized ion trap geometry to measure quadrupole shifts of $^{171}\text{Yb}^+$ clocks. *Chin. Phys. B* **25**, 113703 (2016).
44. Gross, H., Zügge, H., Peschka, M. & Blechinger, F. *Handbook of Optical Systems, Aberration Theory and Correction of Optical Systems* 1–756 (Wiley, Hoboken, 2015).

Acknowledgements

We acknowledge CSIR-National Physical Laboratory and IUCAA for supporting this work. LS thanks Department of Science and Technology (DST) for Inspire fellowship and SD thanks DST for financial support through Quantum Enhanced Science & Technology program.

Author contributions

S.D. conceptualized the technique and supervised the entire work as reported here. L.S. and S.D. performed the theoretical analysis. L.S. performed the simulations. L.S., A.R. and S.D. discussed the results to obtain the most suitable technique. L.S. and S.D. have written the article; A.R. and S.P. provided useful inputs to refine that.

Competing Interests

The authors declare no competing interests.

Additional information

Supplementary Information The online version contains supplementary material available at <https://doi.org/10.1038/s41598-020-78509-6>.

Correspondence and requests for materials should be addressed to S.D.

Reprints and permissions information is available at www.nature.com/reprints.

Publisher's note Springer Nature remains neutral with regard to jurisdictional claims in published maps and institutional affiliations.



Open Access This article is licensed under a Creative Commons Attribution 4.0 International License, which permits use, sharing, adaptation, distribution and reproduction in any medium or format, as long as you give appropriate credit to the original author(s) and the source, provide a link to the Creative Commons licence, and indicate if changes were made. The images or other third party material in this article are included in the article's Creative Commons licence, unless indicated otherwise in a credit line to the material. If material is not included in the article's Creative Commons licence and your intended use is not permitted by statutory regulation or exceeds the permitted use, you will need to obtain permission directly from the copyright holder. To view a copy of this licence, visit <http://creativecommons.org/licenses/by/4.0/>.

© The Author(s) 2020

Atomic flux distribution from a low-divergent dark wall oven

Cite as: Rev. Sci. Instrum. **90**, 053202 (2019); <https://doi.org/10.1063/1.5090199>
Submitted: 25 January 2019 . Accepted: 20 April 2019 . Published Online: 10 May 2019

 Lakhi Sharma,  A. Roy,  S. Panja, and  S. De



View Online



Export Citation



CrossMark

ARTICLES YOU MAY BE INTERESTED IN

[A simple atomic beam oven with a metal thermal break](#)

Review of Scientific Instruments **90**, 053106 (2019); <https://doi.org/10.1063/1.5067306>

[Effusive atomic oven nozzle design using an aligned microcapillary array](#)

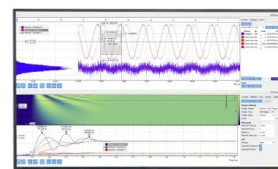
Review of Scientific Instruments **86**, 023105 (2015); <https://doi.org/10.1063/1.4907401>

[A compact and efficient strontium oven for laser-cooling experiments](#)

Review of Scientific Instruments **83**, 103101 (2012); <https://doi.org/10.1063/1.4756936>

Challenge us.

What are your needs for
periodic signal detection?



Zurich
Instruments

Atomic flux distribution from a low-divergent dark wall oven

Cite as: Rev. Sci. Instrum. 90, 053202 (2019); doi: 10.1063/1.5090199

Submitted: 25 January 2019 • Accepted: 20 April 2019 •

Published Online: 10 May 2019



View Online



Export Citation



CrossMark

Lakhi Sharma,^{1,2}  A. Roy,^{1,2}  S. Panja,^{1,2}  and S. De^{1,2,a)} 

AFFILIATIONS

¹CSIR–National Physical Laboratory, Dr. K. S. Krishnan Marg, New Delhi 110012, India

²Academy of Scientific and Innovative Research (AcSIR), Ghaziabad 201002, India

^{a)}Electronic mail: subhadeep@nplindia.org.

ABSTRACT

Nearly collimated atomic beam is of interest for a variety of experiments. This article reports a simple way of modifying the atomic beam distribution using a dark wall oven and describes detailed study of outgoing atoms' spatial distribution. A simple design is obtained by employing the fact that inhomogeneous thermal distribution along a capillary results due to its partial resistive heating. Based on this phenomenon, we have designed a dark wall oven consisting of a reservoir, collimator, and cold absorber at the exit end of atoms, where all three are fabricated out of a single stainless steel capillary. The nearly collimated spatial distribution of the atoms resulting due to the absorber eliminating the atoms diverging above a certain angle is modeled and experimentally verified. A divergence as minimum as $1.2(1)^\circ$ corresponding to a half angle $\theta_{1/2} = 0.9(1)^\circ$ is measured at an oven temperature of 250°C that produces an atomic flux of about 8×10^9 atoms s^{-1} . Total flux as estimated using our measured spatial distribution of atoms matches well with the numerically simulated values of it for the dark wall oven.

Published under license by AIP Publishing. <https://doi.org/10.1063/1.5090199>

I. INTRODUCTION

Atoms are the basis of many advanced techniques aiming for scientific investigations as well as for state-of-the-art technologies. An atomic source is a common requisite in all such techniques where high flux, collimated beam, and unwanted deposition in the vicinity of the experimental volume are specific to the experiment. Depending on the atomic species, oven temperature varies; hence, different heating methods such as resistive,¹ electron bombardment,^{2,3} and inductive^{4,5} are being used. Along with that, different oven geometries are used to produce intense^{6–9} and collimated^{10–13} sources. Resistive heating is widely used up to 1200°C ^{14–19} as temperature control becomes easy by regulating the current flow.^{18,20–23} For collimation, a long tube is used which is further modified with multi-channel^{24,25} and microcapillary arrays^{9,26} to increase the atomic flux. Electron bombardment and inductive heating methods are widely used for heating up to 1800°C ²⁷ and above 2000°C ,^{28,29} respectively. The ovens can have complex designs depending on specific requisites or choice of samples. Spatial distribution of atoms depends on the oven geometry, whereas their velocity distribution depends on the temperature. In case it is required, velocity distribution of

the atoms is modified by the laser cooling technique, as an example, whereas controlling of its spatial distribution can be achieved by proper choice of the oven geometry; dark wall oven³⁰ is one such example.

In order to restrict deposition of the unused atoms at the experimental region of interest as that introduces certain systematic,^{13,31,32} many efforts are made to produce nearly collimated atomic beam.^{8,9,12} Thus, studying atoms' distribution pattern is always a subject of interest.^{25,33–39} Clausing modeled the angular distribution of molecules emerging from cylindrical tubes and analyzed their dimensional dependency,³³ which was later experimentally verified by Dayton.³⁴ Giordmaine and Wang studied peak beam intensities and beam widths from array of long tubes stacked in different shapes.³⁵ The predicted theory justifies only the centerline intensity since it assumed zero number density at the nozzle end of the tube. Olander and Kruger modified that with finite number density at the nozzle end.²⁵ Furthermore, they experimentally verified their model for a multichannel source³⁶ and demonstrated its dependency on the source size.³⁷ Beijerinck and Verster measured the velocity and angular distribution of the atomic beam produced from multichannel arrays in both transparent and opaque modes.²⁴ Krasuski

studied the shapes of angular distribution at different exit zones of a tube which leads to better understanding of the atomic flux pattern.⁴⁰

In this article, we studied the modified spatial distribution of atomic flux coming out of a dark wall oven: theoretically modeled the distribution function, experimentally verified it, and compared it with bright collimating ovens. For this purpose, we developed a simple dark wall oven resulting from nonhomogeneous thermal distribution due to partial heating of a single capillary. This delivers a low-divergent atomic flux that has been tested to produce an Ytterbium (Yb) atomic beam. Due to the dark wall at the exit end, spatial distribution is truncated above an angle. The Finite Element Method (FEM) by using COMSOL Multiphysics® software is performed for studying the thermal distribution throughout of the capillary. This facilitates to choose the suitable oven design parameters. Section II of this article describes details of the oven design and theoretical model of the outgoing atoms' angular distribution pattern. Experimental results and associated discussions are given in Sec. III.

II. OVEN DESIGN AND ITS ATOMIC FLUX DISTRIBUTION

The design of the oven and theoretical model of its expected atomic flux distribution are described in this section. The oven, as shown in Fig. 1(a), consists of a reservoir, a collimating tube, and a cold part at the exit. The oven is operated in the transparent mode, i.e., the ratio of Mean Free Path (MFP) $\lambda = kT/\sqrt{2}\pi d^2 P_{\text{vap}}$ to diameter of the collimating tube $2a$, i.e., the Knudsen number $K_n > 1$.⁴¹ Here, d is the atom's diameter and the vapor pressure is

$$\log P_{\text{vap}} = A + BT^{-1} + C \log T + DT^{-3}, \quad (1)$$

with A , B , C , and D being coefficients for a particular species. In this mode, $\lambda > L > 2a$ leads to free molecular flow in which majority of particles move along a straight path until hitting the wall since atom-atom collisions are suppressed. The aspect ratio of the collimating tube $2a/L$ defines the atomic beam flux as well as its angular divergence. Atoms are stored at the starting end of the capillary which acts as a reservoir where atomic vapor is produced and that propagates through the collimating tube. At the end of the collimating tube, the capillary is partially used as a dark wall, i.e., a cold

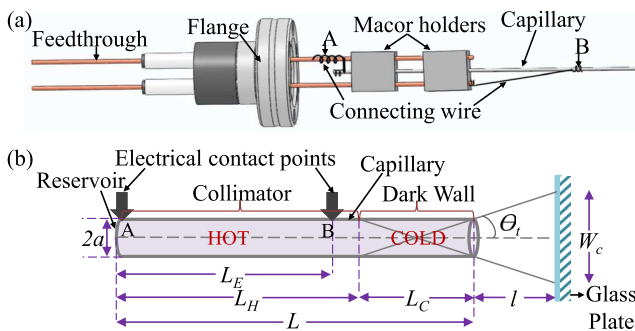


FIG. 1. (a) Drawing of the dark wall oven and its holders for UHV mounting. (b) Schematic of the capillary consisting of three regions: reservoir, collimator, and dark wall.

absorber to truncate the off-axis atoms above a certain angle. In the previously reported dark wall ovens, the reservoir, collimator, and absorber are separate units and assembled together.^{17,18,42} In our simple design, these are made out of a single 316L stainless steel (SS) capillary of inner diameter 0.9 mm and the regions are distinguishable by temperature. Thus, it is easy to mount the oven inside a vacuum chamber. The reservoir end of the capillary is spot welded to a heating wire and closed to stop atoms from exiting. The other electrical contact is separated by a length L_E ($L_E < L$) so that current flows partially through the capillary and the end part of it stays at lower temperature since thermal loss is dominating there [Fig. 1(b)]. By controlling the current's path, the capillary is inhomogeneously heated to create three regions widely separated in temperature. A tungsten wire of AWG 27 is used for electrical contacting of the capillary to the feedthrough pins owing to its high tensile strength of 100 000–500 000 psi at room temperature, a good thermal conductivity of 173 W/m·K, and a high melting point of 3422 °C. Two Macor blocks of dimensions 12 mm × 8 mm × 10 mm are used for holding the capillary along their midway and also for firm mounting of it to the conducting pins of a standard CF16 electrical feedthrough. The cold end truncates the angular distribution at $\theta_i = \tan^{-1}(2a/L_C)$ since atoms traveling beyond that stick to the dark wall at a rate $2\pi a L_C n_o \bar{v}/4$, where $\bar{v} = \sqrt{8kT/\pi m}$ is average thermal velocity. Thus, the expected atomic beam width on a plane, e.g., glass plate placed at a distance l from the exit end of the capillary is,

$$W_c = 2a \left(1 + \frac{2l}{L_C}\right). \quad (2)$$

This assumes that atoms that do not collide the wall are only coming out, which is correct for the atoms having a negligible effusion coefficient at the cold end's temperature.

The vaporized atoms with density n_o within the reservoir are equally probable to move along any direction with a flow rate

$$d^3 \dot{N} = I(\theta) P(v) d^2 \Omega dv, \quad (3)$$

within a solid angle $d\Omega$. Here, $I(\theta)$ and $P(v) = 32v^3 \exp(-4v^2/\pi \bar{v}^2)/\pi^2 \bar{v}^4$ are the angular intensity and the normalized velocity distributions, respectively, for the atoms moving at a speed v along θ relative to the tube's axis. The angular distribution follows

$$\dot{N} = \int_{-\pi}^{\pi} I(\theta) d^2 \Omega = \frac{2\pi n_o \bar{v} a^3}{3L}, \quad (4)$$

where \dot{N} is the flow rate of atoms through a transparent tube.²⁴ Angular distribution of atoms exiting a wall strip of width dz situated at a distance z from the reservoir end is given as³⁵

$$dI(\theta) = \frac{n_o z \bar{v}}{4\pi L_H} 2a \sin \theta \left[1 - \left(\frac{z \tan \theta}{2a}\right)^2\right]^{\frac{1}{2}} dz, \quad (5)$$

where $n(z)$ is the atom's density. The centerline atomic intensity is $I(0) = n_o \bar{v} a^2/4$. The critical angle $\theta_C = \tan^{-1}(2a/L_H)$ is obtained from the geometry [Fig. 1(b)], up to which atoms exit from the collimation tube without colliding with its wall. At half angle $\theta_{\frac{1}{2}} = 1.68a/L_H$, the atomic intensity becomes $I(\theta_{\frac{1}{2}}) = I(0)/2$. The angular distribution has two components: (i) atoms that are flowing with and without hitting the wall $I_u(\theta)$, which dominates up to θ_C , and (ii) atoms effusing out after hitting the wall $I_w(\theta)$, which

dominates at $\theta > \theta_C$. The distribution functions as given in Ref. 35 are

$$\begin{aligned}
 I_u(\theta) &= \frac{n_0 \bar{v}}{4\pi} 2a^2 \cos \theta \left[\cos^{-1}(p) - p\sqrt{1-p^2} \right] \\
 &+ \int_0^{L_H} \frac{n(z) \bar{v}}{4\pi} 2a \sin \theta \left[1 - \left(\frac{z \tan \theta}{2a} \right)^2 \right]^{\frac{1}{2}} dz \\
 &= \frac{a^2 n_0 \bar{v}}{2\pi} \left[R(\theta) + \frac{2}{3} P(\theta) \right] \cos \theta, \quad 0 < \theta \leq \theta_C, \\
 I_w(\theta) &= \int_0^{2a/\tan \theta} \frac{n(z) \bar{v}}{4\pi} 2a \sin \theta \left[1 - \left(\frac{z \tan \theta}{2a} \right)^2 \right]^{\frac{1}{2}} dz \\
 &= \frac{2a^3 \bar{v} n_0 \cos^2 \theta}{3\pi L_H \sin \theta}, \quad \theta_C < \theta < \pi/2,
 \end{aligned} \tag{6}$$

where $R(\theta) = \cos^{-1}(p) - p\sqrt{1-p^2}$, $P(\theta) = [1 - (1-p^2)^{\frac{3}{2}}]/p$, and $p = L_H \tan \theta / 2a$. Thus, the relative angular profiles, i.e., $f(\theta) = I(\theta)/I(0)$, are

$$\begin{aligned}
 f_u(\theta) &= \frac{2}{\pi} \left[R(\theta) + \frac{2}{3} P(\theta) \right] \cos \theta, \quad 0 \leq \theta \leq \theta_C, \\
 f_w(\theta) &= \frac{8a}{3\pi L_H} \frac{\cos^2 \theta}{\sin \theta}, \quad \theta_C \leq \theta \leq \pi/2,
 \end{aligned} \tag{7}$$

which are obtained following Giordmaine and Wang's approach.^{24,35,43} The modified equation following the Olander and Kruger model²⁵ considering nonzero number densities at the source and exit ends of the tube is

$$\begin{aligned}
 f'_u(\theta) &= \zeta_0 \cos \theta + \frac{2}{\pi} \cos \theta \left[\zeta_1 R(\theta) + \frac{2}{3} (\zeta_1 - \zeta_0) P(\theta) \right], \\
 &0 < \theta \leq \theta_C, \\
 f'_w(\theta) &= \zeta_0 \cos \theta + \frac{8a}{3\pi L_H} (\zeta_1 - \zeta_0) \frac{\cos^2 \theta}{\sin \theta}, \quad \theta_C \leq \theta \leq \pi/2.
 \end{aligned} \tag{8}$$

Here, dimensionless parameters $\zeta_0 = 4a/3L$ and $\zeta_1 = (1 - \zeta_0)$ are related to the wall collision rates at the entrance and exit of the capillary, respectively. Figure 2 compares angular profiles of outgoing atoms from effusive ovens with and without collimation, following $L \gg 2a$ and $L < 2a$, respectively. For comparison, truncated distribution from a dark wall oven is also shown there. The angles θ_C , θ_t , and $\theta_{\frac{1}{2}}$ for different aspect ratios of the collimator and the dark wall tubes are shown in the inset, which suggests that stronger collimation can be obtained at longer collimator lengths but at a cost of lower throughput. It is to be noted that the truncated angular distribution expected from a collimator followed by a dark wall has similar nature like θ_C , but they operate at different length scales defined by values of L_H and L_C . Atoms at the tail of the distribution are mostly not useful since they are beyond the capturing capability of a trapped atom experiment; hence, truncation is not inefficient for the atom loading. The rate of flow of atoms up to a velocity v and angle θ can be obtained as

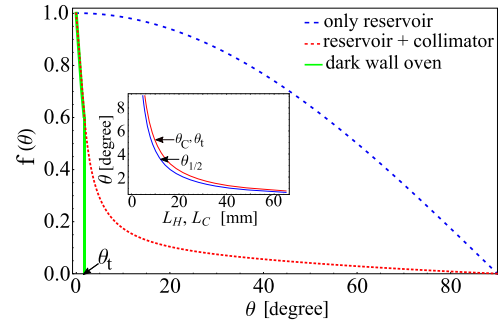


FIG. 2. Angular profile of atoms for different ovens such as reservoir (blue), reservoir attached to a collimator (red), and dark wall oven (green). The inset shows the critical and truncated angle (red) and half-width angle (blue) for different lengths of the capillary. Here, we consider $T = 249$ °C, $L = 65$ mm, $L_H = 35$ mm, $L_C = 30$ mm, and $a = 0.45$ mm.

$$\begin{aligned}
 F_v^\theta \left(\frac{a}{L}, \frac{a}{L_H}, T \right) &= \dot{N} \int_0^\theta F(\theta) 2\pi \sin \theta d\theta \int_0^v P(v) dv \\
 &= \frac{\dot{N}}{2\pi} \left[\pi \sin^2 \theta + (\zeta_1 - \zeta_0) (\sin 2\theta - 2\theta_C - 2\theta) \right] \\
 &\quad \times \left[1 - \exp \left(-\frac{4v^2}{\pi \bar{v}^2} \right) \left(1 + \frac{4v^2}{\pi \bar{v}^2} \right) \right].
 \end{aligned} \tag{9}$$

Here, $F(\theta) = \kappa f'(\theta)/\pi$ is the normalized angular distribution function where $\kappa = \pi I(0)/\dot{N} = 3L/8a$ ²⁴ is the “peaking factor” that characterizes the degree of collimation. In the spirit of our trapped Ytterbium (Yb^+) optical clock experiment,^{44–50} as an example, the maximum velocity v_{cap} that can be captured in the ion trap is defined by its depth $D_{trap} = a^2 Q r^2 V^2 / (4mR^4 \Omega^2)$, which depends on the trapping voltage, V . Here, a and z are trap geometry specific parameters, V is the applied voltage at radio-frequency Ω , Q is the charge, and R is the radius of the trapping volume. The maximum θ can be either θ_t or the maximum capturing angle by the trap depending on whichever is smaller.

III. EXPERIMENTAL RESULT AND DISCUSSION

We used “Electric Currents” and “Fluid Flow” submodules of COMSOL to study the steady state temperature variation and atomic flux flow, respectively, through the microchannel SS capillary. The temperature distribution in the capillary for its different heating configurations is simulated to obtain the desired temperature distribution distinguishing the reservoir, collimator, and dark wall regions. We define a critical oven temperature T_C at which the output flow rate is negligible to use. In the case of an inhomogeneously heated capillary, the point at T_C defines L_H . The capillary's length over which $T > T_C$ acts as the collimator, and the rest of it acts as the dark wall. Although we considered a wide variety of capillary geometries for simulations to identify the suitable one, we report here the results obtained for $L = 65$ mm, $a = 0.45$ mm, and $L_E = 40$ mm giving a variety of L_H and L_C at different currents that we finally used to construct the oven. In the case of heating the entire capillary, i.e., $L_E = L = L_H$ and $L_C = 0$, inhomogeneity

of the temperature distribution is within the accuracy of the simulation, as shown in Fig. 3(a) for different currents. In this case, the entire capillary acts as the collimator, and the current regulated reservoir temperature is shown in Fig. 3(b). Partial heating of the capillary from the reservoir end up to some intermediate point, as an example $L_E = 40$ mm, at different currents is shown in Fig. 3(c). Figure 3(d) clearly shows that for a fixed L_E , the collimator's length L_H increases with stronger heating. Thus, a proper choice of the electrical contact points and current results in a desired length of the dark wall. As obtained from the FEM analysis, we consider $T_C \approx 175^\circ\text{C}$ at which output flux is two orders of magnitude smaller than the desired and this matches well with our experimental observation as described later. The response times of the dark wall oven to reach 250°C and 350°C from the room temperature are 378 s and 402 s, respectively, as obtained by using the FEM analysis, whereas it takes 94 s and 171 s to reach these temperatures from T_C . Thus, rather than reducing the reservoir temperature to room temperature, it may be set near to T_C while the oven is in frequent use. Figure 4(a) shows temperature dependency of vapor pressure and MFP of ^{171}Yb atoms that satisfy $K_n > 1$ at $T > 127^\circ\text{C}$. The temperature dependent output flow rate of atoms following Eq. (4) and their simulated values are shown in Fig. 4(b). The abrupt increase in the flow rate at $T_C = 175^\circ\text{C}$ is highlighted in the figure. As expected, the dark wall oven produces lower flow rate owing to the truncation of off-axis atoms. Figures 4(c) and 4(d) show capturable atoms

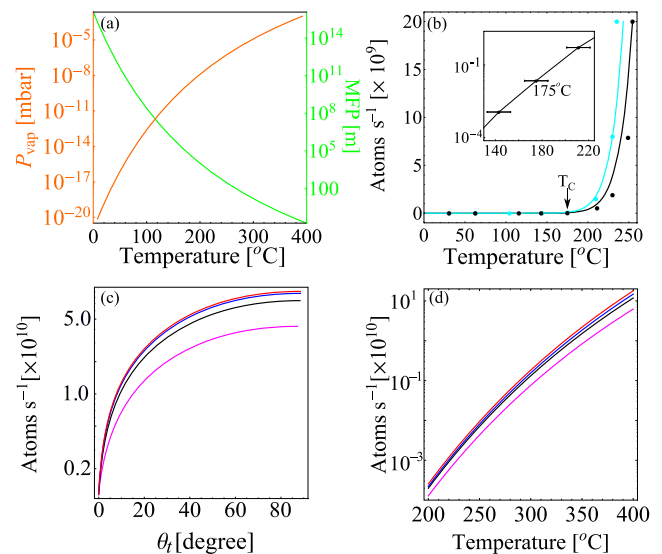


FIG. 4. (a) Variation of Yb vapor pressure (orange) and its mean free path (green) with temperature. (b) Output Yb flux with increasing temperature for a bright oven with collimator (cyan) and a dark wall oven (black) is shown. The discrete points in cyan and black are the corresponding numerical values the inset emphasizes the critical temperature. Flux of atoms at different (c) cutoff angles and (d) oven temperatures for a fixed trap electrode voltage of 250 V (magenta), 350 V (black), 450 V (blue), and 550 V (red) that are available to be captured in our ion trap.

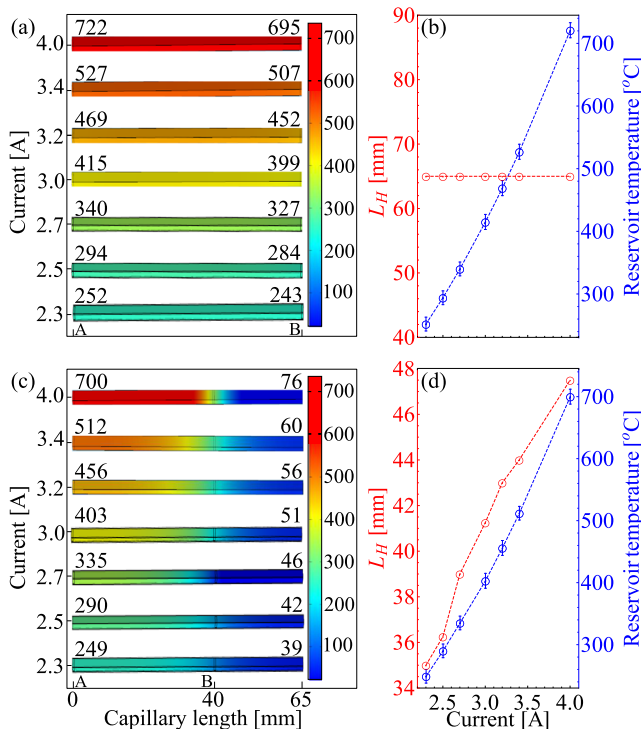


FIG. 3. Numerically simulated variation of temperature (in $^\circ\text{C}$) along the length of the capillary for ovens with a (a) collimator and (c) collimator and cold absorber. (b) and (d) show variation of the collimator's length L_H with current and corresponding reservoir temperature for a fixed operating voltage = 1.7 V.

for different θ_t and oven temperatures, respectively, estimated using Eq. (9). Typically, ions up to a velocity v_{cap} corresponding to 10% of the trap depth can be captured in an ion trap. Considering our ion trap, which captures all atoms up to θ_t and operates at $\Omega = 2\pi \times 15$ MHz and with 45% RF transfer efficiency to the trap electrodes,⁵⁰ we have estimated D_{trap} and hence the maximum capture velocity. As an example, for the oven operating at 300°C and $v_{\text{cap}} \approx 535$ m/s, in case the ion trap operates at 1000 V RF, about 1.6×10^9 ions/s will be available for capturing, assuming 100% ionization of the atoms.

We have tested the performance of our dark wall oven to produce a ^{171}Yb atomic beam and compared the obtained flux distribution with the predicted model. The oven is tested at different currents as the simulation shown in Fig. 3 while heating the entire capillary and also for different cold end lengths during the dark wall mode of its operation. For all the measurements, the oven was kept at 10^{-9} mbar vacuum, $L = 65$ mm and for a fixed run time of 36 h while the spots were recorded on a glass plate at $l = 30$ mm. Deposition of Yb atoms on the glass plate is confirmed through chemical reaction. The glass plate with Yb in metallic silver color deposited on it is exposed to gaseous iodine, and after few hours, it turns to white YbI_3 confirming the presence of Yb. Figure 5(a) shows spatial distribution of atoms while the oven is entirely heated at $T = 252^\circ\text{C}$ without any dark wall. The profile of the spot sizes is measured by STYLUS which has a spatial resolution of $0.5 \mu\text{m}$.⁵¹ In the dark wall mode of operation, at 2.1 A corresponding to $179(10)^\circ\text{C}$, a circular spot of Yb atoms deposited on the glass plate was barely detected by the STYLUS. This temperature is in good agreement

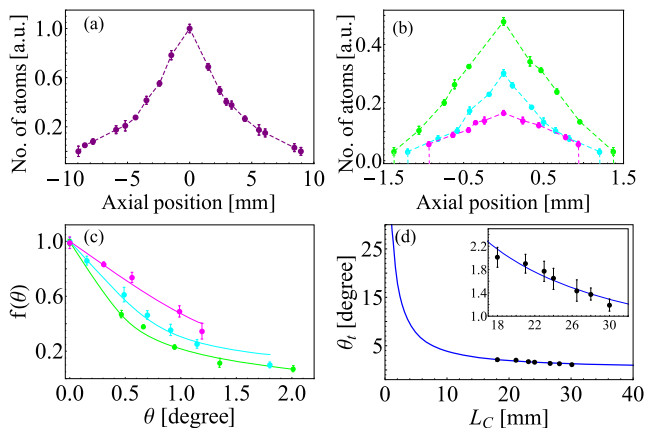


FIG. 5. Measured spatial profiles of the Yb spot for: (a) end-to-end heating of the capillary at 2.3 A and (b) dark wall oven operated at 2.3 A (magenta), 3.2 A (cyan), and 4 A (green). (c) Relative angular profiles along with the fitted curves. (d) Variation of experimentally obtained truncated angle values for varying cold end length along with the fitted model.

with the numerically estimated T_C within its accuracy. Truncated spatial distribution of atoms, as shown in Fig. 5(b), clearly indicates that the spot size increases with higher current due to the decrease in L_C [Fig. 3(c)]. Truncation extends to higher θ_t with increasing current together with the increase in centerline intensity and the total flux following Eq. (9). Assuming radially symmetric deposition of atoms in a circular profile, STYLUS data along several diametric directions were averaged. The relative angular profiles corresponding to varying currents obtained from measured spatial distributions are shown in Fig. 5(c), which are well described by the distribution function as given in Eq. (8). A steep off axial decrease in the atom's density and truncation as described in Fig. 2 is clearly visible at lower current, i.e., longer L_C . The fitted values of L_H , as given in Eq. (8), are in agreement with the numerical simulations [Fig. 3(d)] considering $T_C = 175^\circ\text{C}$. Figure 5(d) depicts experimental θ_t values obtained from distributions, as shown in Fig. 5(c) for varying cold end lengths. The data match well with the theoretical model following Eq. (2). This reconfirms that with decreasing L_C at higher operating current, θ_t increases. Pointing nature of the atoms' distribution toward the center of the spot [Fig. 5(b)] matches very well to the theoretical predictions (Fig. 2). The minimum spot size produced by our dark wall oven has $1.2(1)^\circ$ divergence at 2.3 A and 1.7 V. The corresponding oven temperature $250(10)^\circ\text{C}$ produces a flux of 7.9×10^9 atoms s^{-1} which is good enough for most of the experiments where higher divergence is not tolerable. Figure 6 shows the numerically calculated atomic flux using COMSOL by employing Eq. (4) and those estimated using the experimentally obtained distribution function. Atomic flux up to θ_t can be estimated as $P_{\text{vap}}(T) a^2 \sqrt{8kT} \int_0^{\theta_t} 2\pi f(\theta) d\theta / (4kT \sqrt{\pi m})$, where 2π arises due to the radial symmetry of the distribution. Here, at a particular temperature T , $P_{\text{vap}}(T)$ is estimated as shown in Fig. 4(a) and the fitted function of $f(\theta)$ at different temperatures as shown in Fig. 5(c) is used to estimate the atomic flux. In this case, uncertainties are estimated considering inaccuracies of $f(\theta)$, θ_t , and our confidence on estimating oven temperature. Both the results are comparable to each other within their uncertainties.

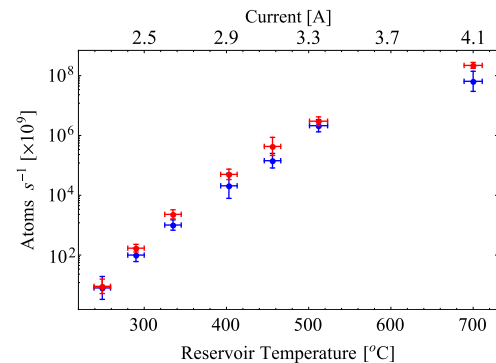


FIG. 6. Temperature dependence of the atomic flux coming out of the dark wall oven, as estimated numerically using COMSOL (blue) and using the measured $f(\theta)$ distribution function (red).

IV. CONCLUSION

Modified spatial distribution of atomic flux coming out of a dark-wall oven is studied in detail, and its high degree of collimation than that of a bright oven with collimator is obtained. A novel design of a simple dark wall oven is presented which is easy to operate for controlling the atomic beam divergence by proper choice of the capillary geometry and the contact points of resistive heating. We performed finite element analysis of the oven heating and atomic flux flow through it, theoretically modeled the distribution function of the atomic flux, and verified it via experimental measurements. The measured critical temperature $179(10)^\circ\text{C}$ at which the atomic flux flow of ^{171}Yb atoms for our oven geometry is negligible to use matches well with the numerically simulated value of 175°C . Also, theoretically obtained distribution function is well characterized with the experimental observations, as shown for different operating conditions. Atomic flux as estimated using our measured spatial distribution of atoms matches to the numerically simulated values. Using a 65 mm capillary of a fine diameter of 0.9 mm including a cold exit end of length 35 mm operating at 2.3 A and 1.7 V, we are able to generate an atomic beam with minimum divergence of $1.2(1)^\circ$ corresponding to $\theta_{\frac{1}{2}} = 0.8(1)^\circ$. This is better than many other complicated oven designs reported earlier. A dark wall oven, as described here, with a multichannel array could be a way for producing a high intensity, nearly collimated atomic beam.

ACKNOWLEDGMENTS

We acknowledge CSIR-NPL, Department of Science and Technology (DST), Grant No. SB/S2/LOP/033/2013 for supporting this work. L.S. thanks DST for the INSPIRE fellowship, and A. Roy thanks CSIR for the SRF Fellowship. We thank Rajeev Rakshit, Manju Singh, and Preetam Singh of CSIR-NPL for allowing us to use their instrument STYLUS.

REFERENCES

- M. O. Krause, Th. A. Carlson, and R. R. Woodruff, *Phys. Rev. A* **24**, 1374 (1981).
- C. Dzionk, W. Fiedler, M. V. Liicke, and P. Zimmermann, *Phys. Rev. Lett.* **62**, 878 (1989).

- ³C. Dzionk, W. Fiedler, M. V. Liicke, and P. Zimmermann, *Phys. Rev. A* **41**, 3572 (1990).
- ⁴S. Aksela, M. Harkoma, M. Pahjola, and H. Aksela, *J. Phys. B: At. Mol. Phys.* **17**, 2227 (1984).
- ⁵E. Forrest, G. K. James, K. J. Ross, and M. Wilson, *J. Phys. B: At. Mol. Phys.* **18**, 3123 (1985).
- ⁶J. P. Gordon, H. J. Zeiger, and C. H. Townes, *Phys. Rev.* **99**, 1264 (1955).
- ⁷S. Stellmer, M. K. Tey, B. Huang, R. Grimm, and F. Schreck, *Phys. Rev. Lett.* **103**, 200401 (2009).
- ⁸M. Schioppo, N. Poli, M. Prevedelli, St. Falke, Ch. Lisdat, U. Sterr, and G. M. Tino, *Rev. Sci. Instrum.* **83**, 103101 (2012).
- ⁹R. Senaratne, S. V. Rajagopal, Z. A. Geiger, K. M. Fujiwara, V. Lebedev, and D. M. Weld, *Rev. Sci. Instrum.* **86**, 023105 (2015).
- ¹⁰S. H. W. Wouters, G. Haaf, P. H. A. Mutsaers, and E. J. D. Vredenburg, *Rev. Sci. Instrum.* **87**, 083305 (2016).
- ¹¹S. C. Bell, M. Junker, M. Jasperse, L. D. Turner, Y.-J. Lin, I. B. Spielman, and R. E. Scholten, *Rev. Sci. Instrum.* **81**, 013105 (2010).
- ¹²A. J. Murray, M. J. Hussey, and M. Needham, *Meas. Sci. Technol.* **17**, 3094–3101 (2006).
- ¹³W. DeGraffenreid, J. R. Serrano, Y. M. Liu, and J. Weiner, *Rev. Sci. Instrum.* **71**, 3668 (2000).
- ¹⁴H. Lew, in *Methods of Experimental Physics*, edited by V. W. Hughes and H. L. Schultz (Academic, New York, 1967), Vol. 4A, p. 155.
- ¹⁵P. Kusch and V. W. Hughes, in *Handbuch der Physik*, edited by Fliigge (Springer, Berlin, 1959), Vol. 37, p. 1.
- ¹⁶L. V. Hertel and K. J. Ross, *J. Sci. Instrum.* **1**, 1245 (1968).
- ¹⁷K. J. Ross and B. Sonntag, *Rev. Sci. Instrum.* **66**, 4409 (1995).
- ¹⁸D. M. P. Holland, K. Codling, and R. N. Chamberlain, *J. Phys. B: At. Mol. Phys.* **14**, 839 (1981).
- ¹⁹C. Vishwakarma, J. Mangaonkar, K. Patel, G. Verma, S. Sarkar, and U. D. Rapol, e-print [arXiv:1810.09090](https://arxiv.org/abs/1810.09090) (2018).
- ²⁰J. G. King and J. R. Zacharias, *Adv. Electron. Electron. Phys.* **8**, 1 (1956).
- ²¹U. Becker, in *X-Ray and Inner Shell Physics*, edited by Th. A. Carlson, M. O. Krause, and S. T. Manson (AJP Conf. Proc., 1990), Vol. 125, p. 621.
- ²²P. H. Kobrin, U. Becker, S. Southworth, C. M. Truesdale, D. W. Lindle, and D. A. Shirley, *Phys. Rev. A* **26**, 842 (1982).
- ²³A. Hausmann, B. Kimmerling, H. Kossmann, and V. Schmidt, *Phys. Rev. Lett.* **23**, 2669 (1988).
- ²⁴H. C. W. Beijerinck and N. F. Verster, *J. Appl. Phys.* **46**, 2083 (1975).
- ²⁵D. R. Olander and V. R. Kruger, *J. Appl. Phys.* **41**, 2769 (1970).
- ²⁶N. Cooper, E. D. Ros, J. Nute, D. Baldolini, P. Jouve, L. Hackermüller, and M. Langer, *J. Phys. D: Appl. Phys.* **51**, 105602 (2018).
- ²⁷M. Richter, M. Meyer, M. Pahler, T. Prescher, E. V. Raven, B. Sonntag, and H. E. Wetzel, *Phys. Rev. A* **39**, 5666 (1989).
- ²⁸L. Feher, Ph.D. thesis, Southampton University, 1987.
- ²⁹D. Bulgin, J. Dyke, J. Goodfellow, N. Jonathan, E. Lee, and A. Morris, *J. Electron Spectrosc.* **12**, 67 (1977).
- ³⁰R. E. Drullinger, D. J. Glaze, and D. B. Sullivan, “A recirculating oven for atomic beam frequency standards,” in *Proceedings of the 39th Annual Symposium on Frequency Control* (IEEE, USA, 1985), p. 13.
- ³¹M. E. Poitzsch, J. C. Bergquist, W. M. Itano, and D. J. Wineland, *Rev. Sci. Instrum.* **67**, 129 (1996).
- ³²A. D. Ludlow, M. M. Boyd, J. Ye, and P. O. Schmidt, *Rev. Mod. Phys.* **87**, 637 (2015).
- ³³P. Clausing, *Z. Phys.* **66**, 471 (1930).
- ³⁴B. B. Dayton, in *1956 National Vacuum Technology Transactions*, edited by E. Perry and J. Durant (Pergamon, London, 1957).
- ³⁵J. A. Giordmaine and T. C. Wang, *J. Appl. Phys.* **31**, 463 (1960).
- ³⁶R. H. Jones, D. R. Olander, and V. R. Kruger, *J. Appl. Phys.* **40**, 4641 (1969).
- ³⁷D. R. Olander, *J. Appl. Phys.* **40**, 4650 (1969).
- ³⁸D. R. Olander, R. H. Jones, and W. J. Siekhaus, *J. Appl. Phys.* **41**, 4388 (1970).
- ³⁹W. J. Siekhaus, R. H. Jones, and D. R. Olander, *J. Appl. Phys.* **41**, 4392 (1970).
- ⁴⁰P. Krasuski, *J. Vac. Sci. Technol. A* **5**, 2488 (1987).
- ⁴¹D. Halwidl, *Development of an Effusive Molecular Beam Apparatus* (Springer Spektrum, Wiesbaden, 2016), Chap. 1, p. 5.
- ⁴²D. O. Sabulsky, Ph.D. thesis, University of Chicago, 2014.
- ⁴³D. E. Kuhl and R. G. Tobin, *Rev. Sci. Instrum.* **66**, 3016 (1995).
- ⁴⁴A. Rastogi, N. Batra, A. Roy, J. Thangjam, V. P. S. Kalsi, S. Panja, and S. De, *MAPAN* **30**, 169 (2015).
- ⁴⁵N. Batra, B. K. Sahoo, and S. De, *Chin. Phys. B* **25**, 113703 (2016).
- ⁴⁶A. Roy, S. De, B. Arora, and B. K. Sahoo, *J. Phys. B: At. Mol. Opt. Phys.* **50**, 205201 (2017).
- ⁴⁷S. De, N. Batra, S. Chakraborty, S. Panja, and A. Sen Gupta, *Curr. Sci.* **106**, 1348 (2014), <https://www.currentscience.ac.in/php/toc.php?vol=106&issue=10>.
- ⁴⁸S. Panja, S. De, S. Yadav, and A. Sen Gupta, *Rev. Sci. Instrum.* **86**, 056104 (2015).
- ⁴⁹N. Batra, S. Panja, S. De, A. Roy, S. Majhi, S. Yadav, and A. Sen Gupta, *MAPAN* **32**, 193 (2017).
- ⁵⁰L. Sharma, A. Roy, S. Panja, V. N. Ojha, and S. De, *Sci. Rep.* **8**, 16884 (2018).
- ⁵¹K. J. Stout and L. Blunt, in *Three-Dimensional Surface Topography*, 2nd ed. (Penton Press, 2000), Chap 2, p. 22.



Optical Atomic Clocks for Redefining SI Units of Time and Frequency

L. Sharma^{1,2}, H. Rathore^{1,2}, S. Utreja^{1,2}, Neelam^{1,2}, A. Roy^{1,2,3}, S. De⁴ and S. Panja^{1,2*}

¹CSIR-National Physical Laboratory, Dr. K. S. Krishnan Marg, New Delhi 110012, India

²Academy of Scientific and Innovative Research (AcSIR), Ghaziabad 201002, India

³Max Planck Institute for the Science of Light, Staudtstr. 2, 91058 Erlangen, Germany

⁴Inter-University Centre for Astronomy and Astrophysics (IUCAA), Post Bag 4, Ganeshkhind, Pune 411007, India

Received: 26 August 2020 / Accepted: 15 September 2020

© Metrology Society of India 2020

Abstract: Nowadays, most of the standards of measurement are based on fundamental constants, and among all, the SI units of time and frequency are realized with the highest precision. The SI unit of time interval, i.e. second, is realized on the basis of a hyperfine transition of ground state of ¹³³Cesium atom in the microwave region. Atomic clocks operating at the optical frequencies have potential of providing better accuracy and higher stability than the microwave atomic clocks, and it is expected that SI second will be redefined on the basis of an optical transition. In this article, we focus on different atomic frequency standards operating in the optical domain of the spectrum by interrogating neutral atoms in optical lattice or a single ion within a radiofrequency ion trap. Recent worldwide developments along with activities at CSIR-National Physical Laboratory (CSIR-NPL) towards building optical atomic clock or optical frequency standard have also been presented.

Keywords: Atomic clocks; Optical clocks; Precision measurements; Frequency standards; Ion trap; Magneto-optical trap; Laser cooling; Systematic shifts; Frequency comb

1. Introduction

In 1955, Louis Essen and J. V. L. Parry realized the first atomic standard of frequency and time interval, which was based on the microwave ground-state hyperfine transition of ¹³³Cesium (¹³³Cs) atoms [1]. In 1967, the Comité International des Poids et Mesures (CIPM) adopted the Cs standard as the SI unit of time and frequency. The SI unit of time interval, i.e. second, was defined via an unperturbed hyperfine transition of atomic ¹³³Cs interrogated with microwave at frequency of 9,192,631,770 Hz [2]. Technological development over more than five decades, in particular development of laser cooling techniques [3], has helped to reduce the measurement uncertainty to which the centre frequency of the hyperfine transition of ground-state ¹³³Cs atom can be measured to $\sim 10^{-16}$ [4–6]. The SI definition of time and frequency got amendment in 1997 where the transition frequency of the cold Cs atoms at

nearly 0 K, realized through a Cs atomic fountain, has been considered as the primary standard. However, clocks with even better accuracy remain as an essential requirement for many of the applied research studies as well as to address many advanced physics problems related to communications, surveillances, testing temporal constancy of fine structure constant or testing electron–proton mass ratio [7]. Precision experiments such as detecting gravitational waves or testing general relativity require a clock with accuracy $\sim 10^{-18}$ or better [8, 9]. The accuracy as well as stability of a clock increases with the increase in operational frequency of the clock, so an optical clock with an operational frequency of several hundreds of THz is capable of providing orders of magnitude higher accuracy than the microwave Cs atomic clocks. With the advent and maturity of certain technologies, realization of optical standards became possible [10]. The evolution of atomic clocks from microwave domain to optical regime is shown in Fig. 1, and at present, the optical frequency standards are superior to the microwave ones in terms of both stability and uncertainty. There are mainly two types of optical

*Corresponding author, E-mail: panjas@nplindia.org

clocks based on the interrogations of ultra-narrow transitions of neutral atoms or atomic ions [10–12]. The neutral atoms are confined within optical lattices tuned to so-called magic wavelength by inducing a dipole moment in the atom and exerting a force on this dipole through a laser field gradient [13, 14]. On the other hand, ions are confined within radio-frequency (RF) ion trap, and in order to avoid any perturbation of the ionic clock transition due to Coulombic interaction among the charged particles, only a single ion is preferred to be interrogated in the field-free region of the trap centre [12, 15].

In optical lattices, several thousands of atoms are interrogated at a time; hence, they are capable of providing better signal strength compared to single trapped ion clocks [16, 17]. Optical clocks based on single trapped ion can be interrogated over longer period of time since the ion is free from interatomic and Coulombic interaction and in that way can have a very long coherence time [18]. Another key advantage of single trapped ion-based optical clocks is that some of the optical transitions of these ions are extremely insensitive to the external perturbations like magnetic field or electromagnetic radiation of the ambient temperature field [19, 20]. Although both types of atomic clocks are capable of providing very high level of accuracy and stability, till date it is not very clear that whether the lattice-based optical clocks or single trapped ion-based optical clocks will be the ideal candidates for redefining SI second. CSIR-National Physical Laboratory (CSIR-NPL) as the National Metrology Institute (NMI) of India is working towards building an optical clock based on the interrogation of a single ytterbium (^{171}Yb) ion, trapped and laser cooled within a specially designed RF trap [21, 22]. This article presents a review on the development of optical atomic clocks based on neutral atoms within optical lattices or single trapped ions within RF trap. Different important technical aspects of optical clocks along with measurement precision and systematic uncertainties associated with

some of the best performing clocks to date have been discussed. A brief description about the activities at CSIR-NPL related to building an optical clock based on single trapped ytterbium ion has also been presented.

2. Working Principle of Optical Frequency Standards

The basis of any atomic frequency standard is an oscillator whose frequency is driven by and stabilized with respect to an atomic transition having ultra-narrow linewidth. The time elapsed corresponding to the cycles of radiation produced by the said transition defines one second and this constitutes a clock. Such atomic standards are far more stable compared to their mechanical counterparts as atomic transitions are ideally not prone to perturbations created by external environmental changes. The working principle of an atomic clock is presented schematically in Fig. 2. As can be seen, key components of an atomic clock are a reference oscillator (*i.e.* a precise atomic transition) which is isolated from the environment, another frequency source or oscillator (laser), the output signal of which is locked to that precise atomic transition and eventually used to realize the unit of time or frequency. A feedback electronics keeps on correcting the local oscillator's, *i.e.* laser's, output frequency by comparing it to that of the reference oscillator. When the operational frequency of the reference atomic oscillator lies in the optical regime which is five orders of magnitude higher than a microwave frequency, the developed clock is called an optical atomic clock. The performance of any frequency standard is defined by two important parameters: instability and inaccuracy. Instability refers to the fluctuations of a measured output about its average value; it is a type of statistical uncertainty. Most widely used protocol for measuring fluctuations in clock frequency over a time period is Allan deviation or Allan variance [23, 24]. Inaccuracy, elseways, refers to the shift in the average value of a measured parameter which cannot be measured, but based on the probable sources of error, it can be estimated [23, 25]. The clock instability, σ_y , for an averaging period τ is given by,

$$\sigma_y \approx \frac{\Delta f}{f_0 \sqrt{N}} \sqrt{\frac{T_c}{\tau}}, \quad (1)$$

where Δf is the transition linewidth, f_0 is the reference oscillation frequency, N is the number of probed species and T_c is the time for single measurement [26, 27]. Here, $f_0/\Delta f$ gives the quality (Q)-factor and $\sqrt{T_c/N\tau}$ gives signal-to-noise ratio. It is clear from Eq. 1 that narrow linewidth, higher clock frequency, large number of species and longer averaging periods are preferable for the better performances of a clock.

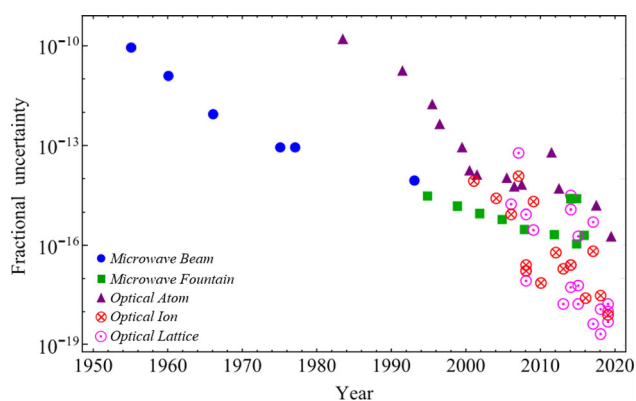
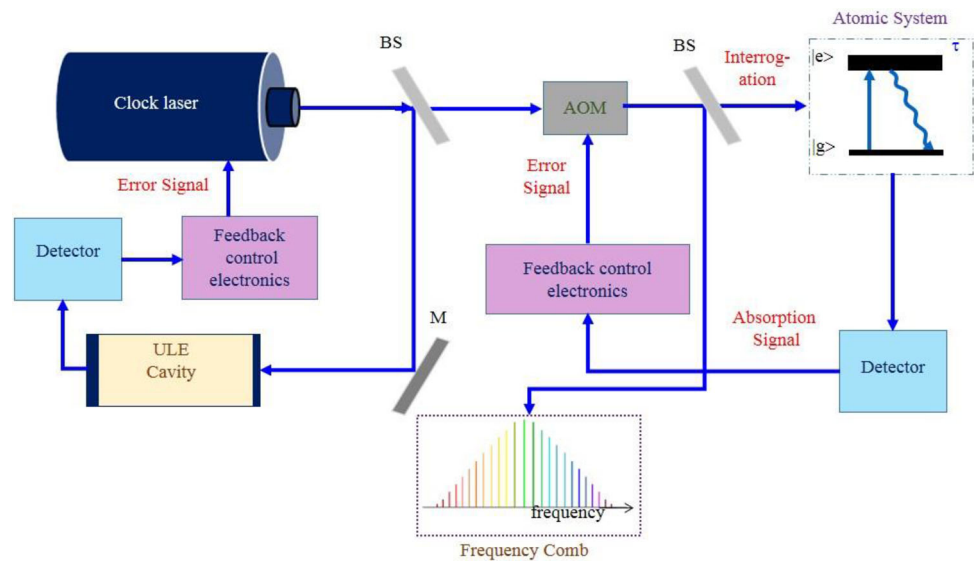


Fig. 1 Evolution of atomic clocks based on the improvement in fractional uncertainties in frequency

Fig. 2 Schematic representation of an atomic frequency standard showing the three key ingredients: natural oscillator, local oscillator and a frequency counter. The local oscillator's frequency is pre-stabilized to a ULE cavity to probe the desired atomic transition. Signal from the probed transition is sent to a servo loop which generates and sends an error signal to the clock laser to tune its frequency to the atomic resonant frequency. The light is finally sent to the frequency counter to measure the clock cycle. BS: beam splitter, AOM: acousto-optic modulator, $\lambda/4$: quarter waveplate, $\lambda/2$: half waveplate



The primary prerequisites of an optical frequency standard are as follows:

1. An atomic frequency reference: The very promising atomic/ionic candidates for an optical clock are those with a superior quality factor (Q-factor), *i.e.* transitions having narrow linewidth excited states, and a higher excitation frequency in the optical domain preferably insensitive to external fields. For considering an atomic transition in the optical domain, it should have frequencies in the range from 300 GHz to 3000 THz. The chosen experimental species must have a metastable excited state, where the possible transitions from them to the ground state are “forbidden” in the electric dipole approximation and only higher-order multi-pole transitions are allowed. The chosen atoms or ions should have a strong allowed transition so that they can be efficiently prepared by laser cooling and trapping. Also, the transitions involved in the experiment for building the clock should have their transitions in the visible or near-infrared domain so that the required lasers are easy to build and easy to handle too.
2. Trapping and cooling of the species at ultra-high vacuum condition: To probe the clock transition of the species, it is important to isolate it from external environment and an ultra-high vacuum (UHV) chamber serves for this purpose. Depending on level of vacuum required for the experiment, rotary, turbo, ion pumps and Ti-sublimation pumps are connected to the experimental chamber. For clock experiments, a vacuum corresponding to 10^{-11} mbar pressure is desirable to get rid of the presence of residual gas which may collide with the trapped species and reduce its trapping lifetime or add to systematic shifts. An atomic source *i.e.* atomic oven, is installed within the vacuum chamber for the production of atoms or atomic ions by photoionization. Once the atoms or ions are confined within the UHV chamber with special arrangements, their movements are to be lowered to lessen down motion-induced systematic shifts. Laser cooling technique developed during the 1980s aids in controlling the trapped species' motion by reducing its internal energy and eventually cools it down to the temperature near sub-millikelvin region.
3. Ultra-narrow linewidth laser for probing atomic transition: Highly stable and narrow linewidth laser is an essential requirement for probing the precise and ultra-narrow linewidth atomic transition. Extended cavity diode lasers (ECDLs) are popularly being used as narrow linewidth lasers for many of the applications. However, the best performing ECDL has typical linewidth of several kHz and also keeps fluctuating and drifting over time. So, the output frequency of an ECDL is not good enough for probing a stable atomic transition of typical linewidth of sub-Hz to few Hz. For producing narrow linewidth laser frequency, the laser is stabilized with respect to an ultra-low expansion (ULE) cavity. For locking the laser frequency, the state-of-the-art Pound–Drever–Hall (PDH) technique is utilized which brought a renaissance in the field of precision laser stabilization systems [28, 29]. The schematic of the PDH technique is depicted in Fig. 3. The basic principle of the PDH technique involves evaluating the laser's offset from a cavity resonance and feeding the error into a servo loop which would compensate for the required frequency [30].
4. Frequency counter for measuring absolute optical frequencies: Once the clock transition of narrow linewidth is probed, the experimental clock set-up

proves useful only if the oscillation cycles of the probing laser can be counted to institute it as a timescale. An optical frequency counter solves this challenge [31, 32]. Although all other ingredients for an optical clock were already available, the absence of a counter in the optical regimes posed a hindrance to its development for many years. The invention of optical frequency comb by T. W. Hänsch and J. L. Hall was therefore a boon for precise frequency standards experiments as it bridged the gap between optical and microwave frequencies [33–36]. The frequency comb is basically a mode-locked femtosecond pulsed laser. It produces a train of burst of light/pulse at a fixed frequency called repetition rate, f_{rep} corresponding to the time taken for a round trip in the laser cavity [36–38]. Its Fourier spectrum consists of discrete visible frequencies separated by f_{rep} and looks like a comb with many teeth. The frequency corresponding to any particular “teeth”, f_n , is given by [39, 40]

$$f_n = f_0 + n \times f_{rep} \quad (2)$$

where n is the mode number and f_0 is the offset frequency which is related to the carrier-envelope phase offset. By stabilizing f_0 and f_{rep} with respect to an accurate frequency source like Cs frequency standard, all the comb modes can be controlled. The optical frequency can be determined by measuring the heterodyne beat note between the comb and the source [41].

3. Types of Optical Atomic Clocks

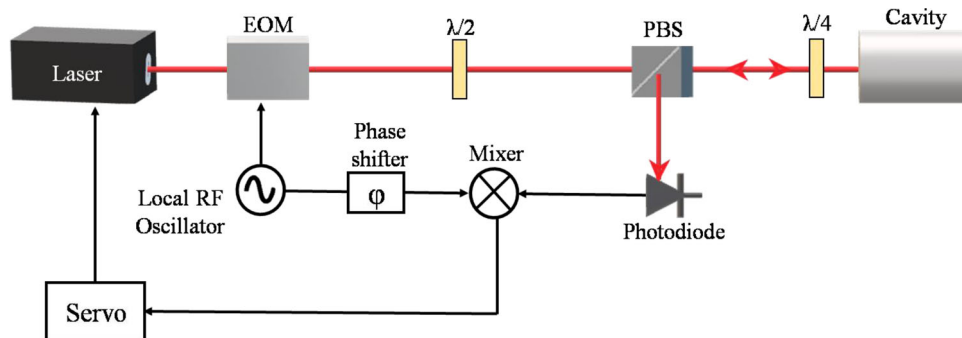
Activities on time and frequency metrology in optical domain have been carried using either neutral atoms or ions. In the following section, a brief description of different species used as a candidate for optical frequency standard or optical clock has been discussed.

3.1. Neutral Atom Optical Clocks

Alkaline earth (-like) atoms such as calcium (Ca), mercury (Hg), magnesium (Mg), strontium (Sr) and ytterbium (Yb) those having narrow intercombination transition are some of the choices for developing atom optical clocks [42]. In most of these species, the presence of (i) a strong $^1S_0-^1P_1$ transition that is used for cooling, trapping and detection, (ii) $^1S_0-^3P_1$ transition for narrow cooling, (iii) $^3P-^3S$ transitions that aid in forming a closed cooling cycle and (iv) the doubly forbidden $^1S_0-^3P_0$ transition offering a high Q-factor are the transitions of interest for clock purpose. As evident in Eq. 1, the large number of interrogating species, *i.e.* atoms, implies higher stability and a better signal-to-noise ratio for a clock, but at the same time, it is prone to more collisional shifts [43]. Neutral atom optical clocks are of two types: (a) free space standards and (b) optical lattice clocks.

The free space standards which had a steady advancement from thermal-based atomic systems to laser cooled systems have been used for decades owing to lesser experimental complexity. In such types, the atom sources used were an atomic vapour cell [44], a thermal atomic beam [45], slowed and laser cooled atoms released by magneto-optical trap (MOT) [46]. To obtain higher precision, spectroscopy techniques, *e.g.* saturation absorption spectroscopy, Ramsey and Ramsey–Bordé spectroscopy, are employed. MOTs use laser field and magnetic field gradient combination for atom confinement but are limited by residual Doppler effect [47, 48]. Such free space frequency standards have already been explored by several groups [49–52]. To mention a few, using Ramsey–Bordé spectrometry, the NIST, USA group achieved a fractional frequency instability below 6×10^{-15} at 1 s with ^{40}Ca atoms [45]; Ido et al. employed ultra-cold ^{88}Sr for which the estimated fractional frequency uncertainty is reported as 7.6×10^{-14} [53] and the achieved uncertainty for frequency measurement in ^{24}Mg optical clock by Friebe et al. is 2.5×10^{-12} [49]. Thus, with free space atoms-based optical clocks it was very difficult to achieve further improvement in the fractional frequency uncertainty

Fig. 3 Schematic diagram of Pound–Drever–Hall locking method for frequency stabilization. EOM: electro-optic modulator, PBS: polarizing beam splitter



(10^{-15}) and so researchers turned towards the optical lattice-based clocks.

Optical lattice clocks are the new class of atomic clocks based on trapping of thousands to millions of cold atoms in energy wells [54]. These energy wells or lattice sites are formed by focusing light to a waist size of 50–100 μm in one direction and back-reflecting the same light onto itself to create a standing-wave pattern. The lattice laser wavelength is tuned to a so-called magic value, where both the states involved in clock transition are equally shifted, thus giving a zero differential shift. The atoms can reside in the lattice sites for about a second during which the relevant measurements are done; they are therefore functioned at frequent measurement cycle. Shifts due to atom–atom interactions, lattice fields, black body radiation (BBR), etc., are to be taken care of in lattice clocks [55]. Sr and Yb have been of special interest for optical lattice clocks [55–57]. Such clocks reduce atomic motions and related shifts and provide a grander stability and are being developed in many laboratories [58–60]. The SYRTE group has developed a ^{199}Hg lattice clock with relative uncertainty of 1.7×10^{-16} [61]. NIST, USA developed and demonstrated the first Yb lattice clock with stability of 1.4×10^{-18} [62] and has achieved the record frequency precision of 2.5×10^{-19} for ^{87}Sr [63], which is the best-known optical clock till date.

3.2. Ion Optical Clocks

Atomic ions with alkali-like or quasi-alkali-like atomic structure such as $^{199}\text{Hg}^+$, $^{88}\text{Sr}^+$, $^{40}\text{Ca}^+$, $^{171}\text{Yb}^+$ or atomic ions with atomic structure similar to alkaline earth elements as aluminium ($^{27}\text{Al}^+$) and indium ($^{115}\text{In}^+$) are used in building single-ion optical clocks. Invention of RF ion trap, commonly known as Paul trap, paved the way to providing an unperturbed environment for confining an ionic species to perform various experiments on it [51, 64, 65]. Such traps use an oscillating AC and a stable DC to trap the ions [65]. Within an RF trap, ions are cooled to millikelvin temperature by laser cooling [66] and can be confined for hours or months giving longer interaction time and hence reduced instability. The trap electrode material is to be chosen keeping in mind the probable dominant systematic shifts that may perturb the clock frequency. Ion-based clocks provide Doppler free environment, but due to a single ion, it has to compromise with lower signal-to-noise ratio. Hence, it requires a very high resolution and diffraction limited imaging system for single-ion detection [67], whereas clock transition is detected by employing electron shelving technique [68]. Thermal motion associated with time-averaged confining potential called as secular motion and driven oscillatory motion at applied RF frequency known as micromotion are

associated with trapped ions [69]. The NIST; SYRTE, NICT; NPL UK, NRC; MPIQ, NICT; PTB, NPL UK; NIST UK groups have worked on trapped $^{27}\text{Al}^+$, $^{40}\text{Ca}^+$, $^{88}\text{Sr}^+$, $^{115}\text{In}^+$, $^{171}\text{Yb}^+$, $^{199}\text{Hg}^+$, respectively, and most of them have achieved appreciable fractional frequency uncertainty of the order of 10^{-17} . In India, several groups have initiated work towards building optical atomic clocks or optical frequency standards based on neutral atoms in optical lattices or ion trapped within RF trap for probing fundamental physics problems as well as for metrological purposes.

4. Systematic Shifts in Optical Clocks

In practice, any physical quantity can never be measured with absolute certainty. Various uncontrollable effects limit the accuracy by which we can measure the resonant frequency of the natural oscillator. In order to overcome or minimize them, causes of their existence and magnitude assessment are to be known prior hand so that their contributions to the clock uncertainty budget could be evaluated. Several such most common systematic shifts limiting performance of optical clocks are discussed in the following section.

4.1. Doppler Shift

Relative motion between the observer and the atoms leads to Doppler effect and is one of the dominant reasons behind systematic shifts in clocks [19]. The resultant frequency shift, $\delta\omega$, for an entity of mass m , moving with velocity v , is given as:

$$\frac{\Delta\omega_D}{\omega_0} = \frac{\langle v_{\parallel} \rangle}{c} - \frac{\langle v^2 \rangle}{c^2} + \frac{\langle v_{\parallel} \rangle^2}{c^2} + O\left(\frac{v}{c}\right)^3 \quad (3)$$

where $\omega_0 = 2\pi f_0$, v_{\parallel} and c are the atomic transition frequency, moving entity's velocity along the probe laser beam direction and speed of light, respectively. The first term of Eq. 3 is the first-order Doppler shift, the next two terms are the second order Doppler shifts, and the last term represents higher orders of the shift. In case of an atomic beam, due to the Maxwellian distribution of velocities, the first-order Doppler effect results in broadening of the spectral lines.

The first-order Doppler shifts can be eradicated by laser cooling of the trapped species to the Lamb-Dicke region, but the second-order Doppler shifts still prevail owing to secular motion and micromotion of the species. At room temperature, this broadening could be of the orders of several GHz, whereas at microkelvin temperatures, corresponding broadening reduces to several hundred kHz. Large storage times may render $\langle v_{\parallel} \rangle = 0$ in laser cooled,

trapped ion system. By laser cooling, the trapped ion may reach to the Doppler cooling limit,

$$T_D = \kappa \frac{\hbar\gamma}{2k_B}, \quad (4)$$

where κ is the laser cooling geometry-dependent parameter, γ is the natural linewidth of cooling transition and k_B is the Boltzmann constant, and by additional resolved sideband cooling [70], the frequency shift resulting from secular motion can be brought down to 10^{-18} level. When atoms/ions are cooled to millikelvin temperature, the second-order shifts are reduced to $\sim 10^{-17}$ level, and at microkelvin level, these shifts lessen down to $< 10^{-20}$ [71–73]. Doppler free spectroscopy, Ramsey and Ramsey–Bordé schemes are also employed to eliminate shifts due to Doppler effects [74].

4.2. Electric and Electromagnetic Field-Based Shifts

Any electric field in the vicinity of the clock species affects its energy levels, leading to splitting of the spectroscopic lines; this effect is called Stark effect and the resulting shift in the absolute frequency is known as the Stark shift. Excess DC or AC fields such as stray static fields, patch potentials developed on trap electrodes due to atom deposition [75, 76], RF fields used for creating trap potentials, probe lasers' electric field, BBR, etc., are examples of few sources, which can lead to shifts in clock transition [77]. In case of trapped ions, applied RF fields produce quadratic Stark shifts; such stray field may deviate the trapped species' position from the null point of the potential. For compensation of such excess electric fields and patch potential, compensation electrodes are used [78]. For atom-based clocks, static electric field effects are usually small, but for achieving higher level of accuracy, they ought to be accounted for [79, 80]. In case of trapped ion clocks, such stray electric fields lead to excess micromotion-related shifts, which further enhances the second-order Doppler shift [69]. The shift in the energy of an atomic level $|J\rangle$ with polarizability α_o and $J \leq 1/2$ is given as [81, 82],

$$h\Delta f_s(\gamma, J, \vec{E}) = -\alpha_o(\gamma, J) \frac{|\vec{E}|^2}{2}. \quad (5)$$

For $J > 1/2$ and $F > 1/2$, F , m -dependent tensor component is to be considered to measure the shifts. Electromagnetic field of probe laser leads to AC Stark shift and is effective in both types of optical clocks. Temperature of objects in the surrounding of clock species leads to emission of electromagnetic radiation, commonly known as BBR, the electric field of which leads to an AC Stark shift called BBR shift [83–85]. Uncertainty in temperature and atomic polarizabilities causes uncertainty in clock frequency. Corresponding BBR shift

due to the electromagnetic radiation at a temperature T can be estimated as,

$$\Delta f_{BBR} = -\frac{(831.945)^2}{2h} \delta\alpha_o \left(\frac{T}{300}\right)^4 [1 + \eta(T)] \quad (6)$$

where h is the Planck's constant, $\delta\alpha_o$ is the differential scalar polarizabilities of the transition and $\eta(T)$ is the dynamic correction factor. Since BBR shift is temperature dependent, it can be suppressed by cryogenic temperature operations [81].

4.3. Magnetic Field-Based Shift

Any external magnetic field interacts with the magnetic moments of the atom, resulting in its energy-level splitting, which is very commonly known as Zeeman effect. Such shifts in atomic transition levels are called Zeeman shifts. The clock frequency shift, Δf_z , for a magnetic field of strength B is proportional to the magnetic quantum number m_F and is given by,

$$\Delta f_z = (g_e m_{F,e} - g_g m_{F,g})B + \beta B^2 \quad (7)$$

where g_e and g_g are the Landé g factors for the excited and ground states, respectively, and β is the quadratic Zeeman shift coefficient [86]. Therefore, proper choice of experimental species with transition states having zero $m_{F,e}$ and $m_{F,g}$ values renders the first-order Zeeman shift null [87, 88]. Only the second-order Zeeman shift remains due to nonzero magnetic moments of other atomic states which can be minimized to 10^{-17} to 10^{-18} level by operating the experiment in low magnetic fields. For nullifying the effect of geomagnetic field and other stray magnetic fields, magnetic shielding around the experimental assembly is done using Helmholtz coils which ensure temporal stability of the magnetic field.

4.4. Gravitational Shift

As per the general relativity and the equivalence principle, clocks tick comparatively slower near massive bodies [89, 90]. In other words, if we consider two identical clocks at two positions x_1 and x_2 , and if there exists a gravitational potential difference ΔU between the two, so that the former is placed in higher altitude by Δh , then the fractional frequency difference between them is,

$$\frac{\Delta f_g}{f_0} = -\frac{\Delta U}{c^2} = g \frac{\Delta h}{c^2} \quad (8)$$

with g being the acceleration due to gravity. For $\Delta h = 1$ cm, resulting frequency shift is 10^{-18} . Such shifts are to be considered during clock comparisons [91–94]. On the other

hand, such height sensitivity of the optical clocks can be used as a tool to study relativistic geodesy [95–97].

4.5. Collisional Shift

It includes shifts in transition frequencies arising due to collisions among atoms under interrogation. In case of neutral atom-based optical clocks, interactions among the atoms within heavily dense cloud perturb the clock frequency, thus affecting its accuracy. The collisional shifts are comparatively less in lattice clocks but are not negligible to be ignored. In case of single-ion-based frequency standards, such collisional effects are absent but any collision between trapped ion and the residual gas can still lead to a differential frequency shift of the order of 10^{-18} [98–100].

5. Clock Candidates

As evident in Eq. 1, atoms or ions with an ultra-narrow transition linewidth in the optical domain are ideal for building atomic optical clocks. As these candidates promise and in fact have come up with unprecedented accuracy and stability compared to the existing Cs-based primary standard, it is expected that in the near future, the SI second will be redefined on the basis of an optical clock either realized through neutral atoms within optical lattices or an ion within RF ion trap. In this section, we will have a look on some of the important atomic as well as ionic species those are used worldwide for building optical atomic clocks or optical frequency standards. The CIPM has recommended eight atomic/ionic candidates as secondary representations of the second (SRs) which may be accounted for atomic clock-based research and frequency comparisons during the preparation of a future redefinition of time and frequency, of which seven are optical frequency standards [101, 102]. Table 1 lists the optical clock candidates and associated parameters, which are used as SRS or as a timescale based on their achievable uncertainties; for SRS candidates, the uncertainty is less than or close to that of the primary standards. As can be seen from Table 1, three SRs have been reported to reach the stability level to 10^{-18} or better; those are ^{87}Sr optical lattice clock, $^{171}\text{Yb}^+$ singly trapped ion clock and the $^{27}\text{Al}^+$ quantum logic clock. We shall now briefly discuss about an example for each of a (i) freely moving neutral atoms-based optical clock, *i.e.* ^{40}Ca optical clock, (ii) optical lattice clock, *i.e.* ^{87}Sr optical lattice clock, and (iii) single trapped ion-based optical clock, *i.e.* $^{27}\text{Al}^+$ single-ion clock along with the relevant energy-level diagrams.

5.1. ^{40}Ca Free Atoms-Based Clock

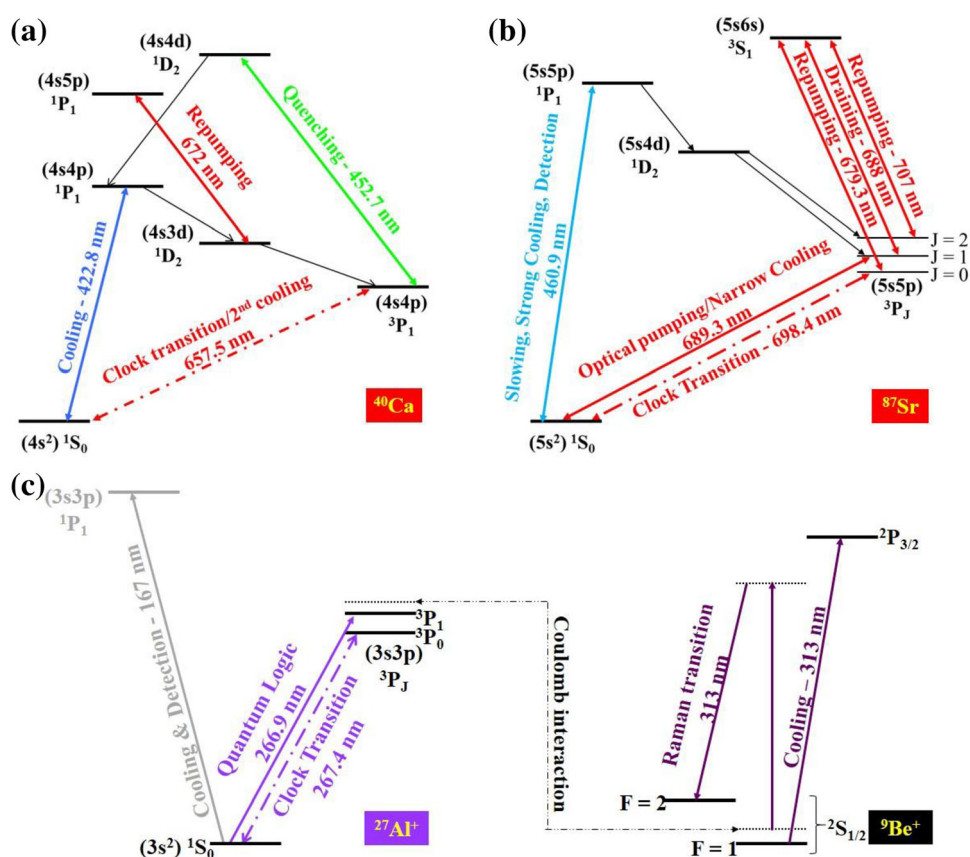
In 1979, Barger and Bergquist demonstrated high-resolution spectroscopy using ^{40}Ca indicating of its possibility to be used as an optical frequency standard [112]. Figure 4a shows the important transitions involved in the clock scheme. The $^1\text{S}_0$ – $^3\text{P}_1$ inter-combination line of ^{40}Ca atom at 657 nm with $\gamma = 400$ Hz along with a laser cooling transition from $^1\text{S}_0$ – $^1\text{P}_1$ at 423 nm attracted researchers towards itself as a potential frequency standard candidate. Different groups initially used thermal beam sources, vapour cells and later atoms released from magneto-optical traps (MOT). In case of thermal beam clock, ^{40}Ca atoms emerge with a most probable velocity of ~ 640 m/s from an oven operating at a temperature ~ 700 °C. Bordé–Ramsey spectroscopy was performed on the thermal beam, and the resulting fringes come with two recoil components. Error signal generated using one of these features is used to keep the laser locked to the resonant optical transition. Optical frequency reference based on thermal calcium atoms is reported in Ref. [113]. The stabilities of such thermal beam-based clocks are always limited by Doppler shifts. Eventually, to enhance the stability and accuracy by reducing motion-induced shifts, researchers employed laser cooling on atomic beams effusing out from atomic oven with the help of MOTs. Groups at PTB, NIST, USA, Tokyo, etc., have worked on ^{40}Ca atomic clocks using MOT chamber [109, 114–116]. The resultant fractional frequency uncertainty achieved by NIST, USA, group for the ^{40}Ca standard is 6.6×10^{-15} [109].

5.2. ^{87}Sr Optical Lattice Clock

Optical clocks realized through interrogating atoms trapped within optical lattices are capable of providing better level of accuracy as well as stability among all neutral atom-based optical clocks [54, 117]. The schematic for ^{87}Sr energy-level diagram is depicted in Fig. 4b. The $5s^2$ $^1\text{S}_0$ ($F = 9/2$)– $5s5p$ $^3\text{P}_0$ ($F = 9/2$) transition at 698 nm of alkaline earth element ^{87}Sr is used as a clock transition because of its narrow transition linewidth, γ of 1 mHz. Sr atomic beam with a speed ~ 460 m/s produced from an atomic oven kept at 500 °C, is slowed down to 50 m/s with a Zeeman slower and laser cooled using 461 nm laser. The slow atoms are then passed through a two-stage MOT for double-cooling process. In the first-stage Doppler cooling, the strong dipole-allowed $5s^2$ $^1\text{S}_0$ ($F = 9/2$)– $5s5p$ $^1\text{P}_1$ ($F = 11/2$) transition at 461 nm with $\gamma = 32$ MHz brings down the atoms' temperature to sub-millikelvin range. For efficient cooling and trapping, repump lasers at 679 nm and 707 nm are also simultaneously used. The second-stage Doppler cooling corresponding to the $5s^2$ $^1\text{S}_0$ ($F = 9/2$)– $5s5p$ $^3\text{P}_1$ ($F = 11/2$) transition at a narrow linewidth of

Table 1 CIPM approved species for secondary representation of second (SRS) and time standard and their relevant parameters along with best achieved fractional frequency uncertainty

Species	λ (nm)	Clock transition	f_0 (Hz)	Theoretical linewidth of clock transition (γ)	Best achieved fractional uncertainty ($\Delta f/f_0$)
<i>SRS candidates</i>					
$^{27}\text{Al}^+$	267	$^1\text{S}_0$ - $^3\text{P}_0$	1121,015,393,207,857.3	8 mHz	9.4×10^{-19} [103]
$^{199}\text{Hg}^+$	282	$^2\text{S}_{1/2}$ - $^2\text{D}_{5/2}$	1064,721,609,899 145.3	1.8 Hz	1.9×10^{-17} [100]
$^{171}\text{Yb}^+$	436	$^2\text{S}_{1/2}$ - $^2\text{D}_{3/2}$	688,358,979,309,308.3	3.1 Hz	1.1×10^{-16} [104]
$^{171}\text{Yb}^+$	467	$^2\text{S}_{1/2}$ - $^2\text{F}_{7/2}$	642,121,496,772,645.0	~ 1 nHz	3.2×10^{-18} [105]
^{171}Yb	578	$^1\text{S}_0$ - $^3\text{P}_0$	518,295,836,590,864.0	7 mHz	1.4×10^{-18} [62]
$^{88}\text{Sr}^+$	674	$^2\text{S}_{1/2}$ - $^2\text{D}_{5/2}$	444,779,044,095,486.6	0.4 Hz	1.2×10^{-17} [106]
^{87}Sr	698	$^1\text{S}_0$ - $^3\text{P}_0$	429,228,004,229,873.2	~ 1 mHz	2.5×10^{-19} [63]
<i>Time scale candidates</i>					
$^{115}\text{In}^+$	237	$^1\text{S}_0$ - $^3\text{P}_0$	1267,402,452,899,920.0	0.8 Hz	8.1×10^{-16} [107]
^1H	243	1S-2S	1233,030,706,593,514.0	1.3 Hz	4.2×10^{-15} [108]
^{199}Hg	266	$^1\text{S}_0$ - $^3\text{P}_0$	1128,575,290,808,154.8	121 mHz	1.7×10^{-16} [61]
^{40}Ca	657	$^1\text{S}_0$ - $^3\text{P}_1$	455,986,240,494,140.0	400 Hz	6.6×10^{-15} [109]
^{88}Sr	689	$^1\text{S}_0$ - $^3\text{P}_0$	429,228,066,418,012.0	7.6 kHz	7.0×10^{-17} [110]
$^{40}\text{Ca}^+$	729	$^2\text{S}_{1/2}$ - $^2\text{D}_{5/2}$	411,042,129,776,398.4	0.14 Hz	5.7×10^{-17} [111]

Fig. 4 Energy-level diagrams relevant to laser cooling and clock transition for **a** ^{40}Ca , **b** ^{87}Sr and **c** $^{27}\text{Al}^+$ with $^9\text{Be}^+$ for quantum logic application

7.5 kHz is probed at 689 nm which cools the atoms to sub-microkelvin level. Once the large number of atoms ($\times 10^6$) is double Doppler cooled and trapped, they are then

transferred to a one-dimensional optical lattice operated at the magic wavelength of 813 nm followed by clock spectroscopy performed at 698 nm using an ultra-stable laser.

Best achieved uncertainty for ^{87}Sr -based optical lattice clock is 2.5×10^{-19} [63]. Groups at JILA, SYRTE, PTB, NICT, NMIJ and RIKEN are involved in experiments of ^{87}Sr -based lattice clock [80, 118–120].

5.3. $^{27}\text{Al}^+$ Single-ion Clock

In 1973, Hans Dehmelt proposed the idea of developing optical frequency standard based on “mono-ion oscillator”, specifically the group 13 singly charged ions [66, 68, 121]. Their $^1\text{S}_0$ – $^3\text{P}_0$ transition features lesser magnetic field shifts, very less sensitivity to BBR and no electric quadrupole shift. The ion species $^{27}\text{Al}^+$ of this group is an outstanding clock candidate owing to its achieved uncertainty of 9.4×10^{-19} realized by the NIST, USA group [103]. As illustrated in Fig. 4c, the dipole-forbidden $3s^2\ ^1\text{S}_0$ – $3s3p\ ^3\text{P}_0$ transition at 267 nm of natural linewidth ~ 8 mHz in singly ionized ^{27}Al is the transition of interest. However, the cooling scheme using 167 nm seems a challenging task due to inaccessibility of the laser. This problem is overcome by using quantum logic spectroscopy [115, 122, 123], where the cooling and state detection protocol is performed in the conventional way on a co-trapped logic ion having an accessible cooling transition [124]. $^9\text{Be}^+$, $^{25}\text{Mg}^+$ or $^{40}\text{Ca}^+$ are some of the used logic ions for $^{27}\text{Al}^+$; those not only provide sympathetic cooling but also help in state preparation and detection of the simultaneously trapped $^{27}\text{Al}^+$. Figure 4c also shows the energy-level diagram for the logic ion, $^9\text{Be}^+$. Both the main and logic ions are trapped in the same harmonic potentials, and their Coulomb coupling is utilized in deporting the electronic state information from $^{27}\text{Al}^+$ to $^9\text{Be}^+$ which helps in detection; thus, quantum jump profile of the main ion is mapped onto the logic ion [125]. A number of groups [123, 126, 127] have worked on $^{27}\text{Al}^+$ of which the NIST, USA group has achieved the best results till date.

6. Development of Optical Frequency Standard at CSIR–NPL

CSIR–NPL is the NMI of India and therefore entrusted with the responsibility of realization, maintenance and dissemination of the local Universal Coordinated Time (UTC–NPLI) and Indian Standard Time (IST). CSIR–NPL has already developed a Cs atomic fountain frequency standard [128], and we are working towards developing an optical frequency standard based on single trapped and laser cooled ^{171}Yb ion. This section will describe in a nutshell the experimental protocol of ^{171}Yb ion-based optical clock and the progress till date on developing such an optical clock at CSIR–NPL.

$^{171}\text{Yb}^+$ is one of the CIPM-recommended SRS candidates and possesses two transitions suitable for clocks in the optical domain of which quadrupole transition (E2) $^2\text{S}_{1/2}; F = 0, m_F = 0 > - ^2\text{D}_{3/2}; F = 2, m_F = 0 >$ and octupole transition (E3) $^2\text{S}_{1/2}; F = 0, m_F = 0 > - ^2\text{F}_{7/2}; F = 3, m_F = 0 >$ come with natural linewidths 3.02 Hz and 1 nHz, at 435.5 nm and 467 nm, respectively. We are working on the E3 transition having a Q-factor $\sim 10^{23}$ as it is advantageous for various reasons, the most important one being its $m_F = 0$ clock transition states which nullifies the first-order Zeeman shift. Also, trapped Yb^+ provides longer storage times as its cooling laser provides the photodissociation resonance for YbH^+ [129]. Additionally, this rare earth element is a fascinating candidate for probing certain basic physics problems, *e.g.* parity violation [130], measurement of temporal variation of fine structure constant [131], search of ultra-light scalar dark matter [132], etc. Many other groups have also worked on $^{171}\text{Yb}^+$ worldwide and have attained appreciable results [105, 119, 133].

The $^{171}\text{Yb}^+$ optical clock plan consists of obtaining ultra-high vacuum $\sim 10^{-11}$ mbar, production of ^{171}Yb thermal atomic beam using an atomic oven, photoionization of the atoms, trapping and laser cooling of single ion, probing clock transition and finally its establishment as an optical frequency standard using frequency comb. As can be seen from the energy-level diagram in Fig. 5, the strong $^2\text{S}_{1/2}; F = 1 > - ^2\text{P}_{1/2}; F = 0 >$ transition at 369.5 nm will be probed for laser cooling of the ion. For trapping the ion, we are using an end-cap-type Paul trap as it provides enough optical access for focusing multiple laser beams at the centre of the ion trap [134, 135]. The detailed design and geometry of the ion trap and the UHV chamber can be found in Refs. [21, 22, 136]. Narrow-bandwidth, high-voltage RF is a critical requirement for trapping potential, and the same is achieved and supplied to the ion trap through a helical resonator in order to evade undesirable power reflection due to impedance mismatching. A helical resonator with a resonant frequency of 27(7) MHz and a Q-factor of 600(8) has been built for this purpose [137, 138]. A narrow and collimated atomic beam source reduces the chances of developing patch potential due to atomic deposition on the trap electrodes or its surroundings. For this, a dark wall oven for Yb atomic source has been built which gives an atomic beam with divergence as low as $1.2(1)^\circ$ measured at an oven temperature of 250°C and produces an atomic flux of about 8×10^9 atoms s^{-1} [139]. Automation of such precision frequency metrology experiment is also a necessary task for running it reliably and continuously over several hours or days, minimizing manual errors [140]. Computer-controlled electronic devices such as DC power supply to supply voltages to the ion trap and compensation electrodes [141], constant current

source for heating atomic oven and driving Helmholtz coils, shutter drivers for controlling exposure time of lasers, frequency drivers for acousto-optic modulator (AOM) and electro-optic modulator (EOM) used for shifting laser frequencies, etc., have been indigenously designed and built. Four lasers along with their modulated frequencies will be used for the production as well as cooling of $^{171}\text{Yb}^+$; 399 nm (for photoexcitation of Yb), 369 nm (for photoionization, laser cooling and fluorescence detection), 760 nm and 935 nm (repump lasers for cooling cycle), and each laser needs to be stabilized to a reference atomic transition or to a Fabry–Perot cavity. An in-house designed and developed FPGA-based all-in-one function generator, lock-in amplifier and auto-relockable PID system serves for those purposes [142]. The narrow linewidth clock laser at 467 nm will be locked to a ULE cavity. A high-resolution imaging system with a minimum number of lenses has been designed for single-ion fluorescence detection. It gives a diffraction-limited performance, resolves ions separated by $\geq 0.68 \mu\text{m}$, minimizes spherical aberrations, magnifies by up to 238 times and performs well in the visible as well as near-infrared regions too. A sectional view of the design of the UHV chamber housing the Paul trap, the atomic oven, compensation electrodes and the in-vacuum lens holder is shown in Fig. 6. Various systematic uncertainties for $^{171}\text{Yb}^+$ optical frequency standard for both the optical clock transitions are also estimated [143]. Theoretical estimation of BBR shift, magic and tune-out wavelengths for the $^6\text{S}_{1/2}$ – $^5\text{D}_{3/2}$ clock transition in $^{171}\text{Yb}^+$ [144, 145] and accurate estimation of BBR shift resulting from excess capacitive load due to machining inaccuracy in the RF carrying parts of the trap-resonator assembly has also been carried out [146]. Recently, with the help of the built atomic oven, we carried out the photoexcitation of neutral Yb atoms and obtained atomic resonance fluorescence spectra for different isotopes as shown in Fig. 7. The ECDL laser is tuned at 398.11 nm and scanned over 2.5 GHz for probing $^1\text{S}_0$ – $^1\text{P}_1$ transition of Yb atoms. The emission signal is collected on a photon multiplier tube (PMT). Total eight emission peaks are obtained corresponding to different isotopes of Yb: ^{176}Yb , ^{173}Yb ($F = 5/2$), ^{174}Yb , ^{173}Yb ($F = 3/2$), ^{172}Yb , ^{173}Yb ($F = 7/2$), ^{171}Yb ($F = 3/2$), ^{171}Yb ($F = 1/2$) and ^{170}Yb . From the obtained spectrum, the transition frequency of ^{171}Yb ($F = 3/2$) is measured to be 751,527,365.77(28) MHz. Transition frequency shifts of the remaining isotopes from ^{171}Yb ($F = 3/2$) are also depicted in the figure. We are currently working on photoionization of $^{171}\text{Yb}^+$ using 369 nm laser.

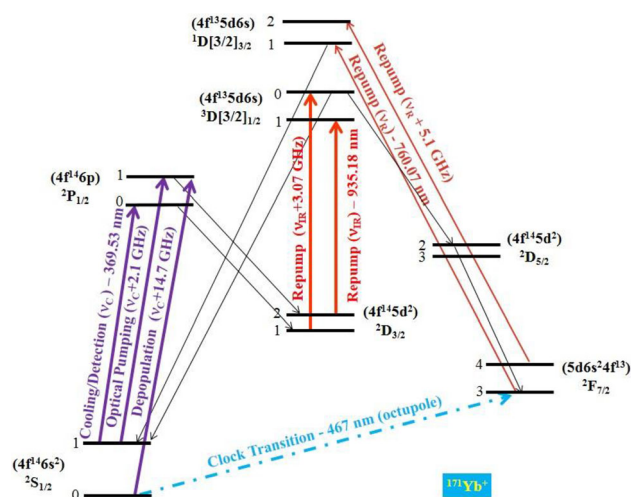


Fig. 5 Energy-level diagrams for $^{171}\text{Yb}^+$ showing the relevant transitions useful for building an optical ion clock

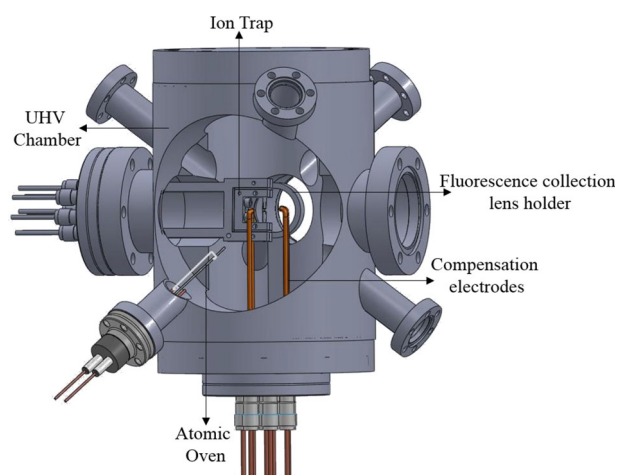


Fig. 6 Schematic of the UHV chamber at CSIR-NPL for building ^{171}Yb ion-based optical atomic clock. It houses the ion trap, atomic oven, compensation electrodes and the lens holder for fluorescence collection

7. Future Prospects

It is expected that in near future, the SI definition of time and frequency will be redefined on the basis of an optical transition of atoms or ion, replacing the existing SI definition based on a microwave transition of Cs atoms. Other than metrological applications, optical clocks have immense applications in different fields. A step up in its accuracy and its stability implies an upgradation and possibilities of new findings in the scientific fields. A few major applications are given in the following.

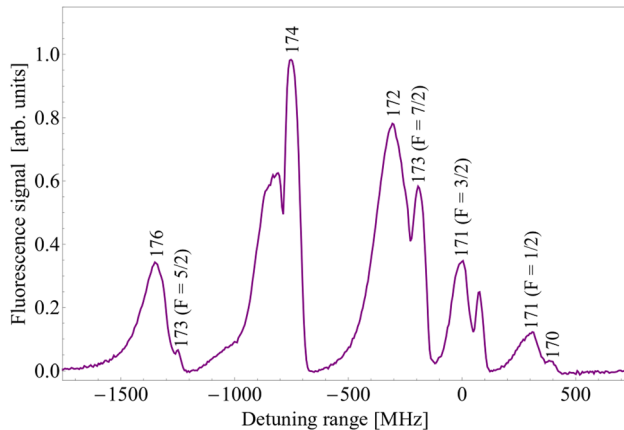


Fig. 7 Fluorescence spectra of various isotopes of Yb atom effusing from an atomic oven. Laser detuning frequency from the central frequency of ^{171}Yb ($F = 3/2$) is shown for the other isotopes

7.1. Relativistic Geodesy

Optical clocks are sensitive to Earth's gravitational potential (relativistic redshift effect), and this presents new perspectives in geodesy such as geoid mapping, establishment of a unified International height reference system, etc. [97, 147, 148].

7.2. Variation of Fundamental Constants

Many theories beyond the Standard Model state that the “fundamental constants” of nature are actually space–time dependent which would lead to variation in atomic and molecular spectra implying a variation in clock frequencies. Therefore, if these constants varied in values, the atomic clock ticking rate would also vary. Optical clock transitions demonstrate dependence on the fine-structure constant through relativistic corrections to the transition frequency [149, 150].

7.3. Technological Applications

Optical clocks can enhance navigation [4, 151, 152] and timekeeping capabilities in radar, radio astronomy and many other applications. It can also aid in optical frequency synthesis used for academic and industry applications.

7.4. Optical Clocks in Space

Optical clocks in space can thrust the significance of tests of fundamental physics such as Einstein's theory of relativity, detection of gravitational wave and aid in navigation with better precision and geoid monitoring [7, 153].

8. Conclusion

The refinement in performance demonstrated by optical frequency standards is of paramount importance as it would not only enhance efficiency of communications, navigation, signal synchronization and timing but most importantly has the potentiality of driving new fundamental physics tests, *e.g.* search for dark matter. These clocks with transitions oscillating in the optical domain can lead to a possible redefinition of SI unit of time and frequency. The thirst to keep excelling has brought us to this stage of accuracy and stability and will also take us beyond. New research trends in this field are based on multiple-ion clocks which exploit quantum entanglement between ions to improve clock stability. Probing nuclear transitions for developing clock is another promising proposal in this arena.

Acknowledgements The authors acknowledge the support from Council of Scientific and Industrial Research (CSIR), India. Lakhi Sharma thanks Department of Science and Technology (DST) for her Inspire fellowship. H. Rathore and Neelam thank University Grants Commission (UGC) for providing fellowship, and S. Utreja thanks CSIR for his fellowship.

References

- [1] L. Essen and J. V. L. Parry, An atomic standard of frequency and time interval: a caesium resonator, *Nature*, **4476** (1955) 280–282.
- [2] B. N. Taylor and A. Thompson, The international system of units (SI), NIST SP 330, U.S. Government Printing Office, 2008.
- [3] D. J. Wineland and W. M. Itano, Laser cooling of atoms, *Phys. Rev. A*, **20** (1979) 1521–1540.
- [4] F.G. Major, The quantum beat: principles and applications of atomic clocks, *Choice Rev. Online*, **45** (2007) 45–1523.
- [5] N. F. Ramsey, History of early atomic clocks, *Metrologia*, **42** (2005) S1–S3.
- [6] B. Guinot and E. F. Arias, Atomic time-keeping from 1955 to the present, *Metrologia*, **42** (2005) S20–S30.
- [7] L. Maleki and J. Prestage, Applications of clocks and frequency standards: from the routine to tests of fundamental models, *Metrologia*, **42** (2005) S145–S153.
- [8] S. G. Turyshev, From quantum to cosmos: fundamental physics research in space, Scientific Publishing Company, Berlin, 2009.
- [9] C. W. Chou, D. B. Hume, T. Rosenband and D. J. Wineland, Optical clocks and relativity, *Science*, **329** (2010) 1630–1633.
- [10] A. D. Ludlow, M. M. Boyd, J. Ye, E. Peik and P. O. Schmidt, Optical atomic clocks, *Rev. Mod. Phys.*, **87** (2015) 637–701.
- [11] N. Poli, C. W. Oates, P. Gill and G. M. Tino, Optical atomic clocks, *La Riv. del Nuovo Cim.*, **46** (2013) 555–624.
- [12] N. Batra, A. Roy, S. Majhi, S. Panja and S. De, Singly charged ions for optical clocks, *Asian J. Phys.*, **25** (2016) 1069–1092.
- [13] H. Katori, T. Ido and M. Kuwata-Gonokami, Optimal design of dipole potentials for efficient loading of Sr atoms, *J. Phys. Soc. Japan*, **68** (1999) 2479–2482.
- [14] J. McKeever, J. R. Buck, A. D. Boozer, A. Kuzmich, H. C. Nägerl, D. M. Stamper-Kurn and H. J. Kimble, State-

- insensitive cooling and trapping of single atoms in an optical cavity, *Phys. Rev. Lett.*, **90** (2003) 133602.
- [15] T. Udem, R. Holzwarth and T. W. Hänsch, Optical frequency metrology, *Nature*, **416** (2002) 233–237.
- [16] K. Beloy, D. R. Leibbrandt and W. M. Itano, Hyperfine-mediated electric quadrupole shifts in Al^+ and In^+ ion clocks, *Phys. Rev. A*, **95** (2017) 043405.
- [17] M. Takamoto, F. L. Hong, R. Higashi and H. Katori, An optical lattice clock, *Nature*, **435** (2005) 321–324.
- [18] F. L. Hong, Optical frequency standards for time and length applications, *Meas. Sci. Technol.*, **28** (2017) 012002.
- [19] C. W. Chou, D. B. Hume, J. C. J. Koelemeij, D. J. Wineland and T. Rosenband, Frequency comparison of two high-accuracy Al^+ optical clocks, *Phys. Rev. Lett.*, **104** (2010) 070802.
- [20] M. S. Safronova, M. G. Kozlov and C. W. Clark, Precision calculation of blackbody radiation shifts for optical frequency metrology, *Phys. Rev. Lett.*, **107** (2011) 143006.
- [21] S. De, N. Batra, S. Chakraborty, S. Panja and A. Sen Gupta, Design of an ion trap for trapping single $^{171}\text{Yb}^+$, *Curr. Sci.*, **106** (2014) 1348–1352.
- [22] A. Rastogi, N. Batra, A. Roy, J. Thangjam, V. P. S. Kalsi, S. Panja and S. De, Design of the ion trap and vacuum system for ^{171}Yb -ion optical frequency standard, *Mapan - J. Metrol. Soc. India*, **30** (2015) 169–174.
- [23] D. W. Allan, Statistics of atomic frequency standards, *Proc. IEEE*, **54** (1966) 221–230.
- [24] D. W. Allan, Time and frequency (time-domain) characterization, estimation, and prediction of precision clocks and oscillators, *IEEE Trans. Ultrason. Ferroelectr. Freq. Control*, **34** (1987) 647–654.
- [25] F. Riehle, Frequency standards: basics and applications, in *Freq. Stand. Basics Appl.*, Weinheim: Wiley-VCH, 2005.
- [26] W. M. Itano, J. C. Bergquist, J. J. Bollinger, J. M. Gilligan, D. J. Heinzen, F. L. Moore, M. G. Raizen and D. J. Wineland, Quantum projection noise: population fluctuations in two-level systems, *Phys. Rev. A*, **47** (1993) 169–183.
- [27] N. Ramsey, *Molecular beams*, Oxford University Press, Oxford, 1985.
- [28] R. W. P. Drever, J. L. Hall, F. V. Kowalski, J. Hough, G. M. Ford, A. J. Munley and H. Ward, Laser phase and frequency stabilization using an optical resonator, *Appl. Phys. B*, **31** (1983) 97–105.
- [29] M. Zhu and J. L. Hall, Stabilization of optical phase/frequency of a laser system: application to a commercial dye laser with an external stabilizer, *J. Opt. Soc. Am. B*, **10** (1993) 802–816.
- [30] E. D. Black, An introduction to Pound–Drever–Hall laser frequency stabilization, *Am. J. Phys.*, **69** (2001) 79–87.
- [31] J. Stenger, H. Schnatz, C. Tamm and H. R. Telle, Ultraprecise measurement of optical frequency ratios, *Phys. Rev. Lett.*, **88** (2002) 073601.
- [32] S. T. Cundiff and J. Ye, Colloquium: femtosecond optical frequency combs, *Rev. Mod. Phys.*, **75** (2003) 325–342.
- [33] J. L. Hall, Nobel lecture: defining and measuring optical frequencies, *Rev. Mod. Phys.*, **78** (2006) 1279–1295.
- [34] T. W. Hänsch, Nobel lecture: passion for precision, *Rev. Mod. Phys.*, **78** (2006) 1297–1309.
- [35] J. L. Hall, Nobel lecture: Defining and measuring optical frequencies, **78** (2006), 1279–1295.
- [36] J. L. Hall, J. Ye, S. A. Diddams, L. S. Ma, S. T. Cundiff and D. J. Jones, Ultrasensitive spectroscopy, the ultrastable lasers, the ultrafast lasers, and the seriously nonlinear fiber: A new alliance for physics and metrology, *IEEE J. Quantum Electron.*, **37** (2001) 1482–1492.
- [37] D. J. Jones, S. A. Diddams, J. K. Ranka, A. Stentz, R. S. Windeler, J. L. Hall and S. T. Cundiff, Carrier-envelope phase control of femtosecond mode-locked lasers and direct optical frequency synthesis, *Science*, **288** (2000) 635–639.
- [38] J. Reichert, R. Holzwarth, Th. Udem and T. W. Hänsch, Measuring the frequency of light with mode-locked lasers, *Opt. Commun.*, **172** (1999) 59–68.
- [39] H. R. Telle, G. Steinmeyer, A. E. Dunlop, J. Stenger, D. H. Sutter and U. Keller, Carrier-envelope offset phase control: A novel concept for absolute optical frequency measurement and ultrashort pulse generation, *Appl. Phys. B Lasers Opt.*, **69** (1999) 327–332.
- [40] Th. Udem, J. Reichert, R. Holzwarth and T. W. Hänsch, Accurate measurement of large optical frequency differences with a mode-locked laser, *Opt. Lett.*, **24** (1999) 881–883.
- [41] S. A. Diddams, T. Udem, J. C. Bergquist, E. A. Curtis, R. E. Drullinger, L. Hollberg, W. M. Itano, W. D. Lee, C. W. Oates, et al., An optical clock based on a single trapped $^{199}\text{Hg}^+$ ion, *Science*, **293** (2001) 825–828.
- [42] J. L. Hall, M. Zhu and P. Buch, Prospects for using laser-prepared atomic fountains for optical frequency standards applications, *J. Opt. Soc. Am. B*, **6** (1989), 2194–2205.
- [43] K. Gibble and S. Chu, Laser-cooled Cs frequency standard and a measurement of the frequency shift due to ultracold collisions, *Phys. Rev. Lett.*, **70** (1993), 1771–1774.
- [44] J. Ye, L. S. Ma and J. L. Hall, Molecular iodine clock, *Phys. Rev. Lett.*, **87** (2001) 270801.
- [45] R. W. Fox, J. A. Sherman, W. Douglas, J. B. Olson, A. D. Ludlow and C. W. Oates, A high stability optical frequency reference based on thermal calcium atoms, *IEEE Int. Freq. Control Symp. Proc.*, Baltimore (2012) 1–3
- [46] T. Kisters, K. Zeiske, F. Riehle and J. Helmcke, High-resolution spectroscopy with laser-cooled and trapped calcium atoms, *Appl. Phys. B Lasers Opt.*, **59** (1994) 89–98.
- [47] T. Trebst, T. Binnewies, J. Helmcke and F. Riehle, Suppression of spurious phase shifts in an optical frequency standard, *IEEE Trans. Instrum. Meas.*, **50** (2001) 535–538.
- [48] G. Wilpers, C. Degenhardt, T. Binnewies, A. Chernyshov, F. Riehle, J. Helmcke and U. Sterr, Improvement of the fractional uncertainty of a neutral-atom calcium optical frequency standard to 2×10^{-14} , *Appl. Phys. B Lasers Opt.*, **76** (2003) 149–156.
- [49] J. Friebe, A. Pape, M. Riedmann, K. Moldenhauer, T. Mehlstäubler, N. Rehbein, C. Lisdar, E. M. Rasel, W. Ertmer, et al., Absolute frequency measurement of the magnesium intercombination transition $^1\text{S}_0 \rightarrow ^3\text{P}_1$, *Phys. Rev. A At. Mol. Opt. Phys.*, **78** (2008) 033830.
- [50] K. Sengstock, U. Sterr, J. H. Müller, V. Rieger, D. Bettermann and W. Ertmer, Optical Ramsey spectroscopy on laser-trapped and thermal Mg atoms, *Appl. Phys. B Lasers Opt.*, **59** (1994) 99–115.
- [51] W. Paul and M. Raether, Das elektrische Massenfilter, *Zeitschrift für Phys.*, **140** (1955) 262–273.
- [52] T. Kurosu, M. Morinaga and F. Shimizu, Observation of the Ca $4s\ ^1\text{S}_0-4p\ ^3\text{P}_1$ transition in continuous free-falling cold atomic flow from an atom trap, *Jpn. J. Appl. Phys.*, **31** (1992) L273–L275.
- [53] T. Ido, T. H. Loftus, M. M. Boyd, A. D. Ludlow, K. W. Holman and J. Ye, Precision spectroscopy and density-dependent frequency shifts in ultracold Sr, *Phys. Rev. Lett.*, **94** (2005) 153001.
- [54] H. Katori, M. Takamoto, V. G. Pal’chikov and V. D. Ovsiannikov, Ultrastable optical clock with neutral atoms in an engineered light shift trap, *Phys. Rev. Lett.*, **91** (2003) 173005.
- [55] A. D. Ludlow, T. Zelevinsky, G. K. Campbell, S. Blatt, M. M. Boyd, M. H. G. De Miranda, M. J. Martin, J. W. Thomsen, S. M. Foreman, et al., Sr lattice clock at 1×10^{-16} fractional

- uncertainty by remote optical evaluation with a Ca clock, *Science*, **319** (2008) 1805–1808.
- [56] C. Shi, J. L. Robyr, U. Eismann, M. Zawada, L. Lorini, R. Le Targat and J. Lodewyck, Polarizabilities of the Sr 87 clock transition, *Phys. Rev. A*, **92** (2015) 012516.
- [57] M. Yasuda, H. Inaba, T. Kohno, T. Tanabe, Y. Nakajima, K. Hosaka, D. Akamatsu, A. Onae, T. Suzuyama, et al., Improved absolute frequency measurement of the ^{171}Yb optical lattice clock towards a candidate for the redefinition of the second, *Appl. Phys. Express*, **5** (2012) 102401.
- [58] N. D. Lemke, A. D. Ludlow, Z. W. Barber, T. M. Fortier, S. A. Diddams, Y. Jiang, S. R. Jefferts, T. P. Heavner, T. E. Parker, et al., Spin-1/2 optical lattice clock, *Phys. Rev. Lett.*, **103** (2009) 063001.
- [59] R. Schwarz, S. Dörscher, A. Al-Masoudi, S. Vogt, Y. Li and C. Lisdat, A compact and robust cooling laser system for an optical strontium lattice clock, *Rev. Sci. Instrum.*, **90** (2019) 023109.
- [60] T. Bothwell, D. Kedar, E. Oelker, J. M. Robinson, S. L. Bromley, W. L. Tew, J. Ye and C. J. Kennedy, JILA SrI optical lattice clock with uncertainty of 2.0×10^{-18} , *Metrologia*, **56** (2019) 065004.
- [61] R. Tyumenev, M. Favier, S. Bilicki, E. Bookjans, R. Le Targat, J. Lodewyck, D. Nicolodi, Y. Le Coq, M. Abgrall, et al., Comparing a mercury optical lattice clock with microwave and optical frequency standards, *New J. Phys.*, **18** (2016) 113002.
- [62] W. F. McGrew, X. Zhang, R. J. Fasano, S. A. Schäffer, K. Beloy, D. Nicolodi, R. C. Brown, N. Hinkley, G. Milani, et al., Atomic clock performance enabling geodesy below the centimetre level, *Nature*, **564** (2018) 87–90.
- [63] G. E. Marti, R. B. Hutson, A. Goban, S. L. Campbell, N. Poli and J. Ye, Imaging Optical Frequencies with 100 μHz Precision and 1.1 μm Resolution, *Phys. Rev. Lett.*, **120** (2018) 103201.
- [64] H. Dehmelt, Experiments with an isolated subatomic particle at rest, *Rev. Mod. Phys.*, **62** (1990) 525–530.
- [65] W. Paul, Electromagnetic traps for charged and neutral particles, *Rev. Mod. Phys.*, **62** (1990) 531–540.
- [66] D. Wineland and H. Dehmelt, Proposed $10^{14} \delta\nu/\nu$ laser fluorescence spectroscopy on Ti^+ mono-ion oscillator III (side band cooling), *Bull. Am. Phys. Soc.*, **20** (1975) 637.
- [67] R. Maiwald, A. Golla, M. Fischer, M. Bader, S. Heugel, B. Chalopin, M. Sondermann and G. Leuchs, Collecting more than half the fluorescence photons from a single ion, *Phys. Rev. A - At. Mol. Opt. Phys.*, **86** (2012) 043431.
- [68] H. G. Dehmelt, Mono-ion oscillator as potential ultimate laser frequency standard, *IEEE Trans. Instrum. Meas.*, **IM-31** (1982) 83–87.
- [69] D. J. Berkeley, J. D. Miller, J. C. Bergquist, W. M. Itano and D. J. Wineland, Minimization of ion micromotion in a Paul trap, *J. Appl. Phys.*, **83** (1998) 5025–5033.
- [70] F. Diedrich, J. C. Bergquist, W. M. Itano and D. J. Wineland, Laser Cooling to the Zero-Point Energy of Motion, *Phys. Rev. Lett.*, **62** (1989) 403–406.
- [71] D. J. Wineland and W. M. Itano, Laser Cooling, *Phys. Today*, **40** (1987) 34–40.
- [72] T. W. Hänsch and A. L. Schawlow, Cooling of gases by laser radiation, *Opt. Commun.*, **13** (1975) 68–69.
- [73] S. Stenholm, Laser cooling and trapping, *Eur. J. Phys.*, **9** (1988) 242–249.
- [74] C. J. Bordé, C. Salomon, S. Avrillier, A. Van Lerberghe, C. Bréant, D. Bassi and G. Scoles, Optical Ramsey fringes with traveling waves, *Phys. Rev. A*, **30** (1984) 1836–1848.
- [75] M. Harlander, M. Brownnutt, W. Hänsel and R. Blatt, Trapped-ion probing of light-induced charging effects on dielectrics, *New J. Phys.*, **12** (2010) 093035.
- [76] Q. A. Turchette, Kielpinski, B. E. King, D. Leibfried, D. M. Meekhof, C. J. Myatt, M. A. Rowe, C. A. Sackett, C. S. Wood, et al., Heating of trapped ions from the quantum ground state, *Phys. Rev. A*, **61** (2000) 063418.
- [77] T. Rosenband, D. B. Hume, A. Brusch, L. Lorini, P. O. Schmidt, T. M. Fortier, J. E. Stalnaker, S. A. Diddams, N. R. Newbury, et al., Frequency comparison of Al^+ and Hg^+ optical standards, 18th Int. Conf. Laser Spectrosc. Proc., Telluride (2008) 297–302.
- [78] C. Tamm, S. Weyers, B. Lipphardt and E. Peik, Stray-field-induced quadrupole shift and absolute frequency of the 688-THz $^{171}\text{Yb}^+$ single-ion optical frequency standard, *Phys. Rev. A*, **80** (2009) 043403.
- [79] J. Lodewyck, P. G. Westergaard, A. Lecallier, L. Lorini and P. Lemonde, Frequency stability of optical lattice clocks, *New J. Phys.*, **12** (2010) 059501.
- [80] T. L. Nicholson, S. L. Campbell, R. B. Hutson, G. E. Marti, B. J. Bloom, R. L. McNally, W. Zhang, M. D. Barrett, M. S. Safronova, et al., Systematic evaluation of an atomic clock at 2×10^{-18} total uncertainty, *Nat. Commun.*, **6** (2015) 7896.
- [81] W. M. Itano, External-field shifts of the $^{199}\text{Hg}^+$ optical frequency standard, *J. Res. Natl. Inst. Stand. Technol.*, **105** (2000) 829–837.
- [82] J. Keller, T. Burgermeister, D. Kalincev, J. Kiethe and T. E. Mehlstäubler, Evaluation of trap-induced systematic frequency shifts for a multi-ion optical clock at the 10^{-19} level, *J. Phys. Conf. Ser.*, **723** (2016) 012027.
- [83] H. S. Margolis, Optical frequency standards and clocks, *Contemp. Phys.*, **51** (2010) 37–58.
- [84] P. Gill, Optical frequency standards, *Metrologia*, **42**(2005) S125–S137.
- [85] N. Poli, C. W. Oates, P. Gill and G. M. Tino, Optical atomic clocks, *La Riv. del Nuovo Cim.*, **36** (2013) 555–624.
- [86] J. W. Farley and W. H. Wing, Accurate calculation of dynamic Stark shifts and depopulation rates of Rydberg energy levels induced by blackbody radiation. Hydrogen, helium, and alkali-metal atoms, *Phys. Rev. A*, **23** (1981) 2397–2424.
- [87] P. Dubé, A. A. Madej, Z. Zhou, J. E. Bernard, Evaluation of systematic shifts of the $^{88}\text{Sr}^+$ single-ion optical frequency standard at the 10^{-17} level. *Phys. Rev. A At. Mol. Opt. Phys.* **87** (2013) 023806.
- [88] H. S. Margolis, G. P. Barwood, G. Huang, H. A. Klein, S. N. Lea, K. Szymaniec and P. Gill, Hertz-level measurement of the optical clock frequency in a single $^{88}\text{Sr}^+$ ion, *Science*, **19** (2004) 1355–1358.
- [89] G. Wegner, Gravitational redshifts and the mass-radius relation, *Int. Astron. Union Colloq. Proc.*, New Hampshire (1989), 401–407.
- [90] R. F. C. Vessot, M. W. Levine, E. M. Mattison, E. L. Blomberg, T. E. Hoffman, G. U. Nystrom, B. F. Farrel, R. Decher, P. B. Eby, et al., Test of relativistic gravitation with a space-borne hydrogen maser, *Phys. Rev. Lett.*, **45** (1980) 2081.
- [91] G. Petit and P. Wolf, Computation of the relativistic rate shift of a frequency standard, *IEEE Trans. Instrum. Meas.*, **46** (1997) 201–204.
- [92] G. Petit and P. Wolf, Relativistic theory for time comparisons: a review, *Metrologia*, **42** (2005) S138–S144.
- [93] L. Blanchet, C. Salomon, P. Teyssandier and P. Wolf, Relativistic theory for time and frequency transfer to order c^{-3} , *Astron. Astrophys.*, **370**(2001) 320–329.
- [94] N. K. Pavlis and M. A. Weiss, The relativistic redshift with 3×10^{-17} uncertainty at NIST, Boulder, Colorado, USA, *Metrologia*, **40** (2003) 66–73.
- [95] S. Schiller, A. Görlitz, A. Nevsky, J. C. J. Koelemeij, A. Wicht, P. Gill, H. A. Klein, H. S. Margolis, G. Miletì, et al., Optical

- clocks in space, *Nucl. Phys. B - Proc. Suppl.*, **166** (2007) 300–302.
- [96] J. Grotti, S. Koller, S. Vogt, S. Häfner, U. Sterr, C. Lisdat, H. Denker, C. Voigt, L. Timmen, et al., Geodesy and metrology with a transportable optical clock, *Nat. Phys.*, **14** (2018) 437–441.
- [97] T. E. Mehlstäubler, G. Grosche, C. Lisdat, P. O. Schmidt and H. Denker, Atomic clocks for geodesy, *Reports Prog. Phys.*, **81** (2018) 064401.
- [98] B. J. Bloom, T. L. Nicholson, J. R. Williams, S. L. Campbell, M. Bishof, X. Zhang, W. Zhang, S. L. Bromley and J. Ye, An optical lattice clock with accuracy and stability at the 10⁻¹⁸ level, *Nature*, **506** (2014) 71–75.
- [99] K. Gibble, Scattering of cold-atom coherences by hot atoms: Frequency shifts from background-gas collisions, *Phys. Rev. Lett.*, **110** (2013) 180802.
- [100] T. Rosenband, D. B. Hume, P. O. Schmidt, C. W. Chou, A. Brusch, L. Lorini, W. H. Oskay, R. E. Drullinger, T. M. Fortier, et al., Frequency ratio of Al⁺ and Hg⁺ single-ion optical clocks; metrology at the 17th decimal place, *Science*, **319** (2008) 1808–1812.
- [101] BIPM - Recommended values of standard frequencies, <https://www.bipm.org/en/publications/mises-en-pratique/standard-frequencies.html>.
- [102] F. Riehle, P. Gill, F. Arias and L. Robertsson, The CIPM list of recommended frequency standard values: Guidelines and procedures, *Metrologia*, **55** (2018) 188–200.
- [103] S. M. Brewer, J. S. Chen, A. M. Hankin, E. R. Clements, C. W. Chou, D. J. Wineland, D. B. Hume and D. R. Leibbrandt, ²⁷Al⁺ quantum-logic clock with a systematic uncertainty below 10⁻¹⁸, *Phys. Rev. Lett.*, **123** (2019) 033201.
- [104] C. Tamm, N. Huntemann, B. Lipphardt, V. Gerginov, N. Nemitz, M. Kazda, S. Weyers and E. Peik, Cs-based optical frequency measurement using cross-linked optical and microwave oscillators, *Phys. Rev. A - At. Mol. Opt. Phys.*, **89** (2014) 023820.
- [105] N. Huntemann, C. Sanner, B. Lipphardt, C. Tamm and E. Peik, Single-Ion Atomic Clock with 3 × 10⁻¹⁸ Systematic Uncertainty, *Phys. Rev. Lett.*, **116** (2016) 063001.
- [106] P. Dubé, A. A. Madej, M. Tibbo and J. E. Bernard, High-accuracy measurement of the differential scalar polarizability of a ⁸⁸Sr⁺ clock using the time-dilation effect, *Phys. Rev. Lett.*, **112** (2014) 173002.
- [107] N. Ohtsubo, Y. Li, N. Nemitz, H. Hachisu, K. Matsubara, T. Ido and K. Hayasaka, Frequency ratio of an ¹¹⁵In⁺ ion clock and a ⁸⁷Sr optical lattice clock, (2020), <https://arxiv.org/abs/2008.06259>.
- [108] C. G. Parthey, A. Matveev, J. Alnis, B. Bernhardt, A. Beyer, R. Holzwarth, A. Maistrou, R. Pohl, K. Predehl, et al., Improved Measurement of the Hydrogen 1S-2S Transition Frequency, *Phys. Rev. Lett.*, **107** (2011) 203001.
- [109] G. Wilpers, C. W. Oates and L. Hollberg, Improved uncertainty budget for optical frequency measurements with microkelvin neutral atoms: Results for a high-stability 40Ca optical frequency standard, *Appl. Phys. B*, **85** (2006) 31–44.
- [110] P. Morzynski, M. Bober, D. Bartoszek-Bober, J. Nawrocki, P. Krehlik, L. Sliwczynski, M. Lipinski, P. Maslowski, A. Cygan, et al., Absolute measurement of the ¹S₀ - ³P₀ clock transition in neutral ⁸⁸Sr over the 330 km-long stabilized fibre optic link, *Sci. Rep.*, **5** (2015) 17495.
- [111] Y. Huang, H. Guan, P. Liu, W. Bian, L. Ma, K. Liang, T. Li and K. Gao, Frequency Comparison of Two ⁴⁰Ca⁺ Optical Clocks with an Uncertainty at the 10⁻¹⁷ Level, *Phys. Rev. Lett.*, **116** (2016) 013001.
- [112] R. L. Barger, J. C. Bergquist, T. C. English and D. J. Glaze, Resolution of photon-recoil structure of the 6573-Å calcium line in an atomic beam with optical Ramsey fringes, *Appl. Phys. Lett.*, **34** (1979) 850–852.
- [113] R. W. Fox, J. A. Sherman, W. Douglas, J. B. Olson, A. D. Ludlow and C. W. Oates, A High Stability Optical Frequency Reference Based on Thermal Calcium Atoms, *IEEE Int. Freq. Control Symp. Proc.*, Baltimore (2012) 1–3.
- [114] C. W. Oates, F. Bondu, F. R.w and L. Hollberg, A diode-laser optical frequency standard based on laser-cooled Ca atoms: sub-kilohertz spectroscopy by optical shelving detection, *Eur. Phys. J. D*, **7** (1999) 449–460.
- [115] U. Sterr, C. Degenhardt, H. Stoehr, C. Lisdat, H. Schnatz, J. Helmcke, F. Riehle, G. Wilpers, C. Oates, et al., The optical calcium frequency standards of PTB and NIST, *C. R. Phys.*, **5** (2004) 845–855.
- [116] C. Degenhardt, H. Stoehr, C. Lisdat, G. Wilpers, H. Schnatz, B. Lipphardt, T. Nazarova, P. E. Pottie, U. Sterr, et al., Calcium optical frequency standard with ultracold atoms: approaching 10⁻¹⁵ relative uncertainty, *Phys. Rev. A*, **72** (2005) 062111.
- [117] H. Katori, Optical lattice clocks and quantum metrology, *Nat. Photonics*, **5** (2011) 203–210.
- [118] R. Le Targat, L. Lorini, Y. Le Coq, M. Zawada, J. Guéna, M. Abgrall, M. Gurov, P. Rosenbusch, D. G. Rovera, et al., Experimental realization of an optical second with strontium lattice clocks, *Nat. Commun.*, **4** (2013) 2109.
- [119] S. Falke, N. Lemke, C. Grebing, B. Lipphardt, S. Weyers, V. Gerginov, N. Huntemann, C. Hagemann, A. Al-Masoudi, et al., A strontium lattice clock with 3 × 10⁻¹⁷ inaccuracy and its frequency, *New J. Phys.*, **16** (2014) 073023.
- [120] H. Hachisu, M. Fujieda, S. Nagano, T. Gotoh, A. Nogami, T. Ido, S. Falke, N. Huntemann, C. Grebing, et al., Direct comparison of optical lattice clocks with an intercontinental baseline of 9000 km, *Opt. Lett.*, **39** (2014) 4072.
- [121] W. Nagourney, N. Yu and H. Dehmelt, High resolution Ba⁺ monoion spectroscopy with frequency stabilized color-center laser, *Opt. Commun.*, **79** (1990) 176–180.
- [122] P. O. Schmidt, T. Rosenband, C. Langer, W. M. Itano, J. C. Bergquist and D. J. Wineland, Physics: Spectroscopy using quantum logic, *Science*, **309** (2005) 749–752.
- [123] S. Hannig, L. Pelzer, N. Scharnhorst, J. Kramer, M. Stepanova, Z. T. Xu, N. Spethmann, I. D. Leroux, T. E. Mehlstäubler, et al., Towards a transportable aluminium ion quantum logic optical clock, *Rev. Sci. Instrum.*, **90** (2019) 053204.
- [124] D. J. Larson, J. C. Bergquist, J. J. Bollinger, W. M. Itano and D. J. Wineland, Sympathetic cooling of trapped ions: A laser-cooled two-species nonneutral ion plasma, *Phys. Rev. Lett.*, **57** (1986) 70–73.
- [125] D. J. Wineland, C. Monroe, W. M. Itano, D. Leibfried, B. E. King and D. M. Meekhof, Experimental issues in coherent quantum-state manipulation of trapped atomic ions, *J. Res. Natl. Inst. Stand. Technol.*, **103** (1998) 259–328.
- [126] J. Zhang, K. Deng, J. Luo and Z. H. Lu, Direct laser cooling Al⁺ ion optical clocks, *Chinese Phys. Lett.*, **34** (2017) 050601.
- [127] K. F. Cui, J. J. Shang, S. J. Chao, S. M. Wang, J. B. Yuan, P. Zhang, J. Cao, H. L. Shu and X. R. Huang, Sympathetic sideband cooling of a ⁴⁰Ca⁺-²⁷Al⁺ pair toward a quantum logic clock, *J. Phys. B At. Mol. Opt. Phys.*, **51** (2018) 045502.
- [128] A. Acharya, V. Bharath, P. Arora, S. Yadav, A. Agarwal and A. S. Gupta, Systematic uncertainty evaluation of the cesium fountain primary frequency standard at NPL India, Mapan - J. Metrol. Soc. India., **32** (2017) 67–76.
- [129] K. Sugiyama and J. Yoda, Production of YbH⁺ by chemical reaction of Yb⁺ in excited states with H₂ gas, *Phys. Rev. A*, **55** (1997) R10–R13.
- [130] K. Tsigtukin, D. Dounas-Frazer, A. Family, J. E. Stalnaker, V. V. Yashchuk and D. Budker, Observation of a large atomic

- parity violation effect in ytterbium, *Phys. Rev. Lett.*, **103** (2009) 071601.
- [131] V. A. Dzuba and V. V. Flambaum, Relativistic corrections to transition frequencies of Ag I, Dy I, Ho I, Yb II, Yb III, Au I, and Hg II and search for variation of the fine-structure constant, *Phys. Rev. A*, **77** (2008) 012515.
- [132] A. Arvanitaki, J. Huang and K. Van Tilburg, Searching for dilaton dark matter with atomic clocks, *Phys. Rev. D*, **91** (2015) 015015.
- [133] S. A. King, R. M. Godun, S. A. Webster, H. S. Margolis, L. A. M. Johnson, K. Szymaniec, P. E. G. Baird and P. Gill, Absolute frequency measurement of the $^2S_{1/2}$ - $^2F_{7/2}$ electric octupole transition in a single ion of $^{171}\text{Yb}^+$ with 10^{-15} fractional uncertainty, *New J. Phys.*, **14** (2012) 013045.
- [134] E. C. Beatty, Simple electrodes for quadrupole ion traps, *J. Appl. Phys.*, **61** (1987) 2118–2122.
- [135] C. A. Schrama, E. Peik, W. W. Smith and H. Walther, Novel miniature ion traps, *Opt. Commun.*, **101** (1993) 32–36.
- [136] N. Batra, B. K. Sahoo and S. De, An optimized ion trap geometry to measure quadrupole shifts of $^{171}\text{Yb}^+$ clocks, *Chinese Phys. B*, **25** (2016) 113703.
- [137] N. Batra, S. Panja, S. De, A. Roy, S. Majhi, S. Yadav and A. Sen Gupta, Design and Construction of a Helical Resonator for Delivering Radio Frequency to an Ion Trap, *Mapan - J. Metrol. Soc. India*, **32** (2017) 193–198.
- [138] S. Panja, S. De, S. Yadav and A. Sen Gupta, Note: Measuring capacitance and inductance of a helical resonator and improving its quality factor by mutual inductance alteration, *Rev. Sci. Instrum.*, **86** (2015) 056104.
- [139] L. Sharma, A. Roy, S. Panja and S. De, Atomic flux distribution from a low-divergent dark wall oven, *Rev. Sci. Instrum.*, **90** (2019) 053202.
- [140] N. Batra, A. Roy, C. Samal, S. Majhi, S. Panja and S. De, Automation of an optical frequency standard experiment, 2nd Int. Conf. Control. Instrumentation, Energy Commun., Kolkata (2016), 78–82.
- [141] A. Roy, N. Batra, S. Majhi, S. Panja, A. Sen Gupta and S. De, Design of a Stable DC Voltage Source and Computer Controlling of It Using an Indigenously Developed All-Digital Addressing-Cum-Control Hardware, *Mapan - J. Metrol. Soc. India*, **33** (2018) 139–145.
- [142] A. Roy, L. Sharma, I. Chakraborty, S. Panja, V. N. Ojha and S. De, An FPGA based all-in-one function generator, lock-in amplifier and auto-relockable PID system, *J. Instrum.*, **14** (2019) 05012.
- [143] N. Batra, S. De, A. Sen Gupta, S. Singh, A. Arora and B. Arora, Systematic Shifts for Ytterbium-ion Optical Frequency Standards, (2014), <https://arxiv.org/abs/1405.5399>.
- [144] A. Roy, S. De, B. Arora and B. K. Sahoo, Accurate determination of black-body radiation shift, magic and tune-out wavelengths for the $^6S_{1/2} \rightarrow ^5D_{3/2}$ clock transition in Yb^+ , *J. Phys. B At. Mol. Opt. Phys.*, **50** (2017) 205201.
- [145] A. Roy, S. De, B. Arora and B. K. Sahoo, Polarizability and Magic Wavelength of Yb^+ Clock Transition $^2S_{1/2} \rightarrow ^2D_{3/2}$, *Proc. of Jt. Conf. Eur. Freq. Time Forum and IEEE Int. Freq. Control Symp.*, Besançon (2017), 753–757.
- [146] L. Sharma, A. Roy, S. Panja, V. N. Ojha and S. De, Estimation of the ion-trap assisted electrical loads and resulting BBR shift, *Sci. Rep.*, **8** (2018) 16884.
- [147] A. Bjerhammar, On a relativistic geodesy, *Bull. Géodésique*, **59** (1985) 207–220.
- [148] W. Shen, J. Ning, J. Liu, J. Li and D. Chao, Determination of the geopotential and orthometric height based on frequency shift equation, *Nat. Sci.*, **03**(2011) 388–396.
- [149] E. J. Angstmann, V. A. Dzuba and V. V. Flambaum, Relativistic effects in two valence-electron atoms and ions and the search for variation of the fine-structure constant, *Phys. Rev. A*, **70** (2004) 014102.
- [150] E. Peik, Fundamental constants and units and the search for temporal variations, *Nucl. Phys. B - Proc. Suppl.*, **203–204** (2010) 18–32.
- [151] M. S. Grewal, L. R. Weill and A. P. Andrews, *Global positioning systems, inertial navigation, and integration*, Wiley, Hoboken, 2006.
- [152] M. J. Rycroft, *Understanding GPS. Principles and applications*, *J. Atmos. Solar-Terrestrial Phys.*, **59** (1997) 598–599.
- [153] S. G. Dittus, Hansjörg, Lämmerzahl, Claus, Turyshev, *Lasers, clocks and Drag-free control - exploration of relativistic gravity in space*, Springer, Berlin, 2008.

Publisher's Note Springer Nature remains neutral with regard to jurisdictional claims in published maps and institutional affiliations.